Dimensional Dependence of Light Interaction with Nanowires

A Thesis

Submitted to the Faculty

of

Drexel University

by

Zhihuan Wang

in partial fulfillment of the

requirements for the degree

of

Doctor of Philosophy

September 2017

© Copyright 2017
Zhihuan Wang. All Rights Reserved.

This work is licensed under the terms of the Creative Commons Attribution-ShareAlike 4.0 International license. The license is available at http://creativecommons.org/licenses/by-sa/4.0/.

DEDICATIONS

This thesis is dedicated to my family. Their unconditional support and love was the foundation of success for my graduate studies. I want you to know that I love you so much and this thesis was only possible thanks to you.

ACKNOWLEDGMENTS

This dissertation summarized the research work I have accomplished during my graduate study in Drexel University. Over all these years, I obtained tremendous help from all the people around and I cannot complete the dissertation without expressing my gratitude to them.

This work would not have been possible without the support of my advisor, Dr. Bahram Nabet. His guidance helped to shape and provided much needed focus to my work. I would also like to thank my dissertation committee of Dr. Timothy Kurzweg, Dr. Baris Taskin, Dr. Nagarajan Kandasamy, Dr. Afshin Daryoush, Dr. Ioannis Savidis and Dr. Goran Karapetrov for their support and suggestions.

Many thanks to our generous collaborators, Dr. Adriano Cola, Dr. Anna Persano, Dr. Paola Prete at IMM-NCR in Italy, Dr. Nico Lovergine at University of Salento in Italy and Dr. Marc Currie from Navel Research Laboratory in Washington D.C. for their tremendous efforts in fabrication of the AlGaAs/GaAs core-shell nanowires and electro-optically sampling, micro-photoluminescence measurements of the devices. Although, I have not had the opportunity of meeting them yet, it is still a great pleasure to communicate with them in Email and I appreciate their valuable thoughts and discussions in many of the experimental results. I would also like to dedicate many thanks to Dr. Fernando Camino, Dr. Aaron Stein, Dr. Chang-Yong Nam, Dr. Mircea Cotlet and many other staffs at CFN of Brookhaven National Laboratory in Long Island for their assistance and suggestions in characterizing the devices.

I would also like to thank my friends in the Photonics Lab for all the help and support they provided, and especially for providing such a friendly and awesome place to work and study at. Pouya Dianat, Weston Aenchbacher and Shrenik Vora have spent countless hours listening to me talk about my research, helping me flesh out my ideas. And a special thanks to Jiajia Liu for accompanying me

during all these years and bringing countless happiness to my life.

Finally, my parents deserve my most sincere gratitude. I appreciate that you spent one or two months each year to be in the States with me, and that you always believed in, encouraged and loved me even when you lived on the other side of the earth.

TABLE OF CONTENTS

LIST OF TABLES vi

LIST OF FIGURES vii

ABSTRACT viii

1. INTRODUCTION 1

1.1 Background 3

1.1.1 Photonics and Optoelectronics 3

1.1.2 Core-Shell Nanowires 4

1.2 Literature Review 7

1.3 Scope and Organization of the Dissertation 11

2. OPTICAL ENHANCEMENT 13

2.1 Growth of Nanowires 14

2.2 Nanowire Morphology 15

2.3 Electrical Characterization of Nanowires 15

2.4 Electro-Optically Sampled Time Response 17

2.5 Optical Characterization of Nanowires 23

2.5.1 Absorption Enhancement 23

2.5.2 Emission Enhancement 25

2.5.3 Optical Amplification and Lasing 26

3. LIGHT CONFINEMENT 30

3.1 Light and Nanowire 30

3.1.1 Modal Analysis of Cylindrical Nanowire 30

3.1.2 Leaky Mode Resonance 34

3.1.3 Whispering Gallery Modes 35

3.1.4 Fabry-Pérot Resonant Mode 38

3.1.5 Helical Resonance Modes 39

3.2 Volumetric Modes 41

3.2.1 FDTD Simulation 41

3.2.2 Generalized Volumetric Modes 45

3.2.3 Geometry Dependence of Resonant Modes 47

3.2.4 Light Engineering of sub-wavelength Nano-structure 49

3.2.5 Continuous Variation of Geometry - The Tapering effect 52

4. ELECTRON DISTRIBUTION 54

4.1 Self-consistent Schrödinger-Poisson Solver 55

4.1.1 Finite Element Method 55

4.1.2 Variational form of Schrödinger and Poisson equations 56

4.1.3 Numerical Implementation 57

4.2 Electronic Distribution in Nanowires 58

4.2.1 Cylindrical Core-Shell Nanowire 60

4.2.2 Hexagonal Core-shell Nanowire 60

4.3 Conclusions 62

5. TRANSITION RATES 64

5.1 Optical Transition in Semiconductor 64

5.2 Optical Transition Rates in Semiconductor 67

5.2.1 Time-dependent Perturbation Theory 67

5.2.2 Fermi's Golden Rule 68

5.2.3 Upward and Downward Transition Rates 71

5.2.4 Photonic Modes Density 73

5.3 The Einstein Relations 75

5.4 Interband Transition Rates 78

5.4.1 Interband Transition Rates for a Bulk Semiconductor 78

5.4.2 Interband Transition Rates in A Quantum Well 83

5.4.3 Interband Transition Rates in nanowire 86

5.5 Contributing Factors 89

5.5.1 Overlap Integral 89

5.5.2 Oscillator Strength 90

5.5.3 Joint Optical Density of States 92

5.6 Spacial Overlapping 92

5.7 Many body effects 95

6. GAIN AND LASING 97

6.1 Background of Semiconductor Lasers 97

6.2 Operation Principle of Semiconductor Lasers 98

6.3 Lasing Characteristics 100

6.3.1 Absorption of Light 100

6.3.2 Optical Gain 102

6.4 Modeling of Nanowire Lasers 105

6.5 Laser Rate Equations 107

6.6 Linewidth Enhancement Factor 112

7. CONCLUSIONS AND FUTURE RESEARCH 115

7.1 Summary of Contributions 115

7.2 Outline of the future work 117

7.2.1 Plasmonic Effects 117

7.2.2 Heterogeneous Integration on PIC 119

BIBLIOGRAPHY 122

APPENDIX A: TIME-DEPENDENT PERTURBATION THEORY 133

APPENDIX B: PARTIAL CONFINEMENT ON THE ELECTRON IN CONDUCTION BAND 138

APPENDIX C: LASING MODELING 142

C.1 Steady-State Gain 144

C.2 Threshold Output Power 146

APPENDIX D: MEEP SIMULATION CODE 149

D.1 Cylindrical Core-Shell Nanowire 149

D.2 Hexagonal Core-Shell Nanowire 151

APPENDIX E: GAIN SPECTRUM AND THRESHOLD CALCULATION MATLAB CODE 154

APPENDIX F: NW LASING MODELING 165

F.1 FDTD Simulation Results Processing 165

F.2 Steady State Rate Calculation 168

VITA 171

LIST OF TABLES

6.1 Parameters and constants used for rate equation calculations. 101

6.2 Input parameters of the core-shell nanowire semiconductor laser. 111

6.3 Calculated parameters of core-shell nanowire semiconductor laser. Some of the parameters are calculated based on the FDTD simulation results. 111

LIST OF FIGURES

1.1 The Stained-glass window and the top modern lamps inside of the St. Patrick's Cathedral, 5th Ave, New York, NY. 2

1.2 Diagram of classification of nano-materials and nano-scale structures 5

1.3 Article with topics on optical properties of nanowires consist of a large portion of all the nanowire-related papers published from 2005 to 2016. 8

1.4 Diagram of nanowires applications and classifications 9

1.5 Scanning Electron Microscopy image of actual glo nanowire chip and the fabricated blue nLED. 11

2.1 Scanning Electron Microscopy image of as-grown GaAs/AlGaAs core-shell nanowires on Si taken at different magnifications and view angles (Image courtesy of Dr.Pouya Dianat) 16

2.2 Scanning Electron Microscopy (SEM) image of one dispersed core-shell nanowire connecting with the transmission line by Focus Ion Beam (FIB). (left) NW with small contact pad to connect the transmission line for I-V measurement. (right) NW with large contact pad to connect the transmission line for C-V measurement. 18

2.3 Current versus Voltage Measurement under illumination of Single Core-Shell Nanowire. 19

2.4 Capacitance versus Voltage Measurement under illumination of Single Core-Shell Nanowire. 20

2.5 Electro-optic sampling (EOS) time response measurement set up and results. 22

2.6 Reflectivity of GaAs (blue) and Si (green) substrates measured with $\sim 1\mu m$ normally incident beam. Courtesy of Dr. Marc Currie at Naval Research Lab. 24

2.7 Reflectivity spectrum of GaAs/AlGaAs core-shells grown on Si (red) and GaAs (black) substrates shows, normalized to volume, nearly two orders of magnitude more absorption of ligth. 25

2.8 Photoluminescence of bulk GaAs, Core-Shell Nanowires grown on GaAs and Si. 26

2.9 Micro-Photoluminescence measurements with fs-pulsed, 532-nm laser excitation at 250kHz repetition rate shows lasing of the as-grown wires. (Courtesy of Dr. Marc Currie at Naval Research Lab) 28

2.10 The pumping power intensity (L) versus output light power intensity (L) of as-grown core-shell nanowire operating at room temperature with a low threshold of $\sim 10\mu W$ and followed by saturation near $22\mu W$. (Courtesy of Dr. Marc Currie at Naval Research Lab) 29

3.1 (Top) Resonant modes in an infinitely long cylinder of GaAs with diameter of 220 nm with light incident parallel to NW axis. (Bottom) The Poynting vector at different time frames with light incident perpendicular to the NW axis from the right. The black lines show the physical boundary between the nanowire and air. 36

3.2 Several configuration of Whispering Gallery resonance modes in infinite long cylindrical and hexagonal nanowires. 37

3.3 Hexlically propagating modes for optical feedback. 40

3.4 A schematic illustration of Finite-Difference-Time-Domain (FDTD) Simulation Set Up. 43

3.5 (a) (top) Transverse plane mode for cylindrical and hexagonal core-only nanowire. (middle) The corresponding longitudinal plane mode. (bottom) Three dimensional simulation schematic for cylindrical and hexagonal nanowires. (b) 3D view of electromagnetic field distribution at the middle of a hexagonal NW. 44

3.6 Volumetric cavity modes' dependence on nanowire diameter. Top row is a radial cut at the middle of the wire, bottom row is the corresponding axial spatial variation. 46

3.7 Cavity modes for (a) core-only cylindrical, (b) core-shell cylindrical, (c) hexagonal core-only, and (d) hexagonal core-shell. The radius of nanowire is 185 nm and the height is 1 μm. 47

3.8 FDTD simulation results for different ratios, (top) $r_{core} = 40\% \ r_{shell}$ (middle) $r_{core} = 60\% \ r_{shell}$ and (bottom) $r_{core} = 80\% \ r_{shell}$, of core-shell radius of (left) air-core/AlGaAs-shell (right) GaAs-core/AlGaAs-shell cylindrical nanowires. 48

3.9 FDTD simulation results for different ratios, (top) $r_{core} = 40\% \ r_{shell}$ (middle) $r_{core} = 60\% \ r_{shell}$ and (bottom) $r_{core} = 80\% \ r_{shell}$, of core-shell radius of (left) air-core/AlGaAs-shell (right) GaAs-core/AlGaAs-shell hexagonal nanowires. 49

3.10 Geometric Dependence TM radius variation for different diameters and length. Top two rows are the transverse plane TM modes with diameters varying from 20 nm to 370 nm. Bottom row is the longitudinal plane TM modes with length varying from 0.5μm to 3μm. 50

3.11 Correlation of the volumetric TM modes' excitation wavelength with NW radius allows optimization of cavity for absorption and emission at desired wavelengths. 51

3.12 FDTD simulated electric field intensity distribution ($|E|^2$) of hexagonal core-shell nanowire on top of Si substrate with 5° tapering effect. (a, b) field intensity distribution along axial direction with different incident light wavelength, (c, d) field intensity distribution in the transverse plane at different positions along the NW. 53

4.1 A flow chart diagram of the Schrödinger-Poisson solver. The procedure is only discussed for electrons in the conduction band for simplicity but it also hold true for holes in the valence band using analogous formulas. 59

4.2 (left) Electron charge distribution in 3D illustration. (right) Conduction and valence band bending (black lines) and electron density distribution (blue line) for cylindrical core-shell nanowire. The inset shows the data captured from a vertical slice of the simulated structure. 60

4.3 (left) Three dimensional electron charge distribution in 3D illustration. (right) Conduction and valence band bending (blue lines) and electron density distribution (red line) for hexagonal core-shell nanowire with a low doping density. The inset shows the data captured from a (top) vertical or (bottom) horizontal slice of the simulated structure. . 61

4.4 (left) Two dimensional electron charge distribution in 3D illustration. (right) Conduction and valence band bending (blue lines) and electron density distribution (red line) for hexagonal core-shell nanowire with a moderate doping density. The inset shows the data captured from a (top) vertical or (bottom) horizontal slice of the simulated structure. . 62

4.5 (left) One dimensional electron charge distribution in 3D illustration. (right) Conduction and valence band bending (blue lines) and electron density distribution (red line) for hexagonal core-shell nanowire with a high doping density. The inset shows the data captured from a (top) vertical or (bottom) horizontal slice of the simulated structure. . 63

5.1 Schematic representation of various semiconductor materials' energy bandgaps (or wavelengths) with corresponding human eye response. 65

5.2 Schematic respresentation of optical absorption process in semiconductor (left) direct and (right) indirect bandgap materials. 66

5.3 Schematic representation of basic interaction of a two-level system and an optical field. . 67

5.4 The transition energy (black line, e_1-hh_1) as well as the spatial overlap integral (blue line) of the electron and hole ground state wave functions as a function of increasing $Al_xGa_{1-x}As$ x alloy content for a hexagonal $GaAs/Al_xGa_{1-x}As$ core-shell structure. . . 90

5.5 Exciton binding energy (solid) and oscillator strength per unit length (dashed) vs well thicknesses d_0 and d_1. 91

5.6 Effective mass value estimated in the wire direction in the lowest valence subband of $GaAs/Al_xGa_{1-x}As$ quantum wire. 93

5.7 The schematic plot of GaAs/AlGaAs core-shell nanowire electron charge distribution with band bending, and the FTDT-simulated (optical) electric field intensity distribution. 94

6.1 Basic structure of a junction laser in the form of a Fabry-Perot cavity, showing the active region and the coherent radiation output. 98

6.2 (left) Optical Process (absorption and emission) in a two level system. (right) Lasing mechanism with stimulated emission and population inversion in a three-levels system. . 99

6.3 Absorption Coefficient versus Photon Energy for 1D 2D and 3D with split plot. 101

6.4 Absorption Coefficient versus Photon Energy for 1D, 2D and 3D with multiple y axis. . 102

6.5 Gain coefficient and spontaneouse emission rate versus photon energy for different dimensionality. 104

6.6 Gain Model Fitting 104

6.7 Schematic diagram of a semiconductor Fabry-Perot laser 106

6.8 Flow chart diagram of modeling a semiconductor nanowire laser. 107

6.9 Calculated optical output power vs. pumping power, i.e., L-L curve. 112

6.10 The calculated steady state optical output power. 113

6.11 The calculated steady state gain G_m of semiconductor nanowire laser. 113

7.1 An FDTD-simulated electric field profile of (a) a hexagonal core-shell nanowire (CSNW), (b) CSNW covered with silver coating, (c) CSNW with embeded silver layer between the core and the shell, (d) CSNW with embedded 2DEG. 118

7.2 Schematic depiction of an optoelectronic nanosystem may include key components such as NW LED/laser source, photodetector/photocapacitor, NW antennas, and NW-enabled network-on-chip integrated on silicon. 121

ABSTRACT

Dimensional Dependence of Light Interaction with Nanowires
Zhihuan Wang
Advisor: Dr. Bahram Nabet

Semiconductor nanowires have been used in a variety of passive and active optoelectronic devices including waveguides, photodetectors, solar cells, LEDs, Lasers, sensors, and optical antennas. We examine GaAs/AlGaAs core-shell nanowires (CSNWs) grown on both GaAs and Si substrates by vapor-liquid-solid (VLS) method followed by Metal-Organic Chemical Vapor Deposition (MOCVD). These nanowires show extremely enhanced optical properties in terms of absorption, guiding, radiation of light, and even lasing. For the wavelength range of 700-1200nm these core-shells which only occupy 15% of the volume compared to thin films of the same height, reflect 2-4% of light for the CSNWs grown on Si, and 3-7% of light for those grown on GaAs substrate. The photoluminescence (PL) spectrum shows 923 times more light emitted from CSNWs grown on GaAs compared to bulk GaAs at room temperature, and optical pumped lasing with threshold of around $5\mu W$, followed by saturation near $12\mu W$. In addition, as-measured full-width half-max (FWHM) of ˜13 ps time response has been demonstrated for CSNW using Electro-Optically Sampling (EOS) measurement.

Analysis of the interaction of light with cylindrical and hexagonal structures with sub-wavelength diameters identifies both transverse and longitudinal plane modes which we generalize to volumetric resonant modes, importantly, without the need for vertical structures such as Bragg mirrors commonly used in vertical cavity surface emitting lasers (VCSEL's). We report on FDTD simulations with the aim of identifying the dependence of these modes on geometry (length, width), tapering, shape (cylindrical, hexagonal), core-shell versus core-only, and dielectric cores with semiconductor shells. This demonstrates how NWs form excellent optical cavities without the need for top and bottom mirrors.

However, optically equivalent structures such as hexagonal and cylindrical wires can have very different optoelectronic properties meaning that light management alone does not sufficiently describe the observed enhancement in upward (absorption) and downward transitions (emission) of light in nanowires, rather, the electronic transition rates should be considered. Using Fermi's Golden Rule in interaction of light and matter, we discuss how the transition rates change due to electronic wave function and identify three factors, namely, oscillator strength, overlap functions, and the joint optical density of states(JDOS), explicitly contributing to the transition rates with strong dependence on dimensionality.

We apply these results to the study of lasing in as-grown CSNW on Si & GaAs and discuss how these subwavelength structures can have enhanced optical gain, quantum efficiency and 175 times more optical output power compared to their bulk counterparts despite their large $> 200nm$ geometries. These results and findings will further facilitate the design and optimization of sub-micron scale optoelectronic devices. In conclusion, we make a case for photonic integrated circuits that can take advantage of the confluence of the desirable optical and electronic properties of these nanostructures.

CHAPTER 1

INTRODUCTION

The practice of staining glass for decorative purposes dates to ancient Rome, but the investigation of light matter interaction starts even back to the begining of history for human beings, when ancient men wondered about the source of light ,sun, or the first time to use a torch for hunting. People never stop studying how the light interacts with our world, meanwhile, this leads to improving our understanding and building a better world with photonic technology. The stained-glass windows such as the one inside of the St. Patrick's Cathedral in Fig. 1.1 served as a 'poor man's Bible' in the Middle Ages, allowing believers who could not read Latin to learn the story of the Gospels. The term stained glass refers to glass that has been coloured by adding metallic salts during its manufacture. Then this coloured glass is crafted into stained glass windows in which small pieces of glass are arranged to form patterns or pictures. Even nowadays, people are still surprised about how beautiful they are and wondering how the light interact with these pieces of art crafts. Besides the arts, lighting technology is also evolving very rapidly, from the ancient torchs to the bulb that Thomas Edison invented and to the modern LEDs such as the ones also shown in Fig. 1.1. From blackbody radiation to electroluminescence, i.e., from thermal radiation to radiative recombination, we are now capable of generating light more efficiently.

Now we find ourselves living through a new revolution in the age of information technology, one with consequences every bit as dramatic and likely even more profound as the data transmission by light. Electrons have served us very well for the past few decades, but the explosion of data. The storage and the transmission of data consumes large amount of power and time, simultaneously. Meeting

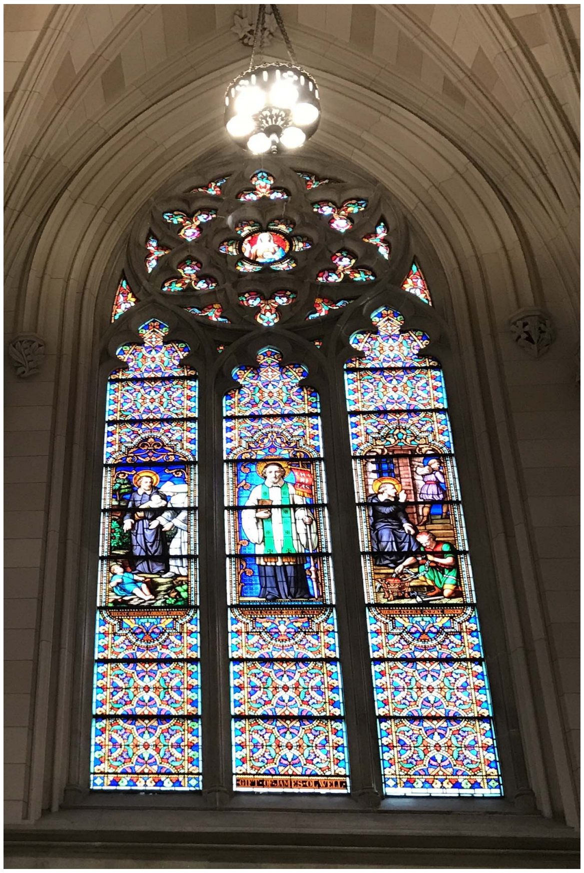

Figure 1.1 The Stained-glass window and the top modern lamps inside of the St. Patrick's Cathedral, 5th Ave, New York, NY.

the energy needs of the communication of information, together with storage and computation form a ”grand challenge” of the information age.

One good example of huge amount of power consumption by data transmission and computation is the data centers, which currently consume 1.5% of global energy production, and up to approximately 4% of U.S. energy produced. Though the statistics seems small, a 1000 times increase in the volume of data is predicted by 2025[1]. Google data center alone consumes enough electricity to power 200,000 homes, since an average Google search or a YouTube video or a message through Gmail uses 0.3 watt-hours of electricity[2]. Having efficient data computation and transmission tools will greatly reduce the total data center power consumption into a greener number. And the data pipelines of light can certainly be very helpful in this regime.

1.1 Background

1.1.1 Photonics and Optoelectronics

Photonics involves the generation, control and detection of lightwaves and photons, which are particles of light, in free space or solid. Optoelectronics is the study and application of effects related to the interaction of light and electronic signals, and may be considered a sub-field of photonics. Both photonics and optoelectronics study the light, and explore a wider variety of wavelengths besides visible lightwave range, from gamma rays to radio, including X-rays, ultraviolet and infrared light.

The invention and development of solar cells[3,4], photodetector[5,6], modulators[7,8], LEDs[9–11] and lasers[12,13] certainly set the example of breakthroughs due to the manipulation of photons in thin films and semiconductor bulk crystals. The continuing success of photonic technologies relies on the discovery of new optical materials and the miniaturization of optoelectronic devices that feature better performance, low cost and low power consumption. For the last few decades, countless efforts in nano-scale materials and devices research have created a rich collection of nanostructures where size, shape and composition can be readily controled. Many such nanostructures exhibit fascinating optical properties that could have significant impact in the future for photonic technology.

1.1.2 Core-Shell Nanowires

The primary principle for constantly miniaturizing the device is not only about the size, but also to have better electronic and optical properties. As the critical dimension of semiconductor solid-state devices keep shrinking, the effect of charge carriers quantization becomes more prominent, and to be more specific, this means the confinement of electrons or holes by constructing quantum confined structures. At the very dawn of electronics, the idea of using heterostructures (i.e., the structure with two layers or regions of dissimilar crystalline semiconductors) has emerged. After Shockley proposed the idea, Alferov and Kroemer introduced the concept that heterojuctions could possess high injection efficiencies in comparison with homojunctions, and which we know now is due to the confinement of carriers[14]. It would be very difficult today to imagine solid-state physics without semiconductor heterostructures for both electronic-based and optical-based applications. The heterostructures and, especially, double heterostructures, including quantum wells, nanowires, and quantum dots, are the fundamental building blocks for current nanoscience research as depicted in Fig. 1.2.

Quantum well is a potential well which confines particles to only move freely in two dimensions in stead of three dimensions, by forcing them to occupy a planar region. These wells are typically formed in semiconductors by having a narrower bandgap material sandwiched between two layers with wider bandgap materials. Electrons in quantum wells are confined in two dimensions either naturally or by doping the barrier of a quantum well, thus a two-dimensional electron gas (2DEG) may be formed at the heterointerface. This not only increases the density of electrons, but also causes a better performance in optoelectronic devices such as laser diodes[15], High Electron Mobility Transistors (HEMTs)[16,17], photodetectors[18,19], and solar cells[20,21].

Quantum dots, as another most common nanostructure in semiconductor physics, exhibit much more enhanced optical properties. They are normally only several nano-meters in size, and either synthesized or self-assembled into a bulk solid. As the particles in the quantum dots are confined in three dimensions, which leave them zero degree of freedom. As a result, the density of states changes

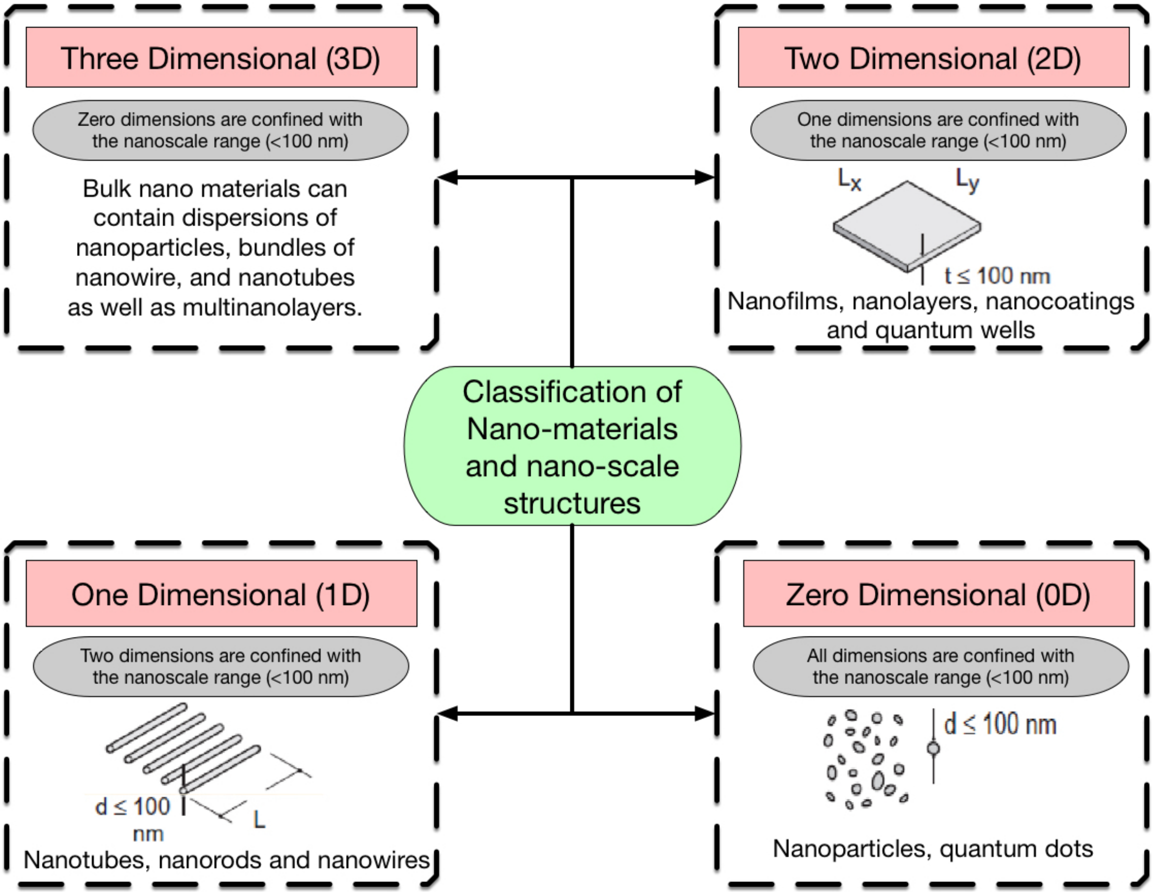
Three Dimensional (3D)
Zero dimensions are confined with the nanoscale range (<100 nm)
Bulk nano materials can contain dispersions of nanoparticles, bundles of nanowire, and nanotubes as well as multinanolayers.
Two Dimensional (2D)
One dimensions are confined with the nanoscale range (<100 nm)
Lx
Ly
t ≤ 100 nm
Nanofilms, nanolayers, nanocoatings and quantum wells
Classification of Nano-materials and nano-scale structures
One Dimensional (1D)
Two dimensions are confined with the nanoscale range (<100 nm)
d ≤ 100 nm
L
Nanotubes, nanorods and nanowires
Zero Dimensional (0D)
All dimensions are confined with the nanoscale range (<100 nm)
d ≤ 100 nm
Nanoparticles, quantum dots

Figure 1.2 Diagram of classification of nano-materials and nano-scale structures

to a delta function as opposed to a smooth square root dependence that is found in bulk materials. The narrower peak spectra and larger magnitude of intensity make them even better candidates in the application of solar cells[22], lasers[23,24] and light emitting diodes (LEDs)[25,26].

However, since the introduction in the 1990's, another important class of semiconductor nanostructures has emerged: structures with cross-sections of tens or hundreds of nano-meters and lengths up to several micro-meters. These structures are named as 'nanowires'[27] different from quantum dots as they are confined only in two dimensions, thus allowing electrons, holes or photons to propagate freely along the third dimension. Besides their own outstanding electro-optical properties, the high-aspect-ratio of these new semiconductor nanostructures allows for the bridging of the nanoscopic and macroscopic world. As P. Yang writes in their review paper:[28] "This nano-macro interface is fundamental to the integration of nanoscale building blocks in electrical or optoelectronic device applications. Conventional photonic platforms often consist of features with large aspect-ratios such as interconnects and waveguides, typically with micrometre dimensions. Thus, when semiconductor nanowires emerged they were immediately recognized as one of the essential building blocks for nanophotonics."

The development of sophisticated nanowires growth techniques[29,30], either bottom-up[31,32] or top-down[33], has stimulated a large body of new work in semiconductor nanowires over the last twenty years or so. Previously, the research activities focused on the growth of higher quality nanowires[34] and the variation of its constituent materials. At that time, most of the nanowires were core-only with ZnO[34], GaAs[35], Si[36], or Ge[37]. However, later on, researchers found out that growing an additional layer of shell can increase quantum yield by passivating the surface trap states. In addition, the shell provides protection against environmental changes, photo-oxidative degradation, and provides another route for modularity. Precise control of the size, shape and composition of both the core and the shell enable engineering the device with many degree of freedom and optoelectronic properties, such as the tuning of the emission wavelength over a wider range of wavelengths than with either individual semiconductor. Undoubtedly, much of this interest was further stimulated by the possibility of novel physics and applications in core-shell nanowires.

The successes of semiconductor nanowires in optoelectronics and the promising physical mechanisms using quantum-confined structures have, furthermore, enlivened the debate over possible applications of optics for functions such as transmission, logic and switching in communications and computation. It is important to emphasize at the outset that quantum confinement produces not only quantitative but also qualitative differences in physics compared to that in bulk structures, which is of course another major motivation for the interest in them. As Dr. Miller discussed in the paper about quantum well:[38] "There are many examples of these differences. The optical absorption spectrum breaks up into a series of steps associated with the quantum-confined electron and hole levels. Excitonic effects become much stronger because of the quantum confinement, giving clear absorption resonances even at room temperature. The relative importance of direct Coulomb screening and exchange effects is quite different in quantum wells (the Coulomb screening is relatively much weaker), giving very different optical saturation behaviour." Similar to quantum wells, nanowires have been observed to have even more profound differences in physics. Thus, the analysis and discussion about different behavior of nanowires and bulk semiconductors when they interact with light will be the primary topic of this dissertation.

1.2 Literature Review

Since the introduction of initially so-called 'nanowhiskers' in the 1990s[39], semiconductor nanowires have been extensively studied and much insight has been gained on tuning their electrical and optical properties. Nanowire related articles have shown a healthy increase in number published from 2005 to 2016, as Fig. 1.3 (blue bars) shows. Article with topics on optical properties of nanowires comprise a good portion in all the nanowire-related papers published in the recent decade, showing clear increasing trend in the number of papers on NW optics or photonics (green bars), presently comprising more than four-fifth of the nanowire-related articles.

The applications and classifications of NWs are shown in Fig. 1.4. In terms of the geometric strcuture, the most common NWs are cylindrical[40,41] and hexagonal[42,43] due to the growth techniques. And as discussed previously, there are core-only[44–46], core-shell[47,48] and core-multi-shell[49,50] configura-

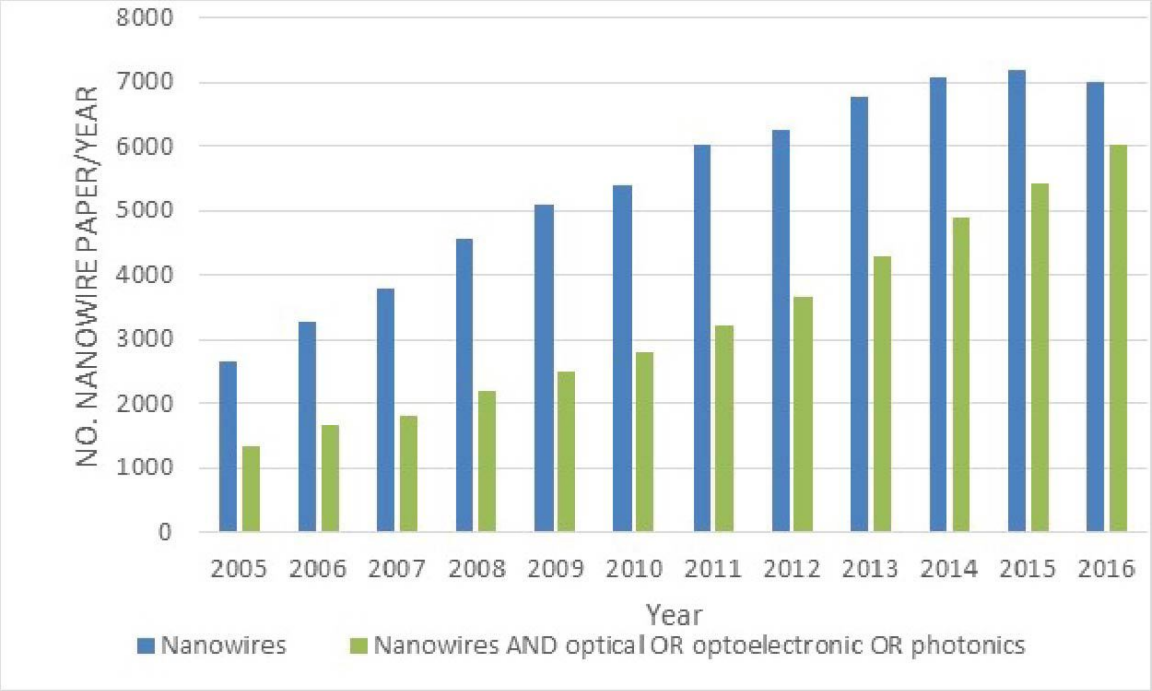

Figure 1.3 Article with topics on optical properties of nanowires consist of a large portion of all the nanowire related papers published from 2005 to 2016. (Source: ISI website, keyword: Nanowire (blue), Nanowire AND optical OR optoelectronic OR photonics (grey))

tions in order to exploit various properties of NWs. In addition, NWs have been used as electronic based devices, such as High Electron Movement Transistors (HEMTs)[51,52], Field Effect Transistors (FETs)[53–55], capacitors[56], diodes[57,58], and optoelectronic based devices, such as lasers[46,59–66], LEDs[67–71], Solar Cells[72–78], Photodetectors[40,79–83], waveguides[84–88], phototransistors[89–93].

Exciting developments have been made in the academia environment from many research groups worldwide, including notably the Lieber group at Harvard University[46,51,65,66,94,95], the Yang group at Berkeley[30,34,82,96,97], the Samuelson group at Lund University[57,81,98–100], and the Wang group at Georgia Tech[45,101–105]. With different perspectives, these research groups focus on a variation of NW materials, growth techniques and applications as shown in Fig. 1.4. The development of semiconductor NW materials follow the similar road as bulk materials, from initial single element (e.g., Si[36], Ge[37], Carbon[106] et al.) to compound binary (ZnO[96], GaN[66,107], CdSe[91], ZnS[108], ZnSe[109], InP[93], CdS[108], GaAs[110] et al.), ternary (InGaAs[111], CdSSe[112], AlGaN[113]) or even quater-

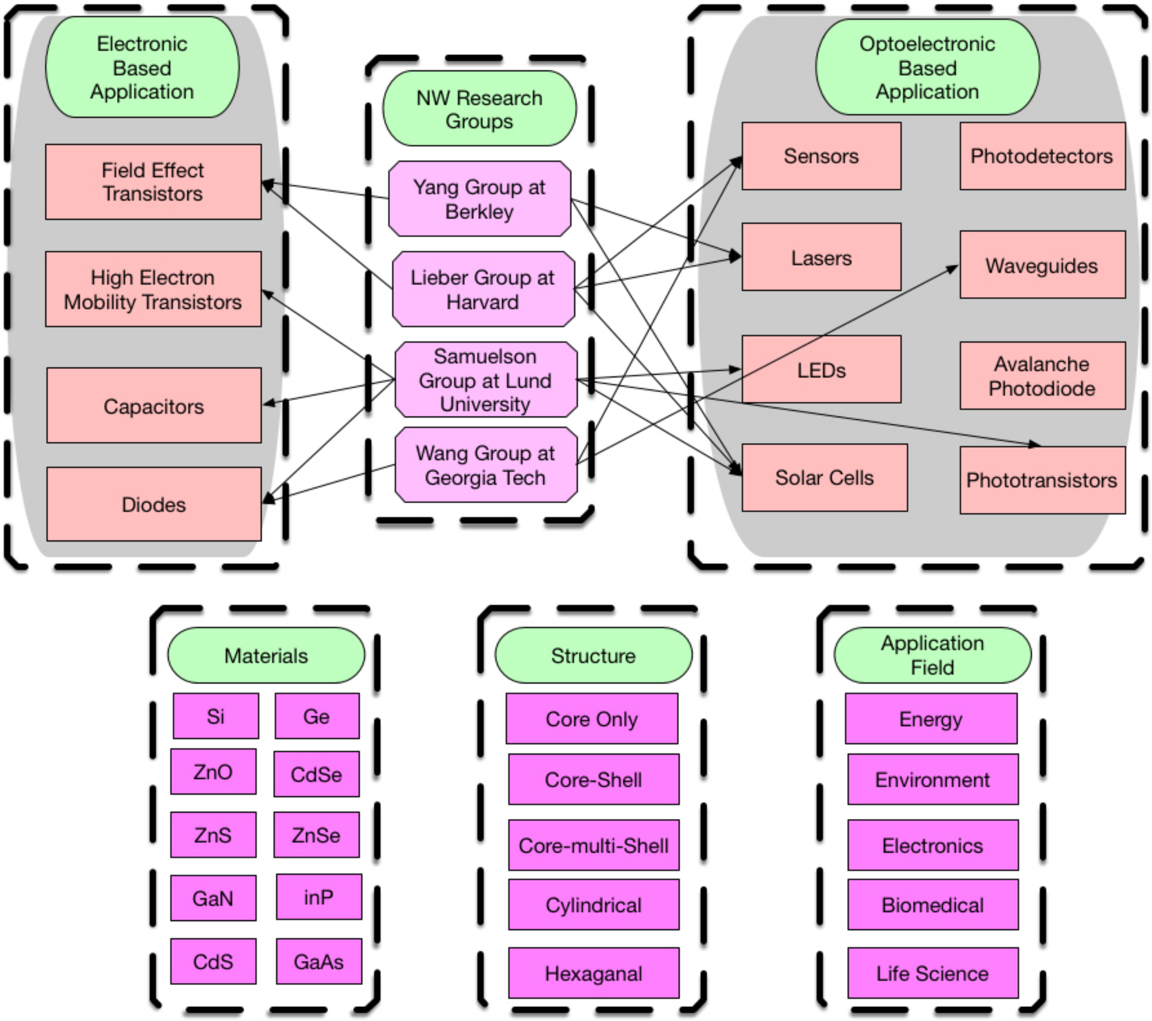
Electronic Based Application
Field Effect Transistors
High Electron Mobility Transistors
Capacitors
Diodes
NW Research Groups
Yang Group at Berkley
Lieber Group at Harvard
Samuelson Group at Lund University
Wang Group at Georgia Tech
Optoelectronic Based Application
Sensors
Photodetectors
Lasers
Waveguides
LEDs
Avalanche Photodiode
Solar Cells
Phototransistors
Materials
Si
Ge
ZnO
CdSe
ZnS
ZnSe
GaN
inP
CdS
GaAs
Structure
Core Only
Core-Shell
Core-multi-Shell
Cylindrical
Hexaganal
Application Field
Energy
Environment
Electronics
Biomedical
Life Science

Figure 1.4 Diagram of nanowires applications and classifications

nary (AlInGaN[114]), then to currently popular III-V heterostructure NWs(e.g., GaAs/AlGaAs[115,116], GaAs/InGaAs[117], InGaN/GaN[118], GaAs/GaAsP[64] et al.).

At the same time, many important electronic and optical properties have been observed, and some of the fundamental applications have been demonstrated as well. The first optical pumped nanowire laser was demonstrated by the Yang group[32] at 2001, and two years later, the Lieber group showed the first electrically injected nanowire laser[46] which makes NW a potential candidate to be integrated in the electronic-based integrated circuits.

In the field of industry and commercialization, several companies have started their adventure in the areas like energy, environment, bio-medicine etc., with products that influencing our daily life. The glo-USA, Inc.[119] is an LEDs manufacturing company at Sunnyvale, CA. They use nanowire arrays which fabricated on chip to generate light as shown in Fig. 1.5(a). Each nanowire acts basically as an individual light-emitting diode (LED) with two circular metal contacts as anode and cathod. The inset is the 45 degree magnified view of the NW array. Except the fabricated blue nLED as in Fig. 1.5(b), all color of the visible spectrum, ranging from deep blue to red, can be realized using nanowire LEDs with industry-standard semiconductor material and manufacturing equipment. Since these nanowires are made using one material system with the active layers grown on the non-polar plane, they can reduce the wavelength shift and efficiency drop that are observed with other commercially-available planar LEDs. This will enable a true white RGB (red, green and blue) LED without the need of lossy phosphor conversion, thus achieving the highest Color Rendering Index (CRI) and efficiency.

From academic research to industrial applications, from efficient electrons transportation to high quality light confinement, and from applications for environmental concerns to electronic devices in the daily life, the interaction of light and nanowires need to be investigated, thus, the major topic of this dissertation is to study the optoelectronics properties of core-shell nanowires and how they interact with light when electrons in this nano-scale structure are confined to lower dimensionality.

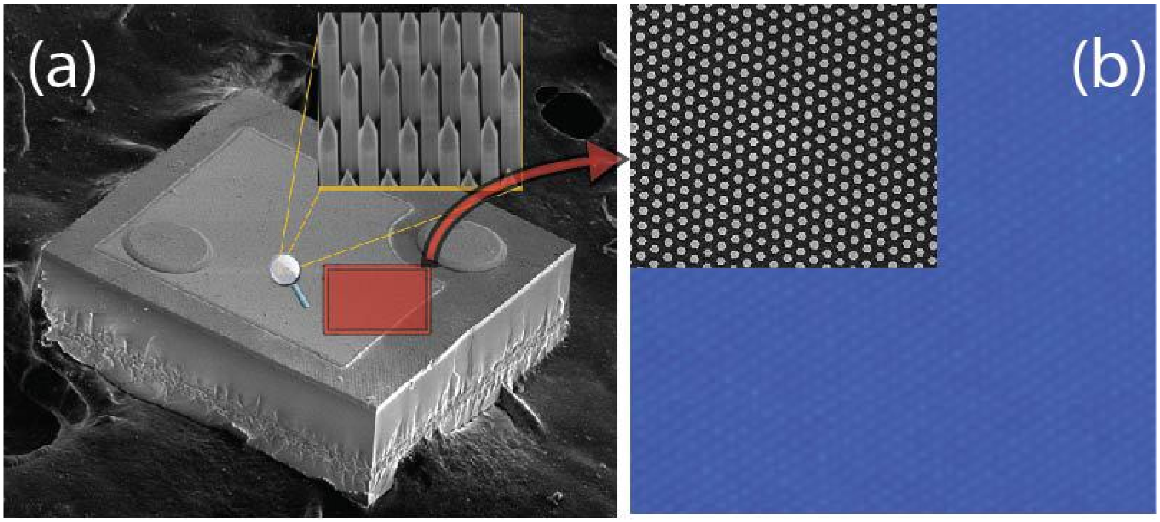

Figure 1.5 (a) SEM of actual glo nanowire chip showing magnified 45 degree view of individual nanowires. (b) The fabricated blue nLED. Each dot represents a nanowire LED. The inset shows top view SEM of nanowire array. Courtesy of glo-USA, Inc.

1.3 Scope and Organization of the Dissertation

This thesis is structured as follows. The growth techniques and electro-optical properties of core-shell nanowires are presented in Chapter 2. After introducing four different light confinement mechanisms, i.e., Leaky Mode Resonance, Whispering Gallery Modes, Fabry-Perot Resonant Mode and Helical Resonance Modes, Chapter 3 presents our findings for a generalized volumetric modes with light management of sub-wavelength cavities. Chapter 4 presents our methods and findings for calculating band-bending and electronic distribution in both cylindrical and hexagonal core-shell nanowire by solving Poisson-Schrodinger equations self-consistantly. In Chapter 5, we apply the inter-band optical transition rates study to understand the extremely enhanced optical properties of hexagonal core-shell nanowires, and identify three primary factors (overlap integral, oscillator strength and joint optical density of states) which are strong function of dimensionality. The quantum mechanical derivation based on perturbation theory and Fermi's Golden Rule used in this chapter are outlined in more detail in Appendix A. The modeling of lasing threshold based on the optical transition rates in Chapter 6 confirmed that our theoretical explanation, analysis and calculation of optical properties of core-shell nanowire have a very strong dependence on electron confinement. Finally, we present our conclusions in Chapter 7.

Throughout this work we use the term *nanowires* (NWs) to represent a specific quantum confined structure with cross-sections of 2-300 nm and lengths upwards of several micrometers. There are other research groups using terms such as *nanopillars*, *nanotubes* or *quantum well wires* (QWRs) to discuss the same nanostructures.

CHAPTER 2

OPTICAL ENHANCEMENT IN CORE-SHELL NANOWIRE

Given that the profound enhancement of optoeletronic properties of nanowires is the major theme of this dissertation, it is dutiful to first summarize the major experimental results, such as fabrication techniques and characteristics of core-shell nanowires (CSNWs).

A CSNW is a quasi-one dimensional structure with a wide band gap materials, such as AlGaAs, wrapping around a low band gap semiconductor, such as GaAs. It is expected that the lower dimensionality of electronic states in CSNW to have a significant influence on both optical and electrical properties of the structure. For instantce, electron systems in lower dimensions are adequately treated through perturbation methods, and the correlations among electrons are much more significant due to higher degrees of confinement. The electrons can be moving in the direction of NW growth axis and any small or localized interaction can cause a collective response from the whole system. Importantly, this one-dimensional electron system (1DES) can experimentally be realized in various material systems. These include carbon nanotubes, electrons at the edges of a two-dimensional electron system (2DES), and in NWs with small diameters.

Electrically it is important account for the electron correlations in order to determine the behavior of the structure. The significant values of exchange and correlation energies in 1DES, makes them an interesting candidate for probing their energy dynamics, and especially the interaction with light. This, however, imposes various experimental challenges and theoretical considerations and will be discussed in the following sections.

2.1 Growth of Nanowires

Freestanding quasi-one-dimensional semiconductor NWs based on III-V compound semiconductors, owing to their unique physical properties[120,121], are considered ideal building blocks for the realization of photonic and electronic nano-scale devices.

Currently, two bottom-up approaches to the fabrication of freestanding nanowires have been considered: (i) selective area epitaxy (SAE)[122] and (ii) metal-catalyst assisted growth through the so-called vapor-liquid-solid (VLS) mechanism[123,124]. The latter method relies on the alloying of a metal catalyst (usually Au) nanoparticle with the semiconductor constituent elements, supplied through a vapor phase. The as-formed alloy acts as an initial nucleation site for the material and further guides the nanowire growth, the diameter of the nanowire being controlled by that of the metal nanoparticle[125].

An advantage of the VLS method over SAE is that it does not require nanolithography processing of the substrate; furthermore, it is compatible with most advanced epitaxial growth techniques for III-V compounds, such as molecular beam epitaxy (MBE)[126,127], chemical beam epitaxy (CBE)[128], and metalorganic vapor phase epitaxy (MOVPE)[129,130]. In addition, the growth of expitaxial NWs allows precise control over the material composition and/or intentional doping along the NW length (i.e., growth direction). Most commonly used precursors of group-V elements are arsine (AsH_3) and phosphine, however, instead of using the toxic hydrides, the alkyl-substituted arsine and phosphine molecules will be much more safer and improve the materials' electronic properties. The detailed fabrication techniques will be discussed next.

GaAs nanowires were grown by our collaborators Drs. Paola Prete and Nico Lovergine of IMM-CNR and University of Salento, respectively, by low (50mbar) pressure MOVPE using an Aixtron reactor model AIX200 RD. Trimethylgallium (TMGa) and tertiarybutylarsine (TBAs) were used as gallium and arsenic precursors, respectively. Au nanoparticle deposited on $(\bar{1}\bar{1}\bar{1})B$ GaAs were used to catalyze the nanowire growth. To this purpose, VGF-grown semi-insulating (undoped) GaAs wafers oriented $(\bar{1}\bar{1}\bar{1})B$ were used. The substrates were then first degreased in isopropanol vapors, etched in $4H_2SO_4 : 1H_2O_2 : 2H_2O$ solution for 8 min at around 40 °c, rinsed in de-ionized water and finally dried under pure N_2. Au nanoparticles with $\sim 60nm$ diameters were prepared by reaction of $HAuCl_4$ with sodium citrate in aqueous solution and randomly deposited on the as-prepared GaAs surface by dropping a small amount of colloidal solution onto the substrate. The solvent (water) was then evaporated by holding the samples on a hot plate (in air) for a few minutes; Au nanoparticle surface densities thus achieved ranged around $(1-4) \times 10^8 cm^{-2}$.

After loading the sample into the reactor chamber, its temperature was raised, and sample annealing was then performed for 10 min to absorb GaAs surface oxides and organic residues originating from the Au nanoparticle synthesis. This annealing step would also allow the initial uptake of Ga atoms from the GaAs substrate into the Au nanoparticles. After ramping down the sample temperature to the final growth value, TMGa was admitted to the reactor chamber and the growth was initiated[130].

2.2 Nanowire Morphology

The nanowire morphology and dimensions were studied by scanning electron microscopy (SEM) observations using a Dual Beam Scanning Electron/Focused Ion Beam Microscope model FEI Helios; a primary electron beam acceleration voltage of 15 kV and a working distance of 10 mm were employed. Figure 2.1 is top view scanning electron microscopy (SEM) image of nanowires with $\sim 100nm$ diameter core of GaAs, $\sim 40nm$ thick of AlGaAs shell, and an additional $\sim 5nm$ GaAs cap layer. The four figures show the CSNWs array at different magnifications and view angles. These images demonstrate the rather sparse distribution of the wires. In addition, the wires are not fully arrayed with various growth directions and lengths. The most magnified view for the left bottom figure clearly indicate the CSNWs have hexagonal structure and tapering effect along the wire growth direction.

2.3 Electrical Characterization of Nanowires

The as-grown CSNWs are used to perform optical characterization measurement. However, in order to measure the CSNWs electrical performance, additional treatments have been taken to make

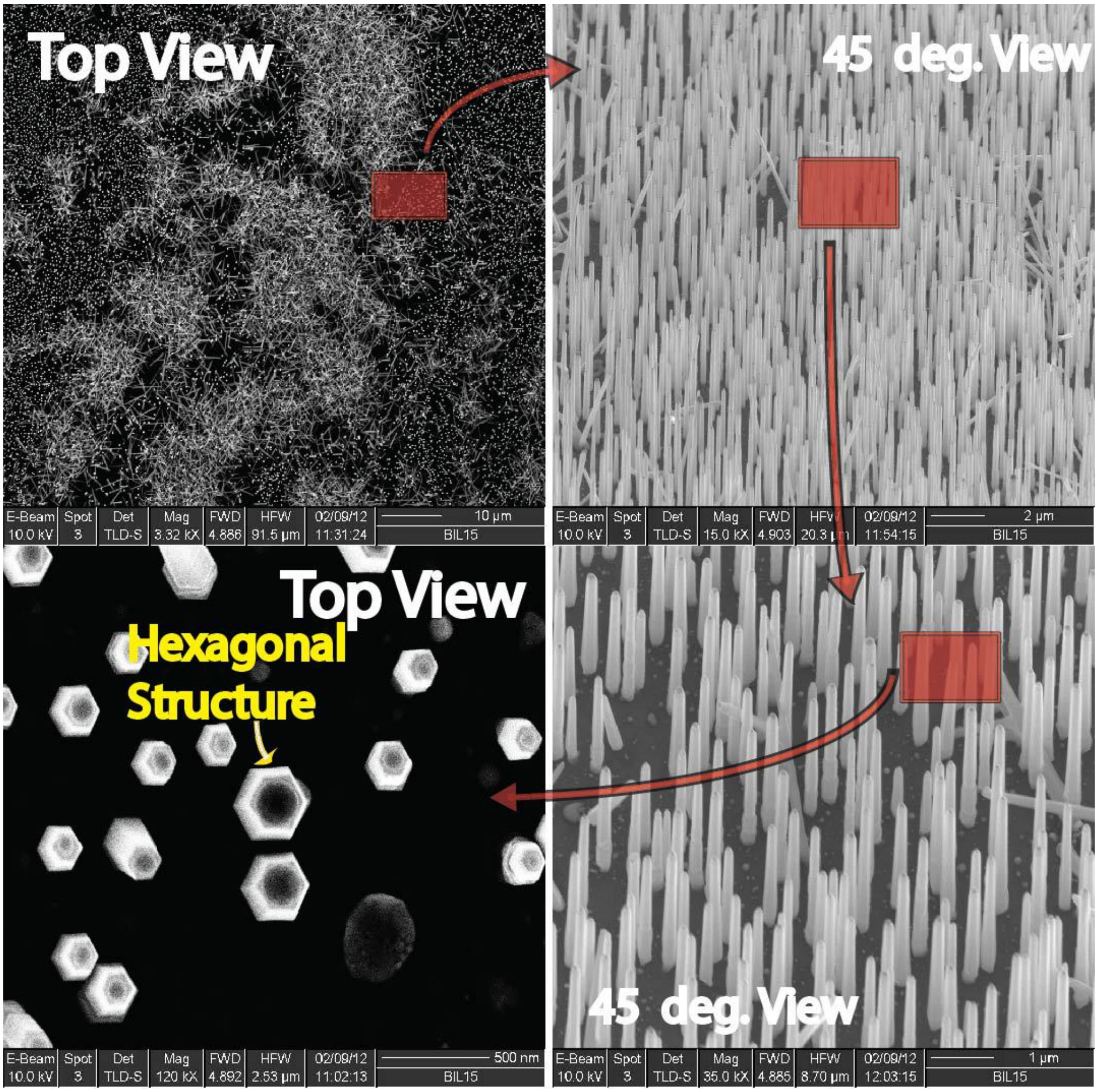
Top View
45 deg. View
E-Beam 10.0 kV | Spot 3 | Det TLD-S | Mag 3.32 kX | FWD 4.886 | HFW 91.5 µm | 02/09/12 11:31:24 | 10 µm | BIL15
E-Beam 10.0 kV | Spot 3 | Det TLD-S | Mag 15.0 kX | FWD 4.903 | HFW 20.3 µm | 02/09/12 11:54:15 | 2 µm | BIL15
Top View
Hexagonal Structure
45 deg. View
E-Beam 10.0 kV | Spot 3 | Det TLD-S | Mag 120 kX | FWD 4.892 | HFW 2.53 µm | 02/09/12 11:02:13 | 500 nm | BIL15
E-Beam 10.0 kV | Spot 3 | Det TLD-S | Mag 35.0 kX | FWD 4.885 | HFW 8.70 µm | 02/09/12 12:03:15 | 1 µm | BIL15

Figure 2.1 Scanning Electron Microscopy image of as-grown GaAs/AlGaAs core-shell nanowires on Si taken at different magnifications and view angles (Image courtesy of Dr.Pouya Dianat)

Ohmic contacts between nanowires and transmission lines. Figure 2.2 show the SEM image of one dispersed core-shell nanowire connecting with the transmission line by Focus Ion Beam (FIB) for (left) I-V and (right) C-V measurement. The CSNWs were first detached from the as-grown Si or GaAs substrate by ultrasonication[105,131] in an ethanol bath and dispersed between two transmission lines, then contacted with the transmission lines by FIB using platinum metal.

Characteristic current-voltage (I-V) curves of the nanowire device are given in Fig. 2.3. The experiment is performed with a room-temperature probe station connected with a Keithley 6487 picoammeter voltage source and a parameter analyzer. The light source is provided by a solar light simulation system with up to $90kW/cm^2$ light intensity. The I-V curve exhibits Ohmic behavior with decreasing of current under higher applied voltage and illumination, confirming that the device is a well-behaved conductor with the electric contact on both sides (Pt) ohmic. The reverse bias dark current of the device is very small, $\sim 4nA$ at -10V, and could be further improved by properly passivating the CSNW surface. Upon illumination, the device shows a photo-resistance response due to the excited electron distribution in the CSNW. And this response is magnified with higher bias voltage. Fig. 2.4 shows the capacitance of the device at 1Khz as a function of applied voltage with or without illumination. The metal contact pads of the CSNW device are made large enough to compensate the geometric capacitance as shown in Fig. 2.2(right). The capacitance of this typical device is measured to be $\sim 20-60pF$ based on a simple parallel-plate model and thus its cutoff frequency is mainly limited by the transit time of the photo-generated charge carriers in the device, which may in principle reach $\sim 100GHz$ after certain parameter optimization. With light illumination, the curve fitted capacitance (red line with red dots) increased to 80 pf with a significant transition of capacitance happened at -3.3V. The similar effect also observed in forward bias situation.

2.4 Electro-Optically Sampled Time Response

Transport properties of these NWs can be probed by high resolution electro-optic sampling (EOS) technique. The EOS set up is shown in Fig 2.5 (a). In essence, the EOS is an ultrafast sampling

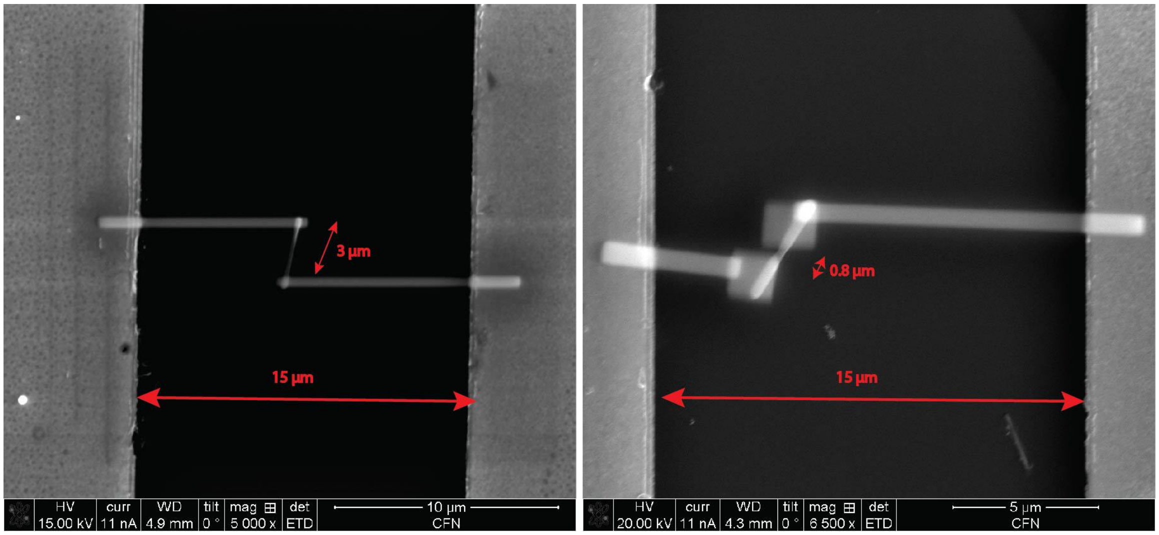

Figure 2.2 Scanning Electron Microscopy (SEM) image of one dispersed core-shell nanowire connecting with the transmission line by Focus Ion Beam (FIB). (left) NW with small contact pad to connect the transmission line for I-V measurement. (right) NW with large contact pad to connect the transmission line for C-V measurement.

oscilloscope that uses femtosecond laser pulses to excite optoelectronic transients and then measures the electronic response by probing the refractive index change of an electro-optic crystal placed on top of the device and/or transmission line. In the experiments performed at Naval Research Lab (NRL) by Dr. M. Currie, the laser is split into two paths: one path, the pump beam, is coupled into a fiber to excite the device and the other path, probe beam, passes through a $LiTaO_3$ crystal to sample the electric field of the propagating response. As shown in Fig. 2.5 (a, b) the CSNW were placed in the middle of a coplanar transmission line (TL), and connected to the TL by Focused Ion Beam (FIB) lithography. The distance between the two FIB contacts is ˜3.5 μm.

By varying the optical path of the sampling beam, the temporal response of the device is observed with a time resolution limited by the laser pulse width and the response of the electro-optic crystal. The amplitude sensitivity is limited by the noise in this detection system. The switching beam was modulated at 80 kHz and performed phase-sensitive detection with a lock-in amplifier on the light analyzed (with a polarizer and differential detection) from the $LiTaO_3$ crystal, in order to increase the sensitivity to sub-mV levels. In this experiment, ˜100 fs pulses from a Ti:sapphire laser with a

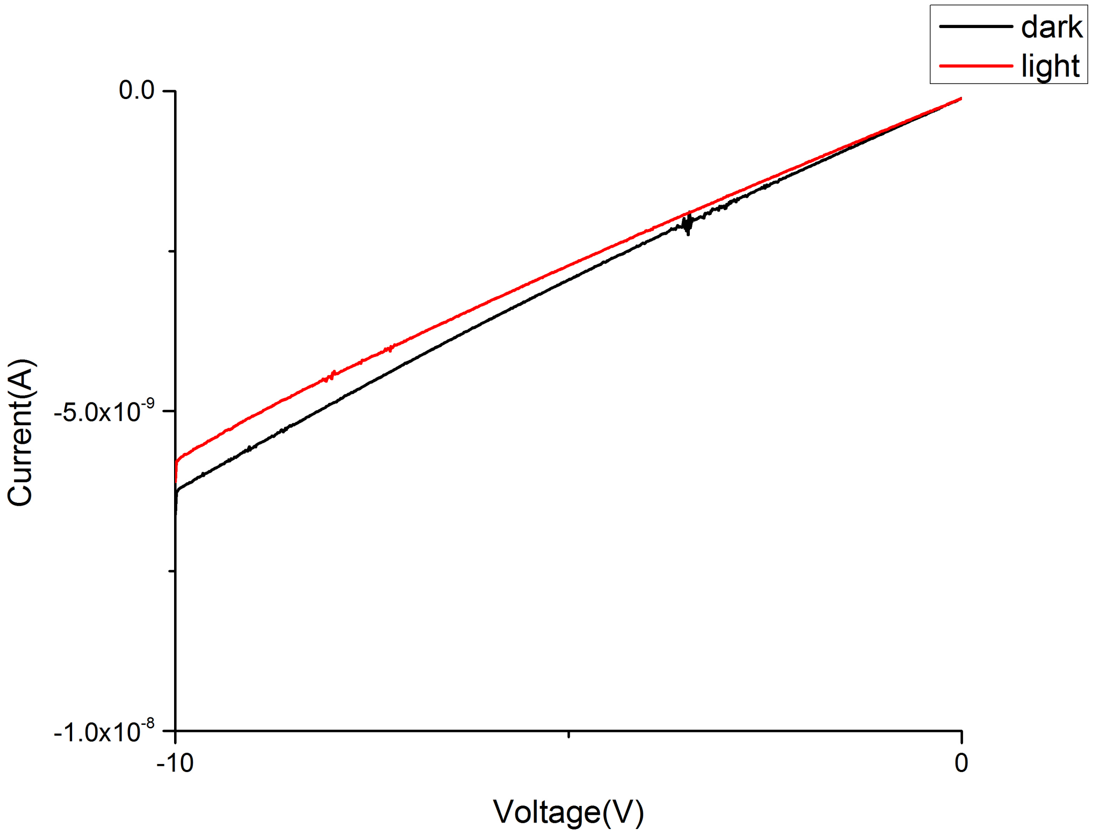

Figure 2.3 Current versus Voltage Measurement under illumination of Single Core-Shell Nanowire.

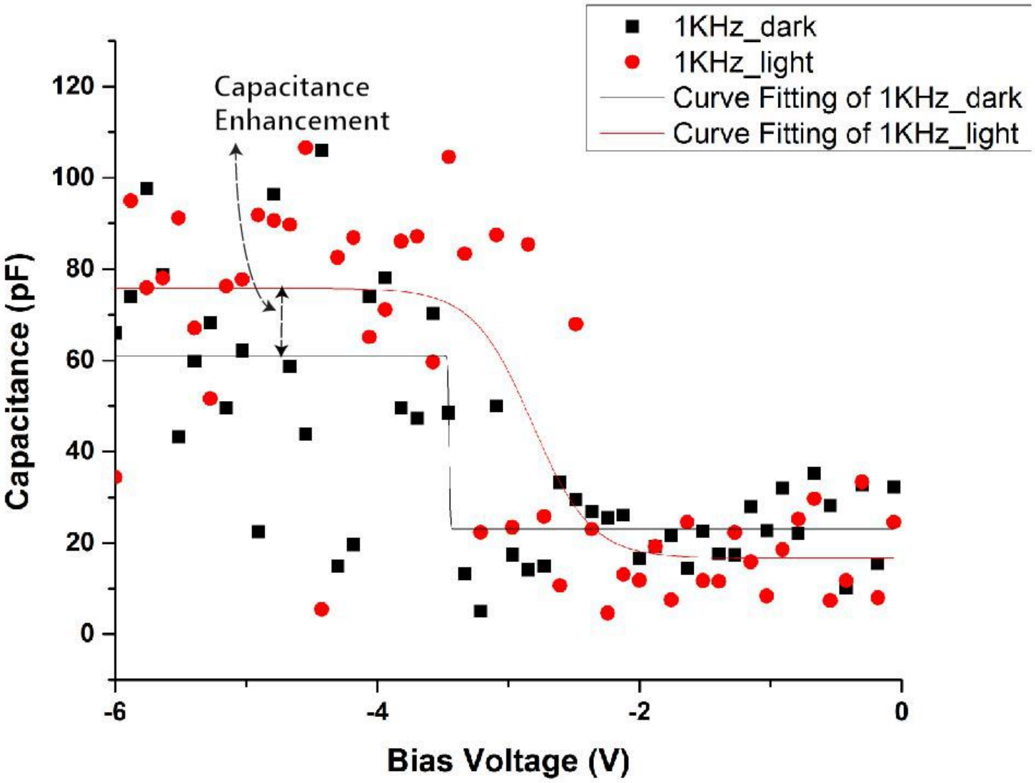

Figure 2.4 Capacitance versus Voltage Measurement under illumination of Single Core-Shell Nanowire.

center wavelength of 830 nm were split into the two paths. The path that is coupled into a fiber to excite the device under test (DUT) is dispersed by the fiber and excites as a 400 fs chirped optical pulse. The second laser path that passes through the $LiTaO_3$ crystal to sample the propagating electric field broadens slightly to a 150 fs optical pulse at the crystal. The photodetectors' electronic response is coupled to a coplanar strip (CPS) transmission line. The separation from the fiber exciting the device to the optical sampling crystal is $250\mu m$. The CPS transmission line is contacted with microwave probes for dc bias and $<$ 50 GHz measurements. Bias values from -10 to +10 V were applied to the CSNW structure with average optical powers ranging from 250 nW to 10 mW.

The current – voltage (I-V) measurements in ambient room light (dark) and under continuous wave (CW) illumination by an 830 nm Ti:sapphire laser were performed. The CSNW shows very low dark current (<0.1pA) which increases to 170nA average photocurrent with 2.6 mW of optical power which is remarkable for a single wire. This corresponds to a responsivity of 0.03 A/W, while the responsivity for the same volume of GaAs in bulk is $0.02\text{x}10^{-3}$ A/W. A three orders of magnitude increase in the responsivity demonstrates that CSNW is not only a good absorber but also converts energy more efficiently compared to their thin film counterparts. This I-V response result shows that the device is an efficient optical detector mostly due to the collection of carriers generated outside of the active region, which are efficiently collected in the low-dimensional electron gas reservoir which will be discussed shortly.

The time response data for the CSNW is shown in Fig. 2.5 (c) under applied bias of 10 V, showing as-measured full-width half-max (FWHM) of ˜13 ps. Several factors are involved in the temporal response measured via electro-optic sampling. The overall response comprises three major elements: 1) the device response, 2) the signal propagation, and 3) the electro-optic sampling system measurement. The measurement is a combination of these responses, resulting in a measured signal that is distorted. Thus, the device's intrinsic speed is even faster when the test set up limitations are considered.

Given the length of the wire, this result shows higher speed of both electron and hole transport in

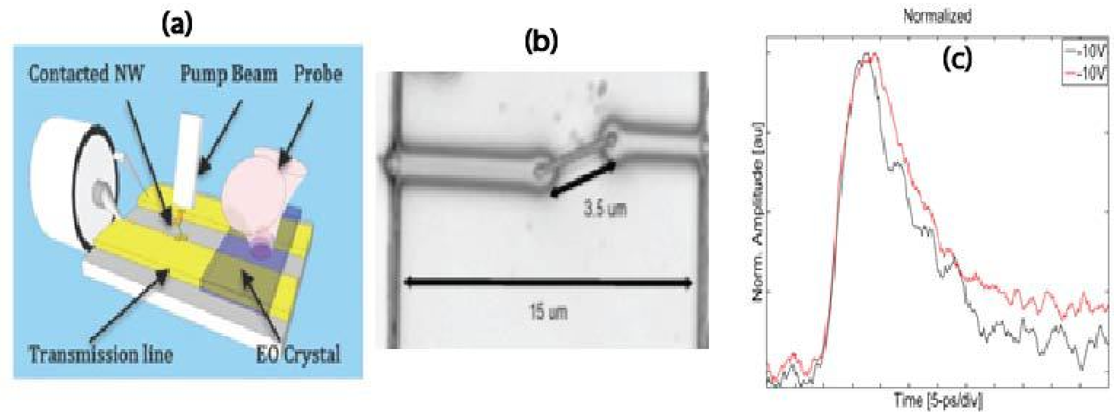

Figure 2.5 (a) Electro-optic sampling (EOS) time response measurement set up: RF probe is at one end of a transmission line in the middle of which the NW is contacted and is excited by 400 fs pulses of light delivered by fiber; probe beam samples the electric field through the electro-optic crystal. (b) Image of the FIB-contacted NWs. (c) Time response data. Courtesy of Dr. Marc Currie at Naval Research Lab.

the wire. This is due to the electron charge distribution in the core-shell nanowire. Different from the core-only nanowires or bulk semiconductor devices, the CSNWs are able to confine electrons primarily at the hetero-interface of GaAs core and AlGaAs shell, with small amount of electrons in the core. The movement of these charge carriers are confined in two-dimensions, forming a two-dimensional electron gas (2DEG) at the heterojunction. If the CSNW has hexagonal facet more optical excitation produces more electron-hole pairs, and higher order confinement or one-dimensional electron gas (1DEG) will be found as six (6) pillars of charge at the corners of the hexagonal CSNW[132]. In addition to the confined charge carriers' distribution in CSNWs, there is an electric field due to applied bias that moves the optically generated electrons to the 2DEG/1DEG. These optically generated carriers perturb the charge reservoirs, eliciting a collective response that is not limited by the transit of the charges to the contacts. Analogous to a drop exciting a wave in a reservoir that is detected more rapidly than the drop's transport by current flow, charge plasma confined in a semiconductor can transfer energy, hence respond much faster than the electric field-induced carrier drift current.

2.5 Optical Characterization of Nanowires

Linear optical spectroscopic techniques, such as absorption, luminescnence and modulation spectroscopy, have for a long time been important tools in understanding the basic physics of semiconductor devices and materials. Also, over the last fifteen years or so, semiconductor optical and optoelectronic properties have become of increasing technological importance in their own right. The ever-growing application of semiconductor diode lasers and related optoelectronic technology in communications and consumer products has helped to give yet further impetus to research to optical, electronic and optoelectronic properties of as-grown core-shell nanowires.

2.5.1 Absorption Enhancement

The reflectance spectra measurement was performed with an Oriel 77501 white light source to illuminate the samples after being coupled through a 1 mm fiber, collimated with a lens and focused onto the sample with a 25x reflecting objective. Reflectivity was measured by using a glass cover slip as a beamsplitter to couple 5% of the light onto the sample while transmitting 95% of the reflected light. The reflected light was coupled into a 1 mm fiber with a 10x objective and the spectra were measured with an Ando6317B OSA. Figure 2.6 shows the reflectivity of a GaAs wafer on which 50 nm thin film of AlGaAs is grown, and compared this to the reflectivity spectrum of a Si substrate[133]. As expected, about 30% to 55% of a normally incident light is reflected in bulk Si and GaAs, with a sharp change for wavelengths near their respective band gaps. All the data are normalized to the reflectivity of gold (Au).

Figure 2.7 contrasts this with the measured reflectance spectra of two types of GaAs core, AlGaAs shell nanowires (CSNWs): those grown on a GaAs substrate (black), and the others heteroexpitaxially grown on a Si substrate (red)[133]. The spectra show that both cases have the signature change of reflectivity at badgap of GaAs, i.e., these spectra are due to the GaAs/AlGaAs CSNWs, not the substrate. Importantly, for the wavelength range of 700-1200nm these core-shells which only occupy 15% of the volume compared to thin films of the same height, reflect 2-4% of light for

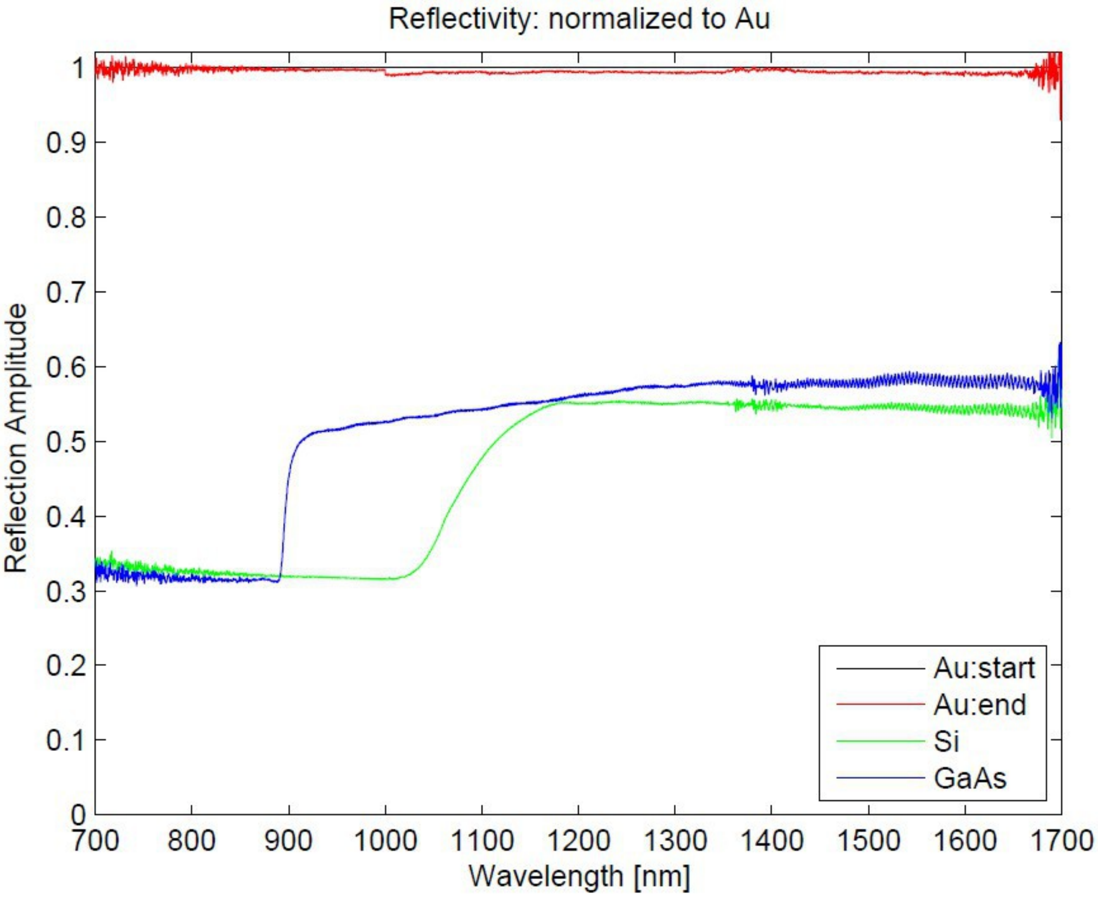

Figure 2.6 Reflectivity of GaAs (blue) and Si (green) substrates measured with $\sim 1\mu m$ normally incident beam. Courtesy of Dr. Marc Currie at Naval Research Lab.

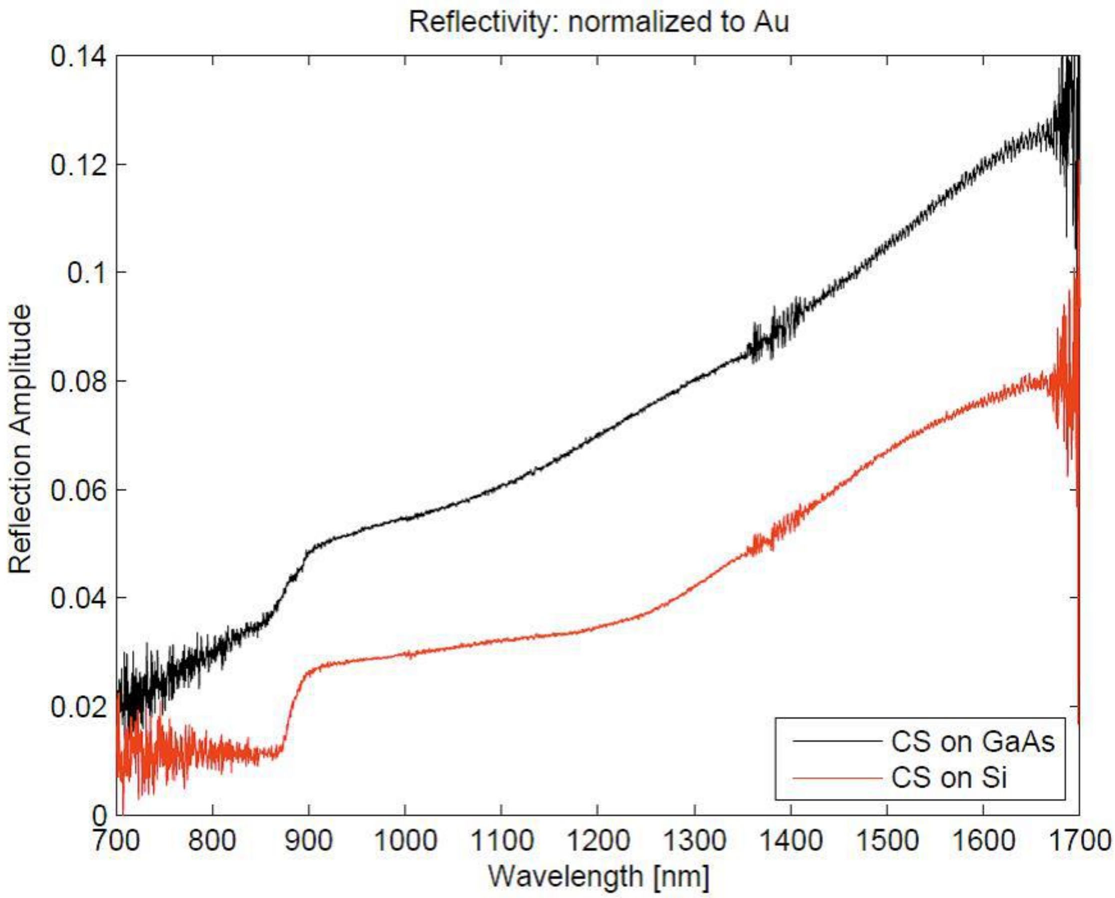

Figure 2.7 Reflectivity spectrum of GaAs/AlGaAs core-shells grown on Si (red) and GaAs (black) substrates shows, normalized to volume, nearly two orders of magnitude more absorption of ligth.

the CSNWs grown on Si, and 3-7% of light for those grown on GaAs substrate. The beam-width of the incident light being $\sim 1\mu m$, this shows that only a few NWs are interrogated by ligth and, normalized to volume, these wires absorb more than two orders of magnitude more ligth than their thin-film counterparts.

2.5.2 Emission Enhancement

A more robust probe of interaction of light and matter can be produced by inspecting the luminescence spectra. Figure 2.8 compares room temperature micro photoluminescence (PL) spectrum of bulk GaAs to CSNWs grown on GaAs, and two cuts of Si[43]. The ratio of peak luminescence of a)

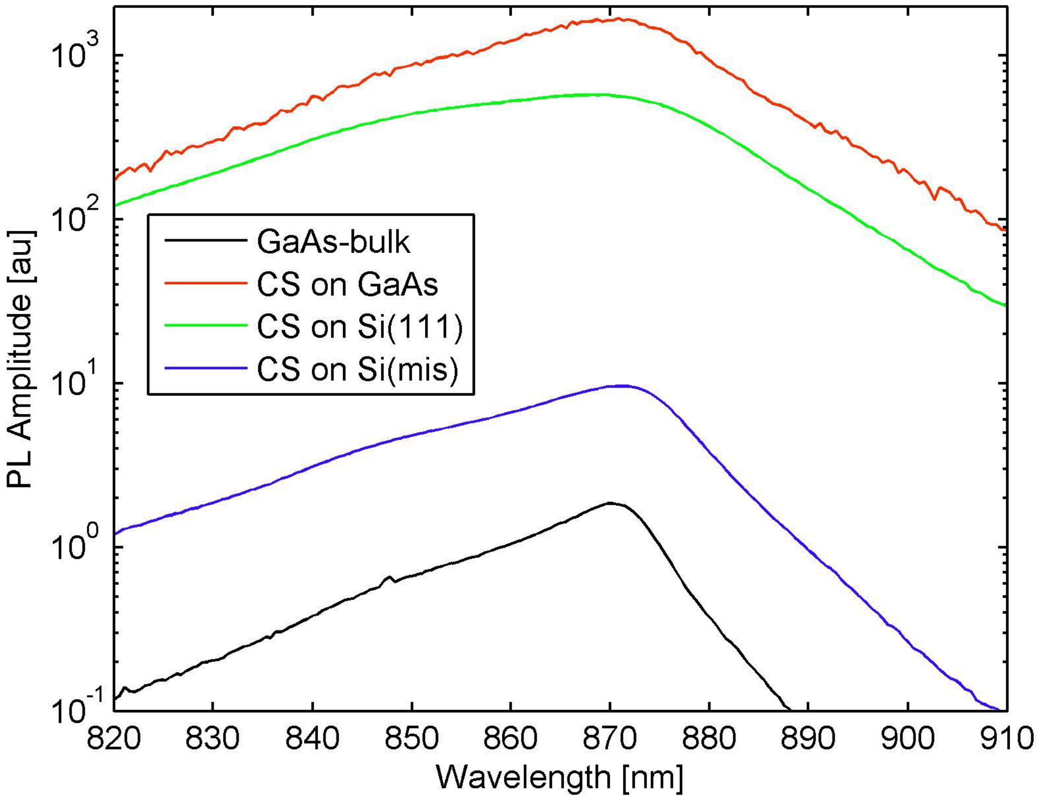

Figure 2.8 Photoluminescence of bulk GaAs, Core-Shell Nanowires grown on GaAs and Si.

CSNWs on GaAs, b) CSNWs on Si[111] and c) Si(miscut) substrates to bulk GaAs are, respectively, 923, 311 and 10. Considering the beam width of $\sim 1\mu m$, 5-10 NW were excited, yet emitted over three order of magnitude more light compared to bulk. An important contribution of this thesis is the explanation of the underlying physics of this behavior, as expanded in Chapter 5.

2.5.3 Optical Amplification and Lasing

Photoluminescence (PL) of bulk GaAs to CSNWs grown on GaAs, and on two directions of Si showed that normalized to the fraction of the volume that these wires occupy, nearly 10,000 times more brightness is observed in these wires compared to thin-film[48] as in Fig. 2.8. Figure 2.9 is the photoluminescence (PL) spectrum at various optical pump intensities. As the excitation laser power increase beyond $5\mu W$ a sudden and highly nonlinear increase in the emission intensity is observed, with pronounced peaks emerging from 800nm to 850nm that rapidly grows to become several orders of magnitude stronger than the background emission. The lasing amplitude versus excitation power demonstrates a threshold of around $5\mu W$, followed by saturation near $12\mu W$. This nonlinear threshold behavior shows in detail in the L-L plot, (i.e., The pumping power intensity (L) versus output light power intensity (L)) as in Fig. 2.10. The sharp peak has a full width half maximum (FWHM) that varies from 1.5 to 3.5 nm. This remarkable behavior is achieved in the as-grown wires with no vertical structure, which means light can be confined and resonated in this sub-wavelength structure with optical gain, allowing transitions from spontaneous emission to stimulated emission. Of importance, these III-V CSNWs can achieve lasing by heterogeneously grown on Si substrate, and compatible with traditional Complementary Metal-Oxide-Semiconductor (CMOS) fabrication technologies, which makes them promising candidates as coherent light source in the photonic integrated circuits.

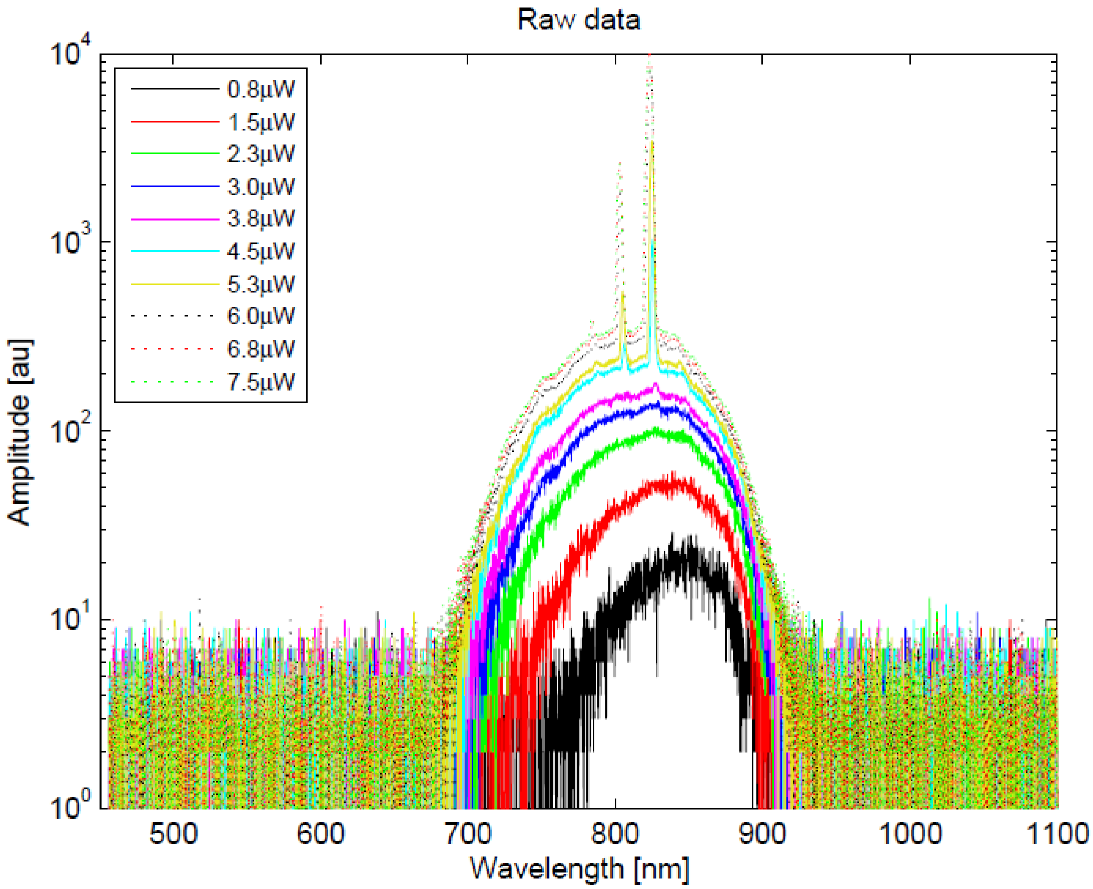

Figure 2.9 Micro-Photoluminescence measurements with fs-pulsed, 532-nm laser excitation at 250kHz repetition rate shows lasing of the as-grown wires. (Courtesy of Dr. Marc Currie at Naval Research Lab)

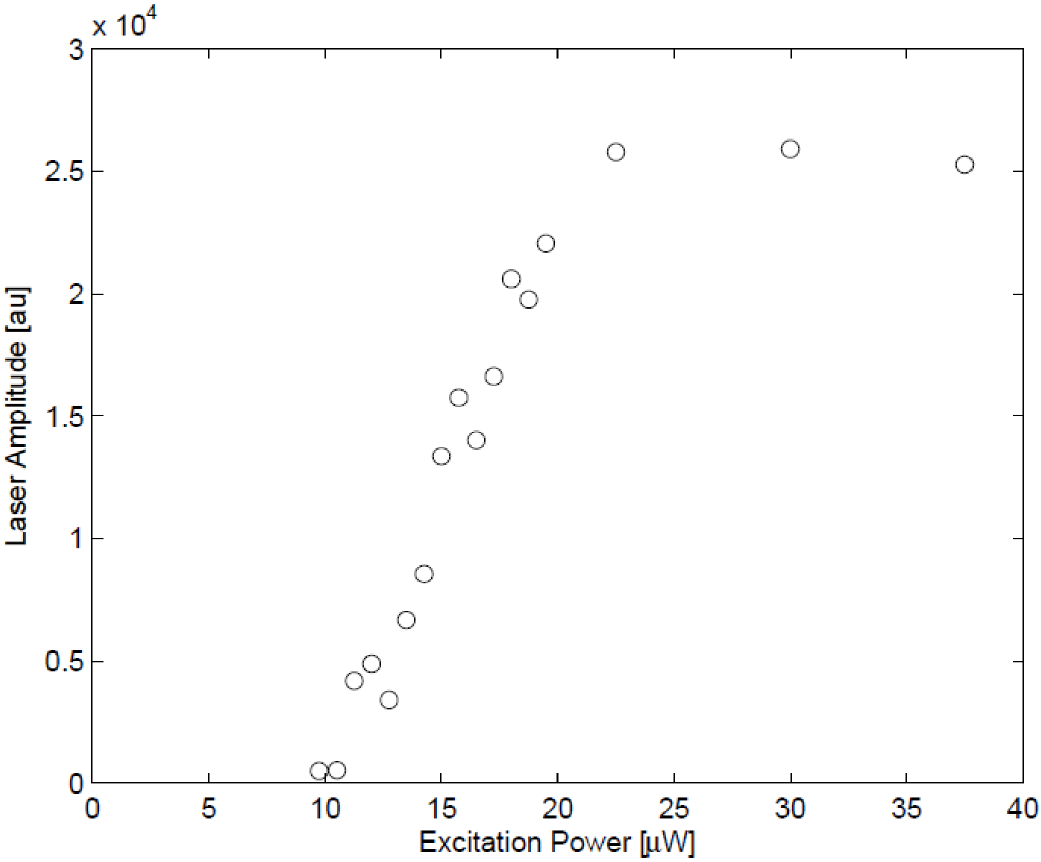

Figure 2.10 The pumping power intensity (L) versus output light power intensity (L) of as-grown core-shell nanowire operating at room temperature with a low threshold of $\sim 10\mu W$ and followed by saturation near $22\mu W$. (Courtesy of Dr. Marc Currie at Naval Research Lab)

CHAPTER 3

LIGHT CONFINEMENT IN SUB-WAVELENGTH NANO-STRUCTURES

3.1 Light and Nanowire

We have demonstrated that core-shell nanowires grown on Si or GaAs substrate have extraordinary enhanced optical and electronic properties compared to their thin film counterparts in the previous chapter. However, the question about how the light interact with these sub-wavelength structures still remains, and one cannot simply apply ray-optics to solve this issue. Thus, in this chapter, a proper model of electromagnetic wave propagation and resonating in the cavities will be proposed, and the general solutions of this eigen problem will be discussed. In addition, with the aim of finite-difference-time-domain (FDTD) simulation, we generalized the volumetric cavity modes in CSNWs, and studied their geometric dependence and light engineering applications.

3.1.1 Modal Analysis of Cylindrical Nanowire

The general equation describing the scalar wave (e.g., single components of the electromagnetic field) is:

$$\nabla^2 u - \frac{1}{c^2}\frac{\partial^2 u}{\partial t^2} = f(r,t) \tag{3.1}$$

where $u(r,t) \in \mathbb{C}$ is the wave field amplitude, c is the wave speed or phase velocity, $f(r,t) \in \mathbb{C}$ represents wave field sources. By applying the technique of separation of variables $u(r,t) = \psi_\zeta(r)e^{-i\omega_z etat}$, $Re(\omega_\zeta) \geq 0$ (from $e^{-i\omega_\zeta t} = e^{-i\Re(\omega_\zeta)t}e^{-i\Im(\omega_\zeta)t}$ we observe that solutions with $\Im(\omega_\zeta) \neq$

0 dissipate in time as "leaky modes") to reduce the complexity of the analysis and considering the free wave equation $f(r,t) \equiv 0$, we obtain the Helmholtz or the amplitude wave equations for a nanostructure representing by electromagnetic field:

$$\nabla^2 \boldsymbol{E} + \omega^2 \mu\epsilon \boldsymbol{E} = 0 \tag{3.2}$$

$$\nabla^2 \boldsymbol{H} + \omega^2 \mu\epsilon \boldsymbol{H} = 0 \tag{3.3}$$

where $\boldsymbol{E}$ and $\boldsymbol{H}$ are the macroscopic electric and magnetic fields, respectively. This is an eigenvalue equation for the operator ∇^2 with eigenvalues $\omega^2\mu\epsilon$ and eigenfunctions $\boldsymbol{E}$ and $\boldsymbol{H}$. Because all other components of both electric and magnetic fields can be derived from their z component, we only consider $\boldsymbol{E}_z$ and $\boldsymbol{H}_z$ here,

$$\frac{\partial^2 \boldsymbol{E}_z}{\partial r^2} + \frac{1}{r}\frac{\partial \boldsymbol{E}_z}{\partial r} + \frac{1}{r^2}\frac{\partial^2 \boldsymbol{E}_z}{\partial \phi^2} + \frac{\partial^2 \boldsymbol{E}_z}{\partial z^2} + \omega^2 \mu\epsilon \boldsymbol{E}_z = 0 \tag{3.4}$$

$$\frac{\partial^2 \boldsymbol{H}_z}{\partial r^2} + \frac{1}{r}\frac{\partial \boldsymbol{H}_z}{\partial r} + \frac{1}{r^2}\frac{\partial^2 \boldsymbol{H}_z}{\partial \phi^2} + \frac{\partial^2 \boldsymbol{H}_z}{\partial z^2} + \omega^2 \mu\epsilon \boldsymbol{H}_z = 0 \tag{3.5}$$

Under specified boundary conditions, these equations can only be solved for a discrete set of eigenfrequencies ω_ζ (resonant angular frequencies) with an index ζ (also called mode numbers). These special solutions (called the eigenmodes) allow us 1) to write the general solution of the free wave equation ($f(r,t) \equiv 0$) as a linear combination of eigenmodes, and 2) to obtain the solution to the harmonically forced wave equation ($f(r,t) = F(r)e^{-i\omega t}$). The general solutions for the above equations can be written as,

$$\boldsymbol{E}_z(r,\phi,z) = \psi(r)e^{-j\beta z}e^{-jv\phi} \tag{3.6}$$

If at the edge of the cavity, only the wave speed changes, c_1 inside the cavity and c_0 outside, and the refractive index inside the cavity defined as $n = c_0/c_1$, outside the cavity as 1 for air. We impose the following boundary conditions: 1) the function $\psi(r)$ should be finite everywhere (no singularities), 2) it should describe only outgoing waves for $r \to \infty$, 3) the wave function should be continuous at the edge of the cavity at $r = a$.

Thus, we have the wave function inside the cylinder ($r < a$),

$$r^2\frac{\partial^2\psi}{\partial r^2} + r\frac{\partial\psi}{\partial r} + r^2({k_0}^2n^2 - \beta^2 - \frac{v^2}{r^2})\psi = 0 \tag{3.7}$$

and outside the cylinder ($r > a$),

$$r^2\frac{\partial^2\psi}{\partial r^2} + r\frac{\partial\psi}{\partial r} + r^2({k_0}^2 - \beta^2 - \frac{m^2}{r^2})\psi = 0 \tag{3.8}$$

where $k_0 = \omega_\zeta/c$ is the wave number, and β is the wave vector in z direction. Define κ and γ as wave vectors in the transverse direction inside and outside of the cylindrical structure;

$$\kappa^2 = {k_0}^2n^2 - \beta^2 \tag{3.9}$$

$$\gamma^2 = {k_0}^2 - \beta^2 \tag{3.10}$$

After applying the separation of variables in a cylindrical coordinates system (r, φ), the Bessel J_m and Hankel functions ${H_m}^{(1)}$ of the first kind of order m will be the proper solution for Eqs. 3.9 and 3.10, respectively:

$$\psi_\zeta(r) = e^{im\varphi} \cdot \begin{cases} A_\zeta \cdot J_m(nk_0r) & ; \quad r < a \\ B_\zeta \cdot {H_m}^{(1)}(k_0r) & ; \quad r > a \end{cases} \tag{3.11}$$

The first boundary condition determines the ratio B_ζ over A_ζ (3.12) and the second one determines the eigenfrequency ω_ζ from the characteristic equations (3.13), which can only be solved numerically due to its transcendental form. Thus,

$$\frac{B_\zeta}{A_\zeta} = \frac{J_m(nk_0a)}{{H_m}^{(1)}(nk_0a)} \tag{3.12}$$

$$\frac{{J_m}'(nk_0a)}{J_m(nk_0a)} = \frac{1}{n} \cdot \frac{{H_m}^{(1)\prime}(nk_0a)}{{H_m}^{(1)}(nk_0a)} \tag{3.13}$$

where the prime denotes ordinary differentiation.

To be more specific, the excitation of leaky modes occurs in an infinitely-long dielectric cylinders of radius a when the following condition is satisfied; i.e., the characteristic equation is[41]:

$$(\frac{1}{\kappa^2} - \frac{1}{\gamma^2})^2 (\frac{\beta m}{a})^2 = {k_0}^2 (n^2 \frac{J'_m(\kappa a)}{\kappa J_m(\kappa a)} - {n_0}^2 \frac{H'_m(\gamma a)}{\gamma H_m(\gamma a)})(\frac{J'_m(\kappa a)}{\kappa J_m(\kappa a)} - \frac{H'_m(\gamma a)}{\gamma H_m(\gamma a)}) \tag{3.14}$$

Equation 3.14 can be split in conditions for purely transverse magnetic (TM) modes, if a cylinder in vacuum and air ($n_0 = 1$) is illuminated by normal incidence ($\beta = 0$), with the magnetic fields in the plane normal to the nanowire axis $[nJ'_m(nK_0a)/J_m(nk_0a) = H'_m(K_0a)/H_m(k_0a)]$ and transverse electric (TE) modes $[J'_m(nK_0a)/nJ_m(nk_0a) = H'_m(K_0a)/H_m(k_0a)]$ with the electric fields normal to the nanowire axis. From these conditions it follows that nanowires tend to support a limited number of TE and TM leaky modes, which increase in number as their radius is increased. Detailed discussion of Leaky Resonant Mode will be present in the following section 3.1.2.

On the other hand, Whispering Gallery Modes (WGM) can also be supported by solving the characteristic equation 3.13 numerically. They correspond to waves circling around the cavity, supported by continuous total internal reflection off the cavity surface, and return to the same point with the same phase after round trip, thus, interfere constructively with themselves, forming standing waves.

One of the most important quantities that describe the performance of any resonator is the quality factor or Q-factor. It can be defined as[134]:

$$Q = \omega_0 \frac{Stored\ energy}{Power\ loss} = \omega_0 \tau = \frac{\omega_0}{\triangle\omega_{FWHM}} = \frac{\Re(\omega_\zeta)}{2|\Im(\omega_\zeta)|} \tag{3.15}$$

where $\omega_0 = 2\pi v_0$ is the angular frequency and v_0 is the frequency of the resonance, τ is the cavity ring down lifetime (i.e., the time required for the field intensity to decay by a factor of e) and $\triangle\omega_{FWHM} = \tau^{-1}$ is the linewidth of the frequency of the resonance in angular frequency.

Large Q-factors are necessary for most applications. The Q-factor measures the characteristic time for the natural decay of the energy stored inside the resonator in terms of the number of full field oscillations (times 2π). This means that for a higher Q-factor the time that energy is stored inside the resonator is proportionally longer, and the total field intensity of the resonating mode will be higher

The last term in Eq. 3.15 express the Q-factor of the resonance mode from the complex propagation constant (wave number): $k_0 = \frac{\omega_\zeta}{c_0} = \beta + \frac{1}{2} i\alpha$, where $\beta = \frac{2\pi}{\lambda_0} = \Re(\omega_\zeta)$ is the phase constant, λ_0 is the wavelength in vacuum or air, and $|\alpha| = 2|\Im(\omega_\zeta)|$ is the intensity attenuation coefficient due to various cavity loss mechanisms.

3.1.2 Leaky Mode Resonance

Interaction of light with a dielectric or metallic cylindrical medium is analyzed by solving Maxwell's equations with the appropriate boundary conditions in the classical waveguide theory[135], which leads to highly confined modes in optical fibers and microscale dielectric resonators. In an infinitely long cylinder, even at deep sub-wavelength diameters this results in a characteristic equation 3.14, the solution to which are the transverse magnetic (TM) and transverse electric (TE) resonant modes. We can define the electromagnetic modes of localized resonators as time-harmonic solutions of the form $\boldsymbol{E}(\boldsymbol{r}, t) = \boldsymbol{E}(\boldsymbol{r}, \omega)e^{-i\omega t}$ to the source-free Maxwell equations. This solution shows that the longitudinal field component distributes outside the NW and is in resonance with the natural modes, such as TE_{11}, TM_{02}, etc., supported by the NW. These modes have been termed leaky-mode resonances (LMR)[41,136], and provide an intuitive tool to facilitate the understanding and optimization of the resonance effect in such nano-structures.

In order to gain an understanding of light confinement and guiding in NWs. We replicate previous results using MEEP, a widely used open-source finite-difference time-domain (FDTD) simulation package[137], to identify how light is confined in an infinitely long GaAs nanowire. The top row of Fig. 3.1 shows several configurations of TM LMR modes for a NW with diameter of 220 nm, with excitation single wavelength light being incident parallel to the NW axis. The blue and red color codes represent the polarization of the electric fields. The TE modes are primarily identical to the TM modes shown here with the electric and magnetic fields exchanged. If the light is incident with an arbitrary angle, then so-called hybrid HE and EH leaky modes will be excited instead of the pure TE or TM mode. The bottom row of Fig. 3.1 shows the directional energy flux density of the electromagnetic field, the Poynting vector, at different time frames with light being incident perpendicular to the NW axis from the right side. The light is seen to propagate from the right and then mostly remain confined at the left part of the cylinder. It is notable that in either case the light energy is spatially distributed along the cross section of the wire but, as expected from a 2D treatment does not vary axially. Figure 3.1 demonstrates that the LMR can gently confine light within subwavelength semiconductor nano-structures, similar to the intuitive ray-optics picture of multiple total internal reflections from the periphery of the cylinder. As shown by in Ref.[41], these LMRs depend on the radius and the height of the dielectric, which allows light engineering of the nanowires so as to increase its absorption efficiency at pre-determined wavelength, e.g., to maximize absorption of sunlight spectrum for higher efficiency solar cells, or to radiate as optical antennas.

3.1.3 Whispering Gallery Modes

Infinitely long cylindrical or hexagonal NW structures can also support Whispering Gallery (WG) modes[111,138–145]. To calculate the resonant WGMs, Maxwell's equations have to be solved numerically[146] taking into consideration the spectral dependence of the material of interest's index of refraction. However, we can deduce a simple plane-wave model from theoretical derivations, and the

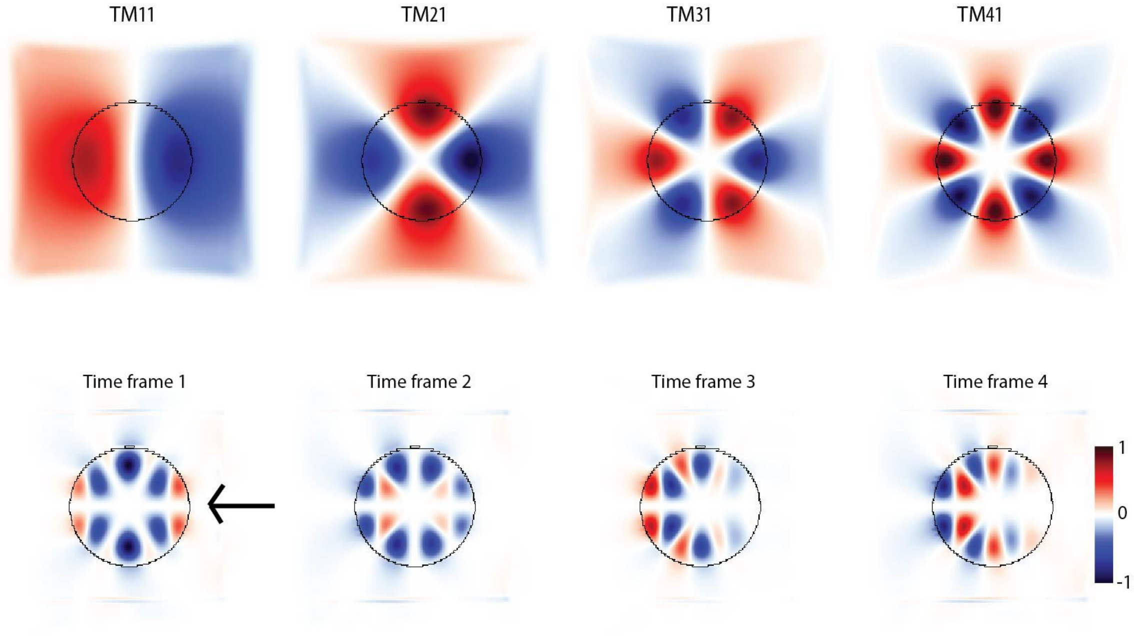

Figure 3.1 (Top) Resonant modes in an infinitely long cylinder of GaAs with diameter of 220 nm with light incident parallel to NW axis. (Bottom) The Poynting vector at different time frames with light incident perpendicular to the NW axis from the right. The black lines show the physical boundary between the nanowire and air.

relationship between resonance wavelength λ and the corresponding mode serial number N can be obtained[145]. The WG modes can also reflect and confine light in the (subwavelength) nanostructure by total internal reflection from the curvature of the structure boundaries. However, a light wave can interfere with itself only when having completed one full circulation within the resonator, which means only the light with one or multiple wavelengths are allowed to perform multiple circulations generating a standing wave. Figure 3.2 from reference[140] shows near-field intensity patterns of low-order TM polarized hexagonal WGMs for $n = 1$ and refractive index $n_r = 2.1$. Each mode pattern is labeled by its respective mode number m (lower right number) and its symmetry class (upper right symbol).

For comparison, four mode patterns of the circular cavity are given in the upper left and lower right together with their angular mode number. We again observe the radial spatial dependence of light intensity. Furthermore, the low order WG modes of hexagonal NWs are essentially similar to the

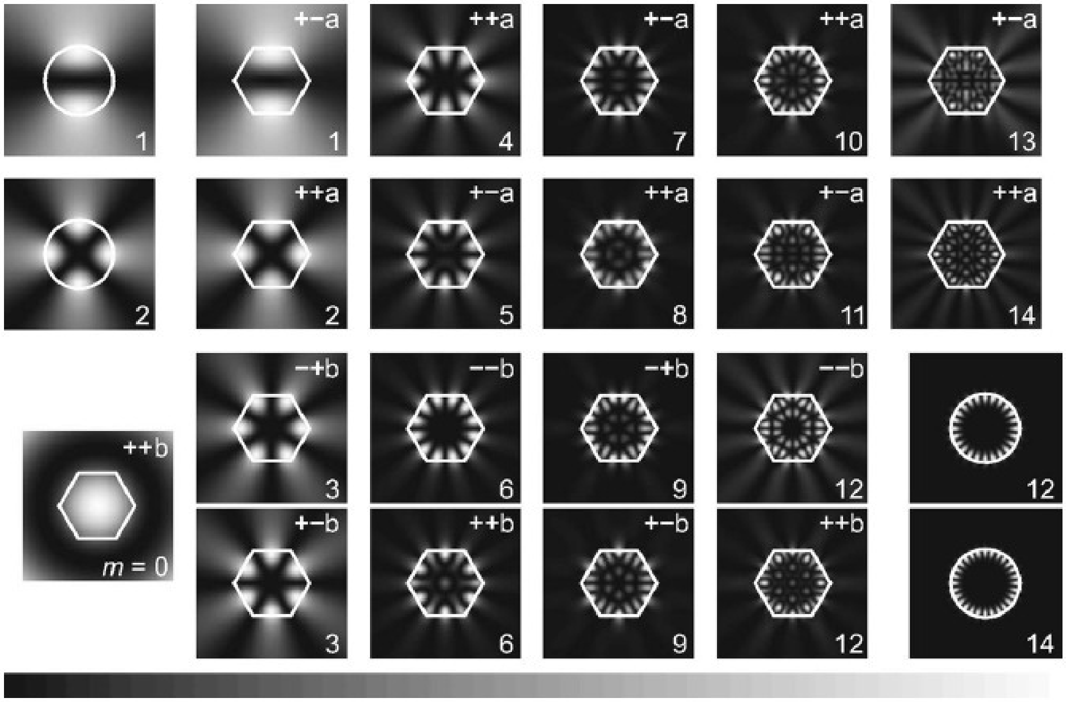

Figure 3.2 Several configurations of Whispering Gallery resonance modes in infinite long cylindrical and hexagonal nanowires. For comparison, four mode patterns of the circular cavity are given in the upper and lower right together with their angular mode number. (Reprinted with permission from[140] , ©2005 by the American Physical Society.)

cylindrical ones, but for higher order modes additional features will arise on the facets of the hexagonal NWs[140]. Simulation results also show little difference between WG mode and Leaky modes in lower order modes for both hexagonal and cylindrical structures. As with the LMR, the resonant WG modes have been used as the basis for a precise theoretical explanation of the enhanced optical behavior of hexagonal NWs, such as enhanced light absorption[41,75,133,147,148] and emission[43,138,149,150]. Furthermore, these numerical solutions have lead to reproduction of experimental resonance spectra, e.g., polarization-resolved micro-photoluminescence ($\mu - PL$) and cathodeluminescence (CL) spectroscopy.

3.1.4 Fabry-Pérot Resonant Mode

The above analysis and results apply to long structures, hence, provide two-dimensional radial modes, independent of the NW axis. However, light confinement has strong axial dependence, necessitating three-dimensional analysis of the cavity modes. FDTD simulation in 3D are used to identify the axial dependence of resonant modes in these nano-structures, revealing modes which are volumetric in nature.

Fabry-Pérot (FP) modes have been analyzed for sub-microcavity, or nano-cavity, NWs with cylindrical or hexagonal structures, specifically in order to determine the axial dependence of the resonance modes [151]. At least two mirrors are needed to construct the reflection structure inside the cavity, whether they are the top and bottom ends, i.e., the air and substrate interfaces with the nanowire, or any of the two opposite facets along the nanowire axis. For subwavelength structures, the longitudinal WG modes have high scattering losses due to diffraction, and axial FP waveguide modes will dominate[144]. However, due to small difference of the refractive index between the substrate and the nanowire dielectric, the existence of the FP mode will only be valid if the nanowire has relatively large radii, e.g., larger than 200 nm[152]. Under these conditions, besides the top and bottom ends, the lateral facets of nanowire can also be treated as two parallel slabs, and with the dielectric in between, it can support the FP mode with mode spacing inversely related to the nanowire length. An application of this analysis is in the design of NW lasers, since the optical cavity modes are observed at threshold for lasing, and have been investigated for both optical and electrical pumped cases [46,153]. As a results the FP resonance mode based nanoscale lasers are not only capable of covering a wide spectral regions, but can also can be integrated as single or multi-color laser source arrays in silicon based photonic integrated circuit or microelectronic devices [46,153]. However, the FP modes supported by the nano-cavity structure have relatively small quality factor due to the small difference of the refractive indices of the substrate and the NWs. In order to address this issue, Bragg gratings can be produced at the NW ends, alternatively, NWs can be placed on metal substrates in order to increase the FP resonance peak intensity by more than one order of magnitude compared to those on Si substrates[154].

3.1.5 Helical Resonance Modes

Nanoneedles of III-V material grown on heterogeneous substrates are optoelectronic devices which have shown interesting optical behavior, including lasing, at room temperature[63]. Figure 3.3 (a) shows SEM image of a nano-laser grown on silicon substrate that has subwavelength dimensions on all sides. Analysis of light propagation shows that unlike the traditional WG mode that lack vertical structure, there is net propagation in axial direction in these structures which leads to volumetric resonant modes which are termed helical mode resonances[63]. The schematic Fig. 3.3(b) suggests a helical ray path with nearly total internal reflection at the nanopillar-silicon interface due to the glancing angle of incidence from the hexagonal facets of the nano-laser shown in Fig. 3.3(a). As such, the faceted shape of the structure affects the optical cavity properties. FDTD-simulated field profile shows a hexagonal WG-like mode pattern in the transverse plane as in Fig. 3.3 (c), which arises from strong azimuthal components of helical modes. Figure 3.3 (d) shows first-order and higher-order standing waves axial variation. The radial mode number (first number, m) describes the transverse field pattern for WG modes, and the axial mode number (second number, n) describes the axial standing wave as is the case for Fabry-Perot resonances. It is seen that light or optical field can be well confined in the nanostructure even with low index contrast at the dielectric interface thus producing the nano-resonators needed for lasing. Although the quality (Q) factors of such nanostructure are usually not large, these helically propagating cavity modes, provide an optical feedback mechanism without the sophisticated mirror structures of the vertical cavity surface emitting lasers (VCSEL's). Additionally, since the nanowires are heteroepitaxially grown on different substrates, they enable heterogeneous integration of photonic emitters and silicon based computational circuitry. Whereas traditional FP modes are inhibited by the interface between semiconductor nanostructure and the silicon substrate, such unique optical structures have been proposed as an avenue for engineering and integrating on-chip nanophotonic devices.

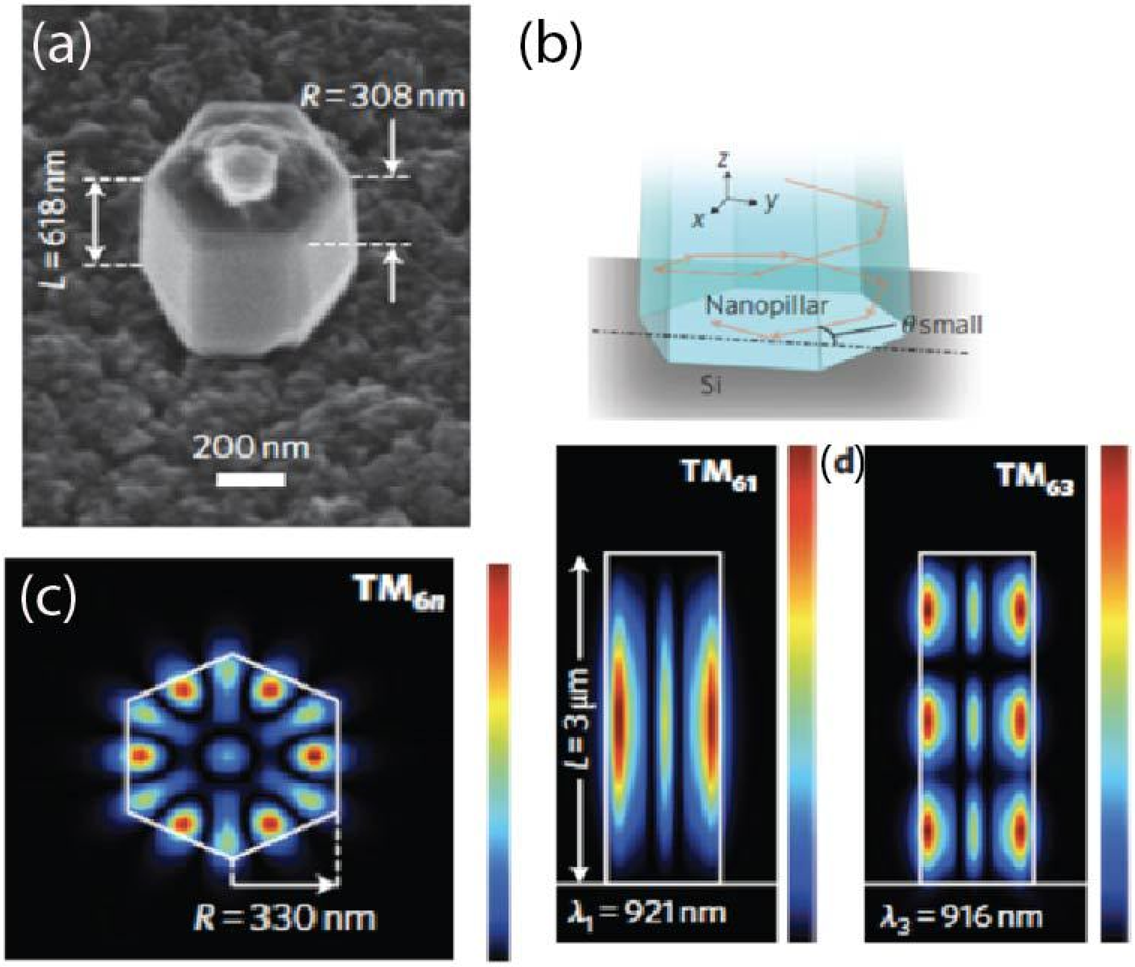

Figure 3.3 Helically propagating modes for optical feedback. (a) SEM image of the nanolaser grown on silicon substrate. (b) Schematic depicting a helical ray path because of glancing angle of incidence from the hexagonal facetes of the nanolaser shown in (a). (c) FDTD-simulated field profile shows a hexagonal WG-like mode pattern in the transverse plane, which arises from strong azimuthal components of helical resonance modes. (d) First-order and higher-order standing waves' axial variation. (Reprinted with permission from Macmillan Publishers Ltd: Nature Photonics[63], ©2011)

3.2 Volumetric Modes

3.2.1 FDTD Simulation

The finite-difference time-domain (FDTD) algorithm is one of the most common computational tools in classical electromagnetism, which divides space and time into a regular grid and simulates the time evolution of Maxwell's equations[155,156]. The starting point for any FDTD solver is the time-derivative parts of Maxwell's equations, which in their simplest form can be written:

$$\frac{\partial \boldsymbol{B}}{\partial t} = -\nabla \times \boldsymbol{E} - \boldsymbol{J}_B \tag{3.16}$$

$$\frac{\partial \boldsymbol{D}}{\partial t} = +\nabla \times \boldsymbol{H} - \boldsymbol{J} \tag{3.17}$$

where $\boldsymbol{E}$ and $\boldsymbol{H}$ are the macroscopic electric and magnetic fields, respectively. $\boldsymbol{D}$ and $\boldsymbol{B}$ are the electric displacement and magnetic induction fields[157], respectively. $\boldsymbol{J}$ is the electric-charge current density, and $\boldsymbol{J}_b$ is a fictitious magnetic-charge current density which is used for the calculation convenience of magnetic-dipole sources. In time-domain calculations, one typically solves the initial-value problem where the fields and currents are zero for $t < 0$, and then nonzero values evolve in response to some currents $\boldsymbol{J}(\boldsymbol{x}, t)$ and/or $\boldsymbol{J}_b(\boldsymbol{x}, t)$. However,the frequency-domain solver assumes a time dependence of $e^{-i\omega t}$ for all currents and fields, and solves the resulting linear equations for the steady-state response or eigen-modes[158].

In this chapter, all the simulation work were carried out by an open-source simulation package MEEP (an acronym for MIT Electromagnetic Equation Propagation)[137], which implemented the FDTD algorithm. The advantages of MEEP compared to other commercially available FDTD software packages are: free and open-source which extends the flexibility provided by access to the source code. In addition, MEEP is full-featured, including: arbitrary anisotropic, nonliear, and dispersive electric and magnetic media; a variety of boundary conditions including symmetries and perfectly matched layers (PML); distributed-memory parallelism; Cartesian (1d/2d/3d) and cylindrical coordinates; and flexible output and field computations.

In order to perform the simulation in 2D by MEEP, a core-shell hexagonal structure has to be constructed using cylindrical coordinates as in Fig. 3.4, which takes the advantages of geometric symmetries to reduce the computation time. The radius of AlGaAs shell is 185 nm, and the radius of GaAs core is 40% of the shell, i.e., 74 nm. The dielectric constant for GaAs and AlGaAs sets to be 3.4 and 3.3, respectively. Air with unit dielectric constant fills between this hexagonal structure and the perfectly matched layer (PML). The PML is an artificial absorbing layer used to truncate computational regions with open boundaries for solving electromagnetic wave equations numerically. The primary difference between PML and an ordinary absorbing materials is that the waves incident upon the PML from a non-PML medium do not reflect at the interface, thus, allow the PML to completely absorb outgoing waves from the interior of a computational region without reflecting them back into the inner region. Finally, a Gaussian pulse source at the right corner of the hexagon with certain center frequency and bandwidth is used to excite the structure. The simulation stops until the sources are finished, and then to run for some additional period of time. In that additional period, the electromagnetic field is processed at a specific point to identify the frequencies and decay rates of the modes that are excited.

3D simulation can be easily performed by adding one additional degree of freedom which is the nanowire length. The simulated cylindrical and hexagonal structures with cylindrical coordinates are sketched at the bottom of Fig. 3.5 (a). The top row of Fig. 3.5 (a) shows the transverse plane mode for cylindrical (left) and hexagonal (right) core-only NW which is a cross-section cut at the center of the wire. The middle row depicts the longitudinal plane mode for cylindrical and hexagonal structures. These results are transverse magnetic (TM) resonance modes adapted from a single time frame of the electromagnetic evolving in the NW structure with respect to time. Figure 3.5 (b) shows the 3D view of electromagnetic field distribution at the middle of a hexagonal NW. The electrical field is tightly confined at the corners and facets of the structure with a little light at the core.

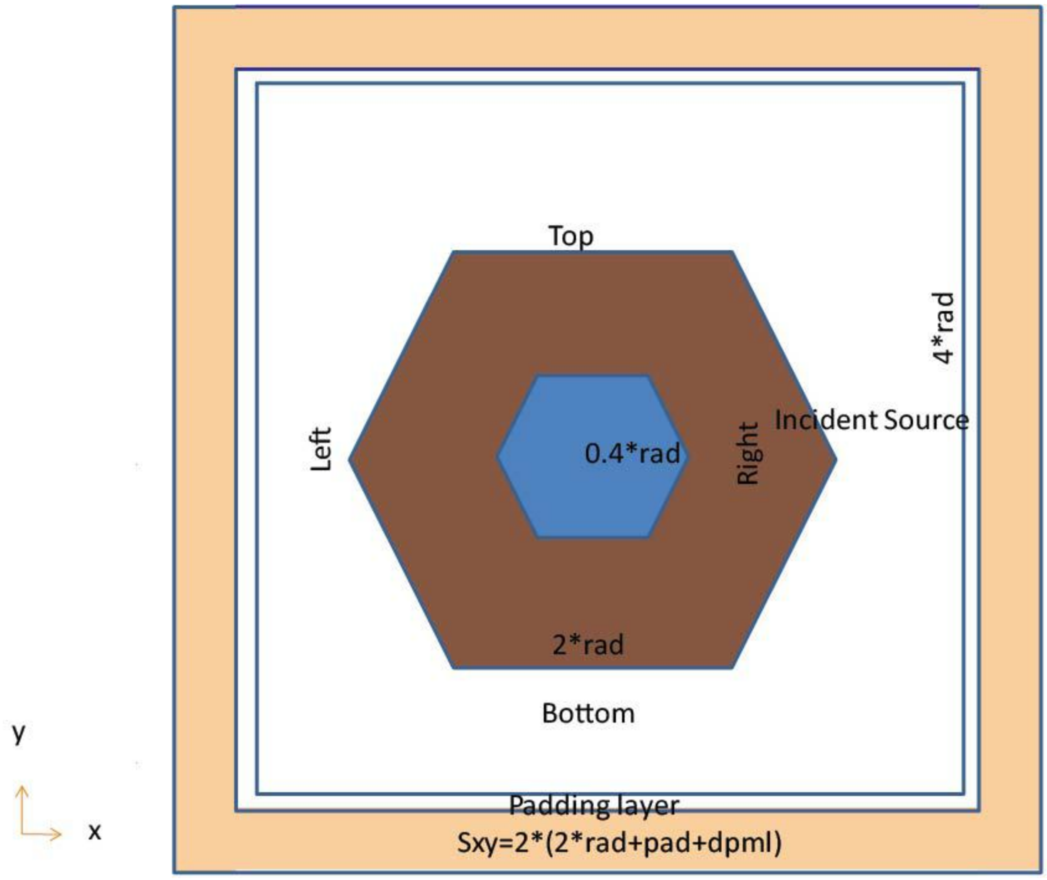
Top
4*rad
Incident Source
Left
0.4*rad
Right
2*rad
Bottom
y
x
Padding layer
Sxy=2*(2*rad+pad+dpml)

Figure 3.4 A schematic illustration of Finite-Difference-Time-Domain (FDTD) Simulation Set Up.

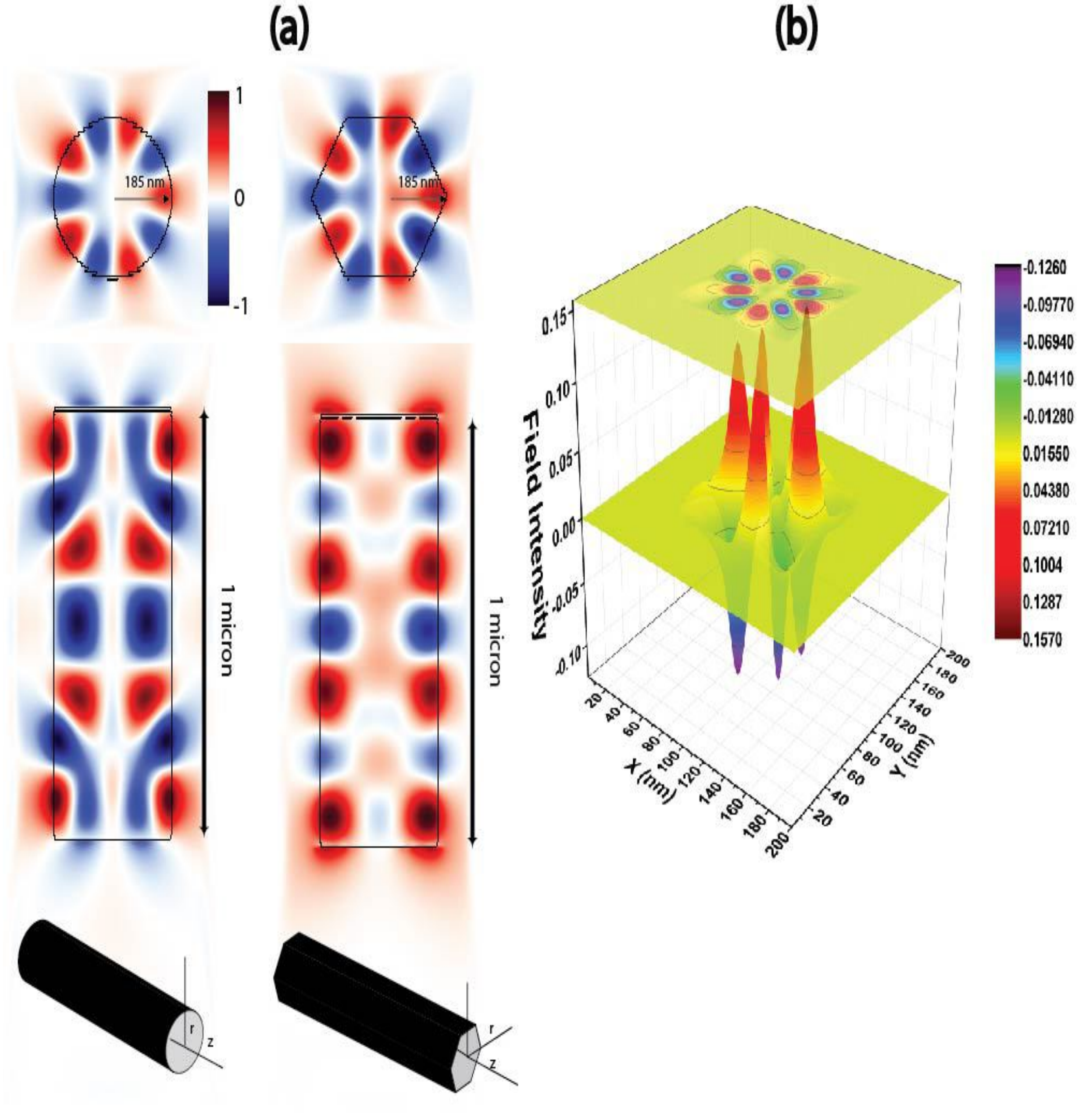

Figure 3.5 (a) (top) Transverse plane mode for cylindrical and hexagonal core-only nanowire. (middle) The corresponding longitudinal plane mode. (bottom) Three dimensional simulation schematic for cylindrical and hexagonal nanowires. (b) 3D view of electromagnetic field distribution at the middle of a hexagonal NW.

3.2.2 Generalized Volumetric Modes

The diameter of the nanostructures which can support the helical resonance modes is near the Rayleigh limit, around the boundary of the validity of ray-optics. FDTD analysis can be applied to deeper subwavelength structure in order to identify the cavity modes which are by nature volumetric, i.e., axially dependent. Figure 3.6 shows simulation results for various diameters of hexagonal structure of 1 μm length. Incident radiation with 532 nm wavelength is nearly parallel to the wire axis and different modes are displayed for different radii. Top row shows radial spatial dependence at the middle of the wire axis, and the bottom row shows the axial dependence. Top row results are similar to Figures 3.1 and 3.2, and the bottom row shows that the light can be confined in volumetric resonance mode in both transverse plane and longitudinal plane even with sub-wavelength diameter of these hexagonal NWs. Unlike helical modes, the explanation of resonance need not rely on an intuitive ray-optics description based on the grazing angle of incident light, but shows similar results in how the deep subwavelength structures can confine the light and produce a resonant cavity without having sophisticated mirrors at the end facets. In this respect nano-cavities of as-grown nanowires outperform microcavities of VCSELs.

The same results that are obtained from hexagonal NWs apply to cylindrical ones as shown in Figure 3.7, which compares the simulation results for cylindrical and hexagonal core-only and core-shell NWs with cylindrical coordinates **r**, **z**. Since these nano-cavities resonances have net propagation in the axial direction, two distinct mode numbers m and n, such as in $\mathrm{TM}_{m,n}$, are used to describe the azimuthal mode and axial mode, respectively. The transverse magnetic resonant mode $\mathrm{TM}_{5,7}$ with electric field perpendicular to the nanowire axis is shown for circular (Fig. 3.7 (a), (b)) and hexagonal (Fig. 3.7 (c), (d)) cross-sections. Top row of Fig. 3.7 are the radial standing wave patterns taken at the middle of the NW, and bottom parts are the axial variation which together demonstrate standing wave patterns in the nano-cavity. The hexagonal and cylindrical NWs present nearly identical optical behavior if the nanowires have the same cross-sectional area, consistent with previous findings[159]. These simulations produce the same results as the two-dimensional analysis of Leaky

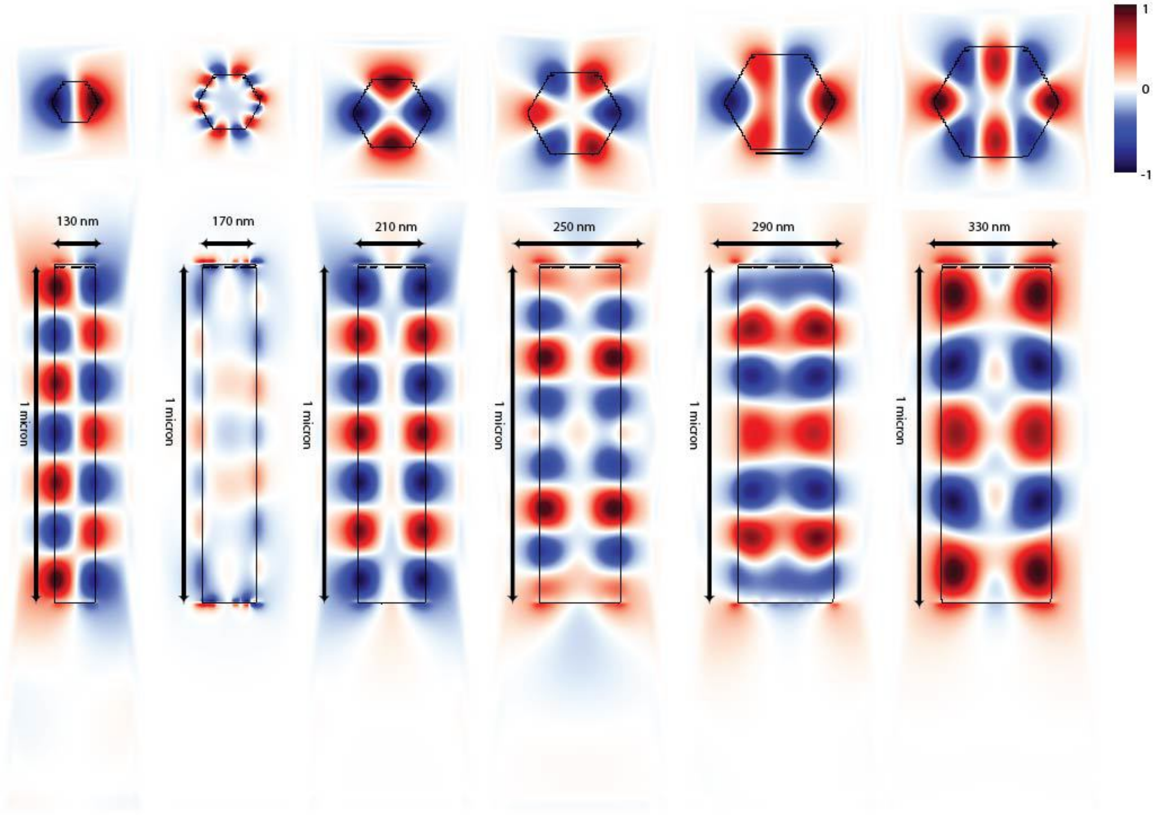

Figure 3.6 Volumetric cavity modes' dependence on nanowire diameter. Top row is a radial cut at the middle of the wire, bottom row is the corresponding axial spatial variation.

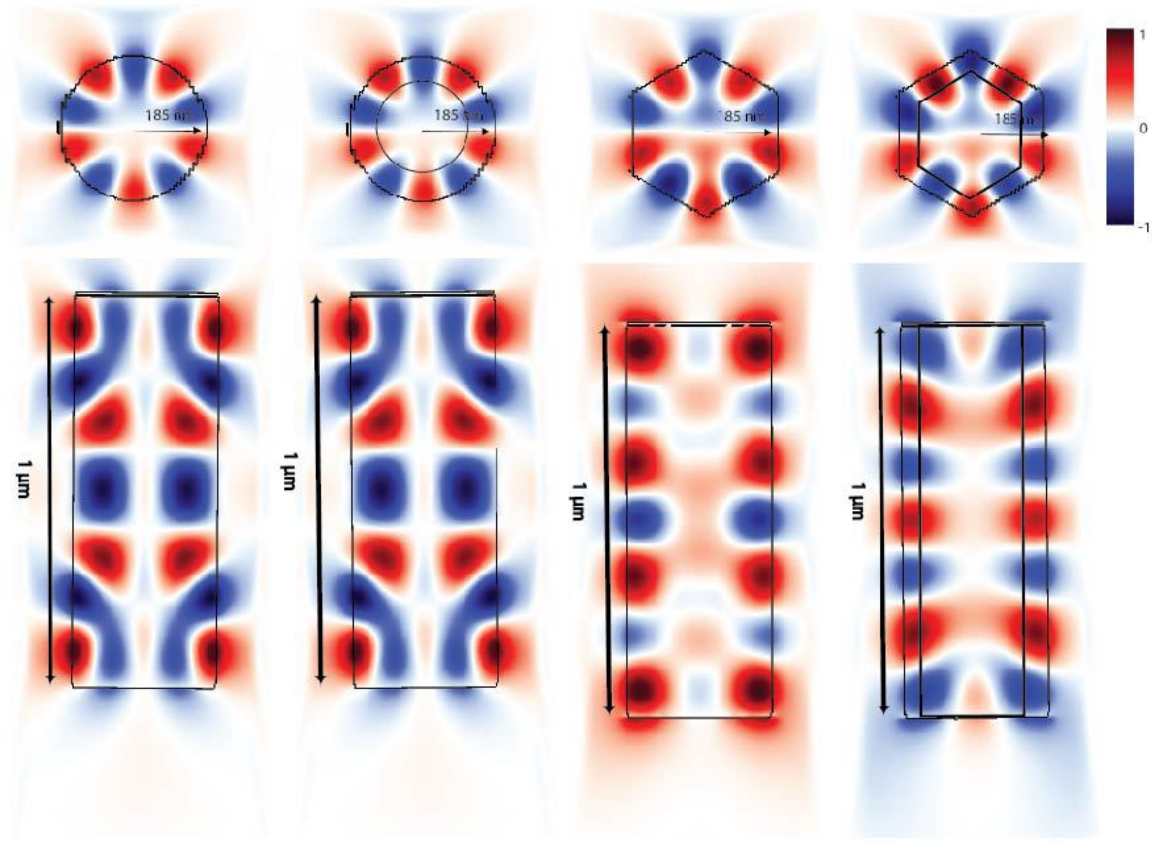

Figure 3.7 Cavity modes for (a) core-only cylindrical, (b) core-shell cylindrical, (c) hexagonal core-only, and (d) hexagonal core-shell. The radius of nanowire is 185 nm and the height is 1 μm.

Modes and Whispering Gallery, as well as the volumetric analysis presented in terms of Fabry-Perot and Helical resonance modes. The results indicate, however, that there is no need for light to reflect from the parallel facets of the wire as in the last two descriptions, rather, the curved surfaces in the sub-wavelength structure can confine the light equally well.

3.2.3 Geometry Dependence of Resonant Modes

We examine the optical properties of CSNW to see whether it significantly differs from core-only or dielectric core NWs. Both the materials and the geometric parameters of the core-shell nanowires

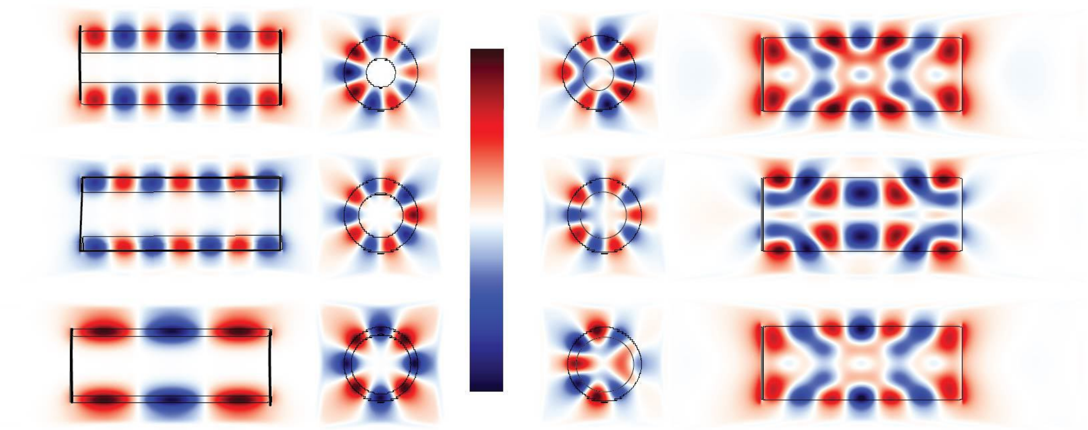

Figure 3.8 FDTD simulation results for different ratios, (top) $r_{core} = 40\% \ r_{shell}$ (middle) $r_{core} = 60\% \ r_{shell}$ and (bottom) $r_{core} = 80\% \ r_{shell}$, of core-shell radius of (left) air-core/AlGaAs-shell (right) GaAs-core/AlGaAs-shell cylindrical nanowires.

can be controlled by the chemical compositions and/or the temperature/reaction rates during the growth process. Figure 3.8 and 3.9 show the FDTD simulation results for both transverse plane and longitudinal plane modes for cylindrical and hexagonal CSNWs at same wavelength (532 nm) of incident light, respectively. The left part of Fig. 3.8 and 3.9 is air-core/AlGaAs-shell, while the right part is GaAs-core/AlGaAs-shell. And they vary with different core/shell radius ratios, i.e., (top) $r_{core} = 40\% \ r_{shell}$ (middle) $r_{core} = 60\% \ r_{shell}$ and (bottom) $r_{core} = 80\% \ r_{shell}$. As expected, a core with unit dielectric constant will confine the light more into the shell. The reduction of the shell thickness will further move the light into the shell with a little light in the core. However, in the right part of Fig. 3.8 and 3.9, the results clear indicated that the increasing of the core-shell radius ratio does not modify the electromagnetic field distribution inside of the CSNWs. The transverse plane modes keep the same mode number, as TM_{5n}, for different ratios. In addition, the materials variation does not alter the mechanisms of confinement of light in the CSNWs, but only a shift of the resonance frequency corresponding to the dielectric constant and the bandgap of the materials.

In Fig. 3.10, the diameters and the length dependence of the CSNWs have been studied. The top two rows are transverse plane TM modes with diameters varying from 20 nm to 370 nm at same wavelength (532 nm) of incident light. Bottom row is the longitudinal plane TM modes with

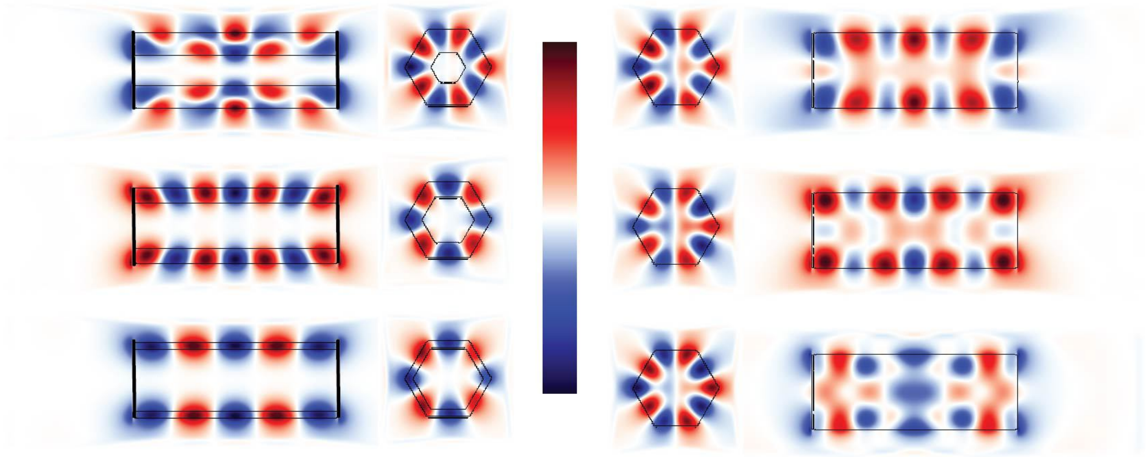

Figure 3.9 FDTD simulation results for different ratios, (top) $r_{core} = 40\% \ r_{shell}$ (middle) $r_{core} = 60\% \ r_{shell}$ and (bottom) $r_{core} = 80\% \ r_{shell}$, of core-shell radius of (left) air-core/AlGaAs-shell (right) GaAs-core/AlGaAs-shell hexagonal nanowires.

length varying from $0.5\mu m$ to $3\mu m$ while remain the same diameters. The results demonstrated that with increasing of the diameters or lengths while remain the other factor same, the resonant mode numbers also increased correspondingly. However, if the diameter of the CSNW is smaller than 150 nm, there is no clear confined resonant modes excited by the structure which is consistent with the findings in Ref.[138].

Additionally, figures 3.7(b) and 3.7(d) show simulation of cylindrical and hexagonal structures, respectively, with core of GaAs and shell of AlGaAs. These simulations show that there is little difference between core-only as in Fig. 3.7 (a, c) and core-shell (b, d) NWs, since the difference of the refractive indices of core and shell is small. Despite being optically identical, these structures have very different optoelectronic properties which will be discussed in Chapter 5 after describing the important ramifications of the optical analysis of NWs.

3.2.4 Light Engineering of sub-wavelength Nano-structure

Dependence of the resonant modes on the cavity geometry offers an important degree of freedom to engineer a cavity for particular optical properties. Figure 3.11 shows the dependence of three volumetric TM resonant modes excitation wavelengths with radius. In this spectral range, only lower

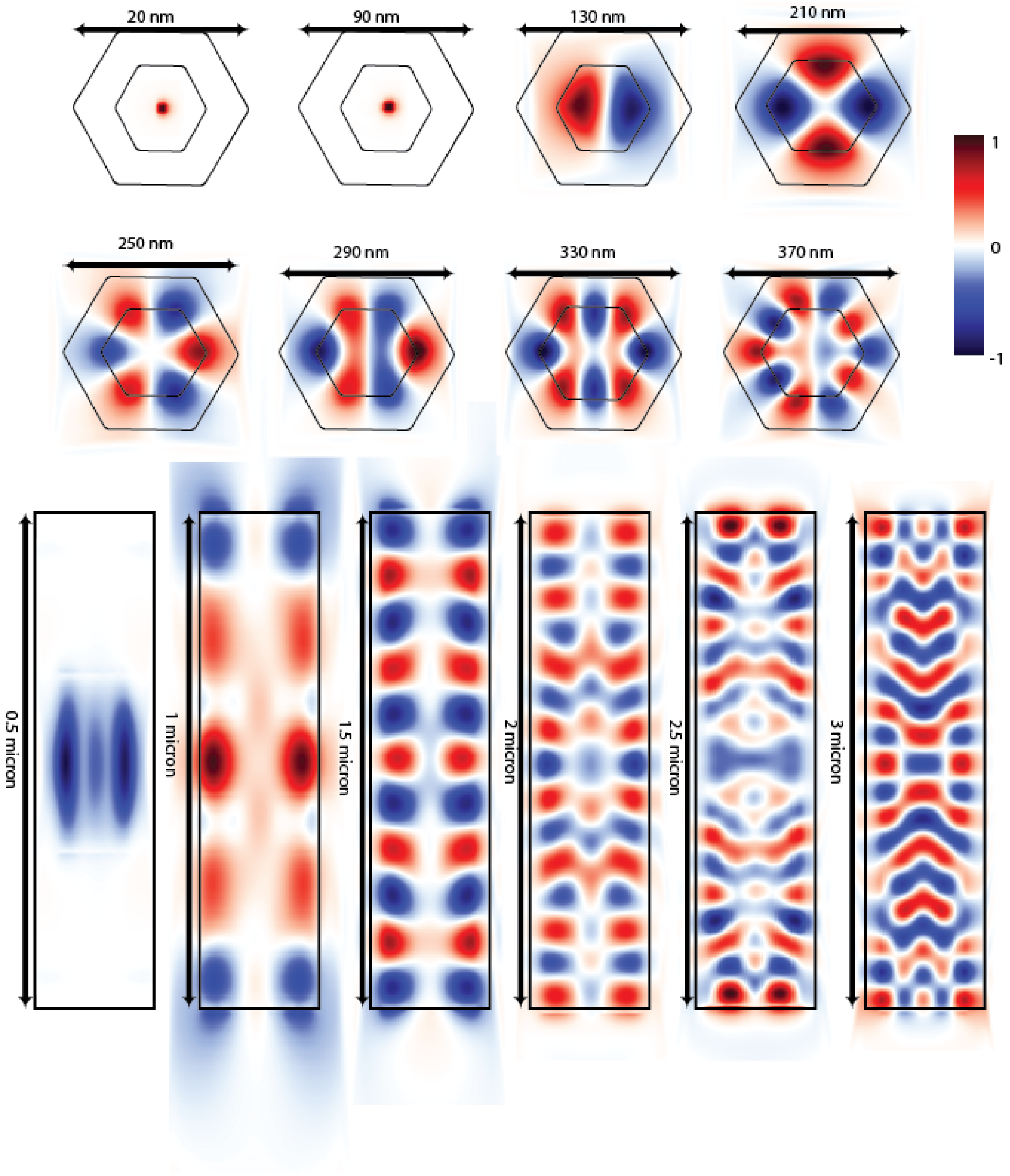

Figure 3.10 Geometric Dependence TM radius variation for different diameters and length. Top two rows are the transverse plane TM modes with diameters varying from 20 nm to 370 nm. Bottom row is the longitudinal plane TM modes with length varying from $0.5\mu m$ to $3\mu m$.

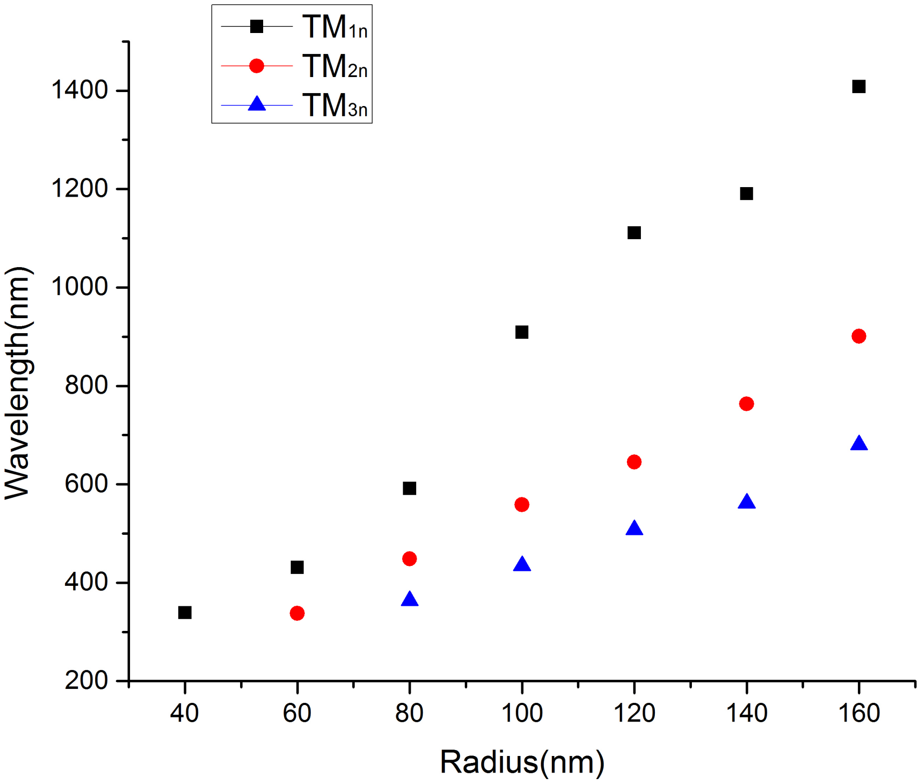

Figure 3.11 Correlation of the volumetric TM modes' excitation wavelength with NW radius allows optimization of cavity for absorption and emission at desired wavelengths.

TM modes can be excited with smaller radii, e.g., r = 40 nm and 60 nm, however, as the radius increases, higher order modes can be excited, and the optical power corresponding to the lower order modes will be reduced. We observe redshift of these volumetric TM modes with increasing NW radius. Also, the wavelength variation of TM_{1n} mode is much larger compared to TM_{2n} and TM_{3n} modes. These observations demonstrate the feasibility to engineer the volumetric mode at certain wavelength, i.e., allow us to optimize absorption or emission at a desired frequency or certain incident optical power by controlling the radius and/or length of a NW thus providing the ability to engineer the absorption spectrum in order to match desired properties.

3.2.5 Continuous Variation of Geometry - The Tapering effect

The dependence of the resonant modes on NW radius also suggests the interesting possibility of having tapered structures which can support more than one resonant mode, thus be able to optimize the spectrum of interest. The metalorganic vapor phase epitaxy (MOVPE) or vapor liquid solid (VLS) growth methods are readily capable of forming nanowires with tapered sidewalls. The resultant cavity, however, does not support the superposition of the modes present in cylindrical structures of the same diameter; in fact tapered sidewalls have been identified as the primary loss mechanism for these sub-wavelength cavities.

The effect of tapering has been studied for hexagonal CSNW that were grown on a silicon substrate with average 5° angles between opposite sidewalls; vertical electrical field intensity ($|E|^2$) profiles for (a) TM_{61} and (b) TM_{62} modes under different excitation wavelength are shown in Fig. 3.12, which similar to the result in Ref.[63]. Figure 3.12 (c, d) show first-order and higher-order transverse plane modes at different positions along the wire growth axis. The modes are primarily confined at the base, and become less resonant as they propagate upwards with decreasing of the radius at top. Higher-order axial modes generally have lower quality factor. Physically, the stronger Fabry-Perot characteristic of higher-order axial modes means that their effective longitudinal wave-vector components become stronger, causing larger penetration and loss into the substrate. Nevertheless, from a different perspective, multi-mode resonances can be achieved within certain wavelength range by controlling the tapering angle in order to form small varying radius along the nanostructure axial direction as in Fig. 3.12 (c, d). One can also red- or blue-shift the resonance peaks, since these volumetric resonance modes are dependent on transverse dimensions. Thus, intentioned tapering offers an alternative way to engineering the multi-mode resonances and finer tunability of these resonance peaks.

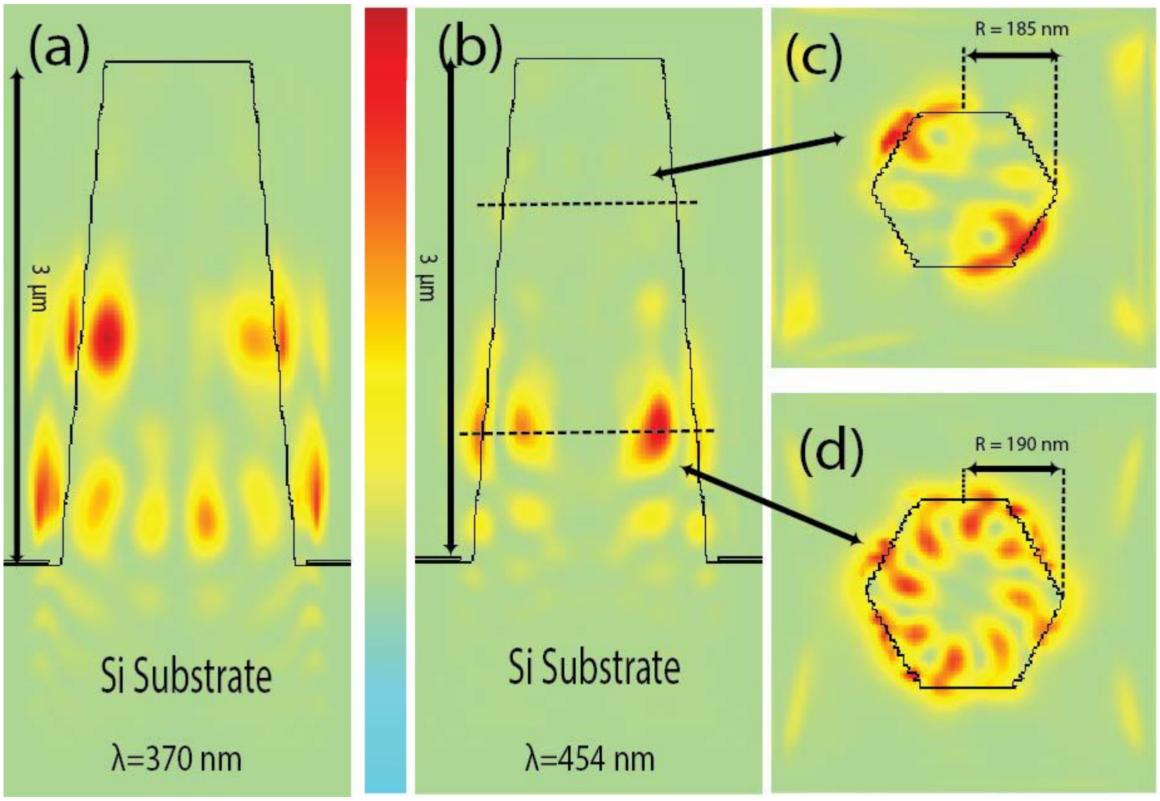

Figure 3.12 FDTD simulated electric field intensity distribution ($|E|^2$) of hexagonal core-shell nanowire on top of Si substrate with 5° tapering effect. (a, b) field intensity distribution along axial direction with different incident light wavelength, (c, d) field intensity distribution in the transverse plane at different positions along the NW.

CHAPTER 4

REDUCED ELECTRONIC DENSITY DISTRIBUTION

A heterojuntion is basically a p-n junction in a semiconductor between materials of different composition. Normal junctions are between p and n type versions of the same material. But in this case we refer to a juntion formed betewen two group III-arsenide usually a GaAs/AlAs interface or a GaAs/AlGaAs interface. Since they are two differnt materials, the band structure is discontinuous from one material to the other and the band alignment across the interface is typically of type I, i.e. the band gap of the lower bandgap material is positioned energetically within the bandgap of the wider bandgap semiconductor.

Polarization fields The usual growth direction for hexagonal III-V materials is along the polar [0001] axis, for which the crystal lacks inversion symeetry. This will result in the formation of polarization fields. There are two kinds of polarization fields. They are spontaneous polarization (SP) and Piezoelectric polarization (PZ). The spontaneous polarization exists in polar semiconductors with a Wurzite or lower symmetry crystal structure and is related to the deviation of the crystal lattice parameters from the ideal values for the structure, thereby creating molecular dipoles in the material building a polarization field just like that formed in ferroelectrics. This field has a fixed direction along the [0001] c-axis in the Wurtzite lattice. Therefore the field resulting from spontaneous polarization will point along the growth direction and this maximizes pontaneous polarization effect in these systems and renders the problem effectively one-dimensional.

The other type of polarization field, the piezoelectric polarization occurs due to the presence of strain in the system. When two layers are joined together to form a heterojunction, the difference in the lattice constant between the two materials will lead to a strain . This strain also occurs due tot he difference in the thermal expansion coefficients in the the layers during cool down after growth. This leads to elastic strain in the layers.

4.1 Self-consistent Schrödinger-Poisson Solver

4.1.1 Finite Element Method

The study of energy band structures of heterostructures needs a detailed knowledge of optical and transport properties of the heterostructures. These properties can be found by solving self-consistently Poisson's and Schrödinger's equations for the electron wave functions.

The finite element method (FEM) is a simple and efficient method for solving ordinary differential equations (ODEs) or partial differential equations (PDSs) in problem regions with simple boundaries[160]. FEM can be used to solve for the Schrödinger and Poisson equation self-consistently. A generic formulation for a PDE with the following form:

$$|D|u(x) = f(x) \in \Omega \tag{4.1}$$

where D is an arbitrary operator, and Ω defines the geometry. In order to solve this PDE using FEM, eq. 4.1 has to be rewritten in weak variational form with the boudary conditions:

$$\begin{cases} u(x) = u_0(x) \qquad on \quad \Gamma_D \\ \frac{\partial u}{\partial n} = g_0(x) \qquad on \quad \Gamma_N \end{cases} \tag{4.2}$$

where Γ_D and Γ_N signifies Dirichlet and Neumann boundary condition. By introducing an arbitrary function v and multiplying the PDF with v, then integrating over all the domain Γ and separating every second-order derivative using integration by parts, the original PDE can be carried out in the weak form as:

$$\int_{\Omega} |D'|(u{\cdot}v)\ d\Omega + \int_{\Gamma_N} gv\ \partial\Omega = \int_{\Omega} fv\ d\Omega \quad \forall v \in \hat{V} \tag{4.3}$$

where D' is the reduced operator after performing integration by part to the second-order derivatives, and $\hat{V}$ is the function space where an arbitrary function v belongs to. The function u lies in V, which could be different than $\hat{V}$. This continuous variational problem need to be reformulated to discrete problem with discrete space $\hat{V}_d \subset \hat{V}$ and $V \subset V$ so that the boundary conditions can be restated as:

$$\int_{\Omega} |D'|(u_d{\cdot}v)\ d\Omega + \int_{\Gamma_N} gv\ \partial\Omega = \int_{\Omega} fv\ d\Omega \quad \forall v \in \hat{V}_d \subset \hat{V} \tag{4.4}$$

It is more convenient to use unified notation for linear weak forms $a(u,v) = L(v)$ with $a(u,v) = \int_{\Omega} |D'|(u_d{\cdot}v)\ d\Omega$ and $L(v) = \int_{\Omega} fv\ d\Omega - \int_{\Gamma_N} gv\partial\Omega$.

4.1.2 Variational form of Schrödinger and Poisson equations

A general Poisson equation for electrostatics is giving by[161]:

$$\frac{d}{dx}(\epsilon_s(x)\frac{d}{dx})\Phi(x) = \frac{-q[N_D(x) - n(x)]}{\epsilon_0} \tag{4.5}$$

where ϵ_s is the dielectric constant of the material, N_D is the ionized donor concentration, Φ is electrostatic potential, and n is the electron density. Since Eq. 4.5 only has a piecewise dielectric constant, the domain can be divided into subdomains by different dielectric constants. The Poisson equation can be rewritten as:

$$\epsilon_s \nabla^2 \Phi(x) = \frac{-q[N_D(x) - n(x)]}{\epsilon_0} \tag{4.6}$$

Note that the operator $|D|$ is replaced by ∇^2, and the source term $f(x)$ is replaced with the scaled difference of the ionized donor concentration and the electron density. Then the Poisson equation can be reformulate to the weak variational form following the previous procedures.

$$\int_\Omega \epsilon_s \epsilon_0 \nabla\Phi\nabla v \; d\Omega = \int_\Omega [-q[N_D(x) - n(x)]]v(x) \; d\Omega \tag{4.7}$$

The weak variational form of Schrödinger's equation can be derived from the general differential form following by the similar manner:

$$-\frac{\hbar^2}{2}\frac{d}{dx}(\frac{1}{m^*(x)}\frac{d}{dx})\psi(x) + V(x)\psi(x) = E\psi(x) \tag{4.8}$$

where $m^*(x)$ is the effective mass. Equation 4.8 can rewritten after taking the effective mass out, as it will remain constant in a single region.

$$\frac{\hbar^2}{2m^*}\nabla^2\psi(x) + [E - V(x)]\psi(x) = 0 \tag{4.9}$$

Multiply both sides by a test function v, which is arbitrary with the condition that it vanishes on the boundaries of the system.

$$\int_\Omega \frac{\hbar^2}{2m^*}\frac{\psi}{x}\frac{v}{x} \; d\Omega + \int_\Omega V(x)\psi(x)v(x) = \int_\Omega E\psi(x)v(x) \; d\Omega \tag{4.10}$$

4.1.3 Numerical Implementation

To obtain the electronic properties, the electrostatic potential $V(x = -q\phi(x) + \triangle E_c(x)$ first sets to zero. Then the envelope functions and the eigen energies are calculated according to the Schrödinger equation 4.8. A Poisson equation 4.5 is solved after the determination of the quasi Fermi level E_F

by solving charge neutrality equation. The electron concentration can now be calculated based on:

$$n(x) = \sum_{k=1}^{m} {\psi^*}_k(x)\psi_k(x)n_k \tag{4.11}$$

$$n_k = \frac{m^*}{\pi\hbar^2}\int_{E_k}^{\infty} \frac{1}{1+e^{(E-E_F)/KT}}dE \tag{4.12}$$

where $\triangle E_c(x)$ is the pseudopotential energy due to the band offset at the heterointerface, n_k is the electron occupation number which can be calculated by Fermi-Dirac distribution function with Fermi level E_F, ψ_k is the wavefunction in the k^{th} state, and E_k is the eigen energy in state k. Finally, a check of the electrostatic potential update decides whether the iteration terminates. The procedure of this Schrödinger-Poisson solver has been demonstrated in the flow chart diagram as in Fig. 4.1.

Implementing the FEM method when solving the Schrödinger and Poisson equations requires the construction of a mesh defining local coordinate surfaces. For each node of this mesh, the unknown eigen functions and eigen values are found, replacing the original differential equations by variational forms. In order to make the FEM method more effective, implementing a small mesh when the wavefunction is changing rapidly and a large mesh during a slow change in the wavefunction is necessary.

4.2 Electronic Distribution in Nanowires

The electronic band structure and the electronic density of cylindrical and hexagonal GaAs/AlGaAs core-shell nanowire are calculated self-consistently by solving Poisson and Schrödinger equations[162,163] using **nextnano^3** simulation packages[164], which is a commercial computer aid software with better physical method for the calculation of the quantum mechanical properties of an arbitrary combination of geometries and materials.

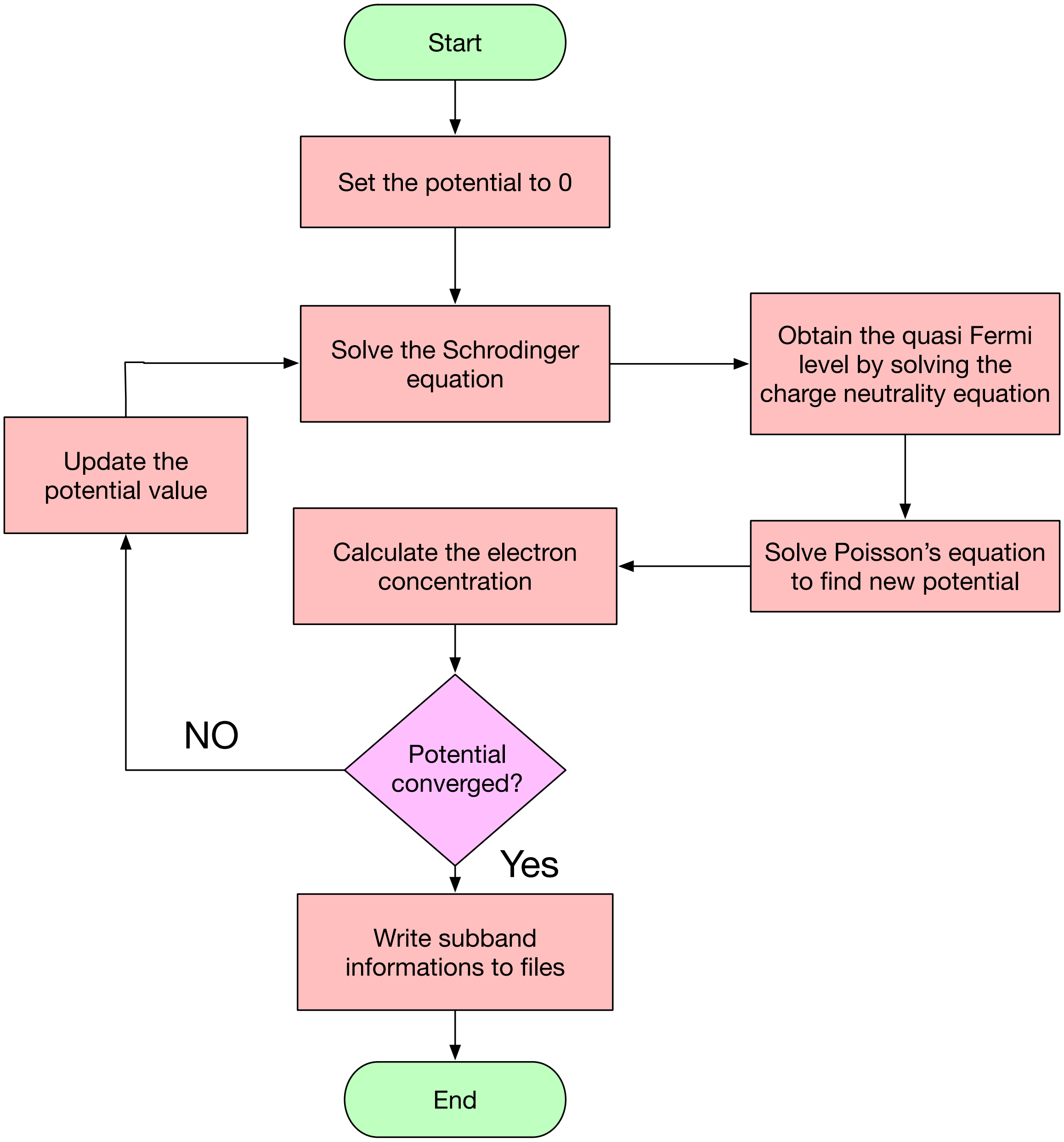
Start
Set the potential to 0
Solve the Schrodinger equation
Obtain the quasi Fermi level by solving the charge neutrality equation
Update the potential value
Calculate the electron concentration
Solve Poisson's equation to find new potential
NO
Potential converged?
Yes
Write subband informations to files
End

Figure 4.1 A flow chart diagram of the Schrödinger-Poisson solver. The procedure is only discussed for electrons in the conduction band for simplicity but it also hold true for holes in the valence band using analogous formulas.

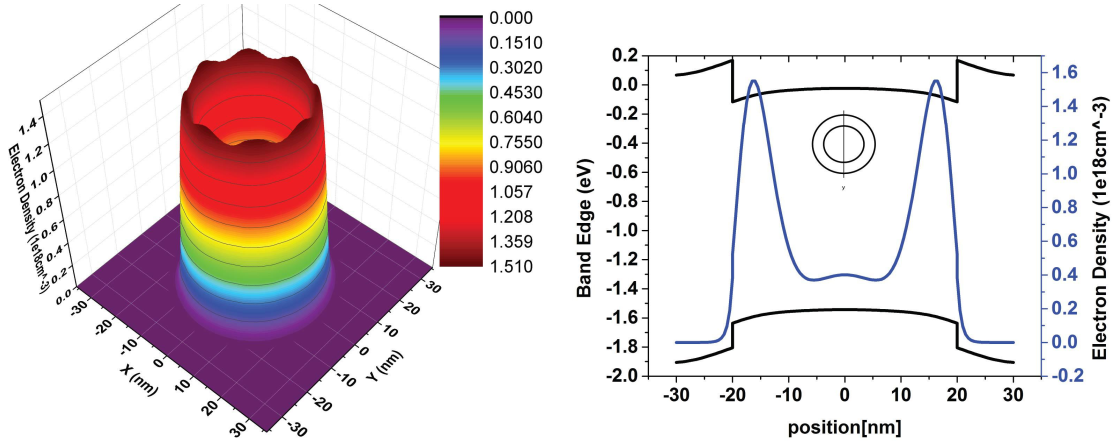

Figure 4.2 (left) Electron charge distribution in 3D illustration. (right) Conduction and valence band bending (black lines) and electron density distribution (blue line) for cylindrical core-shell nanowire. The inset shows the data captured from a vertical slice of the simulated structure.

4.2.1 Cylindrical Core-Shell Nanowire

The cylindrical core-shell nanowire has been investigated with a radius of 20nm GaAs core and 15nm AlGaAs shell. An additional Si-doped AlGaAs layer with a 0.33 mole fraction is placed between the core and shell. The thickness of this layers is 5 nm. The left part of Fig. 4.2 shows the electron density distribution in 3D view. A free-electron gas is formed in the GaAs core and at the inner heterointerface with a small fluctuation of density along the interface. There is a very small amount of electron gas distributed at the center of the core. Further simulation with different doping density ρ_D shows similar distribution of the electron gas but very small variation of the magnitude of the intensity. On the right part of Fig. 4.2, the black line represents the conduction and valence band bending and the blue line shows the electron density along the vertical cut of this cylindrical CSNW.

4.2.2 Hexagonal Core-shell Nanowire

Due to the hetero-interface between the core and shell and the piezoelectric force at the corners, the electronic states distribution inside of the hexagonal core-shell nanowire is not always three-dimensional case or two-dimensional like in cylindrical NWs. Lower-dimensional electron gas arises with increased doping density. A delta-doped hexagonal CSNW heterostructure has been simulated.

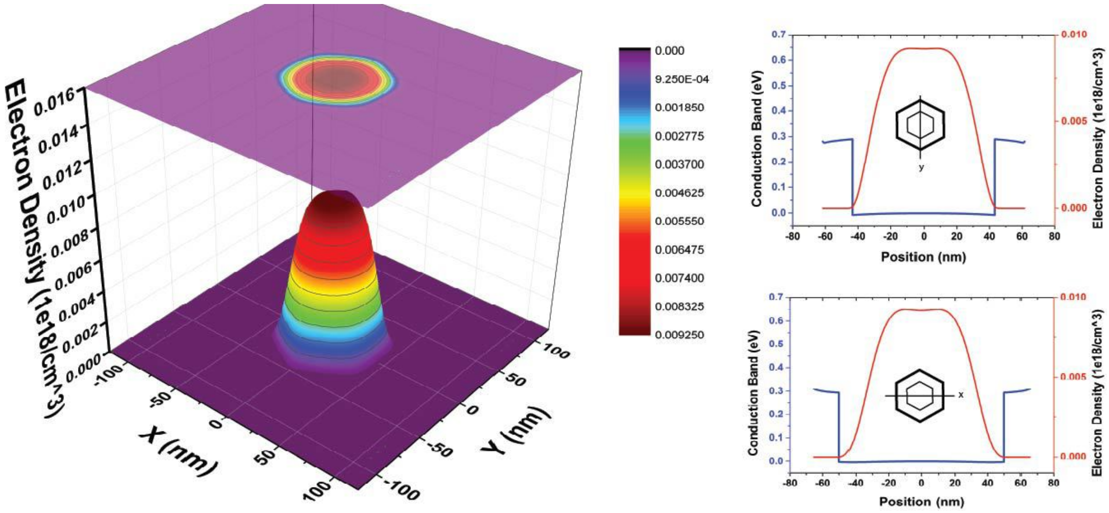

Figure 4.3 (left) Three dimensional electron charge distribution in 3D illustration. (right) Conduction and valence band bending (blue lines) and electron density distribution (red line) for hexagonal core-shell nanowire with a low doping density. The inset shows the data captured from a (top) vertical or (bottom) horizontal slice of the simulated structure.

The radius of GaAs core and AlGaAs shell is 43.3 nm and 45 nm, respectively, with a 17.3 nm AlGaAs spacer in between. The thickness of Si-doped AlGaAs is 1.6 nm with a 0.33 mole fraction of AlGaAs. This Si-doped AlGaAs layer is used to populate a (triangular) quantum well at the heterointerfaces. Such a well can also be produced by sandwiching a GaAs layer radially between two wider bandgap materials.

The left part of Fig. 4.3, 4.4 and 4.5 shows the spatial distribution of the free-electron gas for the three values of the doping density indicated as (Fig. 4.3) $\rho_D = 9.2 \times 10^{18} cm^{-3}$, (Fig. 4.4) $\rho_D = 9.6 \times 10^{18} cm^{-3}$, (Fig. 4.3) $\rho_D = 1.5 \times 10^{19} cm^{-3}$. On the right part, the electronic band structure (blue line) and the electronic density (red line) of hexagonal GaAs/AlGaAs core-shell nanowire are depicted for vertical slice (top, right) or horizontal slice (bottom, right).

At the lowest doping, shown in Fig. 4.3, the charge is distributed deep into the core. The distribution is only slightly modulated (right panels) crossing the core along either the y cross section or x cross section, and slightly depleted in the center of the core.

As the doping is increased in Fig. 4.4, the charge depletion in the center is more pronounced, and the

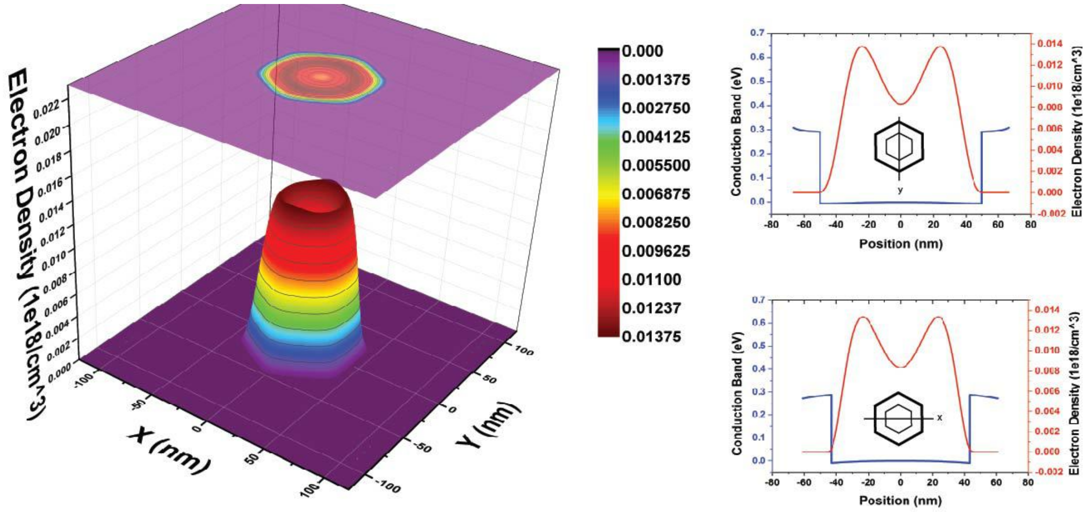

Figure 4.4 (left) Two dimensional electron charge distribution in 3D illustration. (right) Conduction and valence band bending (blue lines) and electron density distribution (red line) for hexagonal core-shell nanowire with a moderate doping density. The inset shows the data captured from a (top) vertical or (bottom) horizontal slice of the simulated structure.

charge moves toward the heterojunction interface, leaving this ”volcano” like charge distribution in the left part of Fig. 4.4. The two-dimensional electron gases (2DEG) are formed at the heterointerface of GaAs core and AlGaAs shell.

As the doping is further increased in Fig. 4.5, the shell 2DEG form at the six (6) core-shell hetero-interface facets, with six (6) pillars of one-dimensional electron gas (1DEG) forming at the 6 vortices. In addition, as shown in the right part of the Fig. 4.3, 4.4 and 4.5, the electronic density of Fig. 4.5 is around two orders of magnitude higher than 2DEG and bulk counterparts. The results also matched the other groups' simulation results very well[162,163].

4.3 Conclusions

In this chapter, the finite-element-method implemented self-consistent Shrödinger-Poisson solver has been discussed. In addition, a cylindrical and hexagonal core-shell nanowire structure has been simulated and compared with different doping density. The simulated results show unique electron density distribution in hexagonal CSNW with large doping density. This unique distribution of

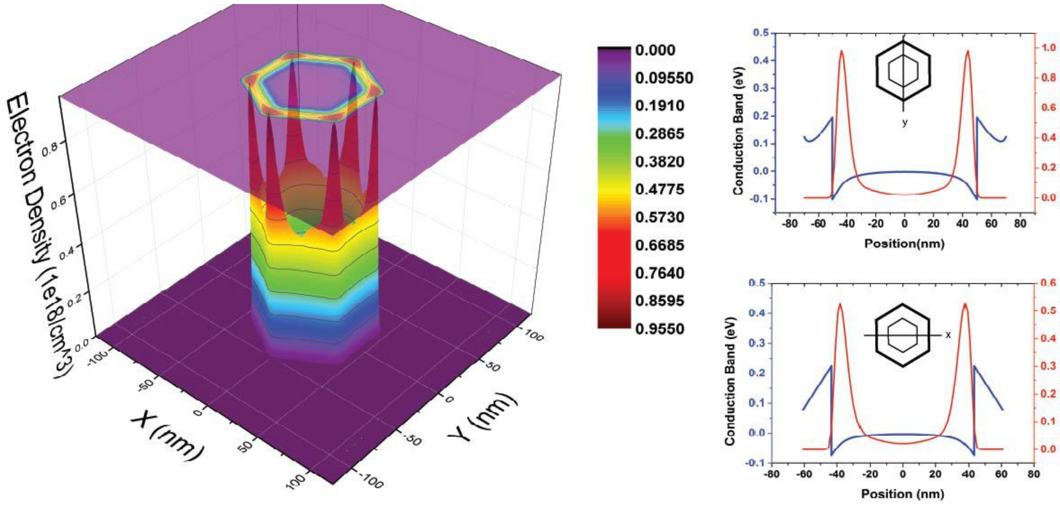

Figure 4.5 (left) One dimensional electron charge distribution in 3D illustration. (right) Conduction and valence band bending (blue lines) and electron density distribution (red line) for hexagonal core-shell nanowire with a high doping density. The inset shows the data captured from a (top) vertical or (bottom) horizontal slice of the simulated structure.

electrons has also been verified experimentally by electron holographic tomography[165]

CHAPTER 5

DIMENSIONAL DEPENDENCE OF OPTICAL TRANSITION RATES

In this chapter, we focuses on the dimensional dependence of the optical transition process, such as absorption, spontaneous emission and stimulated emission behavior in semiconductor when interacting with light. Through time-dependent perturbation theory and Fermi's Golden Rule, we find out the two bands optical transition rates, then based on the light interaction Hamiltonian, time average Poynting vector and matrix element, derive the absorption coefficient, spontaneous and stimulated emission rates for bulk semiconductor (3-dimension), quantum well (2-dimension) and nanowire (1-dimension) structure.

5.1 Optical Transition in Semiconductor

All semiconductor optical or photonic devices can be divided into three groups[166]: (1) devices as light sources that convert electrical energy into optical radiation (such as LED and Lasers); (2) devices that detect optical signals (such as photodetectors); (3) devices that convert optical radiation into electrical energy (such as photovoltaic devices or solar cells). In addition, all these three groups of photonic devices involve the generation and recombination of electron-hole pairs.

In order to generate an electron-hole pair, the photon energy has to be greater than the semiconductor material energy bandgap, $h\gamma \geq E_g$, where γ is the frequency of the photon. A variety of material systems have been employed for different wavelength detection and luminescence due to their proper bandgap values as depicted in Fig. 5.1. Generally, GaAs material is used for fiber opti-

Semiconductor bandgaps (wavelengths) and human eye response

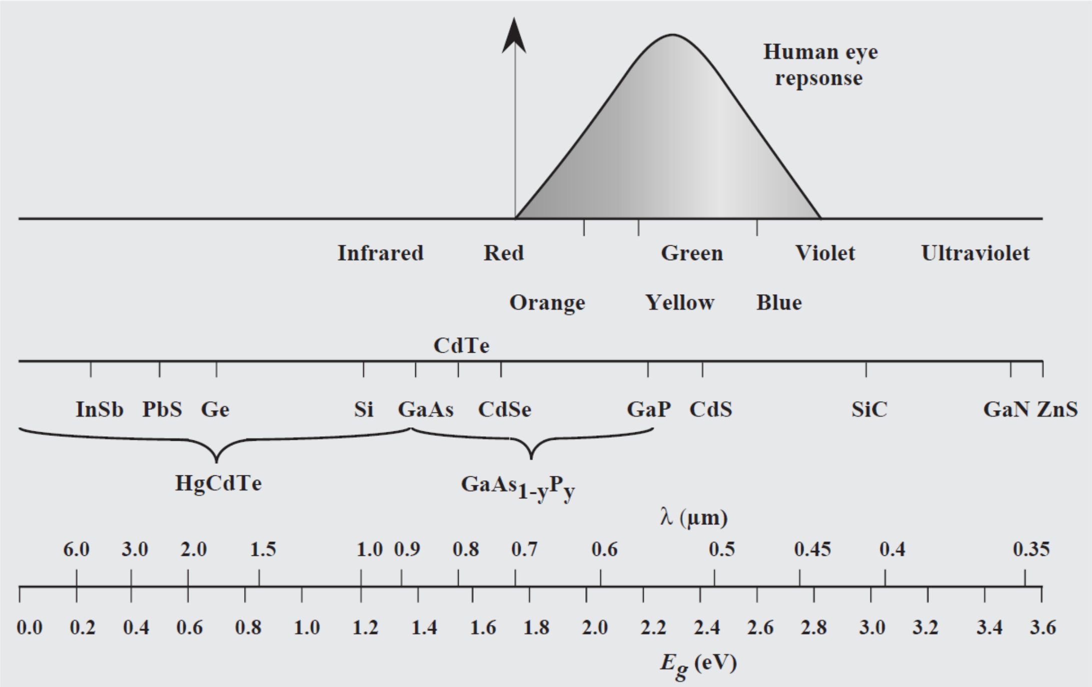
Human eye
repsonse
Infrared
Red
Green
Violet
Ultraviolet
Orange
Yellow
Blue
CdTe
InSb
PbS
Ge
Si
GaAs
CdSe
GaP
CdS
SiC
GaN ZnS
HgCdTe
$GaAs_{1-y}P_y$
λ (μm)
6.0
3.0
2.0
1.5
1.0
0.9
0.8
0.7
0.6
0.5
0.45
0.4
0.35
0.0
0.2
0.4
0.6
0.8
1.0
1.2
1.4
1.6
1.8
2.0
2.2
2.4
2.6
2.8
3.0
3.2
3.4
3.6
E_g (eV)

Figure 5.1 Schematic representation of various semiconductor materials' energy bandgaps (or wavelengths) with corresponding human eye response. Adapted from reference[167]

cal communication applications in the infrared portion of the electromagnetic spectrum. For visible and near visible luminescence, where human eyes have higher sensitivity, GaP and CdS materials are commonly used. GaN and ZnS materials with larger bandgap are primarily used for violet and ultraviolet applications.

Besides the energy conservation which requires photon energy to be greater than the material bandgap, another important condition that is necessary for the interaction of electron and holes by the perturbation of photon energy. Figure 5.2 shows the corresponding energy-momentum (E-k) plots for two different kinds of bandgap. As indicated in the left part of Fig. 5.2, the conduction band has only one minima, on the right-hand side, there are two minima. The one with an arrow is the direct minimum, and the another one is the indirect minimum. Electrons in the direct minimum of the conduction band and holes at the top of the valence band have equal momentum; while elec-

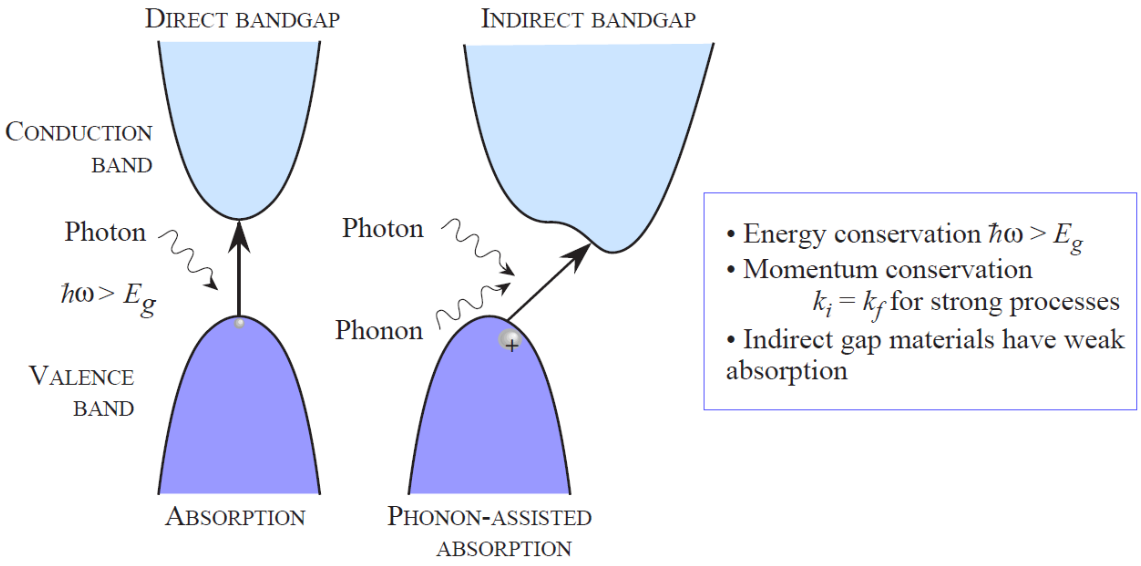
DIRECT BANDGAP
INDIRECT BANDGAP
CONDUCTION BAND
Photon
$\hbar\omega > E_g$
VALENCE BAND
ABSORPTION
Photon
Phonon
PHONON-ASSISTED ABSORPTION
• Energy conservation $\hbar\omega > E_g$
• Momentum conservation
$k_i = k_f$ for strong processes
• Indirect gap materials have weak absorption

Figure 5.2 Schematic representation of optical absorption process in semiconductor (left) direct and (right) indirect bandgap materials. Adapted from reference[167].

trons in the indirect minimum have different momentum. For direct-bandgap semiconductors, such as GaAs and InAs, the momentum is conserved and band-to-band transitions may occur with high probability. The photon energy is then approximately equal to the bandgap energy of the semiconductor. The radiative transition mechanism is predominant in direct-bandgap materials. However, for Si and GaP that are indirect bandgap semiconductors, the probability for interband transitions is extremely small, since phonons or other scattering agents must participate in the process in order to conserve momentum[166].

There are three main optical processes for interaction between a photon and an electron in a solid as depicted in Fig. 5.3.

- An electron excited from a filled state in the valence band to an empty state in the conduction band may absorb one photon. This is called absorption (the left upward arrow in Fig. 5.3) and it is the main process in a photodetector or solar cell.
- An electron in the conduction band can spontaneously return to an empty state in the valence band (recombination), with the emission of a photon. This is called spontaneous emission (the

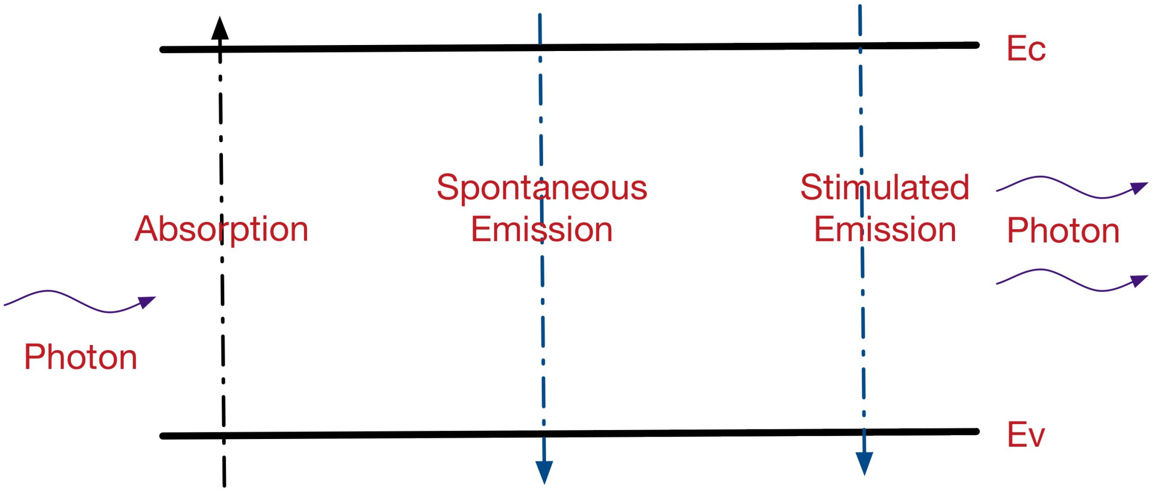

Figure 5.3 Schematic representation of basic interaction of a two-level system and an optical field.

middle downward arrow in Fig. 5.3), as the reverse process of absorption. And this is the primary process for LEDs.

- The incoming photon can stimulate the emission of anohter similar photon by recombination, giving out a net of two photons which are coherent (with same energy). This is called stimulated emission (the right downward arrow in Fig. 5.3), and it is the main process in a laser.

5.2 Optical Transition Rates in Semiconductor

In this section, we review the derivation of general optical transition rates in semiconductor by using time-dependent perturbation theory and Fermi's Golden Rule.

5.2.1 Time-dependent Perturbation Theory

The interaction of light and matter may be analyzed by the time-dependent perturbation theory (detailed derivation can be found in Appendix. A) which gives optical transition rate W_{if} from initial state 'i' to final state 'f', caused by light as:

$$W_{if} = \frac{2\pi}{\hbar}|H'_{fi}|^2\delta(E_f - E_i - \hbar\omega) + \frac{2\pi}{\hbar}|H'_{fi}|^2\delta(E_f + E_i - \hbar\omega) \tag{5.1}$$

Here the prefactor 2 is due to the spins; $H'_{fi} = \int \Phi_f{}^*(r)H'(r)\Phi_i(r)d^3r$ is the matrix element defined by Fermi's Golden Rule[168] that connects the initial state i with the final state f through the perturbation Hamiltonian $H'(r,t) = -\frac{e}{m_0}\mathbf{A}(\mathbf{r},\mathbf{t})\cdot\ \mathbf{p}$, where m_0 is the free electron mass, $\mathbf{A}(\mathbf{r},\mathbf{t})$ is the vector potential accounting for the presence of the electromagnetic field, and $\mathbf{p}$ is the momentum operator. The delta functions indicate the energy conservation, and show the resonance of photons and electrons for absorption of light (first term) and its emission (second term).

5.2.2 Fermi's Golden Rule

When the semiconductor illuminated by light, the interaction between the photons and the electrons in the semiconductor can be described by the Hamiltonian:

$$\mathcal{H} = \frac{1}{2m_0}(\boldsymbol{p} - e\boldsymbol{A})^2 + V(\boldsymbol{r}) \tag{5.2}$$

where m_0 is the free electron mass, $e = -|e|$ for electrons, $\boldsymbol{A}$ is the vector potential accounting for the presence of the electromagnetic field, and $V(\boldsymbol{r})$ is the periodic crystal potential.

The Hamiltonian can be expanded into

$$\mathcal{H} = \tfrac{1}{2m_0}(\boldsymbol{p} - e\boldsymbol{A})^2 + V(\boldsymbol{r}) \quad \approx \mathcal{H}_0 + \mathcal{H}' \tag{5.3}$$

where $\mathcal{H}_0$ is the unperturbed Hamiltonian and $\mathcal{H}'$ is considered as a perturbation due to light

$$\mathcal{H}_0 = \frac{\boldsymbol{p}^2}{2m_0} + V(\boldsymbol{r}) \tag{5.4}$$

$$\mathcal{H}' = -\frac{e}{m_0}\boldsymbol{A}\boldsymbol{p} \tag{5.5}$$

and consider the coulomb gauge has been used.

$$\nabla \cdot \boldsymbol{A} = 0 \tag{5.6}$$

noting that $\boldsymbol{p} = (\hbar/i)\nabla$, so $\boldsymbol{p} \cdot \boldsymbol{A} = (\frac{\hbar}{i})\nabla \cdot \boldsymbol{A} = \boldsymbol{A} \cdot \boldsymbol{p}$. And since we know $\boldsymbol{p} \approx \hbar k \approx \hbar\frac{\pi}{a}$, and a is the lattice constant, usually have a value of $5\mathring{A}$, so $|e\boldsymbol{A}| \ll |\boldsymbol{p}|$, then we can drop the last term $\frac{e^2\boldsymbol{A}^2}{2m_0}$, because it is much smaller than the terms linear in $\boldsymbol{A}$.

Assume the vector potential for the optical electric field of the form

$$\boldsymbol{A} = \hat{e}\boldsymbol{A}_0 \cos k_{op} \cdot \boldsymbol{r} - \omega t \quad = \hat{e}\frac{A_0}{2}e^{ik_{op}\cdot\boldsymbol{r}}e^{-i\omega t} + \hat{e}\frac{A_0}{2}e^{-ik_{op}\cdot\boldsymbol{r}}e^{i\omega t} \tag{5.7}$$

where $\boldsymbol{k_{op}}$ is the wave vector, ω is the optical angular frequency, and $\hat{e}$ is a unit vector in the direction of the optical electric field, we have

$$\boldsymbol{E}(\boldsymbol{r}, t) = -\frac{\partial \boldsymbol{A}}{\partial t} = -\hat{e}\omega_{A0} \sin \boldsymbol{k_{op}} \cdot \boldsymbol{r} - \omega t \tag{5.8}$$

$$\boldsymbol{H}(\boldsymbol{r}, t) = \frac{1}{\mu}\nabla \times \boldsymbol{A} = -\frac{1}{\mu}\boldsymbol{k}_{\text{op}} \times \hat{e}A_0 \sin(\boldsymbol{k}_{\text{op}} \cdot \boldsymbol{r} - \omega t) \tag{5.9}$$

where we have used the fact that the scalar potential φ vanishes ($\rho = 0$) for the optical field, and $\mu = \mu_0$, the permeability of the free space. The Poynting vector for the power intensity (W/cm^2) is given by

$$\boldsymbol{P}(\boldsymbol{r}, t) = \boldsymbol{E}(\boldsymbol{r}, t) \times \boldsymbol{H}(\boldsymbol{r}, t) = \hat{k}\boldsymbol{k}_{\text{op}}\frac{\omega {A_0}^2}{\mu}\ (\boldsymbol{k}_{\text{op}} \cdot \boldsymbol{r} - \omega t) \tag{5.10}$$

which is pointing along the direction of wave propagation $\boldsymbol{k}_{\text{op}}$. The time average of the Poynting flux is simply

$$\begin{aligned}
\boldsymbol{P} = \left|\boldsymbol{P}\left(\boldsymbol{r}, t\right)\right| &= \tfrac{\omega {A_0}^2}{2\mu} \boldsymbol{k}_{\mathrm{op}} \\
&= \tfrac{\omega^2 {A_0}^2 n_r}{2\mu c} \\
&= \tfrac{\omega^2 {A_0}^2 n_r \sqrt{\mu_0 \varepsilon_0}}{2\mu_0} \\
&= \tfrac{\omega^2 {A_0}^2 n_r \sqrt{\varepsilon_0}}{2\sqrt{\mu_0}} \\
&= \tfrac{\omega^2 {A_0}^2 n_r \sqrt{\varepsilon_0}\sqrt{\varepsilon_0}}{2\sqrt{\mu_0}\sqrt{\varepsilon_0}} \\
&= \tfrac{\omega^2 {A_0}^2 n_r \varepsilon_0 c}{2} \qquad (5.11)
\end{aligned}$$

Noting the time average of the $\sin^2()$ function is $\frac{1}{2}$ and $\boldsymbol{k}_{\mathrm{op}} = \omega\sqrt{\mu\varepsilon_0} = \frac{\omega}{\nu} = \frac{\omega}{\frac{c}{n_r}}$, $c = \frac{1}{\sqrt{\mu_0 \varepsilon_0}}$

The interaction Hamiltonian

$$\begin{aligned}
\mathcal{H}'\left(\boldsymbol{r}, t\right) &= -\tfrac{e}{m_0}\ \boldsymbol{A}(\boldsymbol{r}, t) \cdot \boldsymbol{p} \\
&= \mathcal{H}'\left(\boldsymbol{r}\right) \boldsymbol{e}^{-\boldsymbol{i}\boldsymbol{\omega}\boldsymbol{t}} + \mathcal{H}'^{+}\left(\boldsymbol{r}\right) \boldsymbol{e}^{+\boldsymbol{i}\boldsymbol{\omega}\boldsymbol{t}} \qquad (5.12)
\end{aligned}$$

where

$$\mathcal{H}'\left(\boldsymbol{r}\right) = -\frac{eA_0 \boldsymbol{e}^{\boldsymbol{i}\boldsymbol{k}_{\mathrm{op}} \cdot \boldsymbol{r}}}{2m_0}\ \cdot \hat{e} \cdot \boldsymbol{p} \qquad (5.13)$$

The superscript “+” means the Hermitian adjoint operator.

The transition rate for the absorption of a photon:

If the electron is at state a initially. And assume $E_b > E_a$

$$W_{\text{abs}} = \frac{2\pi}{\hbar} \left|\left\langle b\middle|\mathcal{H}^{'}\left(\boldsymbol{r}\right)\middle|a\right\rangle\right|^2 \delta(E_b - E_a - \hbar\omega) \tag{5.14}$$

The total upward transition rate per unit volume ($s^{-1}\text{cm}^{-3}$) in the crystal taking into account the probability that state a is occupied and state b is empty:

$$R_{a\to b} = \frac{2}{V}\sum_{\boldsymbol{k}_a}\sum_{\boldsymbol{k}_b}\frac{2\pi}{\hbar}\left|\mathcal{H}^{'}{}_{\text{ba}}\right|^2 \delta(E_b - E_a - \hbar\omega) f_a(1 - f_b) \tag{5.15}$$

where we sum over the initial and final states and assume that the Fermi-Dirac distribution f_a is the probability that the state a is occupied. A similar expression holds for f_b with E_a replaced by E_b, and $(1 - f_b)$ is the probability that the state b is empty. The prefactor 2 takes into account the sum over spins, and the matrix element $\mathcal{H}^{'}{}_{\text{ba}}$ is given by **Fermi's Golden Rule**

$$\mathcal{H}^{'}{}_{\text{ba}} \equiv \left|\left\langle b\middle|\mathcal{H}^{'}\left(\boldsymbol{r}\right)\middle|a\right\rangle\right| = \int \Psi_b^*\left(\boldsymbol{r}\right) H^{'}\left(\boldsymbol{r}, t\right) \Psi_a\left(\boldsymbol{r}\right) d^3\boldsymbol{r} \tag{5.16}$$

5.2.3 Upward and Downward Transition Rates

Similarly, the transition rate for the emission of a photon if an electron is initially at state b is

$$W_{\text{ems}} = \frac{2\pi}{\hbar} \left|\left\langle a\middle|\mathcal{H}^{'}\left(\boldsymbol{r}\right)\middle|b\right\rangle\right|^2 \delta(E_a - E_b + \hbar\omega) \tag{5.17}$$

The downward transition rate per unit volume ($s^{-1}\text{cm}^{-3}$) is

$$R_{b\to a} = \frac{2}{V}\sum_{\boldsymbol{k}_a}\sum_{\boldsymbol{k}_b}\frac{2\pi}{\hbar}\left|\mathcal{H}^{'+}{}_{\text{ab}}\right|^2 \delta(E_a - E_b + \hbar\omega) f_b(1 - f_a) \tag{5.18}$$

Using the even property of the delta function, $\delta\left(-x\right) = \delta\left(x\right)$, and $\mathcal{H}^{'}{}_{\text{ba}} = \mathcal{H}^{'+}{}_{\text{ab}}$, the net upward transition rate per unit volume can be written as

$$R = R_{a\to b} - R_{b\to a} = \frac{2}{V}\sum_{\boldsymbol{k}_a}\sum_{\boldsymbol{k}_b}\frac{2\pi}{\hbar}\left|\mathcal{H}'_{\mathrm{ba}}\right|^2\delta(E_b - E_a - \hbar\omega)(f_a - f_b) \tag{5.19}$$

The absorption coefficient $\alpha(1/cm)$ in the crystal is the fraction of photons absorbed per unit distance:

$$\alpha = \frac{\text{Number of photons absorbed per second per unit volume}}{\text{Number of injected photons per second per unit area}} \tag{5.20}$$

The injected number of photons per second per unit area is the optical intensity $P(W/\mathrm{cm}^2)$ divided by the energy of a photon $\hbar\omega$:

$$\alpha\left(\hbar\omega\right) = \frac{R}{\frac{P}{\hbar\omega}} = \frac{\hbar\omega}{\left(\frac{n_r c\epsilon_0\omega^2 A_0^2}{2}\right)}R \tag{5.21}$$

Using the long wavelength approximation that $\boldsymbol{A}\left(\boldsymbol{r}\right) = \boldsymbol{A}e^{i\boldsymbol{k}_{\mathrm{op}}\cdot\boldsymbol{r}} \approx \boldsymbol{A}$, we find that the matrix element can be written in terms of the momentum matrix element

$$\mathcal{H}'_{\mathrm{ba}} = -\frac{e}{m_0}\,\boldsymbol{A}\cdot\langle b|\boldsymbol{p}|a\rangle = \frac{eA_0}{2m_0}\,\cdot\hat{e}\cdot\boldsymbol{p}_{\mathrm{ba}} \tag{5.22}$$

The absorption coefficient becomes

$$\alpha\left(\hbar\omega\right) = C_0\tfrac{2}{V}\textstyle\sum_{\boldsymbol{k}_a}\sum_{\boldsymbol{k}_b}\left|\hat{e}\cdot\boldsymbol{p}_{\mathrm{ba}}\right|^2\delta(E_b - E_a - \hbar\omega)(f_a - f_b)$$

$$C_0 = \tfrac{\pi e^2}{n_r\varepsilon_0 c m_0^2\omega} \tag{5.23}$$

We can see that the factors containing ${A_0}^2$ are canceled because the linear optical absorption coefficient is independent of the optical intensity.

5.2.4 Photonic Modes Density

In order to find the density of states for the photon field, We need to first calculate the number of modes in a cube (mode density) of refractive index $\mathbf{n_r}$ and side length $\boldsymbol{L}$ in a frequency interval between ν and $\nu + d\nu$, assuming that $\boldsymbol{L}$ is much larger than the wavelength of the mode under consideration. As is usual, the photon field can be describes by a plane wave:

$$e^{i\boldsymbol{k}\cdot\boldsymbol{r}} = e^{ik_x x + ik_y y + ik_z z} \tag{5.24}$$

Using the periodic boundary conditions that the wave function should be periodic in the x, y and z directions with a period L.

$$k_x = l\frac{2\pi}{L} \ , \ k_y = m\frac{2\pi}{L} \text{ and } k_z = n\frac{2\pi}{L} \tag{5.25}$$

With

$$k^2 = k_x^2 + k_y^2 + k_z^2 = (\frac{2\pi}{L})^2 = (\frac{2\pi\nu n_r}{c})^2 \tag{5.26}$$

A combination of l, m and n describes a mode. The volume of a state in the k-space is $\left(\frac{2\pi}{L}\right)^3$. Therefore the number of modes per unit volume of k-space in the frequency range 0 to ν (or having wavevectors in the interval 0 to k) is obtained by dividing the volume of a sphere with radius ν (or k) by the volume per mode$\left(\frac{2\pi}{L}\right)^3$.

$$N_v = \frac{8\pi^3 v^3 n_r^3 L^3}{3c^3\pi^2} \quad = \frac{k^3 L^3}{3\pi^2} \tag{5.27}$$

The enclosed volume is $V_v = L^3$, the number of modes per unit volume in the frequency range 0 to

ν is

$$\frac{N_v}{V_v} = \frac{8\pi v^3 n_r^3}{3c^3} \qquad (\mathrm{cm}^{-3}) \tag{5.28}$$

As the initial assumption that the enclosure size $\boldsymbol{L}$ is much larger than the wavelength of the enclosed mode. This implies a large mode density closely spaced in frequency; however, as a nanowire, the diameter and length of the lasing cavity comes to subwavelength, we may have to alter the mode density function. Taking the derivative of Eq. 5.28 with respect to ν gives us the mode density per unit frequency interval per unit volume between ν and $\nu + d\nu$,

$$n_v = \frac{1}{V_v}\frac{\mathrm{dN}_v}{\mathrm{dv}} = \frac{8\pi v^2 n_r^2}{c^3} \qquad (\mathrm{s.cm}^{-3}) \tag{5.29}$$

Similarly, the mode density per unit energy interval is

$$n_\varepsilon = \frac{8\pi {n_r}^3 \varepsilon^2}{(2\pi)^3 h^3 c^3} = \frac{{n_r}^3 \varepsilon^2}{\pi^2 \hbar^3 c^3} \quad \mathrm{cm}^{-3}(eV)^{-1} \tag{5.30}$$

This equation gives the number of electromagnetic modes with different l, m, n, per unit volume, having energy in the interval between ε and $\varepsilon+\mathbf{d}\varepsilon$.

The radiation density of the modes in a frequency interval dv is given by

$$\varphi(v)\, d\nu = v n_v u_v \mathrm{dv} \tag{5.31}$$

And in an energy interval $\mathbf{d}\varepsilon$ by

$$\varphi(\mathcal{E})\, d\mathcal{E} = hv n_\varepsilon u_\varepsilon d\varepsilon \tag{5.32}$$

hv on the right-hand side is the energy per photon, the second term n_ε is the mode density, and the third term u_ε is the average number of photons per mode in the energy interval between ε and ε+**d**ε, which is the same as the occupation factor that following the Bose-Einstein statistics for photons:

$$u_\varepsilon = \frac{1}{e^{\frac{\hbar\omega_k}{k_BT}} - 1} \tag{5.33}$$

Then the photon density per unit energy interval can be defined as $N_p = n_\varepsilon u_\varepsilon$:

$$N_p = \frac{{n_r}^3\varepsilon^2}{\pi^2\hbar^3c^3}\frac{1}{e^{\frac{\varepsilon}{k_BT}} - 1} \quad \mathrm{cm}^{-3}(eV)^{-1} \tag{5.34}$$

5.3 The Einstein Relations

Consider two energy levels ε_1 and ε_2 with populations $\mathbf{N}_1$ and $\mathbf{N}_2$ in an atomic system in thermal equilibrium. ε_2 is larger than ε_1 and normally $\mathbf{N}_2$ is smaller than $\mathbf{N}_1$. In such a system, the rate of the upward transition must equal the rate of the downward transitions.

Then define Einstein's B_{12} Coefficients as

$$B_{12} = \frac{2\pi}{\hbar}\left|\mathcal{H}'_{12}\right|^2 \tag{5.35}$$

where B_{12} is known as the Einstein coefficient for stimulated upward transitions, or absorption rate per incident photon within an energy interval, (eV/s). So the upward transition rate per unit volume ($s^{-1}\mathrm{cm}^{-3}$) is proportional to $\mathbf{N}_1$ and the radiation density $\varphi(v)$,

$$r_{12}= B_{12}\mathbf{N}_1\varphi(v) \tag{5.36}$$

Thus, for the total upward transition rate per unit volume ($s^{-1}\mathrm{cm}^{-3}$) for a broad spectrum is

$$R_{12}= B_{12}S(E_{21}) \tag{5.37}$$

where

$$S\left(E_{21}\right)=N\left(E_{21}\right)n_{\varepsilon} \tag{5.38}$$

is the number of photons per unit volume per energy interval with a dimension of $\mathrm{cm}^{-3}(eV)^{-1}$,

$$n_{\varepsilon}=\frac{1}{e^{\frac{E_{21}}{k_{B}T}}-1} \tag{5.39}$$

is the number of photons per state at an optical energy E_{21}.

If we take into account the occupation probabilities of level 1 and level 2 using Fermi-Dirac distributions, f_1 and f_2, respectively, the expression for R_{12} will be modified,

$$\begin{aligned} R_{12}(=r_{12}(E_{21})dE) &= \tfrac{1}{V}\textstyle\sum_{k} B_{12}\delta\left(E_{2}-E_{1}-\hbar\omega_{k}\right)2n_{\varepsilon}\cdot f_{1}(1-f_{2}) \\ &= B_{12}f_{1}(1-f_{2})S\left(E_{21}\right) \end{aligned} \tag{5.40}$$

Where $r_{12}(E_{21})dE$ means that the upward transition rate per unit volume has been integrated for a light with a spectral width dE near $E=E_{21}$, $r_{12}(E)$ is the number of $1 \rightarrow 2$ transitions per second per unit volume per energy interval ($s^{-1}\mathrm{cm}^{-3}\mathrm{eV}^{-1}$).

Similarly, a stimulated emission rate per unit volume can be given

$$R_{21}^{\mathrm{stim}}=r_{21}^{\mathrm{stim}}(E)dE=B_{21}f_{2}(1-f_{1})S\left(E_{21}\right) \tag{5.41}$$

In the case of spontaneous emission, where the photons created by recombination escape, the spontaneous emission rate per unit volume is independent of the photon density and is given by

$$R_{21}^{\text{spon}} = r_{21}^{\text{spon}}(E)dE = A_{21}f_2(1-f_1) \tag{5.42}$$

A_{21} is the Einstein coefficient for spontaneous emission. As A and B coefficient are not changed whether in thermal equilibrium or not, we can use the following properties in the future. At thermal equilibrium, there is only one Fermi level; therefore $F_1 = F_2$. We balance the total downward transition rate with the upward transition rate:

$$R_{12} = R_{21}^{\text{stim}} + R_{21}^{\text{spon}} \tag{5.43}$$

or

$$B_{12}f_1\left(1-f_2\right)S\left(E_{21}\right) = B_{21}f_2\left(1-f_1\right)S\left(E_{21}\right) + A_{21}f_2(1-f_1) \tag{5.44}$$

We have

$$\frac{A_{21}}{B_{12}e^{\frac{E_{21}}{k_BT}} - B_{21}} = N\left(E_{21}\right)\frac{1}{e^{\frac{E_{21}}{k_BT}} - 1} \tag{5.45}$$

By comparing the left- and right-hand sides, we find $B_{12} = B_{21}$, and

$$\frac{A_{21}}{B_{21}} = N\left(E_{21}\right) = \frac{n_r^3E_{21}^2}{\pi^2\hbar^3c^3} \tag{5.46}$$

Thus, the ratio of the stimulated and spontaneous emission rate is:

$$\frac{R_{21}^{\text{stim}}}{R_{21}^{\text{spon}}} = \frac{B_{21}f_2\left(1-f_1\right)S\left(E_{21}\right)}{A_{21}f_2(1-f_1)} = n_\varepsilon \tag{5.47}$$

which is the number of photons per state.

5.4 Dimensional Dependence of Interband Transition Rates

Optical interband transition rates are strong function of dimensionality. Shrinking the size of the devices not only introduced the confinement of electron and hole movement, but also modified the optical interband transition rates dramatically.

5.4.1 Interband Transition Rates for a Bulk Semiconductor

Here, we evaluate the optical matrix element:

$$\mathcal{H}'_{\mathrm{ba}} = \left\langle b \middle| -\frac{e\boldsymbol{A(r)}}{m_0} \boldsymbol{\cdot p} \middle| a \right\rangle \tag{5.48}$$

The vector potential for the optical field is

$$\boldsymbol{A}\left(\boldsymbol{r}\right) = \boldsymbol{A}\cdot e^{i\boldsymbol{k}_{\mathrm{op}}\cdot r} = \frac{\hat{e}A_0}{2} e^{i\boldsymbol{k}_{\mathrm{op}}\cdot r} \tag{5.49}$$

The Bloch functions for electrons in the valence band E_a and the conduction band E_b are:

$$\Psi_a\left(\boldsymbol{r}\right) = u_v(\boldsymbol{r}) \frac{e^{i\boldsymbol{k_v}\cdot r}}{\sqrt{V}} \tag{5.50}$$

$$\Psi_b\left(\boldsymbol{r}\right) = u_c(\boldsymbol{r}) \frac{e^{i\boldsymbol{k_c}\cdot r}}{\sqrt{V}} \tag{5.51}$$

where $u_v(\boldsymbol{r})$ and $u_c(\boldsymbol{r})$ are the periodic parts of the Bloch functions, and the remainders are the envelope functions (plane waves) for a free electron. The momentum matrix element is derived from

$$
\begin{aligned}
\mathcal{H}'_{\rm ba} &= -\tfrac{eA_0}{2m_0}\ \hat{e}\cdot\int \Psi_b^* e^{i\boldsymbol{k}_{\rm op}\cdot r}\boldsymbol{p}\Psi_a d^3\boldsymbol{r} \\
&= -\tfrac{eA_0}{2m_0}\ \hat{e}\cdot\int u_c(\boldsymbol{r})e^{i\boldsymbol{k_c}\cdot r}e^{i\boldsymbol{k}_{\rm op}\cdot r}\left[\left(\tfrac{\hbar}{i}\nabla u_v(\boldsymbol{r})\right)e^{i\boldsymbol{k_v}\cdot r}+\hbar\boldsymbol{k_v}u_v(\boldsymbol{r})e^{i\boldsymbol{k_v}\cdot r}\right]\tfrac{d^3\boldsymbol{r}}{V} \\
&\approx -\tfrac{eA_0}{2m_0}\ \hat{e}\cdot\int_\Omega {u_c}^*(\boldsymbol{r})\tfrac{\hbar}{i}\nabla u_{_v}(\boldsymbol{r})\tfrac{d^3\boldsymbol{r}}{\Omega}\int_V e^{i(-\boldsymbol{k_c}+\boldsymbol{k}_{\rm op}+\boldsymbol{k_v})\cdot r}\tfrac{d^3\boldsymbol{r}}{V} \\
&= -\tfrac{eA_0}{2m_0}\ \hat{e}\cdot\boldsymbol{p}_{\rm cv}\delta_{\boldsymbol{k_c},\boldsymbol{k}_{\rm op}+\boldsymbol{k_v}} \qquad (5.52)
\end{aligned}
$$

$$\boldsymbol{p}_{\rm cv} = \int_\Omega {u_c}^*(\boldsymbol{r})\frac{\hbar}{i}\nabla u_{_v}(\boldsymbol{r})\frac{d^3\boldsymbol{r}}{\Omega} \qquad (5.53)$$

where we noted that $\left[{u_c}^*(\boldsymbol{r})\frac{\hbar}{i}\nabla u_v(\boldsymbol{r})\right]$ and $[{u_c}^*(\boldsymbol{r})u_v(\boldsymbol{r})]$ are periodic functions with the period of a unit cell, whereas the envelope functions are slowly varying functions over a unit cell. Therefore, the integral over $d^3\boldsymbol{r}$ can be separated into the product of two integrals, one over the unit cell Ω for the periodic part, and the other over the slowly varying part. In another word, we use the approximation:

$$\int_V \left[{u_c}^*(\boldsymbol{r})\frac{\hbar}{i}\nabla u_{_v}(\boldsymbol{r})\right]F(\boldsymbol{r})d^3\boldsymbol{r} \approx \int_V F(\boldsymbol{r})d^3\boldsymbol{r}\int_\Omega {u_c}^*(\boldsymbol{r})\frac{\hbar}{i}\nabla u_{_v}(\boldsymbol{r})\frac{d^3\boldsymbol{r}}{\Omega} \qquad (5.54)$$

where $F(\boldsymbol{r})$ is slowly varying over a unit cell, and we have used the periodic property of the Bloch periodic functions

$${u_c}^*(\boldsymbol{r})\frac{\hbar}{i}\nabla u_{_v}(\boldsymbol{r}) = \sum_{\boldsymbol{G}}\boldsymbol{C_G}e^{i\boldsymbol{G}\cdot r} \qquad (5.55)$$

where the vectors $\boldsymbol{G}'s$ are the reciprocal lattice vectors. Because $F(\boldsymbol{r})$ is slowly varying over a unit cell, we may approximate $F(\boldsymbol{r}+\boldsymbol{R}) = F(\boldsymbol{R})$ and put it outside of the integral over a unit cell. Here the $\boldsymbol{R}$s are the lattice vectors, and $e^{i\boldsymbol{G}\cdot\boldsymbol{R}} = 1.\omega$ is the volume of a unit cell. Note that the orthogonal property

$$\int_\Omega {u_c}^* u_v d^3\boldsymbol{r} = 0,$$
$$\frac{1}{\Omega}\int_\Omega {u_c}^* u_c d^3\boldsymbol{r} = \frac{1}{\Omega}\int_\Omega {u_v}^* u_v d^3\boldsymbol{r} = 1 \tag{5.56}$$

From the matrix element, we see the momentum conservation

$$\hbar\boldsymbol{k}_c = \hbar\boldsymbol{k}_v + \hbar\boldsymbol{k}_{\mathrm{op}} \tag{5.57}$$

is obeyed. The electron at the final state has its crystal momentum $\hbar\boldsymbol{k}_{\mathrm{c}}$ equal to its initial momentum$\hbar\boldsymbol{k}_v$ plus the photon momentum$\hbar\boldsymbol{k}_{\mathrm{op}}$. Because $\boldsymbol{k}_{\mathrm{op}} \sim \frac{2\pi}{\lambda_0}$, and the magnitudes $\boldsymbol{k}_{\mathrm{c}}$, $\boldsymbol{k}_{\mathrm{v}}$ are of the order $\frac{2\pi}{a_0}$, where a_0 is the lattice constant of the semiconductors, which is typically of the order $5.5\mathring{A}$ and is much smaller than we may ignore $\boldsymbol{k}_{\mathrm{op}}$ and obtain

$$\mathcal{H}'_{\mathrm{ba}} \approx -\frac{eA_0}{2m_0}\ \hat{e}\cdot\boldsymbol{p}_{\mathrm{cv}}\delta_{\boldsymbol{k_c},\boldsymbol{k_v}} \tag{5.58}$$

which is the **K**-selection Rule.

1) Interband momentum matrix element $\boldsymbol{p}_{\mathrm{cv}}$ depend only on the periodic parts of the Bloch functions (u_c and u_v),

2) The original optical momentum matrix element $\boldsymbol{p}_{\mathrm{ab}}$, depends on the full wave functions (i.e. including the envelope function).

Using the **K**-selection rule in the matrix element, we find that the absorption coefficient for a bulk semiconductor is

$$\alpha\left(\hbar\omega\right)=C_0\tfrac{2}{V}\textstyle\sum_{\boldsymbol{k}_a}\sum_{\boldsymbol{k}_b}\left|\hat{e}\cdot\boldsymbol{p}_{\mathrm{cv}}\right|^2\delta(E_c-E_v-\hbar\omega)(f_v-f_c)$$

$$C_0=\tfrac{\pi e^2}{n_r\varepsilon_0 c m_0^2\omega} \tag{5.59}$$

where the Fermi-Dirac distributions for the electrons in the valence bend and in the conduction band are, respectively.

$$f_v\left(k\right)=\frac{1}{1+e^{\frac{\left(E_v(k)-F_v\right)}{\mathrm{KT}}}},f_c\left(k\right)=\frac{1}{1+e^{\frac{\left(E_c(k)-F_c\right)}{\mathrm{KT}}}} \tag{5.60}$$

Assume:

1) $\boldsymbol{k}_{\mathrm{c}}\ =\boldsymbol{k}_{\mathrm{v}}\ =\boldsymbol{k},$ $F_v=F_c=E_F$ (thermal equilibrium)

2) $f_v=1$ *and* $f_c=0$

3) $\left|\hat{e}\cdot\boldsymbol{p}_{\mathrm{cv}}\right|^2$ is independent of $\boldsymbol{k}$ and denote the absorption spectrum at thermal equilibrium.

$$\alpha\left(\hbar\omega\right)=C_0\left|\hat{e}\cdot\boldsymbol{p}_{\mathrm{cv}}\right|^2\int\frac{2d^3\boldsymbol{k}}{\left(2\pi\right)^3}\delta(E_g+\frac{\hbar^2\boldsymbol{k}^{\mathbf{2}}}{2m_r^*}-\hbar\omega) \tag{5.61}$$

where used the reduced effective mass m_r^*

$$E_c=E_g+\frac{\hbar^2\boldsymbol{k}^{\mathbf{2}}}{2m_r^*}\qquad E_v=-\frac{\hbar^2\boldsymbol{k}^{\mathbf{2}}}{2m_r^*}$$
$$\frac{1}{m_r^*}=\frac{1}{m_e^*}+\frac{1}{m_h^*}$$

Here all energies are measured from the top of the valence band. Therefore, both E_c and F_c contain the band-gap energy E_g. Let

$$X = E_g + E - \hbar\omega \quad E = \frac{\hbar^2 \boldsymbol{k^2}}{2m_r^*} \tag{5.62}$$

we find, by a change of variables, the integration can be carried out with the contribution at $X = 0,\ and\ E = \hbar\omega - E_g$

$$\alpha_{3D}\left(\hbar\omega\right) = C_0 \left|\hat{e} \cdot \boldsymbol{p}_{\mathrm{cv}}\right|^2 \rho_r\left(\hbar\omega - E_g\right)\left(f_v - f_c\right) \tag{5.63}$$

$$\rho_r\left(\hbar\omega - E_g\right) = \tfrac{1}{2\pi^2}\left(\tfrac{2m_r^*}{\hbar^2}\right)^{\frac{3}{2}}\left(\hbar\omega - E_g\right)^{\frac{1}{2}} \tag{5.64}$$

Therefore, the absorption coefficient depends on the momentum matrix element and the joint optical density of states. Below the band-gap energy E_g, the absorption does not occur because the photons see a forbidden band gap.

For the derivation of spontaneous emission rate, we start from the absorption spectrum within a spectral width dE:

$$\begin{aligned}\alpha\left(E_{21}\right) dE &= \tfrac{r_{\mathrm{net}}^{\mathrm{abs}}\left(E_{21}\right)\mathrm{dE}}{P\left(E_{21}\right)\frac{c}{n_r}} \\ &= \tfrac{n_r}{c} B_{12}\left(f_1 - f_2\right)\end{aligned} \tag{5.65}$$

where $P\left(E_{21}\right)$ is the irradiance of the photon beam or energy crossing the unit area in unit time ($\mathrm{cm}^{-3}\mathrm{eV}^{-1}$).

The ratio of the spontaneous emission spectrum and the absorption spectrum can be expressed as:

$$\frac{r_{21}^{\mathrm{spon}}(E_{21})}{\alpha(E_{21})} = \frac{A_{21}f_2(1-f_1)}{\frac{n_r}{c}B_{12}(f_1-f_2)} \quad = \frac{c}{n_r}\cdot N\left(E_{21}\right)\frac{1}{e^{\frac{(E_{21}-F)}{k_BT}}-1} \tag{5.66}$$

or

$$r_{21}^{\mathrm{spon}}\left(E_{21}\right) = \left(\frac{n_r^2E_{21}^2}{\pi^2\hbar^3c^2}\right)\frac{1}{e^{\frac{(E_{21}-F)}{k_BT}}-1}\alpha\left(E_{21}\right) \tag{5.67}$$

and $F = F_2 - F_1$ is the quasi-Fermi level separation. Now, the spontaneous emission rate can be carried out as:

$$r_{3D}^{\mathrm{spon}}(\hbar\omega) = \frac{n_re^2\omega {p_{cv}}^2}{\pi\epsilon_0{m_0}^2C^3\hbar}\frac{{m_r}^{*3/2}}{2\pi^2\hbar^3}\sqrt{(\hbar\omega-E_g)}f_c(1-f_v) \tag{5.68}$$

In addition, based on the relationship between spontaneous emission and stimulated emission as in Eq. 5.47, the stimulated emission can also be derived as:

$$r_{3D}^{\mathrm{sti}}(\hbar\omega) = \left(\frac{n_r\omega e^2(1+u_\varepsilon)}{3\pi\hbar c^3\epsilon_0m_0^2}\right)|\hat{e}\cdot\mathbf{p_{cv}}|^{\mathbf{2}}f_c(1-f_v)\frac{1}{2\pi^2}\left(\frac{2m_r^*}{\hbar^2}\right)^{3/2}(\hbar\omega-E_g)^{1/2} \tag{5.69}$$

5.4.2 Interband Transition Rates in A Quantum Well

The central cell functions in the quantum wells are relatively unaffected by the presence of the confining potential. There are only two changes compared to bulk semiconductor, first, the nature of wavefunction for the low lying states are confined to the well region, second, the density of the state have the usual step-like form for parabolic 2-dimensional bends.

Ignore the excitonic effects due to the Coulomb interaction between electrons and holes.

Within a two-band model, the Bloch wave functions can be described by

$$\Psi_a\left(\boldsymbol{r}\right) = u_v(\boldsymbol{r})\frac{e^{i\boldsymbol{k_t}\cdot\rho}}{\sqrt{A}}g_m(z) \tag{5.70}$$

for a hole wave function in the heavy-hole or a light-hole subband m. and

$$\Psi_b\left(\boldsymbol{r}\right) = u_c(\boldsymbol{r})\frac{e^{i\boldsymbol{k_t}\cdot\rho}}{\sqrt{A}}\Phi_n(z) \tag{5.71}$$

for an electron in the conduction subband n. The momentum matrix element $\boldsymbol{p}_{\mathrm{ba}}$ is given by

$$\boldsymbol{p}_{\mathrm{ba}} = \langle\Psi_b|\boldsymbol{p}|\Psi_a\rangle \approx \langle u_c|\boldsymbol{p}|u_v\rangle\,\delta_{k_t,k_t'}\ I_{\mathrm{hm}}^{\mathrm{en}} \tag{5.72}$$

where

$$I_{\mathrm{hm}}^{\mathrm{en}} = \int_{-\infty}^{+\infty} \mathrm{dz}\Phi_n^*(z)g_m(z) \tag{5.73}$$

- This is the overlap integral of the conduction and valence band envelope functions
- **K**-Selection rule applied
- Take into account the quantization of the electron and hole energies E_a and E_b

$$E_a = E_{\mathrm{hm}} - \frac{\hbar^2\boldsymbol{k_t}^2}{2m_h^*} \tag{5.74}$$

$$E_b = E_g + E_{\mathrm{en}} + \frac{\hbar^2\boldsymbol{k_t}^2}{2m_e^*} \tag{5.75}$$

And $E_{\text{hm}} < 0$,

$$E_b - E_a = E_{\text{hm}}^{\text{en}} + E_t, \quad E_t = \frac{\hbar^2 \boldsymbol{k_t}^2}{2m_e^*} \tag{5.76}$$

where

$$E_{\text{hm}}^{\text{en}} = E_g + E_{\text{en}} - E_{\text{hm}} \tag{5.77}$$

is the band edge transition energy ($\boldsymbol{k_t} = 0$). The summations over the quantum numbers $\boldsymbol{k}_a$ and $\boldsymbol{k}_b$become summations over $(\boldsymbol{k_t'}, m)$ and $(\boldsymbol{k_t}, n)$. Noting in the matrix element $\boldsymbol{k_t} = \boldsymbol{k_t'}$

$$\alpha\left(\hbar\omega\right) = C_0 \sum_{n,m} \left|I_{\text{hm}}^{\text{en}}\right|^2 \frac{2}{V} \sum_{\boldsymbol{k}_t} \left|\hat{e} \cdot \boldsymbol{p}_{\text{cv}}\right|^2 \delta(E_{\text{hm}}^{\text{en}} + E_t - \hbar\omega)(f_v^m - f_c^n) \tag{5.78}$$

Use the two-dimensional joint density of states

$$\frac{2}{V}\sum_{\boldsymbol{k}_t} = \frac{2A}{V}\int \frac{d^2\boldsymbol{k_t}}{(2\pi)^2} = \frac{1}{\pi L_z}\int_0^\infty \boldsymbol{k_t} d\boldsymbol{k_t} = \int_0^\infty d\frac{\hbar^2 \boldsymbol{k_t}^{\boldsymbol{2}}}{2m_r^*} \cdot \frac{m_r^*}{\pi\hbar^2 L_z} = \int_0^\infty dE_t \rho_r^{2D} \tag{5.79}$$

$$\rho_r^{2D} = \frac{m_r^*}{\pi\hbar^2 L_z} \tag{5.80}$$

where A is the area of the cross section, $\text{AL}_z = V$, L_z is an effective period of the quantum wells, and V is a volume of a period. The delta function gives the contribution at $E_{\text{hm}}^{\text{en}} + E_t = \hbar\omega$, and the absorption edges occur at $\hbar\omega = E_{\text{hm}}^{\text{en}}$. For an unpumped semiconductor, $f_v^m = 1 \textit{ and } f_c^n = 0$, we have the absorption spectrum at thermal equilibrium $\alpha_0\left(\hbar\omega\right)$

$$\alpha_0\left(\hbar\omega\right) = C_0 \sum_{n,m} \left|I_{\text{hm}}^{\text{en}}\right|^2 \left|\hat{e} \cdot \boldsymbol{p}_{\text{cv}}\right|^2 \rho_r^{2D} H(\hbar\omega - E_{\text{hm}}^{\text{en}}) \tag{5.81}$$

Because the integration of the delta function gives the step function, shown as H or the Heaviside step function, $H(x) = 1 \ for \ x > 0, \ and \ 0 \ for \ x < 0$. For a symmetric quantum well, we find $I_{\mathrm{hm}}^{\mathrm{en}} = \delta_{\mathrm{nm}}$ using an infinite well model, and the absorption spectrum is

$$\alpha_{2D}(\hbar\omega) = C_0 \left|\hat{e} \cdot \boldsymbol{p}_{\mathrm{cv}}\right|^2 \tfrac{m_r^*}{\pi\hbar^2 L_z}(f_v - f_c)$$

$$C_0 = \tfrac{\pi e^2}{n_r \varepsilon_0 c m_0^2 \omega} \tag{5.82}$$

Use the same relationship between absorption, spontaneous emission and stimulated emission, we can derive the spontaneous emission and stimulated emission rates as follows:

$$r_{2D}^{\mathrm{spon}}(\hbar\omega) = \frac{n_r e^2 \omega p_{cv}^2}{\pi\epsilon_0 m_0{}^2 C^3 \hbar} \frac{m_r^*}{\pi\hbar^2 L_z} f_c(1 - f_v) \tag{5.83}$$

$$r_{2D}^{\mathrm{sti}}(\hbar\omega) = \left(\frac{n_r \omega e^2 (1 + u_\varepsilon)}{\pi\hbar c^3 \epsilon_0 m_0^2}\right) |\hat{e} \cdot \mathbf{p_{cv}}|^{\mathbf{2}} f_c(1 - f_v) \frac{m_r^*}{\pi\hbar^2 L_z} \tag{5.84}$$

5.4.3 Interband Transition Rates in nanowire

For nanowire structure, the confining potential also only changes the nature of wavefuction and the density of the state as in the 2-dimensional case. Also ignore the excitonic effects due to the Coulomb interaction between electrons and holes, then follow the similar procedure in 2-dimensional.

We consider a nanowire with cross section $a \times b$, and the length of wire is $L_z \gg a, b$.

Within a semiconductor model, the valence band Bloch wave functions can be described by

$$\Psi_v(\boldsymbol{r}) = u_v(\boldsymbol{r}) \frac{e^{i\boldsymbol{k_t} \cdot \rho}}{\sqrt{L_z}} g_m(x, y) \tag{5.85}$$

$$g_m(x, y) = \frac{2}{\sqrt{\mathrm{ab}}} \sin\left(\frac{m\pi}{a} x\right) \sin\left(\frac{n\pi}{b} y\right) \tag{5.86}$$

and the conduction band Block wave function as,

$$\Psi_c\left(\boldsymbol{r}\right) = u_c(\boldsymbol{r})\frac{e^{i\boldsymbol{k_t}\cdot\rho}}{\sqrt{L_z}}\Phi_n(x,y) \tag{5.87}$$

$$\Phi_n(x,y) = \frac{2}{\sqrt{\mathrm{ab}}}\sin\left(\frac{m^{'}\pi}{a}x\right)\sin\left(\frac{n^{'}\pi}{b}y\right) \tag{5.88}$$

where

$$E_v^{m^{'}n^{'}} = E_{v0} - \frac{\hbar^2}{2m_h^*}[\left(\frac{m^{'}\pi}{a}\right)^2 + \left(\frac{n^{'}\pi}{b}\right)^2 + \boldsymbol{k_t^2}] \tag{5.89}$$

$$E_c^{\mathrm{mn}}\left(k_t\right) = E_{c0} + \frac{\hbar^2}{2m_e^*}[\left(\frac{m\pi}{a}\right)^2 + \left(\frac{n\pi}{b}\right)^2 + \boldsymbol{k_t^2}] \tag{5.90}$$

The momentum matrix element $\boldsymbol{p}_{\mathrm{ba}}$ is given by

$$\boldsymbol{p}_{\mathrm{ba}} = \langle\Psi_b|\boldsymbol{p}|\Psi_a\rangle \approx \langle u_c|\boldsymbol{p}|u_v\rangle\,\delta_{k_t,k_t^{\prime}}\;I_{\mathrm{hm}}^{\mathrm{en}} \tag{5.91}$$

where

$$I_{\mathrm{hm}}^{\mathrm{en}} = \int_{-\infty}^{+\infty}\mathrm{dxdy}\Phi_n^*(x,y)g_m(x,y) \tag{5.92}$$

- This is the overlap integral of the conduction and valence band envelope functions
- **K**-Selection rule applied

Use the one-dimensional joint density of states,

$$\frac{2}{V}\sum_{\boldsymbol{k}_t} = \frac{2L_z}{V}\int\frac{d\boldsymbol{k_t}}{2\pi} = \frac{1}{\pi L_x L_y}\int_0^\infty\frac{\mathbf{1}}{\boldsymbol{k_t}}d\boldsymbol{k_t} = \int_0^\infty dE_t\rho_r^{1D} \tag{5.93}$$

$$\rho_r^{1D} = \sum_{m,n} \frac{(2m_r^*)^{\frac{1}{2}}}{\pi\hbar} \frac{\mathbf{1}}{\sqrt{(\hbar\omega - E_c^{\mathrm{mn}})}} \quad forE > E_c^{\mathrm{mn}} \tag{5.94}$$

$$\rho_r^{1D} = \frac{(m_r^*)^{\frac{3}{2}}}{\pi\hbar m_e^* L_x L_y} \frac{\mathbf{1}}{\sqrt{(\hbar\omega - E_g)}} \tag{5.95}$$

The electron density is given by the occupation of the wire states, and at zero temperature it can be integrated analytically,

$$n = \sum_{m,n} \frac{(2m_r^*)^{\frac{1}{2}}}{\pi\hbar L_x L_y} \sqrt{(F_c - E_c^{\mathrm{mn}})} \tag{5.96}$$

where $L_z L_x L_y = V$, $L_x, L_{y,} L_z$ are effective period of the quantum wire along different directions, L_z along the axial of the quantum wire, and V is a volume of a period. The delta function gives the contribution at $E_{\mathrm{hm}}^{\mathrm{en}} + E_t = \hbar\omega$, and the absorption edges occur at $\hbar\omega = E_{\mathrm{hm}}^{\mathrm{en}}$. For an unpumped semiconductor, $f_v^m = 1 \; and \; f_c^n = 0$, we have the absorption spectrum at thermal equilibrium $\alpha_0 (\hbar\omega)$

$$\alpha_0 (\hbar\omega) = C_0 \sum_{n,m} \left| I_{\mathrm{hm}}^{\mathrm{en}} \right|^2 \left| \hat{e} \cdot \boldsymbol{p}_{\mathrm{cv}} \right|^2 \rho_r^{1D} H(\hbar\omega - E_{\mathrm{hm}}^{\mathrm{en}}) \tag{5.97}$$

Because the integration of the delta function gives the step function, shown as H or the Heaviside step function, $H(x) = 1 \; for \; x > 0, \; and \; 0 \; for \; x < 0$. For a symmetric quantum wire, we find $I_{\mathrm{hm}}^{\mathrm{en}} = \delta_{\mathrm{nm}}$ using an infinite wire model, and the absorption spectrum is

$$\begin{gathered} \alpha_{1D} (\hbar\omega) = C_0 \left| \hat{e} \cdot \boldsymbol{p}_{\mathrm{cv}} \right|^2 \tfrac{(2m_r^*)^{\frac{1}{2}}}{\pi\omega L_x L_y} \tfrac{\mathbf{1}}{\sqrt{(\hbar\omega - E_{\mathrm{cv}}^{\mathrm{mn}})}} (f_v - f_c) \\ E_{\mathrm{cv}}^{\mathrm{mn}} = E_g + \tfrac{\hbar^2}{2m_r^*} [\left(\tfrac{m\pi}{a}\right)^2 + \left(\tfrac{n\pi}{b}\right)^2] \\ C_0 = \tfrac{\pi e^2}{n_r \varepsilon_0 c m_0^2 \omega} \end{gathered} \tag{5.98}$$

Similarly, the spontaneous emission and stimulated emission rates can be carried out as:

$$r_{1D}^{\text{spon}}(\hbar\omega) = \frac{n_r e^2 \omega p_{cv}^2}{\pi\epsilon_0 m_0{}^2 C^3 \hbar} \frac{m_r^{*3/2}}{\pi\hbar m_e^* L_x L_y} \frac{1}{\sqrt{(\xi-\xi_g)}} f_c(1-f_v) \tag{5.99}$$

$$r_{1D}^{\text{sti}}(\hbar\omega) = \left(\frac{n_r \omega e^2 (1+u_\varepsilon)}{\pi\hbar c^3 \epsilon_0 m_0^2}\right) |\hat{e}\cdot\mathbf{p_{cv}}|^{\mathbf{2}} f_c(1-f_v) \frac{(m_r^*)^{3/2}}{\pi\hbar m_e^* L_x L_y} \frac{1}{\sqrt{(\hbar\omega - E_g)}} \tag{5.100}$$

5.5 Contributing Factors

The derived transition rates (absorption, spontaneous emission and stimulated emission rates) are both strong function of dimensionality. Carrier confinement in core-shells, and the effect of local forces shown by band bending affects transition rates due to the following factors:

5.5.1 Overlap Integral

The confined structure alters the overlap integral between initial and final wave function as in Eq. 5.101, Where $\Phi_n^*(z)$ and $g_m(z)$ are electron envelope function in the conduction subband n and heavy-hole or light-hole envelope function in the subband m, respectively. Higher overlap results in higher optical transition rates in reduced dimensions in much the same manner that the Quantum Confined Stark Effect (QCSE) is much stronger than the bulk Franz-Keldysh effect[169]. This has been exploited in NW light-emitting devices and lasers for increased luminosity[170].

$$I_{hm}^{en} = \int_{-\infty}^{\infty} \Phi_n^*(z) g_m(z)\, \mathrm{d}z, \tag{5.101}$$

Figure 5.4 shows the transition energy (black line, first confined conduction band to the first confined heavy hole band i.e., e_1-hh_1) as well as the spatial overlap integral (blue line) of the electron and hole ground state wave functions as a function of increasing x alloy content of a hexagonal $GaAs/Al_xGa_{1-x}As$ core-shell structure. The hexagonal GaAs core has an outer radius of 10 nm, while the AlGaAs shell has a diameter of 40 nm and surrounded by an infinite barrier.The results

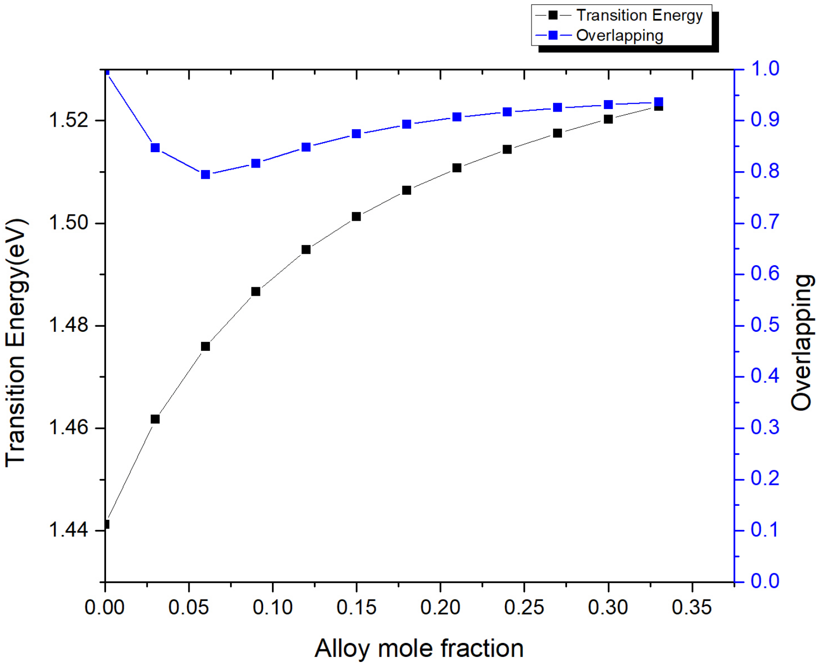

Figure 5.4 The transition energy (black line, e_1-hh_1) as well as the spatial overlap integral (blue line) of the electron and hole ground state wave functions as a function of increasing $Al_xGa_{1-x}As$ x alloy content for a hexagonal $GaAs/Al_xGa_{1-x}As$ core-shell structure.

show with increasing of the alloy mole fraction, as expected, the transition energy increased. And most importantly, the overlapping of the electron and hole ground state wavefunction remain a relative large number over 80% with a minima at around 5% of mole fraction, showing electron and hole wavefunctions strongly confined in this hexagonal nanostructure.

5.5.2 Oscillator Strength

According to Thomas-Reiche-Kuhn (TRK) sum rule[171], the integrated oscillator strength of an absorber equals the total number of electrons in the structure. The increased number of photo-induced electrons in lower-dimensional electronic states manifest in proportional increase in probability of optical transition. The optical matrix element for the electron-to-heavy hole transition induced

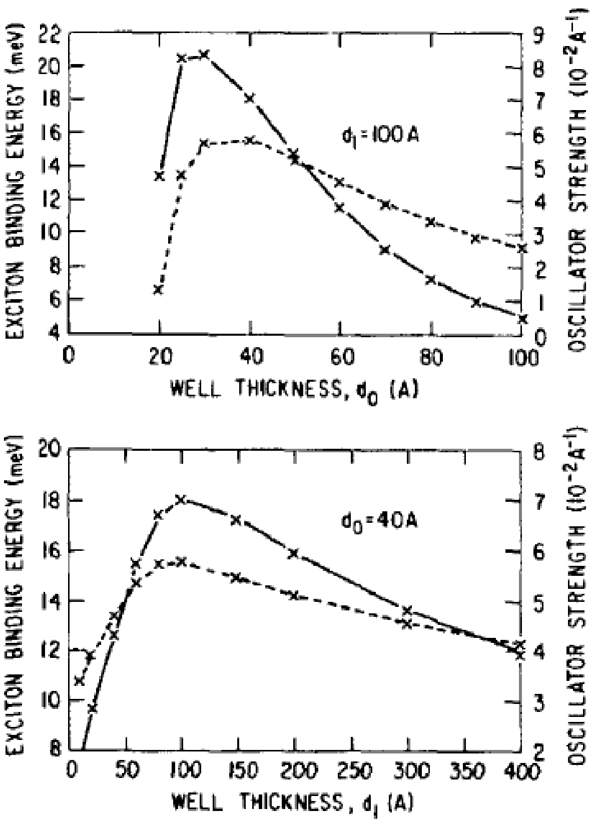

Figure 5.5 Exciton binding energy (solid) and oscillator strength per unit length (dashed) vs well thicknesses d_0 and d_1. Figure adapted from reference[172].

oscillator strength per unit length can be expressed as:

$$\frac{f_0}{L} = \frac{2p_{cv}^2}{E_g m_0} \left| \int \Psi_0^{(e)}(x,z)\Psi_0^{(h)}(x,z)\, \mathrm{d}x\, \mathrm{d}z\, F_{ex}(r) \right|^2 , \tag{5.102}$$

where the squared part is the exciton wave function with $F_{ex}(r)$ being the envelope part; $\Psi_0^{(e)}(x,z)$ and $\Psi_0^{(h)}(x,z)$ are the ground state wave functions for electrons and heavy holes, respectively, in the absence of their interaction. Esaki et al.[172] have demonstrated that the oscillator strength per unit volume of a GaAs/AlGaAs quantum wire is $3 \times 10^{-5}\text{Å}^{-3}$, nearly an order of magnitude larger than for bulk GaAs value of $3.5 \times 10^{-6}\text{Å}^{-3}$ as shown in Fig. 5.5.

5.5.3 Joint Optical Density of States

Thirdly, the joint optical density of states (JDOS) function is strongly dependent on dimensionality which comes from the summation over wave numbers k, from continuous JDOS for 3D to step-like JDOS for 2D, and discrete form for 1D, as explicitly shown in Eqs. (5.103, 5.104 and 5.105). As this function connects electron hole pairs involved in a transition, it has a reduced effective mass $\frac{1}{m_r^*} = \frac{1}{m_e^*} + \frac{1}{m_h^*}$ which for 3D is equivalent to that of electrons, but in 2D and 1D changes substantially due to separation of heavy, light, and split-off bands in valence band. In fact, the hole effective mass is reduced to $0.027m_0$ for 1D quantum wire structure, and to $0.118m_0$ for 2D quantum well, compared with $0.51m_0$ for bulk GaAs[173] as shown in Fig. 5.6.

$$\rho_r^{3D} = \frac{1}{2\pi^2}(\frac{2m_r^*}{\hbar^2})^{3/2}(\hbar\omega - E_g)^{1/2} \tag{5.103}$$

$$\rho_r^{2D} = \frac{m_r^*}{\pi\hbar^2 L_z} \tag{5.104}$$

$$\rho_r^{1D} = \frac{(m_r^*)^{3/2}}{\pi\hbar m_e^* L_x L_y}\frac{1}{\sqrt{(\hbar\omega - E_g)}} \tag{5.105}$$

5.6 Spacial Overlapping of confined light and electronic wavefunctions

The electronic band structure of hexagonal core-shells is calculated self-consistently by solving Poisson and Schródinger equations showing that, as expected, at high doping concentrations of the shell two-dimensional electron gasses (2DEG) form at the six (6) core-shell heterointerface facets, with six (6) pillars of one-dimensional electron gas (1DEG) forming at the six vortices; this is schematically shown in Fig. 5.7(a). The electronic wave function is calculated and shown in Fig. 5.7(b) for core of GaAs and shell of AlGaAs, with high doping assumed for the shell, in two cuts: one along two opposing vortices and one along two opposing facets. Clearly, 2DEG and 1DEG exist, respectively, at facets and vortices. Calculation of transition rates with incorporation of dimensionality shows

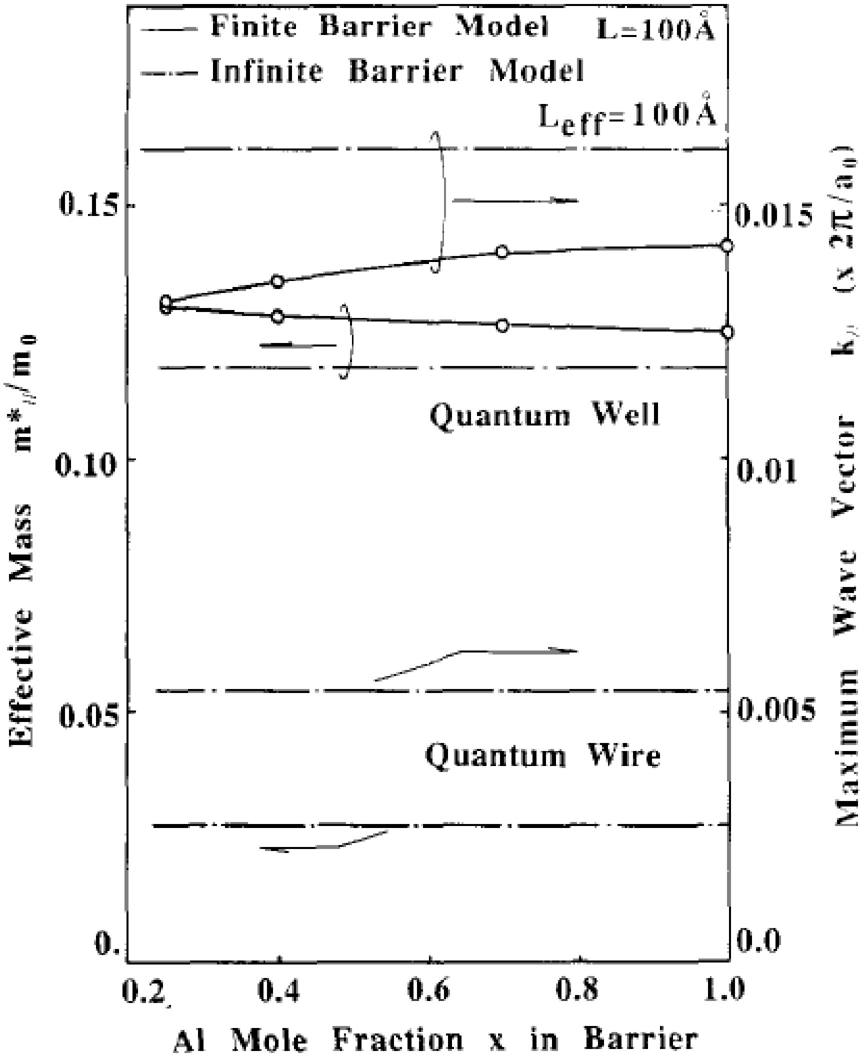

Figure 5.6 Effective mass value estimated in the wire direction in the lowest valence subband of $GaAs/Al_xGa_{1-x}As$ quantum wire. The solid line is the finite barrier model. The dashed line is the infinite barrier model, where the effective mass value is independent of the well width. The maximum wave vector where the parabolic approximation holds within the accuracy of 1 meV is also shown. Figure adapted from reference[173].

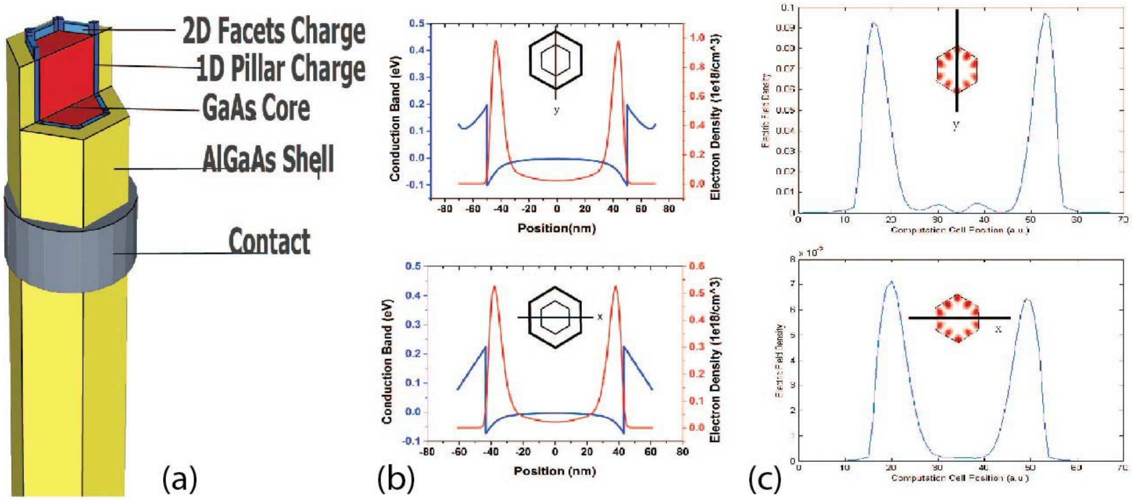

Figure 5.7 (a) The schematic plot of GaAs/AlGaAs core-shell nanowire with electron charge positions. (b) The calculated conduction band energy diagram and the electron density at y cross section (top) and x cross section (bottom) with high doping density. (c) FDTD-simulated (optcial) electric field intensity of a hexagonal nanowire at y cross section (top) and x cross section (bottom). The insets are mode patterns (TM_{5n}) in the transverse plane. The black boundaries represent the interface between semiconductor and air.

over one order of magnitude increase for the 2D and over two orders of magnitude for 1D compared to the same material in 3D. Furthermore, for the stimulated emission rate calculation, the mode occupancy number u_ε in Eq. 5.33 plays an important role, as expected.

Figure 5.7(C) shows the FDTD-simulated electric field density of a hexagonal nanowire at y cross section (top) and x cross section (bottom). The photon energy of this mode shown as the insets of Fig. 5.7 (C) is concentrated primarily along the 6 corners and secondarily along the facets with little light in the 3D core of GaAs. Hence, we suggest that the fortuitous spatial overlap of the resonant optical modes on reduced dimensional electronic wavefunctions plays a significant role in the remarkable optoelectronic properties of core-shell nanowires. Restated, the superposition of the photon modes on reduced electronic states that form on the facets and vortices of the hexagonal CSNWs strongly enhances both upward and downward transition rates. Thus, the reduced dimensionality transition rate distinguishes the core-shell nanostructure from the optically equivalent core-only structure due to its significantly modified rate management. These nanostructures are not only excellent optical cavities, but despite their large size also provide the right reduced dimensional electronic structures which enhance optoelectronic interactions. It should be noted the present analysis is for direct optical transitions; although it can be extended to incorporate k-vector changes as in phonon scattering, other important factors such as many-body interactions need to be included in a more detailed analysis.

5.7 Many body effects

The preceding discussion of dimensional dependent optical transition rates involving time-dependent perturbation theory and Fermi's Golden Rule considers each electron in isolation as it interacts with the electromagnetic field. In this derivation, a single-particle theory has been used to obtain the optical transition rates and the optical gain spectrum, which will be presented in Chapter 6. In reality, there is a large density of both electrons and holes present in the system. The mutual interactions between these particles are generally referred to as many-body effects[174]. These effects included lineshape broadening, which is related to collisions between particles and/or phonons in the crystal and will also be discussed in Chapter 6. In addition to this important effect, there are two other significant consequences of many-body effects: exciton states[173] and bandgap shrinkage[175]. Exciton states exist primarily at low carrier densities and low temperatures, where bandgap shrinkage becomes noticeable at high carrier densities.

Exciton pair can be formed under conditions of low carrier density and low temperature, as there is possibility that an electron and hole to orbit each other for an extended period of time. Such exciton pairs have a binding energy associated with them that is equal to the energy required to separate the electron and hole. As a result, electrons that are elevated from the valence band to one of these exciton states will absorb radiation at energies equal to the bandgap substracting the binding energy (the bandgap will appear to be red-shifted). In addition, the overlap integral (and hence the matrix element) of these two-particle states can be quite large. As a result, band-to-exciton transitions tend to dominate the absorption spectrum. However, exciton states are limited to states near $k = 0$, and hence band-to-exciton transitions are clustered at the band edge (or subband edge). The overall effect is the appearance of very strong absorption peaks near the subband edges in two-dimensions or one-dimension electronic states, and near the band edge in bulk case[174].

Exciton absorption peaks are clearly visible in quantum wells at room temperature for a typical GaAs QW. The first two steps in the ”staircase” absorption spectrum predicted from the density of states. However, the exciton peaks riding on top of the steps, particularly the $n = 1$ peaks, dominate the absorption spectrum. Each observed exciton peak corresponds to one of the subband transitions. This phenomenon will become more prominent in one-dimensional case with discrete joint optical density of states.

The second many-body effect occurs at high carrier densities, where the charges actually screen out the atomic attractive forces. With a weaker effective atomic potential, the single-atom electron wavefunctions of interest become less localized and the nearest-neighbor electron overlap becomes higher. The large overlap increases the width of the energy bands (δE is larger), reducing the gap between bands. Although this description is only qualitative, it does reveal that the bandgap should shrink with increasing carrier density[174]. And this bandgap shrinkage is inversely related to the average spacing between carriers, which means the closer the carriers are, the more their own Coulomb potentials screen out the atomic potential. The net effect of bandgap shrinkage is that as carrier density increases, the entire gain spectrum red-shifts by a noticeable amount. In principle, the shift is accompanied by a slight distortion (i.e, reshaping and enhancement) of the spectrum.

CHAPTER 6

STIMULATED EMISSION, OPTICAL GAIN AND LASING IN CORE-SHELL NANOWIRES

In this chapter, we review the history and operation principle of semiconductor lasers, then through the derivation of the gain spectrum for different dimensionality, the threshold carrier density and the quantum efficiency are calculated, showing that lower dimensional structures are capable to generate more output power due to the extremely enhanced optical transition rates. In addition, a nanowire transient response model under ultrafast pulse excitation is discussed, revealed the large carriers and optical power generated when the excitation power above the threshold condition.

6.1 Background of Semiconductor Lasers

Semiconductor laser is an essential component for building optical communication systems, while intensive research results and achievements are published in this field. In 1917, Einstein predicted the existence of spontaneous and stimulated emission as depicted in Fog. 6.2 by which an atom can emit radiation[176]. After the proposal of p-n junction semiconductor lasers in 1961[177], the first semiconductor lasers were fabricated in 1962 using homojunctions[178]. These lasers have high threshold current density ($19000/A/cm^2$) and operated at very low temperature, thus, not efficient enough due to high optical and electrical losses. The concept of heterojuntion or double heterojunction semiconductor lasers were realized in the late 1960s by Alferov and others with a lower threshold current density ($1600A/cm^2$) operating at room temperature[179]. These double-heterostructure diode lasers provide both carrier and optical confinements, which improve the efficiency for stimulated emission. The concept of quantum well structures for semiconductor lasers was proposed and realized experi-

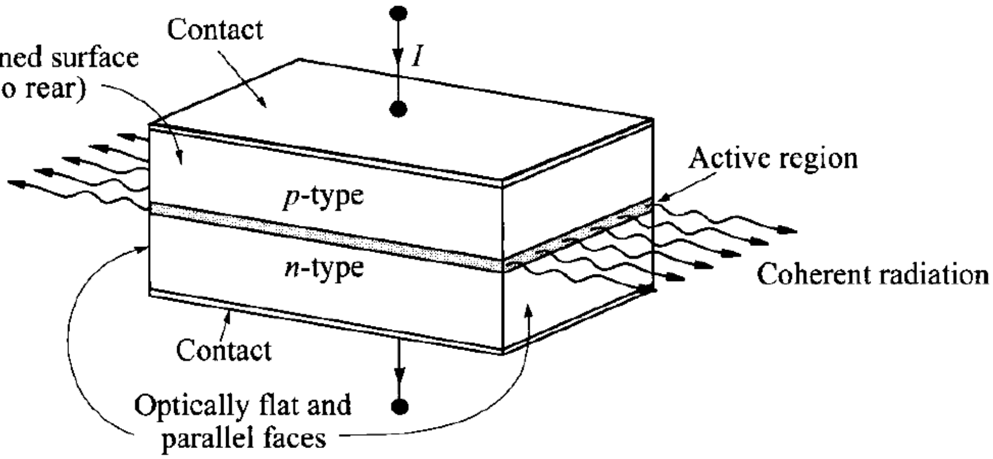

Figure 6.1 Basic structure of a junction laser in the form of a Fabry-Perot cavity, showing the active region and the coherent radiation output. Figure adapted from the reference[166].

mentally in the late 1970s. In these lasers the active region, in which electrons and holes recombine to give off light, is less than 100Å wide. Such small transverse dimensions are obtained using molecular beam epitaxy and employ most often a GaAs active region sandwiched between higher energy band gap materials layers, such as AlGaAs. The threshold current density was reduced to less than 500 A/cm^2, which improved the laser performance significantly.

6.2 Operation Principle of Semiconductor Lasers

The semiconductor laser (or laser diode) in its simplest form is a p-n junction of semiconductor material arranged in a cavity, as shown in 6.1. Two metal contacts connected to the p-type or n-type semiconductor materials separately with a junction active region in between. On the optically flat and parallel side faces, there are two mirror like reflectors to confine and forming the feedback of light, in order to produce coherent radiation at one side of the device. The type and configuration of the material used determine the optical characteristics of the laser diode emission. Like others in various oscillators or wave sources, the fundamental elements in the semiconductor lasers are the following three elements:

- **Population Inversion** In order to provide net optical gain and achieve non-equilibrium con-

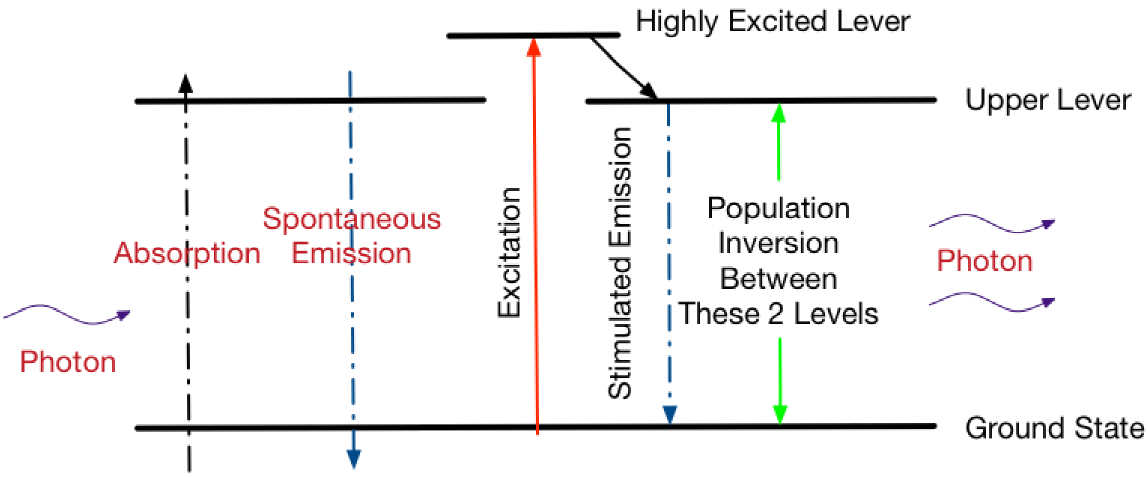
Highly Excited Lever
Upper Lever
Absorption
Spontaneous Emission
Photon
Excitation
Stimulated Emission
Population Inversion Between These 2 Levels
Photon
Ground State

Figure 6.2 (left) Optical Process (absorption and emission) in a two level system. (right) Lasing mechanism with stimulated emission and population inversion in a three-levels system.

dition, electrons must be excited to a highly excited level as depicted in a three level laser in Fig. 6.2. The excited electrons will recombine radiationless with holes and release their energy to the upper level, where the population of electrons will be greater than the population in ground state, and achieving population inversion with optical amplification.

- **External Pumping and p-n Junction** Either electrical injection or optical pumping can provide the source of input energy and optical radiation obtained by injecting minority carriers into the vicinity of a semiconductor p-n junction where radiative transitions take place.
- **Reflectors of Cavity** The structural requirement for a laser is an optical resonator in the direction of the light output. The optical resonator mainly serves to trap the light and build up the intensity inside. Based on the types of reflector, the most common semiconductor lasers are including Fabry-Perot(FP) lasers[46] or distributed feedback (DFB)[180]/distributed Bragg reflector (DBR)[181] lasers.

6.3 Lasing Characteristics

6.3.1 Absorption of Light

The light and matter interaction includes absorption, spontaneous emission and stimulated emission. We first quantify the enhancement of absorption of light caused by reduced dimensionality by introducing the absorption coefficient. This is the absorption rate without considering the occupation factors. As derived in Chapter 5, the absorption coefficient for 3D can be expressed as:

$$\begin{aligned} \alpha_{3D}(\hbar\omega) = \quad & C_0|\hat{e}\cdot\mathbf{p_{cv}}|^{\mathbf{2}}(f_v - f_c)\tfrac{1}{2\pi^2}(\tfrac{2m_r^*}{\hbar^2})^{3/2}(\hbar\omega - E_g)^{1/2}, \\ & C_0 = \tfrac{\pi e^2}{n_r\epsilon_0 c m_0^2\omega}, \end{aligned} \tag{6.1}$$

and for 2D and 1D case, we have:

$$\begin{aligned} \alpha_{2D}(\hbar\omega) &= C_0|\hat{e}\cdot\mathbf{p_{cv}}|^{\mathbf{2}}\frac{m_r^*}{\pi\hbar^2 L_z}, \\ \alpha_{1D}(\hbar\omega) &= C_0|\hat{e}\cdot\mathbf{p_{cv}}|^{\mathbf{2}}\frac{(m_r^*)^{3/2}}{\pi\hbar m_e^* L_x L_y}\frac{1}{\sqrt{(\hbar\omega - E_g)}}, \end{aligned} \tag{6.2}$$

The split plots of absorption coefficient for 3D, 2D and 1D are shown in Fig. 6.3. Note the unique shapes of joint optical density of states (JODS), i.e., from continuous JODS for 3D to step-like JODS for 2D, and discrete form for 1D, as explicitly shown in the last terms of Eqs. (6.1 and 6.2). The parameters used for rate equations calculation are presented in table 6.1.

Then the overlay plot with multiple y axis as in Fig. 6.4 with the different scales indicating the integrated absorption rates for 1D is 35 times larger than 3D. The maximum absorption coefficient is $1.0 \times 10^6 (cm^{-1})$ for 3D, $6.1 \times 10^6 (cm^{-1})$ for 2D and $1.4 \times 10^8 (cm^{-1})$ for 1D.

Table 6.1. Parameters and constants used for rate equation calculations.

Parameters	Symbol	Values and Units
Reduced Planck's constant	$\hbar$	$1.05 \times 10^{-34}\ J \cdot s$
Speed of light	c	$3 \times 10^{1}0\ m/s$
Elementary charge	e	$1.6 \times 10^{-19}\ C$
Energy Bandgap for GaAs at 300k	E_g	$1.424\ eV$
Permeability of vacuum	μ_0	$4\pi \times 10^{-7}\ H/m$
Permittivity of vacuum	ε_0	$8.854 \times 10^{-12}\ F/m$
Electron rest mass	m_0	$9.109 \times 10^{-31}\ kg$
Electron effective mass	m_e	$0.067 m_0$
Hole effective mass for GaAs 3D	m_{h3D}	$0.47 m_0$
Hole effective mass for GaAs 2D	m_{h2D}	$0.118 m_0$
Hole effective mass for GaAs 1D	m_{h1D}	$0.027 m_0$
Thermal voltage at 300k	V_t	$0.02585\ eV$
Energy Parameter for GaAs	E_p	$25.7\ eV$

Note. — The rest of the parameters that are not listed here have its conventional meaning and values.

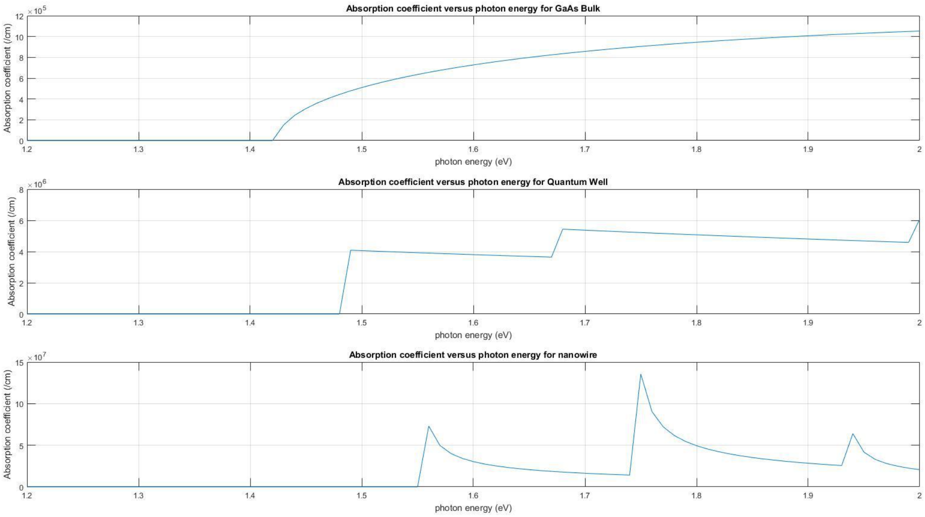

Figure 6.3 Absorption Coefficient versus Photon Energy for 1D 2D and 3D with split plot.

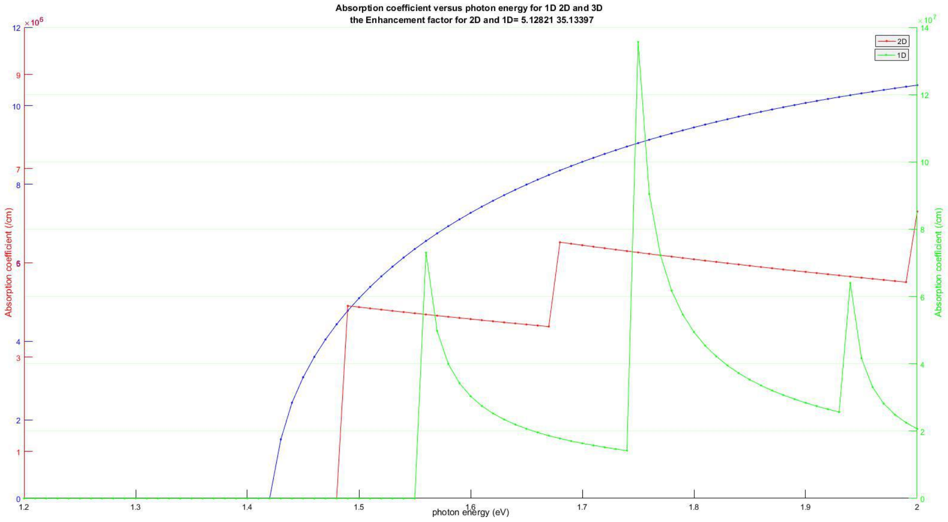

Figure 6.4 Absorption Coefficient versus Photon Energy for 1D, 2D and 3D with multiple y axis.

6.3.2 Optical Gain

The net stimulated emission rate is given by $r_{\mathrm{sti}}^{\mathrm{net}}(\hbar\omega) = r_{\mathrm{sti}}(\hbar\omega) - \alpha_{\mathrm{abs}}(\hbar\omega)$, and the optical gain is equal to the net stimulated emission rate divided by the photon flux as $g(\hbar\omega) = r_{\mathrm{sti}}^{\mathrm{net}}(\hbar\omega)/(cn_{\varepsilon}u_{\varepsilon}/n_r)$, where n_{ε} is the photon mode density. Thus, an expression for the gain spectra $g(\hbar\omega)$ can be derived for 3D, 2D and 1D[174] with consideration also of occupation factor by calculating the Fermi levels:

$$\begin{aligned} g_{3D}(\hbar\omega) &= \frac{\sqrt{2}e^2 m_r^{*3/2} p_{cv}^2}{3\pi n_r \epsilon_0 {m_0}^2 c\hbar^3\omega}\sqrt{(\hbar\omega - E_g)}(f_c - f_v), \\ g_{2D}(\hbar\omega) &= \frac{e^2 m_r^* p_{cv}^2}{3n_r\epsilon_0 {m_0}^2 c\hbar^2 L_z\omega}(f_c - f_v), \\ g_{1D}(\hbar\omega) &= \frac{e^2 m_r^{*3/2} p_{cv}^2}{3n_r\epsilon_0 {m_0}^2 c\hbar\omega L_x L_y}\frac{1}{\sqrt{(\hbar\omega - E_g)}}(f_c - f_v). \end{aligned} \tag{6.3}$$

With decreasing dimensionality of the active region of an injection laser, the joint optical density of states and gain spectra become narrower, which leads to a decrease in the number of states to be filled to make the active region transparent (zero population inversion and zero gain) and to achieve lasing (round trip gain equal to loss). Consequently, the transparency current (or inversion current, i.e., the injection current at which the population inversion is zero) and the threshold current (injection current at which the gain is equal to the loss and lasing begins) decrease and their temperature dependence becomes weaker[182]. The decrease in the threshold current and increase in its temperature stability reflect one of the main areas of development and improvement of injection lasers. Owing to the continuous nature of the carrier spectrum within the allowed subbands, the use of quantum wells (QWs) or quantum well wires (QWRs) as active medium for optical transitions can quantitatively improve the parameters of devices based on them compared with devices with a bulk active region.

Among the advantages of QWR lasers over the presently used QW lasers are their narrower gain spectra, much lower threshold currents, and ultrahigh temperature stability, as well as the wider possibilities for controlling their lasing wavelength.

Now the gain spectrum respect to photon energy for (a) 3D, (b) 2D and (c) 1D can be calculated in Figure 6.5. As expected, the gain spectrum also follows the unique shapes of density of states. The inset of Fig. 6.5(a) is the maximum gain versus electron carrier concentration varing from $3 \times 10^{18} (cm^{-3})$ to $3 \times 10^{19} (cm^{-3})$. Using parameters $N_{tr} = 2 \times 10^{18} cm^{-3}$, $N_s = 4 \times 10^{18} cm^{-3}$, and $g_0 = 6.11 \times 10^5 cm^{-1}$, we fit the curve in inset of Fig. 6.5(a) to build a logarithmic gain model of the form for 3D case:

$$g(N) = g_0 \ln \left(\frac{N + N_s}{N_{tr} + N_s} \right) \tag{6.4}$$

where N_s is a shift to force the natural logarithm to be finite at $N = 0$ such that the gain equals the unpumped absorption due to the band-to-band transitions, N_{tr} is the transparency carrier density, and g_0 is the empirical gain coefficient. N_{tr} and g_0 will be different for different dimensionality.

After fitting the curve in Fig. 6.6, we can estimate the threshold carrier density is $N_{th} = 4.533 \times 10^{18} cm^{-3}$. Then plotting the spontaneous emission rate with respect to the threshold carrier density N_{th} for 3D, 2D and 1D as following:

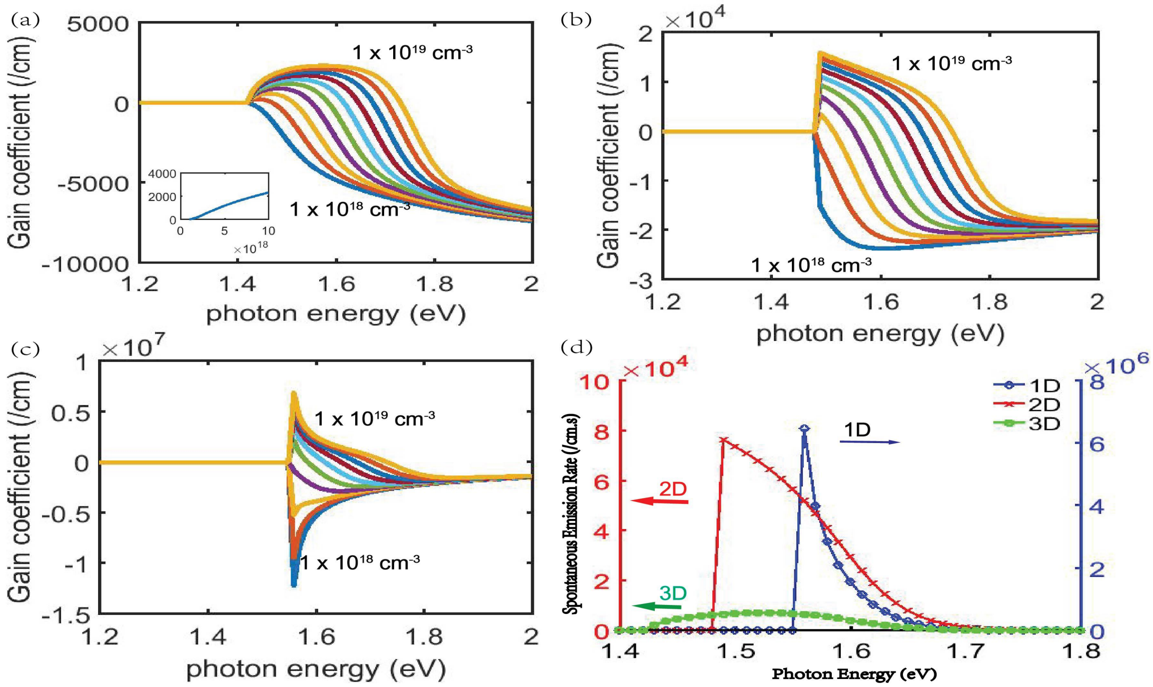

Figure 6.5 Gain Coefficient versus Photon Energy for (a) 3D (b) 2D and (c) 1D as a function of carrier concentration. The inset of (a) is the maximum gain versus injected/pumped electron carrier concentration varing from $3 \times 10^{18} (cm^{-3})$ to $3 \times 10^{19} (cm^{-3})$. (d) Spontaneous Emission Rate versus Photon Energy with respect to threshold carrier concentration for 3D(green), 2D(red) and 1D(blue). Note the scales difference for different dimensionality cases.

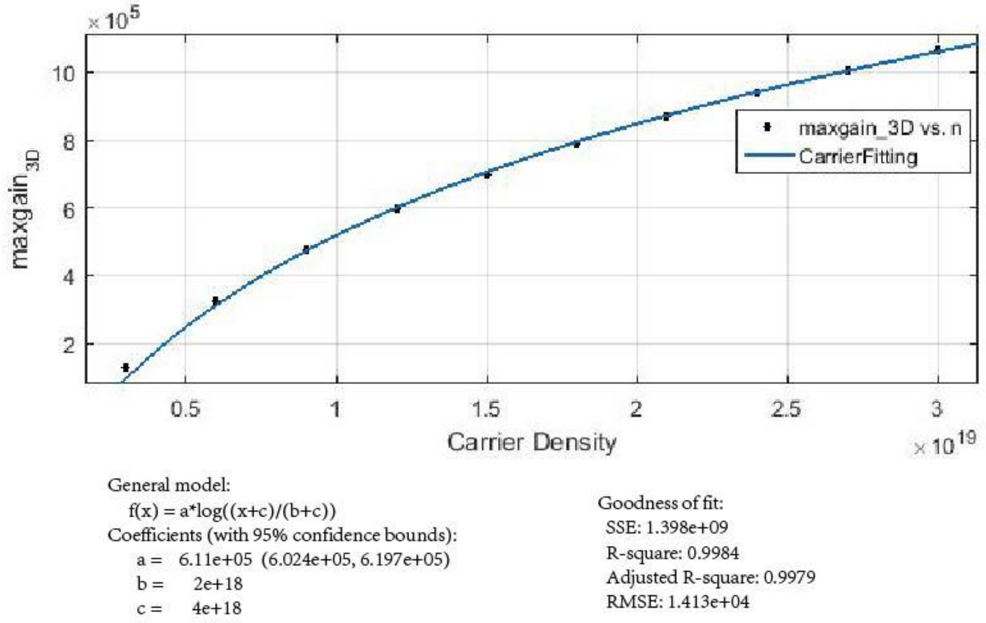

General model:
f(x) = a*log((x+c)/(b+c))
Coefficients (with 95% confidence bounds):
a = 6.11e+05 (6.024e+05, 6.197e+05)
b = 2e+18
c = 4e+18

Goodness of fit:
SSE: 1.398e+09
R-square: 0.9984
Adjusted R-square: 0.9979
RMSE: 1.413e+04

Figure 6.6 Gain Model Fitting

$$
\begin{aligned}
r_{3D}^{\mathrm{spon}}(\hbar\omega) &= \frac{n_r e^2 \omega p_{cv}^2}{\pi\epsilon_0 {m_0}^2 C^3 \hbar} \frac{m_r^{*3/2}}{2\pi^2\hbar^3} \sqrt{(\hbar\omega - E_g)} f_n(\xi_2)(1 - f_p(\xi_1)), \\
r_{2D}^{\mathrm{spon}}(\hbar\omega) &= \frac{n_r e^2 \omega p_{cv}^2}{\pi\epsilon_0 {m_0}^2 C^3 \hbar} \frac{m_r^{*}}{\pi\hbar^2 L_z} f_n(\xi_2)(1 - f_p(\xi_1)), \\
r_{1D}^{\mathrm{spon}}(\hbar\omega) &= \frac{n_r e^2 \omega p_{cv}^2}{\pi\epsilon_0 {m_0}^2 C^3 \hbar} \frac{m_r^{*3/2}}{\pi\hbar m_e^* L_x L_y} \frac{1}{\sqrt{(\hbar\omega - E_g)}} f_n(\xi_2)(1 - f_p(\xi_1)),
\end{aligned}
\tag{6.5}
$$

Figure 6.5(d) shows the spontaneous emission rate spectrum with the estimated threshold carrier density for 3D(green), 2D(red) and 1D(blue) based on Eqs. 6.5 with $(1 + u_\varepsilon) \cong 1$. Besides the expected narrower linewidth, the peak rate for 1D is $6.4\times10^6(cm^{-1})$, compared with $7.6\times10^4(cm^{-1})$ for 2D and $7.1 \times 10^3(cm^{-1})$ for 3D.

The total spontaneous emission rate per unit volume per second is $R_{sp} = \int_\xi r_{sp} d\xi$, and can be calculated for different dimensionalities by integrating over entire photon energy spectrum, where $\xi = \hbar\omega$. The optical output power created at threshold is $P_{out} = h\nu R_{sp}|_{N_{th}}$. The total generated optical output power at the same injected carrier N_{th} is seen to be 6.5 times and 175.3 times more for 2D and 1D, respectively, compared to the 3D case. In other words, with the same amount of carriers injected either by optical pumping or electrical injection, highly confined electronic structure can produce more than two orders of magnitude more light compared to bulk.

6.4 Modeling of Nanowire Lasers

In this section, we model an idealized semiconductor nanowire laser from the general formulations through the rate equations and wave equations based on the generalized Fabry-Perot (FP) lasers.

Considering different aspects of the energy conservation rule, there are two basic classical methods to model the operation of semiconductor lasers. The first method applies the concept of photon/electron particles exchange with the abstract optical parameters and is suitable for the FP lasers as depicted in Fig. 6.7. The FP laser is conceptually a cavity with a pair of end mirrors or facets. The mirrors are needed to create the feedback mechanism of light inside an amplifying medium for lasing to occur. The lasing medium can only amplify (undergo stimulated emission) over a fairly narrow

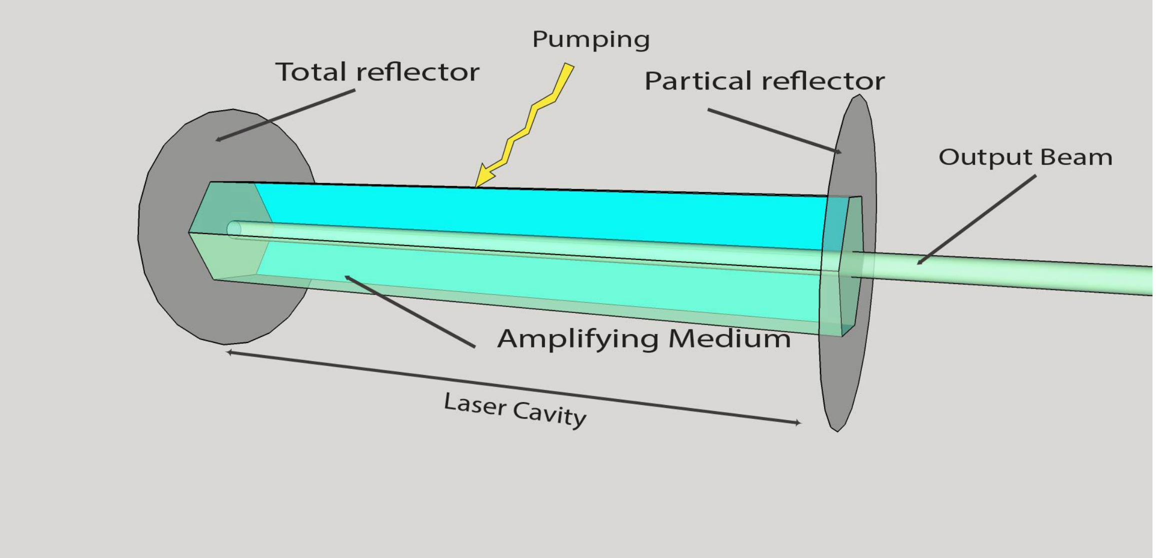

Figure 6.7 Schematic diagram of a semiconductor Fabry-Perot laser

range because of the characteristics of the material. On the other hand, strong non-uniformities of index distribution of the DBR/DFB lasers alters the interaction between electromagnetic fields and the electronic particles. These two methods are compatible with each another. Here, because the nanowire based lasers have net propagating resonant mode in the axial direction and the resonant modes are very similar to the FP modes, we employ the first method, which is the standard rate equation approach.

As discussed previously, there are three fundamental elements in the semiconductor lasers: semiconductor band structure, current injection/optical pumping, and cavity. The former two are related to the material and junction structure, and the later is related to the laser structure. The key part of modeling semiconductor laser is to deal with the interaction between electromagnetic fields and gain medium. Figure 6.8 illustrated the basic procedure of modeling semiconductor nanowire lasers. Starting from the optical pumping power, the carrier density, N, can be calculated by solving Poisson and carrier continuity equations. Then some optical parameters, such as effective refractive index and confinement factor related to the optical modes, can be extrapolated from the FDTD simulation results. Simultaneously, the optical gain of the gain medium is given by the optical transition rate

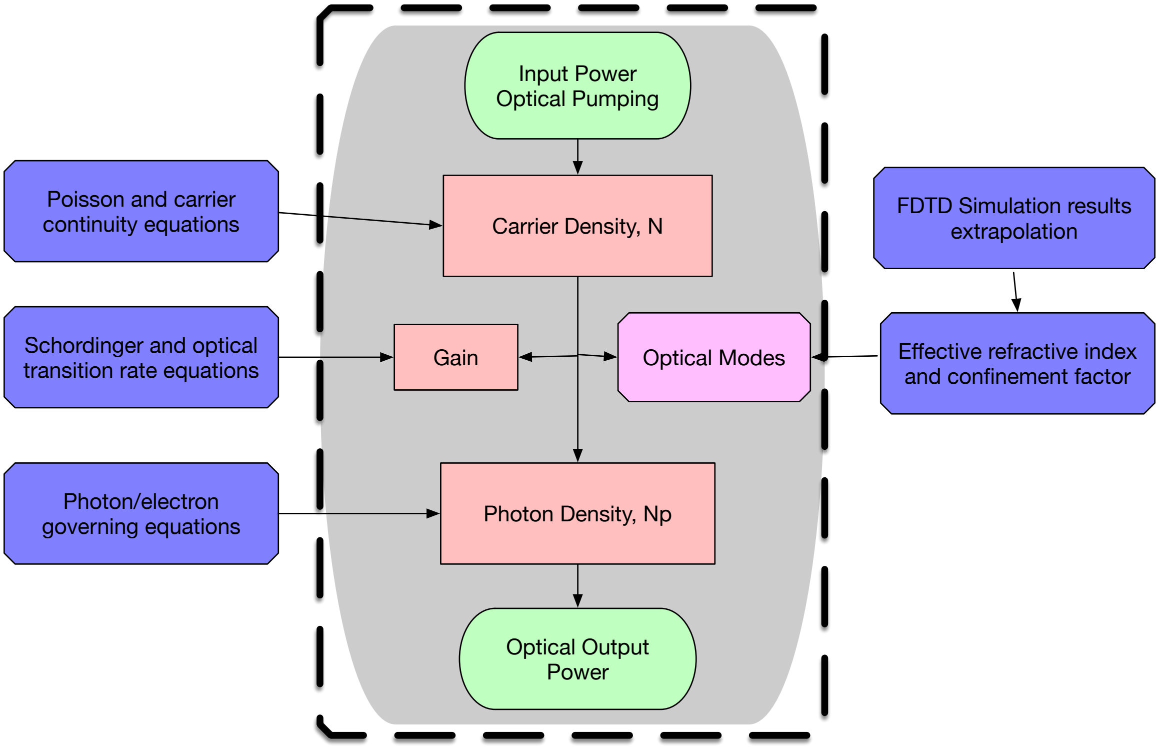
Input Power
Optical Pumping
Poisson and carrier continuity equations
Carrier Density, N
FDTD Simulation results extrapolation
Schordinger and optical transition rate equations
Gain
Optical Modes
Effective refractive index and confinement factor
Photon/electron governing equations
Photon Density, Np
Optical Output Power

Figure 6.8 Flow chart diagram of modeling a semiconductor nanowire laser.

equations. Finally, the optical output power is proportional to the photon density N_p, which is numerically solved by the rate equations and coupling between carrier and photon density using the traveling-wave approach (in time domain). It solves the time-dependent coupled-wave equations for the forward and the backward traveling waves directly and therefore is valid even the laser cavity has relatively small Q-factor and/or the characteristic time of the laser dynamics is very short. Of importance, the traveling-wave model can be applied to lasers operated with multiple cavity modes which is the case for the as-grown core-shell nanowires.

6.5 Laser Rate Equations

We start with the governing equations of carrier density N and photon density N_p in the active region of a semiconductor laser which is governed by a dynamic process[174]:

$$\begin{aligned} \frac{dN}{dt} &= \frac{\eta_i I}{qV} - \frac{N}{\tau} - R_{st}, \\ \frac{dN_p}{dt} &= \Gamma v_g g N_p + \Gamma \beta_{sp} R_{sp} - \frac{N_p}{\tau_p}, \end{aligned} \tag{6.6}$$

where β_{sp} is the spontaneous emission factor, defined as the percentage of the total spontaneous emission coupled into the lasing mode. And it is just the reciprocal of the number of available optical modes in the bandwidth of the spontaneous emission for uniform coupling to all modes. The g is the incremental gain per unit length. η_i is the injection efficiency, which defined as the fraction of terminal current that generates carriers in the active region. τ and τ_p is the carrier lifetime and photon lifetime, respectively.

The first term on the right hand side of equation 6.6(top) is the generation rate of injected electrons $G_{gen} = \Gamma_i I/qV$, where $\Gamma_i I/q$ is the number of electrons per second being injected into the active region, where V is the volume of the active region. The rest terms are the rate of recombining of electrons per unit volume in the active region. There are several mechanisms should be considered, including a spontaneous recombination rate, R_{sp}, a nonradiative recombination rate, R_{nr}, a carrier leakage rate, R_l and a net stimulated recombination, R_{st}, including both stimulated absorption and emission. Thus, the total recombination rate is the sum of all rates:

$$R_{rec} = R_{sp} + R_{nr} + R_l + R_{st} \tag{6.7}$$

The first three terms on the right refer to the natural or unstimulated carrier decay processes. The fourth one, R_{st}, require the presence of photon.

Equation 6.6 uses input current intensity, I, for electrically injected lasing situation, however, if optical pump, P, used as the lasing source, then we need to rewrite the governing equations as:

$$\begin{aligned}\frac{dN}{dt} &= \frac{\eta_i P}{h\nu V} - \frac{N}{\tau} - R_{st},\\ \frac{dN_p}{dt} &= \Gamma v_g g N_p + \Gamma \beta_{sp} R_{sp} - \frac{N_p}{\tau_p},\end{aligned} \tag{6.8}$$

P is the optical pump used for exciting nano-cavity laser emission and is time-dependent of the form $P_p sech^2(\frac{1.76t}{\delta t})$, where P_p is the peak power amplitude, and δt is the time pulse width.

The cavity loss can be characterized by a photon decay constant or lifetime, τ_p, and the threshold can be reached when the round trip gain overcomes losses. By assuming steady-state conditions (i.e. $dN_p/dt = 0$), and solving for this steady-state or threshold gain, g_{th}, where the generation term equals the recombination term for photons. We assume only a small fraction of the spontaneous emission is coupled into the mode (i.e. β_{sp} is quite small), and only consider light emission into a single mode of the resonant cavity, then the second term can be neglected, and we have the solution:

$$\Gamma g_{th} = \frac{1}{v_g \tau_p} = < \alpha_i > + \alpha_m \tag{6.9}$$

The product, Γg_{th}, is referred to as the threshold modal gain because it represents the net gain required for the mode as a whole that experiences the cavity loss. $< \alpha_i >$ is the average internal loss, and α_m is the mirror loss if we considered an in-plane wave laser. However, since the refractive index difference between CSNW and the Si or GaAs substrate is very small, we may change the mirror loss into leaky loss due to the confined volumetric resonant mode α_l.

At threshold, the steady-state carrier rate equation can be expressed as:

$$\frac{\eta_i P_{th}}{h\nu V} = (R_{sp} + R_{nr} + R_l)_{th} = \frac{N_{th}}{\tau} \tag{6.10}$$

where $(R_{sp} + R_{nr} + R_l) = AN + BN^2 + CN^3$ depends monotonically on N, and this recombination rate will saturate at its threshold value. Thus, we can substitute Eq 6.10 into the carrier rate equation Eq 6.8 to obtain an above threshold carrier rate equations:

$$\frac{dN}{dt} = \eta_i \frac{(P - P_{th})}{h\nu V} - v_g g N_p, \quad (P > P_{th}) \tag{6.11}$$

The steady-state photon density can be also calculated when pumping power above threshold where $g = g_{th}$,

$$N_p = \frac{\eta_i (P - P_{th})}{h\nu v_g g_{th} V} \quad (steady\ state) \tag{6.12}$$

Then the optical output power intensity is obtained by multiplying the photon density, N_p, by the energy per photon, hv, and the group velocity, g_v.

$$P_{op} = \frac{\eta_i (P - P_{th})}{g_{th} V} \tag{6.13}$$

Therefore, the optical output power is simply calculated as:

$$P_0 = P_{op} wd = \eta_i \frac{(P - P_{th}) wd}{g_{th} V} = \eta_i \frac{(P - P_{th})}{g_{th} L} \quad (P > P_{th}) \tag{6.14}$$

where w, d and L are the width, thickness and length of the active region, respectively. All input parameters for the modeling of semiconductor nanowire laser are listed in Table 6.2.

It is desirable to reduce the cavity loss ($< \alpha_i > + \alpha_m$) and volume, V, in order to retaining a reasonably large confinement factor, Γ. However, CSNWs based semiconductor laser as a good resonant cavity are able to confine light with a large quality factor. The extrapolated confinement factor based on the FDTD simulation results is 0.756, along with other calculated parameters listed in Table 6.3.

Now, we are able to generate the transient responses of carrier and photon densities with respect to the pumping power. Figure 6.9 shows the optical output power versus the input pumping power with

Table 6.2. Input parameters of the core-shell nanowire semiconductor laser.

Parameters	Symbol	Values and Units
Cavity length	L	3 μm
Active-region width	w	300 nm
Active-region thickness	d	300 nm
Carrier lifetime	τ_r	1 ns
Spontaneous emission lifetime	τ_{sp}	1 ns
Gain coefficient	g_0	3.0×10^{-16} cm^{-2}
Carrier density at threshold	n_{th}	4.5×10^{18} cm^{-3}
Cavity loss	α_c	20 cm^{-1}
Pumping power	p_0	200 μW
Reference wavelength	λ_0	800 nm
Planck's constant	h	6.625×10^{-34} Js
Electron charge	e	1.6×10^{-19} C
Nonradiative recombination coefficient	A	1.43×10^{8} s^{-1}
Auger recombination coefficient	C	3.5×10^{-30} $cm^6 \cdot s$

Note. — The rest of the parameters that are not listed here have its conventional meaning and values.

Table 6.3. Calculated parameters of core-shell nanowire semiconductor laser. Some of the parameters are calculated based on the FDTD simulation results.

Parameters	Symbol	Values and Units	Reference
Area of top section of active part	A_I	9.0×10^5 nm^2	$A_I = Lw$
Area of cross section of active part	A_p	9.0×10^4 nm^2	$A_p = wd$
Effective refractive index	n_r	2.728	
Group refractive index	n_g	3.5	
Group velocity of light	v_g	8.56×10^7 m/s $v_g = c/n_g$	
Confinement factor	Γ	0.756	
Photon lifetime	τ_{ph}	5.84 ps	$\tau_{ph} = I/v_g\alpha_c$
Gain coefficient for power	g_p	1.94×10^{-12} cm^3/s	$g_p = \Gamma v_g g_0$
Pumping power density	P_0	2.22×10^9 W/m^2	$P_0 = p_0/A_p$
Carrier density at transparency	n_0	4.41×10^{18} cm^{-3}	
Threshold pumping power density	P_{th}	3.35×10^8 W/m^2	
The operating frequency	f	3.75×10^{14} Hz	$f = c/\lambda_0$
Threshold pumping power	$Power_{th}$	3.0×10^{-5} W	$Power_{th} = P_{th}A_p$
Analytical power	P_{analyt}	0.439 W	

Note. — The rest of the parameters that are not listed here have its conventional meaning and values.

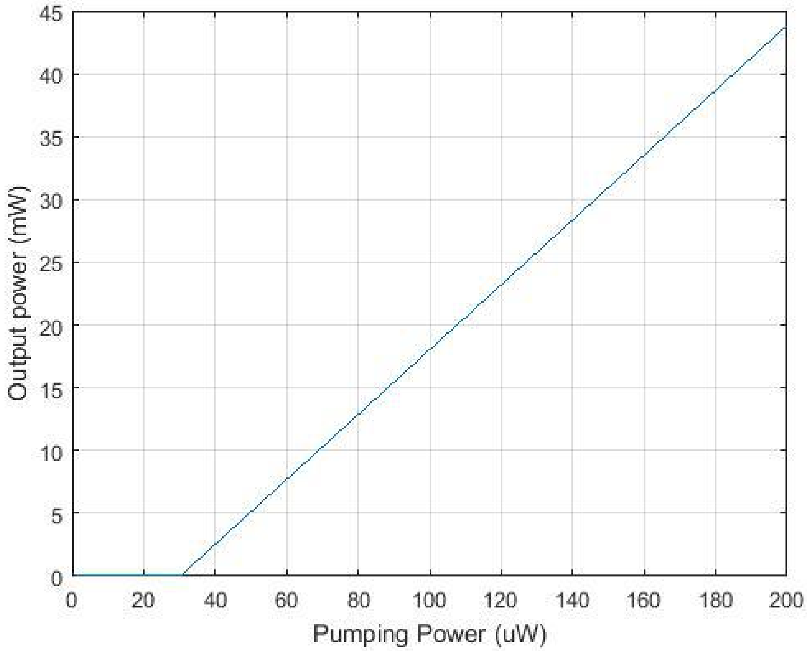

Figure 6.9 Calculated optical output power vs. pumping power, i.e., L-L curve.

a threshold pumping power at $30\mu W$. The gain switching occurs because of ultrafast excitation. By generating a large amount of carriers at a very short times cale, picosecond pump pulses excite carrier densities significantly above threshold, resulting in a strong peak of stimulated emission as shown in Fig. 6.10 and Fig. 6.11. Thus, the optical output power reaches maximum value when the gain at its maxim, and quickly drops below threshold after this initial spike.

6.6 Linewidth Enhancement Factor

Electrons and holes frequently interact with other carriers and with phonons, thereby changing their energy within the sub-band. Such intra-band scatter events happen about every 0.1 ps, much more often than band-to-band recombination events. Thus, scattering leads to an uncertainty of the electron energy, which can be accounted for by introducing a symmetrical linewidth broadening function L into the gain formula[183]. In fact, positive gain is now possible even for photon energies slightly below the bandgap. Cauchy himself exploited such a density function in 1827[184], with an infinitesimal scale parameter, in defining a Dirac delta function, while among physicists, it is known

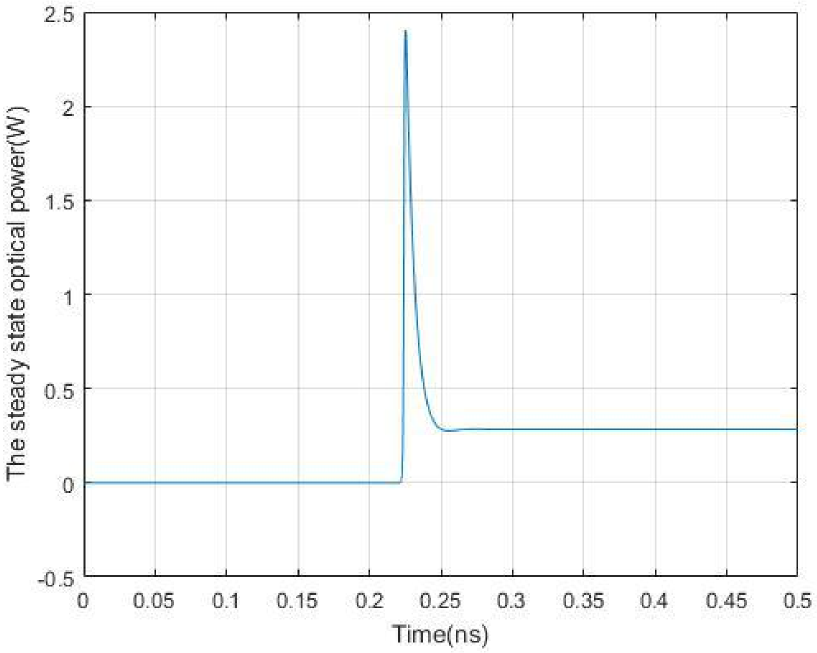

Figure 6.10 The calculated steady state optical output power.

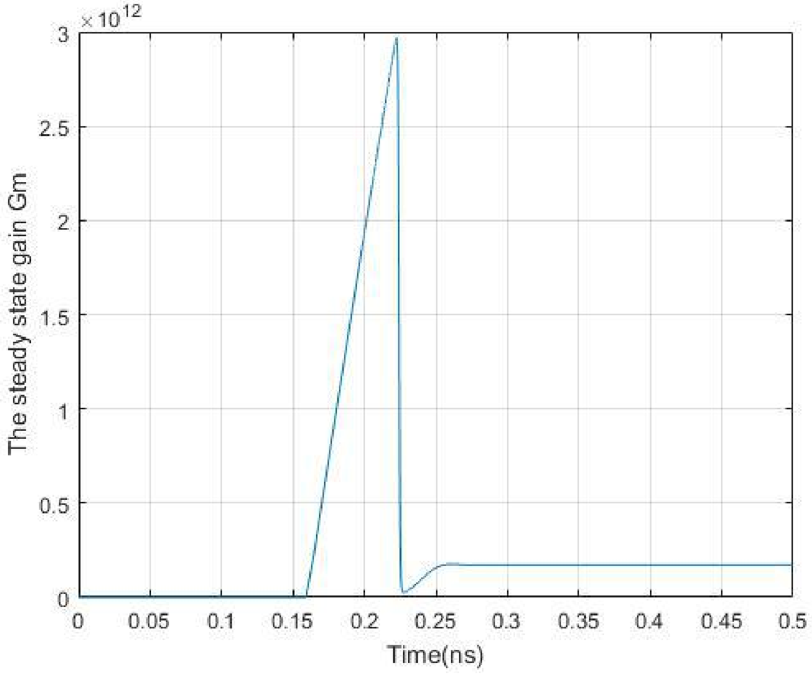

Figure 6.11 The calculated steady state gain G_m of semiconductor nanowire laser.

as the Lorentzian lineshape function L as in Eq. 6.15 with the half-width. This function is based on the assumption that the occupation probability of an electron state decays proportionally to $exp^{(-t/\tau)}$. And the Fourier transformation of this exponential function into the energy domain gives the Lorentzian lineshape function.

$$L(E-E_{21}) = \frac{1}{\pi}\frac{\hbar/\tau_{in}}{(\hbar/\tau_{in})^2 + (E-E_{21})^2} \tag{6.15}$$

The intraband relaxation time, τ_{in}, is the tiem constant associated with the exponetial decay of the elctron. $\Gamma = \hbar/\tau_{in}$ is the average of the broadening in the conduction and in the valence band. The full linewidth 2Γ is related to the average intra-band scattering time, which includes scattering events in the conduction band and valence band. For each band, linewidth contributions from different scattering processes are adding up. This convolution integral means that gain at the photon energy can now receive contributions from electron transitions within sub-bands.

CHAPTER 7

CONCLUSIONS AND FUTURE RESEARCH

In this chapter, conclusions about the dissertation will be drawn and the author's contributions will be presented. Further work in the future, including investigation and application of Plasmonic effects in CSNW; heterogeneous integration of CSNW active and passive components on the silicon-based photonic integrated circuit, will be discussed.

7.1 Summary of Contributions

As mentioned previously, communication of information, together with storage and computation form a grand challenge of the information age. Recently, the analysis of big data has become the engine for societal, financial, scientific, and technological endeavors. This demands an infrastructure that is capable of fast and reliable high volume data processing. Traditionally, this requirement was fulfilled by silicon technology. However, silicon-based technology has its own limitations, such as speed limit and heat dissipation problem. In order to process high volume data, we need data computation, storage and communication work as three fundamental functions of a computation cell. And core-shell nanowires will play an important role in this regime with their extraordinary optical properties.

In conclusion, fabrication techniques, electrical and optical properties of core-shell nanowires grown on GaAs or Si substrates were discussed here emphasizing the analysis of resonant optical modes which depend both radially and axially on the geometries of the nanowires. This shows how such sub-wavelength structures can form optical cavities as-grown, without needing sophisticated facet mirrors. In addition, we show how the fortuitous overlap of the reduced dimensional electronic wave functions and the photonic modes is responsible for the extraordinary optoelectronic properties of core-shell nanowires. Such nano-structures have been developed on heterogeneous substrates, particularly silicon, and as such becoming an important component in the next generation of photonic integrated circuits which are particularly useful in meeting the grand challenge of low energy and fast speed computation.

In this dissertation, we designed and fabricated the CSNWs based heterostructure devices, measured and simulated their opto-electronic properties, and compared it with bulk structures. The static behavior simulations, including 2-D potential profile, electric field distributions, and carrier concentration, were performed with commercially available software. The light confinement and distribution in the CSNWs was investigated by FDTD simulation. The simulation revealed the transverse and longitudinal plane waves in the resonance frequency enhanced the optical confinement of these sub-micron scale cavities.

We showed that how low dimensional electron density distribution change the optical transition rates when a small perturbation is introduced by light which results in large enhancement of optical properties.

In addition, we designed a CSNW based laser and modeled its static and dynamic lasing behavior by calculating the optical gain and threshold current density, demonstrated that how reduced dimensional electron states enhance the overall gain and emission efficiency compared to its bulk counterpart.

The major contributions of this thesis are (1) design, fabricate and characterize the hexagonal CSNWs grown on Si or GaAs substrates, revealing enhanced optical properties, such as absorption, emission and lasing; (2) simulation and analysis of light confinement and propagation mechanism in CSNWs; (3) simulation and analysis of electron distribution in the hexagonal CSNWs; (4) derived dimensional dependent band-to-band transition rates and proposed the spacial overlapping of the confined light with reduced electronic wave function greatly enhanced the optical transition rates; (5)

modeled and calculated the optical gain and output power in order to justify that lower dimensional electron states will facilitate the lasing behaviors of CSNW based laser and produced more light compare to their bulk counterparts.

7.2 Outline of the future work

Several aspects of research, such as in-depth theoretical work, wide ranges of applications, further material explorations, can be extended from the present work in the future as both breadth and depth are concerned. These issues include collective behavior in low dimensional structures, optimization of growth techniques and materials, development of Schottky contacts and exploiting electrical injection applications, employment of plasmonic effects, heterogeneous integration on Silicon based photonic integrated circuits.

7.2.1 Plasmonic Effects

Low dimensional electron gases exist at the heterointerfaces of core-shell nanowires (CSNWs). For example, the GaAs/AlGaAs CSNWs typically form a hexagonal structure in which six (6) pillars of 1D charge at the vortices, and six (6) sheets of 2D charge at facets are formed[132]. At the same time, nanowires (NW) have also been shown to be capable of confining light in their sub-wavelength nanostructure, supporting photonic modes, and producing resonant cavities without the need for polished end facets. We have previously shown how the electronic wave functions that are thus formed affect the optical transition rates, resulting in orders of magnitude enhancement in absorption and emission of light. Here we propose the plasmonic effects of the confined charge on the optical properties of CSNWs.

The finite difference time domain (FDTD) simulations identify the surface plasmon resonance modes which affect light confinement in hexagonal CSNWs, and help form a high quality factor resonant cavity. We compare regular CSNW, with a) wires covered with metal which produces surface plasmon-polaritons (SPP); b) NWs covered with metal that is sandwiched between the core and the outer, shell; and c) two-dimensional electron gas (2DEG) which embedded at the heterointerace of

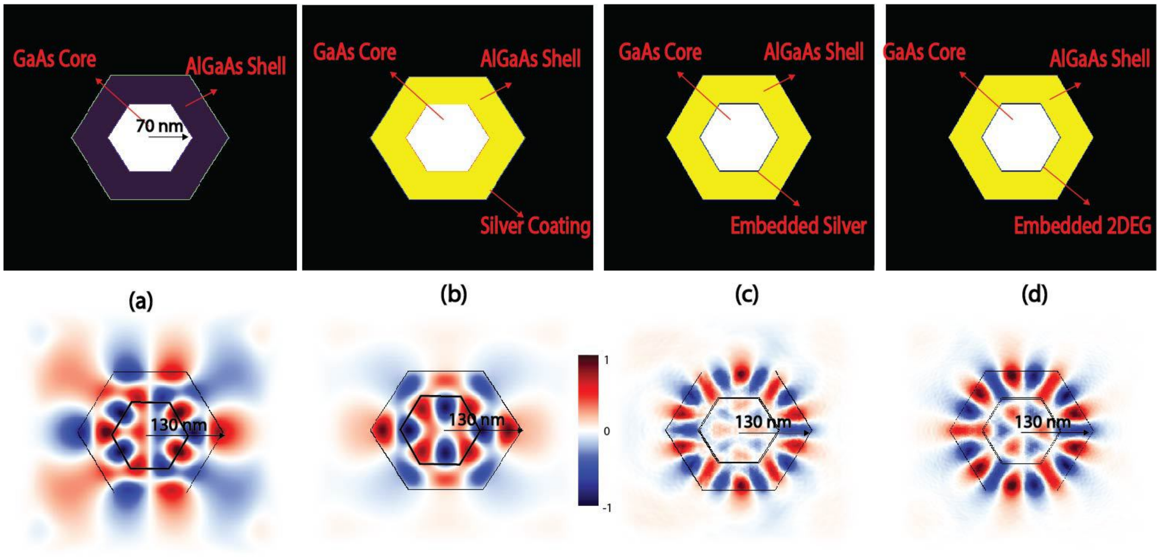

Figure 7.1 An FDTD-simulated electric field profile (linear scale) of (a) a hexagonal core-shell nanowire (CSNW), (b) photonic modes are affected by plamonic modes in a CSNW covered with silver coating, (c) CSNW with embedded silver layer between the core and the shell; (d) plasmonic and photonic modes of CSNW with embedded 2DEG show similar effects compared to embedded metal. The black boundaries represent the interface betweeen layers of the structure.

CSNWs. Results show that the 2DEG behaves similarly to an embedded metallic surface, allowing for highly localized light confinement in these wires without the need for vertical structures such as Bragg mirrors commonly used in vertical cavity surface emitting lasers (VCSELs). Besides affecting the cavity, the 2DEG enhances the transition rates due to the plasmon-electron interaction, facilitating not only photonic stimulated emission and lasing, but also surface plasmon amplification by stimulated emission of radiation[185].

The electromagnetic wave traveling of the Surface Plamon Polariton (SPP) involves both charge motion in electron reservoir (e.g., metal, graphene and 2DEG) and waves in the dielectric or air. Instead of using any metallic materials, Core-Shell nanowires (CSNWs) can naturally form two-dimensional electron gas (2DEG) at the heterojunction interface and even large one-dimensional pillar of charge at the corners of thier hexagonal facets.

Figure 7.1 shows the FDTD-simulated electric field profile (linear scale) in the transverse plane of (a) CSNW; (b) CSNW with silver coating; (c) CSNW with and embedded silver layer between the core and the shell; (d) CSNW with 2DEG at the hetero-interface. As shown in Fig 7.1, coating the wire with metal introduces plasmonic modes in the structure that enhance light confinement. Metal embedded between the core and the shell has similar effect. Importantly, we observe that similar plasmonic features can be obtained due to the 2DEG that is embedded in CSNW[186].

7.2.2 Heterogeneous Integration on PIC

Recently, the increasing demand for high-speed low-power computation and communication has driven the growth of photonics integrated circuit (PIC) technology with projected market size of a billion dollars by 2018. Silicon photonics have received significant attention as it benefits from well-established complementary metal-oxide-semiconductor (CMOS) technology. Lack of an efficient silicon-based light source and photodetector, has motivated development of technologies for heterogeneous integration of efficient III-V semiconductor light sources and detector with silicon chips. Here we present core-shell nanowires (CSNWs) as versatile low-dimensional optoelectronic systems as a replacement to their conventional thin film counterparts in heterogeneous integration in silicon photonics. These CSNWs have extraordinary performance in light generation, absorption, light modulation, energy generation, and high-speed optical detection. Finally, we elaborate on a vision for a low-cost high-performance silicon photonics chip based on a core-shell nanowire platform. In this scheme, CSNWs are applied as high-speed low-power optical detectors, light source, and waveguides.

In order to process high volume data, we need data computation, storage, and communication to work in concert as the three fundamental functions of a computation cell. As schematically shown in Fig. 7.2, a monolithic nanosystem may be envisioned, which incorporates NWs as waveguides, detectors, photovoltaic cells, antennas, modulators, (photo)capacitors, LEDs and lasers. These components may be incorporated in circuit layers, such as network-on-chip. Different layers can communicate using NW through-silicon vias (TSVs). Similar low-power/high-performance advantags can be realized through achievement of high interconnect densities on the 2.5D through-Si-interposer (TSI) as reported in reference[187]

Performance enhancement of CSNWs can be attributed to the formation of confined quasi-one-dimensional electron gas at the vortices, and two-dimensional electron gas at the facets of the hexagonally shaped GaAs/AlGaAs core-shell hetero-interface. These reduced dimensional confined charge plasma affect optical transition rates, facilitate population inversion, and collect optically generated electrons and wholes before they transit to the contacts. Additionally these plasmons, which are unique to CSNWs, affect waveguiding and optical cavity properties of CSNWs and can be used as waveguides, modulators and photocapacitors.

The proposed integrated photonic platform is schematically depicted at the bottom part of Fig. 7.2 with multiple key components implemented through utilizing core-shell nanowires. This monolithic nanosystem incorporates CSNWs as waveguides, detectors, photovoltaic cells, antennas, modulators, LEDs, and lasers. These components may be incorporated in circuit layers, such as networks on chip. Additionally, they can be used for 3D integration using NW through-silicon vias (TSVs). Such a circuit may compete with manufacturing methods such as flip-chip bonding and achieves further miniaturization by incorporating high-performance nanowires in vertical architectures to replace large surface area thin film structures such as vertical cavity surface emitting lasers (VCSELs).

In conclusion, CSNW demonstrate unique combination of plasmonic, photonic, and electronic properties which makes them versatile high-performance optoelectronic devices including Lasers, LEDs, photodetectors, solar cells, waveguides, and optical amplifiers. Since they can be grown from a wide range of material including GaAs, InP, and GaN, at different directions and on foreign substrates such as oxides, Graphene, Si, and III-Vs, they offer a competitive platform for photonic integrated circuits, and specifically for heterogeneous integration in silicon photonics chips, photodetectors/photocapacitors, antennas and waveguides.

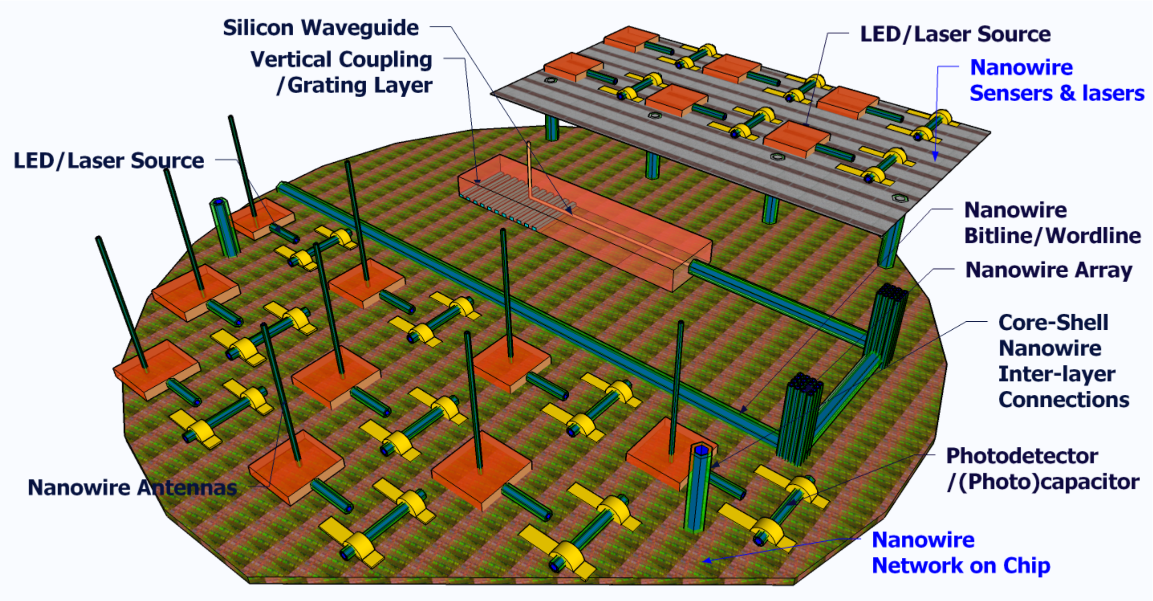
Silicon Waveguide
Vertical Coupling /Grating Layer
LED/Laser Source
LED/Laser Source
Nanowire Sensers & lasers
Nanowire Bitline/Wordline
Nanowire Array
Core-Shell Nanowire Inter-layer Connections
Photodetector /(Photo)capacitor
Nanowire Antennas
Nanowire Network on Chip

Figure 7.2 Schematic depiction of an optoelectronic nanosystem may include key components such as NW LED/laser source, photodetector/photocapacitor, NW antennas, and NW-enabled network-on-chip integrated on silicon.

BIBLIOGRAPHY

[1] M. Hilbert and P. López, “The world’s technological capacity to store, communicate, and compute information,” *Science*, vol. 332, no. 6025, pp. 60–65, 2011.

[2] J. Glanz and P. Sakuma, “Google details, and defends, its use of electricity,” *The new york times*, vol. 8, 2011.

[3] S. Sun, Z. Fan, Y. Wang, and J. Haliburton, “Organic solar cell optimizations,” *Journal of materials science*, vol. 40, no. 6, pp. 1429–1443, 2005.

[4] J. Perlin, *From space to earth: the story of solar electricity.* Earthscan, 1999.

[5] M. Razeghi and A. Rogalski, “Semiconductor ultraviolet detectors,” *Journal of Applied Physics*, vol. 79, no. 10, pp. 7433–7473, 1996.

[6] A. Rogalski, “Infrared detectors: an overview,” *Infrared Physics & Technology*, vol. 43, no. 3, pp. 187–210, 2002.

[7] E. Chen and A. Murphy, *Broadband optical modulators: science, technology, and applications.* CRC press, 2011.

[8] J. A. Schuller, E. S. Barnard, W. Cai, Y. C. Jun, J. S. White, and M. L. Brongersma, “Plasmonics for extreme light concentration and manipulation,” *Nature materials*, vol. 9, no. 3, pp. 193–204, 2010.

[9] H. Spanggaard and F. C. Krebs, “A brief history of the development of organic and polymeric photovoltaics,” *Solar Energy Materials and Solar Cells*, vol. 83, no. 2, pp. 125–146, 2004.

[10] E. F. Schubert and J. K. Kim, “Solid-state light sources getting smart,” *Science*, vol. 308, no. 5726, pp. 1274–1278, 2005.

[11] E. F. Schubert, T. Gessmann, and J. K. Kim, *Light emitting diodes.* Wiley Online Library, 2005.

[12] W. W. Chow, S. W. Koch, and M. I. Sargent, *Semiconductor-laser physics.* Springer Science & Business Media, 2012.

[13] E. Yablonovitch, “Inhibited spontaneous emission in solid-state physics and electronics,” *Physical review letters*, vol. 58, no. 20, p. 2059, 1987.

[14] Z. Alferov, “Double heterostructure lasers: early days and future perspectives,” *IEEE Journal of Selected Topics in Quantum Electronics*, vol. 6, no. 6, pp. 832–840, 2000.

[15] S. Nakamura, M. Senoh, S.-i. Nagahama, N. Iwasa, T. Yamada, T. Matsushita, H. Kiyoku, and Y. Sugimoto, “Ingan-based multi-quantum-well-structure laser diodes,” *Japanese Journal of Applied Physics*, vol. 35, no. 1B, p. L74, 1996.

[16] J. Kuzmík, “Inaln/(in) gan high electron mobility transistors: some aspects of the quantum well heterostructure proposal,” *Semiconductor Science and Technology*, vol. 17, no. 6, p. 540, 2002.

[17] J. Rosenberg, M. Benlamri, P. Kirchner, J. Woodall, and G. Pettit, "An in 0.15 ga 0.85 as/gaas pseudomorphic single quantum well hemt," *IEEE Electron Device Letters*, vol. 6, no. 10, pp. 491–493, 1985.

[18] B. Levine, "Quantum-well infrared photodetectors," *Journal of applied physics*, vol. 74, no. 8, pp. R1–R81, 1993.

[19] H. Liu, C. Song, A. SpringThorpe, and J. Cao, "Terahertz quantum-well photodetector," *Applied physics letters*, vol. 84, no. 20, pp. 4068–4070, 2004.

[20] K. Barnham, I. Ballard, J. Connolly, N. Ekins-Daukes, B. Kluftinger, J. Nelson, and C. Rohr, "Quantum well solar cells," *Physica E: Low-dimensional Systems and Nanostructures*, vol. 14, no. 1, pp. 27–36, 2002.

[21] N. Ekins-Daukes, K. Barnham, J. Connolly, J. Roberts, J. Clark, G. Hill, and M. Mazzer, "Strain-balanced gaasp/ingaas quantum well solar cells," *Applied Physics Letters*, vol. 75, no. 26, pp. 4195–4197, 1999.

[22] A. Nozik, "Quantum dot solar cells," *Physica E: Low-dimensional Systems and Nanostructures*, vol. 14, no. 1, pp. 115–120, 2002.

[23] V. Klimov, A. Mikhailovsky, S. Xu, A. Malko, J. Hollingsworth, C. Leatherdale, H.-J. Eisler, and M. Bawendi, "Optical gain and stimulated emission in nanocrystal quantum dots," *Science*, vol. 290, no. 5490, pp. 314–317, 2000.

[24] V. M. Ustinov, *Quantum dot lasers*, vol. 11. Oxford University Press on Demand, 2003.

[25] N.-M. Park, T.-S. Kim, and S.-J. Park, "Band gap engineering of amorphous silicon quantum dots for light-emitting diodes," *Applied Physics Letters*, vol. 78, no. 17, pp. 2575–2577, 2001.

[26] Q. Sun, Y. A. Wang, L. S. Li, D. Wang, T. Zhu, J. Xu, C. Yang, and Y. Li, "Bright, multicoloured light-emitting diodes based on quantum dots," *Nature photonics*, vol. 1, no. 12, pp. 717–722, 2007.

[27] Y. Xia, P. Yang, Y. Sun, Y. Wu, B. Mayers, B. Gates, Y. Yin, F. Kim, and H. Yan, "One-dimensional nanostructures: synthesis, characterization, and applications," *Advanced materials*, vol. 15, no. 5, pp. 353–389, 2003.

[28] R. Yan, D. Gargas, and P. Yang, "Nanowire photonics," *Nature Photonics*, vol. 3, no. 10, pp. 569–576, 2009.

[29] R. G. Hobbs, N. Petkov, and J. D. Holmes, "Semiconductor nanowire fabrication by bottom-up and top-down paradigms," *Chemistry of Materials*, vol. 24, no. 11, pp. 1975–1991, 2012.

[30] Y. Wu and P. Yang, "Direct observation of vapor- liquid- solid nanowire growth," *Journal of the American Chemical Society*, vol. 123, no. 13, pp. 3165–3166, 2001.

[31] W. Lu and C. M. Lieber, "Nanoelectronics from the bottom up," *Nature materials*, vol. 6, no. 11, pp. 841–850, 2007.

[32] M. H. Huang, S. Mao, H. Feick, H. Yan, Y. Wu, H. Kind, E. Weber, R. Russo, and P. Yang, "Room-Temperature Ultraviolet Nanowire Nanolasers," *Science*, vol. 292, no. 5523, pp. 1897–1899, 2001.

[33] I. Park, Z. Li, A. P. Pisano, and R. S. Williams, "Top-down fabricated silicon nanowire sensors for real-time chemical detection," *Nanotechnology*, vol. 21, no. 1, p. 015501, 2009.

[34] P. Yang, H. Yan, S. Mao, R. Russo, J. Johnson, R. Saykally, N. Morris, J. Pham, R. He, and H.-J. Choi, "Controlled growth of ZnO nanowires and their optical properties," *Advanced Functional Materials*, vol. 12, no. 5, p. 323, 2002.

[35] A. I. Persson, M. W. Larsson, S. Stenström, B. J. Ohlsson, L. Samuelson, and L. R. Wallenberg, "Solid-phase diffusion mechanism for gaas nanowire growth," *Nature materials*, vol. 3, no. 10, pp. 677–681, 2004.

[36] A. I. Hochbaum, R. Fan, R. He, and P. Yang, "Controlled growth of si nanowire arrays for device integration," *Nano letters*, vol. 5, no. 3, pp. 457–460, 2005.

[37] Y. Wu and P. Yang, "Germanium nanowire growth via simple vapor transport," *Chemistry of Materials*, vol. 12, no. 3, pp. 605–607, 2000.

[38] S. Schmitt-Rink, D. Chemla, and D. Miller, "Linear and nonlinear optical properties of semiconductor quantum wells," *Advances in Physics*, vol. 38, no. 2, pp. 89–188, 1989.

[39] M. Yazawa, M. Koguchi, and K. Hiruma, "Heteroepitaxial ultrafine wire-like growth of inas on gaas substrates," *Applied Physics Letters*, vol. 58, no. 10, pp. 1080–1082, 1991.

[40] L. Cao, J.-S. Park, P. Fan, B. Clemens, and M. L. Brongersma, "Resonant Germanium Nanoantenna Photodetectors," *Nano Letters*, vol. 10, no. 4, pp. 1229–1233, 2010.

[41] L. Cao, J. S. White, J.-S. Park, J. A. Schuller, B. M. Clemens, and M. L. Brongersma, "Engineering light absorption in semiconductor nanowire devices," *Nature Materials*, vol. 8, no. 8, pp. 643–647, 2009.

[42] M. Royo, C. Segarra, A. Bertoni, G. Goldoni, and J. Planelles, "Aharonov-Bohm oscillations and electron gas transitions in hexagonal core-shell nanowires with an axial magnetic field," *arXiv preprint arXiv:1501.06694*, 2015.

[43] M. Currie, Z. Wang, P. Dianat, P. Prete, I. Miccoli, N. Lovergine, and B. Nabet, "Large Light Emission Enhancement in GaAs/AlGaAs CoreShell Nanowires," in *International Conference on One-Dimensional Nanomaterials, ICON2013*, (Annecy, France), 2013.

[44] Y. W. Heo, B. S. Kang, L. C. Tien, D. P. Norton, F. Ren, J. R. La Roche, and S. J. Pearton, "UV photoresponse of single ZnO nanowires," *Appl. Phys. A*, vol. 80, no. 3, pp. 497–499, 2004.

[45] J. H. He, C. L. Hsin, J. Liu, L. J. Chen, and Z. L. Wang, "Piezoelectric gated diode of a single zno nanowire," *Advanced Materials*, vol. 19, no. 6, pp. 781–784, 2007.

[46] X. Duan, Y. Huang, R. Agarwal, and C. M. Lieber, "Single-nanowire electrically driven lasers," *Nature*, vol. 421, no. 6920, pp. 241–245, 2003.

[47] K. Moratis, S. L. Tan, S. Germanis, C. Katsidis, M. Androulidaki, K. Tsagaraki, Z. Hatzopoulos, F. Donatini, J. Cibert, and Y.-M. Niquet, "Strained GaAs/InGaAs Core-Shell Nanowires for Photovoltaic Applications," *Nanoscale Res Lett*, vol. 11, no. 1, pp. 1–7, 2016.

[48] Z. Wang, M. Currie, P. Prete, N. Lovergine, and B. Nabet, "Lasing from As Grown GaAs-AlGaAs Core-Shell Nanowires up to Room Temperature," in *Frontiers in Optics 2015*, (San Jose, California), p. LTh2I.4, Optical Society of America, 2015.

[49] B. Badada, T. Shi, H. Jackson, L. Smith, Q. Gao, H. H. Tan, and C. Jagadish, "Photocurrent spectroscopy of single GaAs/AlGaAs core-multishell nanowire devices," in *Device Research Conference (DRC), 2015 73rd Annual*, pp. 81–82, 2015.

[50] O. Takehiro, A. Keita, T. Kohei, W. Takao, and S. Kazuhiko, "Emission wavelength control of self-catalytic InP/GaInAs/InP core–multishell nanowire on InP substrate grown by metal organic vapor phase epitaxy," *Japanese Journal of Applied Physics*, vol. 55, no. 3, p. 031201, 2016.

[51] Y. Li, J. Xiang, F. Qian, S. Gradecak, Y. Wu, H. Yan, D. A. Blom, and C. M. Lieber, "Dopant-free gan/aln/algan radial nanowire heterostructures as high electron mobility transistors," *Nano letters*, vol. 6, no. 7, pp. 1468–1473, 2006.

[52] H. Sakaki, “Scattering suppression and high-mobility effect of size-quantized electrons in ultrafine semiconductor wire structures,” *Japanese Journal of Applied Physics*, vol. 19, no. 12, p. L735, 1980.

[53] J. Xiang, W. Lu, Y. Hu, Y. Wu, H. Yan, and C. M. Lieber, “Ge/si nanowire heterostructures as high-performance field-effect transistors,” *Nature*, vol. 441, no. 7092, pp. 489–493, 2006.

[54] N. Singh, A. Agarwal, L. Bera, T. Liow, R. Yang, S. Rustagi, C. Tung, R. Kumar, G. Lo, N. Balasubramanian, *et al.*, “High-performance fully depleted silicon nanowire (diameter/spl les/5 nm) gate-all-around cmos devices,” *IEEE Electron Device Letters*, vol. 27, no. 5, pp. 383–386, 2006.

[55] S. D. Suk, S.-Y. Lee, S.-M. Kim, E.-J. Yoon, M.-S. Kim, M. Li, C. W. Oh, K. H. Yeo, S. H. Kim, D.-S. Shin, *et al.*, “High performance 5nm radius twin silicon nanowire mosfet (tsnwfet): fabrication on bulk si wafer, characteristics, and reliability,” in *Electron Devices Meeting, 2005. IEDM Technical Digest. IEEE International*, pp. 717–720, IEEE, 2005.

[56] Z. Liu, Y. Zhan, G. Shi, S. Moldovan, M. Gharbi, L. Song, L. Ma, W. Gao, J. Huang, R. Vajtai, F. Banhart, P. Sharma, J. Lou, and P. M. Ajayan, “Anomalous high capacitance in a coaxial single nanowire capacitor,” *Nat Commun*, vol. 3, p. 879, 2012.

[57] J. Wallentin, J. M. Persson, J. B. Wagner, L. Samuelson, K. Deppert, and M. T. Borgstrom, “High-performance single nanowire tunnel diodes,” *Nano Lett*, vol. 10, no. 3, pp. 974–979, 2010.

[58] Y. Heo, L. Tien, D. Norton, S. Pearton, B. Kang, F. Ren, and J. LaRoche, “Pt/ zno nanowire schottky diodes,” *Applied physics letters*, vol. 85, no. 15, pp. 3107–3109, 2004.

[59] K. H. Li, X. Liu, Q. Wang, S. Zhao, and Z. Mi, “Ultralow-threshold electrically injected AlGaN nanowire ultraviolet lasers on Si operating at low temperature,” *Nat Nano*, vol. 10, no. 2, pp. 140–144, 2015.

[60] W. Wei, Y. G. Liu, X. Zhang, Z. Wang, and X. M. Ren, “Evanescent-wave pumped room-temperature single-mode GaAs/AlGaAs core-shell nanowire lasers,” *Applied Physics Letters*, vol. 104, no. 22, p. 223103, 2014.

[61] D. Saxena, S. Mokkapati, P. Parkinson, N. Jiang, Q. Gao, H. H. Tan, and C. Jagadish, “Optically pumped room-temperature GaAs nanowire lasers,” *Nature Photonics*, vol. 7, no. 12, pp. 963–968, 2013.

[62] B. Mayer, D. Rudolph, J. Schnell, S. Morkotter, J. Winnerl, J. Treu, K. Muller, G. Bracher, G. Abstreiter, G. Koblmuller, and J. J. Finley, “Lasing from individual GaAs-AlGaAs core-shell nanowires up to room temperature,” *Nat Commun*, vol. 4, p. 2931, 2013.

[63] R. Chen, T. T. D. Tran, K. W. Ng, W. S. Ko, L. C. Chuang, F. G. Sedgwick, and C. Chang-Hasnain, “Nanolasers grown on silicon,” *Nature Photonics*, vol. 5, no. 3, pp. 170–175, 2011.

[64] B. Hua, J. Motohisa, Y. Kobayashi, S. Hara, and T. Fukui, “Single GaAs/GaAsP coaxial core-shell nanowire lasers,” *Nano Letters*, vol. 9, no. 1, pp. 112–116, 2009.

[65] R. Agarwal, C. J. Barrelet, and C. M. Lieber, “Lasing in Single Cadmium Sulfide Nanowire Optical Cavities,” *Nano Letters*, vol. 5, no. 5, pp. 917–920, 2005.

[66] S. Gradečak, F. Qian, Y. Li, H.-G. Park, and C. M. Lieber, “GaN nanowire lasers with low lasing thresholds,” *Applied Physics Letters*, vol. 87, no. 17, p. 173111, 2005.

[67] S. Zhao, A. T. Connie, M. H. Dastjerdi, X. H. Kong, Q. Wang, M. Djavid, S. Sadaf, X. D. Liu, I. Shih, H. Guo, and Z. Mi, “Aluminum nitride nanowire light emitting diodes: Breaking the fundamental bottleneck of deep ultraviolet light sources,” *Scientific Reports*, vol. 5, p. 8332, 2015.

[68] M. Nami and D. Feezell, “Optical properties of Ag-coated GaN/InGaN axial and core–shell nanowire light-emitting diodes,” *Journal of Optics*, vol. 17, no. 2, p. 025004, 2015.

[69] L. C. Chuang, F. G. Sedgwick, R. Chen, W. S. Ko, M. Moewe, K. W. Ng, T. T. Tran, and C. Chang-Hasnain, “GaAs-based nanoneedle light emitting diode and avalanche photodiode monolithically integrated on a silicon substrate,” *Nano Lett*, vol. 11, no. 2, pp. 385–390, 2011.

[70] A. L. Bavencove, D. Salomon, M. Lafossas, B. Martin, A. Dussaigne, F. Levy, B. Andre, P. Ferret, C. Durand, J. Eymery, L. Dang, and P. Gilet, “Light emitting diodes based on GaN core/shell wires grown by MOVPE on n-type Si substrate,” *Electronics Letters*, vol. 47, no. 13, pp. 765–766, 2011.

[71] H. M. Kim, Y. H. Cho, H. Lee, S. I. Kim, S. R. Ryu, D. Y. Kim, T. W. Kang, and K. S. Chung, “High-brightness light emitting diodes using dislocation-free indium gallium nitride/gallium nitride multiquantum-well nanorod arrays,” *Nano Letters*, vol. 4, no. 6, pp. 1059–1062, 2004.

[72] S. Wang, X. Yan, X. Zhang, J. Li, and X. Ren, “Axially connected nanowire core-shell p-n junctions: a composite structure for high-efficiency solar cells,” *Nanoscale Res Lett*, vol. 10, no. 1, p. 22, 2015.

[73] Y. Yu, L. Huang, and L. Cao, “Semiconductor solar superabsorbers,” *Scientific Reports*, vol. 4, p. 4107, 2014.

[74] W. Wang, S. Wu, R. J. Knize, K. Reinhardt, Y. Lu, and S. Chen, “Enhanced photon absorption and carrier generation in nanowire solar cells,” *Opt Express*, vol. 20, no. 4, pp. 3733–3743, 2012.

[75] M. D. Kelzenberg, S. W. Boettcher, J. A. Petykiewicz, D. B. Turner-Evans, M. C. Putnam, E. L. Warren, J. M. Spurgeon, R. M. Briggs, N. S. Lewis, and H. A. Atwater, “Enhanced absorption and carrier collection in Si wire arrays for photovoltaic applications,” *Nature Materials*, vol. 9, no. 3, pp. 239–244, 2010.

[76] E. C. Garnett and P. Yang, “Silicon nanowire radial p-n junction solar cells,” *Journal of the American Chemical Society*, vol. 130, no. 29, pp. 9224–9225, 2008.

[77] L. Tsakalakos, J. Balch, J. Fronheiser, B. A. Korevaar, O. Sulima, and J. Rand, “Silicon nanowire solar cells,” *Applied Physics Letters*, vol. 91, no. 23, p. 233117, 2007.

[78] B. Tian, X. Zheng, T. J. Kempa, Y. Fang, N. Yu, G. Yu, J. Huang, and C. M. Lieber, “Coaxial silicon nanowires as solar cells and nanoelectronic power sources,” *Nature*, vol. 449, no. 7164, pp. 885–889, 2007.

[79] S. Chen, L. You, W. Zhang, X. Yang, H. Li, L. Zhang, Z. Wang, and X. Xie, “Dark counts of superconducting nanowire single-photon detector under illumination,” *Opt Express*, vol. 23, no. 8, p. 10786, 2015.

[80] A. de Luna Bugallo, M. Tchernycheva, G. Jacopin, L. Rigutti, F. H. Julien, S.-T. Chou, Y.-T. Lin, P.-H. Tseng, and L.-W. Tu, “Visible-blind photodetector based on p–i–n junction GaN nanowire ensembles,” *Nanotechnology*, vol. 21, no. 31, p. 315201, 2010.

[81] H. Pettersson, J. Trägårdh, A. I. Persson, L. Landin, D. Hessman, and L. Samuelson, “Infrared Photodetectors in Heterostructure Nanowires,” *Nano Letters*, vol. 6, no. 2, pp. 229–232, 2006.

[82] H. Kind, H. Yan, B. Messer, M. Law, and P. Yang, “Nanowire Ultraviolet Photodetectors and Optical Switches,” *Adv. Mater.*, vol. 14, no. 2, pp. 158–160, 2002.

[83] S. Liang, H. Sheng, Y. Liu, Z. Huo, Y. Lu, and H. Shen, “ZnO Schottky ultraviolet photodetectors,” *Journal of Crystal Growth*, vol. 225, no. 2-4, pp. 110–113, 2001.

[84] S. Grego, K. H. Gilchrist, J.-Y. Kim, M.-K. Kwon, and M. S. Islam, “Nanowire-based devices combining light guiding and photodetection,” *Appl. Phys. A*, vol. 105, no. 2, pp. 311–316, 2011.

[85] R. F. Oulton, V. J. Sorger, D. A. Genov, D. F. P. Pile, and X. Zhang, "A hybrid plasmonic waveguide for subwavelength confinement and long-range propagation," *Nature Photonics*, vol. 2, no. 8, pp. 496–500, 2008.

[86] H. Yamada, M. Shirane, T. Chu, H. Yokoyama, S. Ishida, and Y. Arakawa, "Nonlinear-Optic Silicon-Nanowire Waveguides," *Japanese Journal of Applied Physics*, vol. 44, no. 9A, pp. 6541–6545, 2005.

[87] D. J. Sirbuly, M. Law, P. Pauzauskie, H. Yan, A. V. Maslov, K. Knutsen, C. Z. Ning, R. J. Saykally, and P. Yang, "Optical routing and sensing with nanowire assemblies," *Proceedings of the National Academy of Sciences*, vol. 102, no. 22, pp. 7800–7805, 2005.

[88] S. Chandrasekhar, J. C. Campbell, A. G. Dentai, and G. J. Qua, "Monolithic integrated waveguide photodetector," *Electronics Letters*, vol. 23, no. 10, pp. 501–502, 1987.

[89] A. Zhang, H. Kim, J. Cheng, and Y. H. Lo, "Ultrahigh responsivity visible and infrared detection using silicon nanowire phototransistors," *Nano Lett*, vol. 10, no. 6, pp. 2117–2120, 2010.

[90] H. W. Seo, L. W. Tu, Q. Y. Chen, C. Y. Ho, Y. T. Lin, K. L. Wu, D. J. Jang, D. P. Norman, and N. J. Ho, "Photogated transistor of III-nitride nanorods," *Applied Physics Letters*, vol. 96, no. 10, p. 101114, 2010.

[91] A. Persano, M. De Giorgi, A. Fiore, R. Cingolani, L. Manna, A. Cola, and R. Krahne, "Photoconduction properties in aligned assemblies of colloidal CdSe/CdS nanorods," *ACS Nano*, vol. 4, no. 3, pp. 1646–1652, 2010.

[92] D. Park and K. Yong, "Photoconductivity of vertically aligned ZnO nanoneedle array," *Journal of Vacuum Science & Technology B*, vol. 26, no. 6, pp. 1933–1936, 2008.

[93] V. J. Logeeswaran, A. Sarkar, M. S. Islam, N. P. Kobayashi, J. Straznicky, X. Li, W. Wu, S. Mathai, M. R. T. Tan, S. Y. Wang, and R. S. Williams, "A 14-ps full width at half maximum high-speed photoconductor fabricated with intersecting InP nanowires on an amorphous surface," *Appl. Phys. A*, vol. 91, no. 1, pp. 1–5, 2008.

[94] F. Patolsky and C. M. Lieber, "Nanowire nanosensors," *Materials today*, vol. 8, no. 4, pp. 20–28, 2005.

[95] F. Qian, Y. Li, S. Gradečak, H.-G. Park, Y. Dong, Y. Ding, Z. L. Wang, and C. M. Lieber, "Multi-quantum-well nanowire heterostructures for wavelength-controlled lasers," *Nature materials*, vol. 7, no. 9, pp. 701–706, 2008.

[96] J. C. Johnson, H. Yan, P. Yang, and R. J. Saykally, "Optical cavity effects in ZnO nanowire lasers and waveguides," *The Journal of Physical Chemistry B*, vol. 107, no. 34, pp. 8816–8828, 2003.

[97] Y. Y. Wu, H. Q. Yan, M. Huang, B. Messer, J. H. Song, and P. D. Yang, "Inorganic semiconductor nanowires: Rational growth, assembly, and novel properties," *Chemistry-a European Journal*, vol. 8, no. 6, pp. 1261–1268, 2002.

[98] B. Ganjipour, S. Sepehri, A. W. Dey, O. Tizno, B. Mattias Borg, K. A. Dick, L. Samuelson, L. E. Wernersson, and C. Thelander, "Electrical properties of GaSb/InAsSb core/shell nanowires," *Nanotechnology*, vol. 25, no. 42, p. 425201, 2014.

[99] K. Storm, F. Halvardsson, M. Heurlin, D. Lindgren, A. Gustafsson, P. M. Wu, B. Monemar, and L. Samuelson, "Spatially resolved Hall effect measurement in a single semiconductor nanowire," *Nat Nanotechnol*, vol. 7, no. 11, pp. 718–722, 2012.

[100] C. Thelander, L. E. FrobergFroberg, C. Rehnstedt, L. Samuelson, and L.-E. Wernersson, "Vertical enhancement-mode InAs nanowire field-effect transistor with 50-nm wrap gate," *Electron Device Letters, IEEE*, vol. 29, no. 3, pp. 206–208, 2008.

[101] Z. W. Pan, Z. R. Dai, and Z. L. Wang, "Nanobelts of semiconducting oxides," *Science*, vol. 291, no. 5510, pp. 1947–1949, 2001.

[102] Z. L. Wang and J. Song, "Piezoelectric nanogenerators based on zinc oxide nanowire arrays," *Science*, vol. 312, no. 5771, pp. 242–246, 2006.

[103] Z. L. Wang, *Nanowires and Nanobelts: Materials, Properties and Devices. Volume 1: Metal and Semiconductor Nanowires.* Springer Science & Business Media, 2013.

[104] J. Bae, M. K. Song, Y. J. Park, J. M. Kim, M. Liu, and Z. L. Wang, "Fiber supercapacitors made of nanowire-fiber hybrid structures for wearable/flexible energy storage," *Angewandte Chemie International Edition*, vol. 50, no. 7, pp. 1683–1687, 2011.

[105] X. Wang, J. Song, J. Liu, and Z. L. Wang, "Direct-current nanogenerator driven by ultrasonic waves," *Science*, vol. 316, no. 5821, pp. 102–105, 2007.

[106] X. Zhao, Y. Ando, Y. Liu, M. Jinno, and T. Suzuki, "Carbon nanowire made of a long linear carbon chain inserted inside a multiwalled carbon nanotube," *Physical review letters*, vol. 90, no. 18, p. 187401, 2003.

[107] A. Das, J. Heo, M. Jankowski, W. Guo, L. Zhang, H. Deng, and P. Bhattacharya, "Room Temperature Ultralow Threshold GaN Nanowire Polariton Laser," *Physical Review Letters*, vol. 107, no. 6, 2011.

[108] J. X. Ding, J. A. Zapien, W. W. Chen, Y. Lifshitz, S. T. Lee, and X. M. Meng, "Lasing in ZnS nanowires grown on anodic aluminum oxide templates," *Applied Physics Letters*, vol. 85, no. 12, pp. 2361–2363, 2004.

[109] B. Xiang, H. Zhang, G. Li, F. Yang, F. Su, R. Wang, J. Xu, G. Lu, X. Sun, Q. Zhao, *et al.*, "Green-light-emitting znse nanowires fabricated via vapor phase growth," *Applied Physics Letters*, vol. 82, no. 19, pp. 3330–3332, 2003.

[110] H. J. Joyce, Q. Gao, H. H. Tan, C. Jagadish, Y. Kim, X. Zhang, Y. N. Guo, and J. Zou, "Twin-free uniform epitaxial GaAs nanowires grown by a two-temperature process," *Nano Letters*, vol. 7, no. 4, pp. 921–926, 2007.

[111] J. Zhao, X. Liu, W. Qiu, Y. Ma, Y. Huang, J.-X. Wang, K. Qiang, and J.-Q. Pan, "Surface-plasmon-polariton whispering-gallery mode analysis of the graphene monolayer coated InGaAs nanowire cavity," *Optics Express*, vol. 22, no. 5, pp. 5754–5761, 2014.

[112] A. Pan, H. Yang, R. Yu, and B. Zou, "Fabrication and photoluminescence of high-quality ternary cdsse nanowires and nanoribbons," *Nanotechnology*, vol. 17, no. 4, p. 1083, 2006.

[113] K. H. Li, LiuX, WangQ, ZhaoS, and MiZ, "Ultralow-threshold electrically injected AlGaN nanowire ultraviolet lasers on Si operating at low temperature," *Nat Nano*, vol. advance online publication, 2015.

[114] R. Wang, X. Liu, I. Shih, and Z. Mi, "High efficiency, full-color AlInGaN quaternary nanowire light emitting diodes with spontaneous core-shell structures on Si," *Applied Physics Letters*, vol. 106, no. 26, p. 261104, 2015.

[115] K. Peng, P. Parkinson, L. Fu, Q. Gao, N. Jiang, Y.-N. Guo, F. Wang, H. J. Joyce, J. L. Boland, M. B. Johnston, H. H. Tan, and C. Jagadish, "Single GaAs/AlGaAs nanowire photoconductive terahertz detectors," in *Optoelectronic and Microelectronic Materials & Devices (COMMAD), 2014 Conference on*, pp. 221–222, 2014.

[116] W. Wei, Y. Liu, X. Zhang, Z. Wang, and X. Ren, "Evanescent-wave pumped room-temperature single-mode GaAs/AlGaAs core-shell nanowire lasers," *Applied Physics Letters*, vol. 104, no. 22, p. 223103, 2014.

[117] R. Chen, T.-T. D. Tran, K. W. Ng, W. S. Ko, L. C. Chuang, F. G. Sedgwick, and C. Chang-Hasnain, "Nanolasers grown on silicon," *Nature Photonics*, vol. 5, no. 3, pp. 170–175, 2011.

[118] G. Zhang, Z. Li, X. Yuan, F. Wang, L. Fu, Z. Zhuang, F.-F. Ren, B. Liu, R. Zhang, and H. H. Tan, "Single nanowire green InGaN/GaN light emitting diodes," *Nanotechnology*, vol. 27, no. 43, p. 435205, 2016.

[119] "glō-USA, Inc. Sunnyvale, CA, led technology description." `http://www.glo.se/technology.html`. Accessed: 2017-06-10.

[120] Y. Huang, X. Duan, Y. Cui, and C. M. Lieber, "Gallium nitride nanowire nanodevices," *Nano Letters*, vol. 2, no. 2, pp. 101–104, 2002.

[121] M. Law, J. Goldberger, and P. D. Yang, "Semiconductor nanowires and nanotubes," *Annual Review of Materials Research*, vol. 34, pp. 83–122, 2004.

[122] J. Motohisa, J. Noborisaka, J. Takeda, M. Inari, and T. Fukui, "Catalyst-free selective-area movpe of semiconductor nanowires on (111) b oriented substrates," *Journal of Crystal Growth*, vol. 272, no. 1, pp. 180–185, 2004.

[123] R. Wagner and W. Ellis, "Vapor-liquid-solid mechanism of single crystal growth," *Applied Physics Letters*, vol. 4, no. 5, pp. 89–90, 1964.

[124] E. Givargizov, "Fundamental aspects of vls growth," *Journal of Crystal Growth*, vol. 31, pp. 20–30, 1975.

[125] Y. Cui, L. J. Lauhon, M. S. Gudiksen, J. Wang, and C. M. Lieber, "Diameter-controlled synthesis of single-crystal silicon nanowires," *Applied Physics Letters*, vol. 78, no. 15, pp. 2214–2216, 2001.

[126] H. L. Zhou, T. B. Hoang, D. L. Dheeraj, A. T. van Helvoort, L. Liu, J. C. Harmand, B. O. Fimland, and H. Weman, "Wurtzite GaAs/AlGaAs core-shell nanowires grown by molecular beam epitaxy," *Nanotechnology*, vol. 20, no. 41, p. 415701, 2009.

[127] C. Colombo, D. Spirkoska, M. Frimmer, G. Abstreiter, and A. F. i Morral, "Ga-assisted catalyst-free growth mechanism of gaas nanowires by molecular beam epitaxy," *Physical Review B*, vol. 77, no. 15, p. 155326, 2008.

[128] D. Ercolani, F. Rossi, A. Li, S. Roddaro, V. Grillo, G. Salviati, F. Beltram, and L. Sorba, "Inas/insb nanowire heterostructures grown by chemical beam epitaxy," *Nanotechnology*, vol. 20, no. 50, p. 505605, 2009.

[129] J. Noborisaka, J. Motohisa, S. Hara, and T. Fukui, "Fabrication and characterization of freestanding GaAs/AlGaAs core-shell nanowires and AlGaAs nanotubes by using selective-area metalorganic vapor phase epitaxy," *Applied Physics Letters*, vol. 87, no. 9, pp. –, 2005.

[130] P. Paiano, P. Prete, N. Lovergine, and A. Mancini, "Size and shape control of gaas nanowires grown by metalorganic vapor phase epitaxy using tertiarybutylarsine," *Journal of applied physics*, vol. 100, no. 9, p. 094305, 2006.

[131] Q. Wan, Q. Li, Y. Chen, T.-H. Wang, X. He, J. Li, and C. Lin, "Fabrication and ethanol sensing characteristics of zno nanowire gas sensors," *Applied Physics Letters*, vol. 84, no. 18, pp. 3654–3656, 2004.

[132] Z. Wang and B. Nabet, "Nanowire Optoelectronics," *Nanophotonics*, vol. 4, no. 1, 2015.

[133] Z. Wang, M. Currie, P. Dianat, G. Konica, P. Prete, N. Lovergine, and B. Nabet, "On Dimensional Dependence of Interaction of Light and Nano Structures," in *Frontiers in Optics*, (Orlando, FL), Optical Society of America, 2013.

[134] L. Y. Tobing and P. Dumon, "Fundamental principles of operation and notes on fabrication of photonic microresonators," in *Photonic Microresonator Research and Applications*, pp. 1–27, Springer, 2010.

[135] N. Kapany, *Optical waveguides*. Elsevier, 2012.

[136] K. T. Fountaine, W. S. Whitney, and H. A. Atwater, "Resonant absorption in semiconductor nanowires and nanowire arrays: Relating leaky waveguide modes to Bloch photonic crystal modes," *Journal of Applied Physics*, vol. 116, no. 15, pp. –, 2014.

[137] A. F. Oskooi, D. Roundy, M. Ibanescu, P. Bermel, J. D. Joannopoulos, and S. G. Johnson, "Meep: A flexible free-software package for electromagnetic simulations by the FDTD method," *Computer Physics Communications*, vol. 181, no. 3, pp. 687–702, 2010.

[138] M. A. Zimmler, J. Bao, F. Capasso, S. Muller, and C. Ronning, "Laser action in nanowires: Observation of the transition from amplified spontaneous emission to laser oscillation," *Applied Physics Letters*, vol. 93, no. 5, p. 051101, 2008.

[139] M. H. Huang, S. Mao, H. Feick, H. Yan, Y. Wu, H. Kind, E. Weber, R. Russo, and P. Yang, "Room-temperature ultraviolet nanowire nanolasers," *science*, vol. 292, no. 5523, pp. 1897–1899, 2001.

[140] T. Nobis and M. Grundmann, "Low-order optical whispering-gallery modes in hexagonal nanocavities," *Physical Review A*, vol. 72, no. 6, p. 063806, 2005.

[141] C. Czekalla, T. Nobis, A. Rahm, B. Cao, J. Zúñiga Pérez, C. Sturm, R. Schmidt Grund, M. Lorenz, and M. Grundmann, "Whispering gallery modes in zinc oxide micro-and nanowires," *physica status solidi (b)*, vol. 247, no. 6, pp. 1282–1293, 2010.

[142] D. J. Gargas, M. E. Toimil-Molares, and P. Yang, "Imaging single ZnO vertical nanowire laser cavities using UV-laser scanning confocal microscopy," *Journal of the American Chemical Society*, vol. 131, no. 6, pp. 2125–2127, 2009.

[143] J. Fallert, F. Stelzl, H. Zhou, A. Reiser, K. Thonke, R. Sauer, C. Klingshirn, and H. Kalt, "Lasing dynamics in single ZnO nanorods," *Opt Express*, vol. 16, no. 2, pp. 1125–1131, 2008.

[144] J. C. Johnson, H.-J. Choi, K. P. Knutsen, R. D. Schaller, P. Yang, and R. J. Saykally, "Single gallium nitride nanowire lasers," *Nat Mater*, vol. 1, no. 2, pp. 106–110, 2002.

[145] T. Nobis, E. M. Kaidashev, A. Rahm, M. Lorenz, and M. Grundmann, "Whispering gallery modes in nanosized dielectric resonators with hexagonal cross section," *Physical Review Letters*, vol. 93, no. 10, p. 103903, 2004.

[146] J. Wiersig, "Hexagonal dielectric resonators and microcrystal lasers," *Physical Review A*, vol. 67, no. 2, p. 023807, 2003.

[147] S.-K. Kim, X. Zhang, D. J. Hill, K.-D. Song, J.-S. Park, H.-G. Park, and J. F. Cahoon, "Doubling Absorption in Nanowire Solar Cells with Dielectric Shell Optical Antennas," *Nano Letters*, 2014.

[148] X. Zhang, X.-H. Sun, and L.-D. Jiang, "Absorption enhancement using nanoneedle array for solar cell," *Applied Physics Letters*, vol. 103, no. 21, p. 211110, 2013.

[149] B. H. Le, S. R. Zhao, N. H. Tran, and Z. T. Mi, "Electrically injected near-infrared light emission from single InN nanowire p-i-n diode," *Applied Physics Letters*, vol. 105, no. 23, p. 231124, 2014.

[150] G. Grzela, R. Paniagua-Domínguez, T. Barten, Y. Fontana, J. A. Sánchez-Gil, and J. Gómez Rivas, "Nanowire antenna emission," *Nano Letters*, vol. 12, no. 11, pp. 5481–5486, 2012.

[151] A. V. Maslov and C. Z. Ning, "Reflection of guided modes in a semiconductor nanowire laser," *Applied Physics Letters*, vol. 83, no. 6, pp. 1237–1239, 2003.

[152] B. Hua, J. Motohisa, Y. Ding, S. Hara, and T. Fukui, "Characterization of Fabry-Pérot microcavity modes in GaAs nanowires fabricated by selective-area metal organic vapor phase epitaxy," *Applied Physics Letters*, vol. 91, no. 13, pp. –, 2007.

[153] D. Saxena, F. Wang, Q. Gao, S. Mokkapati, H. H. Tan, and C. Jagadish, “Mode Profiling of Semiconductor Nanowire Lasers,” *Nano Letters*, 2015.

[154] S. Arab, P. D. Anderson, M. Yao, C. Zhou, P. D. Dapkus, M. L. Povinelli, and S. B. Cronin, “Enhanced Fabry-Perot resonance in GaAs nanowires through local field enhancement and surface passivation,” *Nano Research*, vol. 7, no. 8, pp. 1146–1153, 2014.

[155] D. M. Sullivan, *Electromagnetic simulation using the FDTD method.* John Wiley & Sons, 2013.

[156] A. Taflove and S. C. Hagness, *Computational electrodynamics.* Artech house, 2005.

[157] J. D. Jackson and R. F. Fox, “Classical electrodynamics,” *American Journal of Physics*, vol. 67, no. 9, pp. 841–842, 1999.

[158] J. D. Joannopoulos, S. G. Johnson, J. N. Winn, and R. D. Meade, *Photonic crystals: molding the flow of light.* Princeton university press, 2011.

[159] A.-L. Henneghien, B. Gayral, Y. Désières, and J.-M. Gérard, “Simulation of waveguiding and emitting properties of semiconductor nanowires with hexagonal or circular sections,” *JOSA B*, vol. 26, no. 12, pp. 2396–2403, 2009.

[160] K.-J. Bathe, *Finite element procedures.* Klaus-Jurgen Bathe, 2006.

[161] I.-H. Tan, G. Snider, L. Chang, and E. Hu, “A self-consistent solution of schrödinger–poisson equations using a nonuniform mesh,” *Journal of applied physics*, vol. 68, no. 8, pp. 4071–4076, 1990.

[162] B. M. Wong, F. Léonard, Q. Li, and G. T. Wang, “Nanoscale effects on heterojunction electron gases in GaN/AlGaN core/shell nanowires,” *Nano Letters*, vol. 11, no. 8, pp. 3074–3079, 2011.

[163] A. Bertoni, M. Royo, F. Mahawish, and G. Goldoni, “Electron and hole gas in modulation-doped $GaAs/Al_{1-x}Ga_xAs$ radial heterojunctions,” *Physical Review B*, vol. 84, no. 20, 2011.

[164] S. Birner, T. Zibold, T. Andlauer, T. Kubis, M. Sabathil, A. Trellakis, and P. Vogl, “Nextnano: general purpose 3-d simulations,” *IEEE Transactions on Electron Devices*, vol. 54, no. 9, pp. 2137–2142, 2007.

[165] D. Wolf, H. Lichte, G. Pozzi, P. Prete, and N. Lovergine, “Electron holographic tomography for mapping the three-dimensional distribution of electrostatic potential in III-V semiconductor nanowires,” *Applied Physics Letters*, vol. 98, no. 26, pp. 264103–264103–3, 2011.

[166] S. M. Sze and K. K. Ng, *Physics of semiconductor devices.* John wiley & sons, 2006.

[167] J. Singh, *Semiconductor devices: basic principles.* John Wiley & Sons, 2007.

[168] E. Fermi, *Nuclear physics: a course given by Enrico Fermi at the University of Chicago.* University of Chicago Press, 1950.

[169] S. Schmitt-Rink, D. Miller, and D. S. Chemla, “Theory of the linear and nonlinear optical properties of semiconductor microcrystallites,” *Physical Review B*, vol. 35, no. 15, p. 8113, 1987.

[170] C.-K. Tan and N. Tansu, “Nanostructured lasers: Electrons and holes get closer,” *Nat Nano*, vol. advance online publication, 2015.

[171] S. Wang, “Generalization of the thomas-reiche-kuhn and the bethe sum rules,” *Physical Review A*, vol. 60, no. 1, p. 262, 1999.

[172] Y. C. Chang, L. L. Chang, and L. Esaki, “A New One-Dimensional Quantum Well Structure,” *Applied Physics Letters*, vol. 47, no. 12, pp. 1324–1326, 1985.

[173] I. Suemune, L. A. Coldren, and S. W. Corzine, “Polarization Dependent Absorption-Spectra in Quantum Wire Structures,” *Superlattices and Microstructures*, vol. 4, no. 1, pp. 19–22, 1988.

[174] L. A. Coldren, S. W. Corzine, and M. L. Mashanovitch, *Diode lasers and photonic integrated circuits*, vol. 218. John Wiley & Sons, 2012.

[175] D. W. Wang and S. Das Sarma, "Many-body effects on excitonic optical properties of photoexcited semiconductor quantum wire structures," *Physical Review B*, vol. 64, no. 19, p. 195313, 2001.

[176] A. Einstein, "On the quantum mechanics of radiation," *Physikalische Zeitschrift*, vol. 18, pp. 121–128, 1917.

[177] N. Basov, O. Krokhin, and Y. M. Popov, "Generation of coherent light by means of solids," *Vestn. Akad. Nauk SSSR*, vol. 3, pp. 61–66, 1961.

[178] R. N. Hall, G. E. Fenner, J. Kingsley, T. Soltys, and R. Carlson, "Coherent light emission from gaas junctions," *Physical Review Letters*, vol. 9, no. 9, p. 366, 1962.

[179] Z. I. Alferov, V. Andreev, E. Portnoi, and M. Trukan, "Alas-gaas heterojunction injection lasers with a low room-temperature threshold," *Sov Phys Semiconductors*, vol. 3, no. 9, pp. 1107–1110, 1970.

[180] Z. Wang, B. Tian, M. Pantouvaki, W. Guo, P. Absil, J. Van Campenhout, C. Merckling, and D. Van Thourhout, "Room temperature inp dfb laser array directly grown on (001) silicon," *arXiv preprint arXiv:1501.03025*, 2016.

[181] L. Chen and E. Towe, "Nanowire lasers with distributed-bragg-reflector mirrors," *Applied physics letters*, vol. 89, no. 5, p. 053125, 2006.

[182] L. Asryan and R. Suris, "Theory of threshold characteristics of semiconductor quantum dot lasers," *Semiconductors*, vol. 38, no. 1, pp. 1–22, 2004.

[183] J. Piprek, *Semiconductor Optoelectronic Devices: Introduction to Physics and Simulation.* Academic Press, 2013.

[184] S. M. Stigler, *Statistics on the table: The history of statistical concepts and methods.* Harvard University Press, 2002.

[185] D. J. Bergman and M. I. Stockman, "Surface Plasmon Amplification by Stimulated Emission of Radiation: Quantum Generation of Coherent Surface Plasmons in Nanosystems," *Physical Review Letters*, vol. 90, no. 2, p. 027402, 2003.

[186] K. Montazeri, Z. Wang, and B. Nabet, "Plasmonic effect of low-dimensional electron gas in core-shell nanowires," in *Frontiers in Optics*, pp. JTh2A–6, Optical Society of America, 2016.

[187] X. Zhang, J. K. Lin, S. Wickramanayaka, S. Zhang, R. Weerasekera, R. Dutta, K. F. Chang, K.-J. Chui, H. Y. Li, D. S. Wee Ho, L. Ding, G. Katti, S. Bhattacharya, and D.-L. Kwong, "Heterogeneous 2.5D integration on through silicon interposer," *Applied Physics Reviews*, vol. 2, no. 2, p. 021308, 2015.

[188] S. L. Chuang, *Physics of photonic devices.* Hoboken, N.J.: John Wiley & Sons, 2nd ed., 2009.

[189] V. V. Mitin, V. A. Kochelap, and M. A. Stroscio, *Quantum heterostructures : microelectronics and optoelectronics.* Cambridge ; New York: Cambridge University Press, 1999.

APPENDIX A

TIME-DEPENDENT PERTURBATION THEORY

In this appendix section, we review the time-dependent perturbation theory in detail as in reference[188]. The method and conclusion will be used as the fundamental blocks in the derivation of the optical transition rates in Chapter 5. Starting from the Schrödinger equation:

$$\mathcal{H}\Psi(r,t) = -\frac{\hbar}{i}\frac{\partial}{\partial t}\Psi(r,t) \tag{A.1}$$

The Hamiltonian $\mathcal{H}$ can be expressed as:

$$\mathcal{H} = \mathcal{H}_0 + \mathcal{H}'(r,t) \tag{A.2}$$

where $\mathcal{H}_0$ is the unperturbed part Hamiltonian and is time-independent, $\mathcal{H}'(r,t)$ is the small perturbation.

The solution to the unperturbed part is assumed known:

$$\mathcal{H}_0\Psi_n(r,t) = -\frac{\hbar}{i}\frac{\partial}{\partial t}\Phi_n(r,t), \tag{A.3}$$

$$\Phi_n(r,t) = \Phi_n(r)e^{-iE_nt/\hbar} \tag{A.4}$$

The time-dependent perturbation is assumed to have the form:

$$\mathcal{H} = \begin{cases} \mathcal{H}'(r)e^{-i\omega t} + \mathcal{H}'^{+}(r)e^{+\omega t}, & t \geq 0 \\ 0, & t < 0 \end{cases} \tag{A.5}$$

Expand the wave function in terms of the unperturbed solution, we find out $\Psi(r,t)$:

$$\Psi(r,t) = \sum_n a_n(t)\Phi_n(r)e^{(-iE_n t/\hbar)} \tag{A.6}$$

$|a_n(t)|^2$ gives the probability that the electron is in the state n at time t.

Substituting the expansion for Ψ into Schrödinger equation and using A.3, we have

$$\sum_n \frac{da_n(t)}{dt}\Psi_n(r)e^{-iE_n t/\hbar} = -\frac{\hbar}{i}\sum_n \mathcal{H}'(r,t)a_n(t)\Phi_n(r)e^{(-iE_n t/\hbar)} \tag{A.7}$$

Taking the inner product with the wave function ${\Phi_m}^{\star}(r)$, and using the orthonormal property,

$$\int d^3\boldsymbol{r}\Phi^*{}_m(\boldsymbol{r})\Phi_n(\boldsymbol{r}) = \delta_{mn} \tag{A.8}$$

We find:

$$\frac{da_n(t)}{dt} = -\frac{i}{\hbar}\sum_n a_n(t)\mathcal{H}'{}_{mn}(t)e^{i\omega_{mn}t} \tag{A.9}$$

where

$$
\begin{aligned}
\mathcal{H'}_{mn}(t) &= \langle m|\mathcal{H}'(\boldsymbol{r},t)|n\rangle \\
&= \int \Phi^{*}{}_{m}(\boldsymbol{r})\mathcal{H}'(\boldsymbol{r},t)\Psi_{n}(\boldsymbol{r})d^{3}\boldsymbol{r} \\
&= \mathcal{H'}_{mn}e^{-i\omega t} + \mathcal{H'}_{mn}e^{+i\omega t}
\end{aligned}
\tag{A.10}
$$

$$\omega_{mn} = (E_m - E_n)/\hbar \tag{A.11}$$

and the matrix element is:

$$\mathcal{H'}_{mn}(t) = \int \Phi^{*}{}_{m}(\boldsymbol{r})\mathcal{H}'(\boldsymbol{r},t)\Psi_{n}(\boldsymbol{r})d^{3}\boldsymbol{r} \tag{A.12}$$

Introducing the perturbation parameter λ

$$\mathcal{H} = \mathcal{H}_0 + \lambda\mathcal{H}'(\boldsymbol{r},t) \tag{A.13}$$

and letting

$$a_n(t) = a^{(0)}{}_{n} + \lambda a^{(1)}{}_{n}(t) + \lambda^2 a^{(2)}{}_{n}(t) + \cdots \tag{A.14}$$

we can take the derivative and set $\lambda = 1$

$$\begin{aligned}\frac{da^{(0)}{}_n(t)}{dt} &= 0\\ \frac{da^{(1)}{}_n(t)}{dt} &= -\frac{i}{\hbar}\sum_n a_n^{(0)}(t)\mathcal{H}'{}_{mn}(t)e^{i\omega_{mn}t}\\ \frac{da^{(2)}{}_n(t)}{dt} &= -\frac{i}{\hbar}\sum_n a_n^{(1)}(t)\mathcal{H}'{}_{mn}(t)e^{i\omega_{mn}t}\end{aligned}\tag{A.15}$$

Thus, the zeroth-order solutions for equation A.15 are constant. Let the electron be at the state i initially

$$a^{(0)}{}_i(t=0) = 1; \quad a^{(0)}{}_m(t) = 0, \quad m \neq i \tag{A.16}$$

We have the zeroth-order solution

$$a_i{}^{(0)}(t=0) = 1; \quad a^{(0)}{}_m(t) = 0, \quad m \neq i \tag{A.17}$$

Therefore, the electron stays at the state i in the absence of any perturbation. The first order solution is

$$\begin{aligned}\frac{da_n^{(1)}}{dt} &= -\frac{i}{\hbar}\mathcal{H}'{}_{mn}(t)e^{i\omega_{mn}t}\\ &= -\frac{i}{\hbar}[\mathcal{H}'{}_{mi}e^{-i(\omega_{mi}-\omega)t} + \mathcal{H}'{}_{mi}e^{+i(\omega_{mi}+\omega)t}]\end{aligned}\tag{A.18}$$

If for final state $m = f$; then integrate above equation, we have

$$a_f^{(1)}(t) = -\frac{i}{\hbar}[\mathcal{H}'{}_{fi}\frac{e^{-i(\omega_{mi}-\omega)t}}{\omega_{fi}-\omega} + \mathcal{H}'^{+}{}_{fi}\frac{e^{+i(\omega_{mi}-\omega)t}}{\omega_{fi}+\omega}] \tag{A.19}$$

If we consider the photon energy to be near resonance, either $\omega \sim \omega_{fi}$ or $\omega \sim -\omega_{fi}$, we find the dominant terms:

$$a_f^{(1)}(t) = \frac{4|\mathcal{H'}_{fi}|^2}{\hbar^2} \frac{sin^2 \frac{t}{2}(\omega_{fi} - \omega)}{(\omega_{fi} - \omega)^2} + \frac{4|\mathcal{H'}_{fi}|^2}{\hbar^2} \frac{sin^2 \frac{t}{2}(\omega_{fi} + \omega)}{(\omega_{fi} + \omega)^2} \tag{A.20}$$

where the cross-term has been dropped because it is small compared with either of the above two terms.

When the interaction time is long enough, using approcimation

$$\frac{sin^2(\frac{xt}{2})}{x^2} \rightarrow \frac{\pi t}{2}\delta(x) \tag{A.21}$$

Then

$$|a_f^{(1)}(t)|^2 = \frac{2\pi t}{\hbar^2}|\mathcal{H'}_{fi}|^2 \delta(\omega_{fi} - \omega) + \frac{2\pi t}{\hbar^2}|\mathcal{H'}_{fi}|^2 \delta(\omega_{fi} + \omega) \tag{A.22}$$

The transition rate should be, after using the property of

$$\delta(\hbar\omega) = \frac{\delta(w)}{\hbar} \tag{A.23}$$

$$W_{if} = \frac{d|a_f^{(1)}(t)|^2}{dt} \tag{A.24}$$

$$= \frac{2\pi}{\hbar}|\mathcal{H'}_{fi}|^2 \delta(E_f - E_i - \hbar\omega) + \frac{2\pi}{\hbar}|\mathcal{H'}_{fi}|^2 \delta(E_f - E_i + \hbar\omega) \tag{A.25}$$

where $E_f = E_i + \hbar\omega$ represents the absorption of a photon by an electron, and $E_f = E_i - \hbar\omega$ corresponds with the emission of a photon.

APPENDIX B

PARTIAL CONFINEMENT ON THE ELECTRON IN CONDUCTION BAND

If the one-dimensional confinement only apply to the electrons in the conduction band, i.e., the holes in the valance band are free to move as in the bulk semiconductor, the wavefunction in the conduction band and valance band will change accordingly. The overlap of the conduction and valance band envelope function will no longer exist.

Within a two-band model, the Bloch wave functions can be described by

$$\Psi_a\left(\boldsymbol{r}\right) = u_v(\boldsymbol{r}) \frac{e^{i\boldsymbol{k_t}\cdot\rho}}{\sqrt{L_z}} \tag{B.1}$$

for a hole wave function in the heavy-hole or a light-hole subband m. and

$$\Psi_b\left(\boldsymbol{r}\right) = u_c(\boldsymbol{r}) \frac{e^{i\boldsymbol{k_t}\cdot\rho}}{\sqrt{L_z}} \Phi_n(x, y) \tag{B.2}$$

for an electron in the conduction subband n. The momentum matrix element $\boldsymbol{p}_{\mathrm{ba}}$ is given by

$$\boldsymbol{p}_{\mathrm{ba}} = \langle \Psi_b | \boldsymbol{p} | \Psi_a \rangle \approx \langle u_c | \boldsymbol{p} | u_v \rangle \, \delta_{k_t, k_t'} \; I_{\mathrm{en}} \tag{B.3}$$

where

$$
\begin{aligned}
I_{\mathrm{en}} &= \textstyle\int_{-\infty}^{+\infty} \mathrm{dxdy}\Phi_n^*(x,y) \\
&= \textstyle\int_{-\infty}^{+\infty} dxdy \cdot const \times e^{-\alpha^2 y^2} \mathcal{H}_{n_1}(\alpha y) sin \tfrac{\mathrm{x}n_2}{L_x}
\end{aligned} \tag{B.4}
$$

Here introduce the notations

$$\alpha = \frac{m_e^* \omega}{\hbar} \ , \quad \mathcal{H}_n(y) = (-1)^n e^{y^2} \frac{d^n}{dy^n} e^{-y^2} \tag{B.5}$$

where $\mathcal{H}_n$ are the Hermite polynomials[189], n_1 and n_2 are two quantum numbers.

There is no overlap of the conduction and valence band envelope functions and the **K**-Selection rule also applied. The energy levels, which arise in quantum wires, are strongly dependent on the form of the confining potentials. And the additional confinement of electrons leads to an increase of the lowest energy level.

Take into account the quantization of the electron and hole energies E_a and E_b

$$E_a = E_{\mathrm{hm}} - \frac{\hbar^2 \boldsymbol{k_t}^2}{2m_h^*} \tag{B.6}$$

$$E_b = E_g + E_{\mathrm{en}} + \frac{\hbar^2 \boldsymbol{k_t}^2}{2m_e^*} \tag{B.7}$$

And $E_{\mathrm{hm}} < 0$,

$$E_b - E_a = E_{\mathrm{hm}}^{\mathrm{en}} + E_t, E_t = \frac{\hbar^2 \boldsymbol{k_t}^2}{2m_e^*} \tag{B.8}$$

where

$$E_{\mathrm{hm}}^{\mathrm{en}} = E_g + E_{\mathrm{en}} - E_{\mathrm{hm}} \tag{B.9}$$

is the band edge transition energy ($\boldsymbol{k_t} = 0$). The summations over the quantum numbers $\boldsymbol{k}_a$ and $\boldsymbol{k}_b$become summations over $(\boldsymbol{k_t'}, m)$ and $(\boldsymbol{k_t}, n)$. Noting in the matrix element $\boldsymbol{k_t = k_t'}$

$$\alpha\left(\hbar\omega\right) = C_0 \sum_n \left|I_{\mathrm{en}}\right|^2 \frac{2}{V} \sum_{\boldsymbol{k}_t} \left|\hat{e} \cdot \boldsymbol{p}_{\mathrm{cv}}\right|^2 \delta(E_{\mathrm{hm}}^{\mathrm{en}} + E_t - \hbar\omega)(f_v^m - f_c^n) \tag{B.10}$$

Similarly, for this quasi-one dimensional case, assume the one-dimensional joint density of states also apply

$$\frac{2}{V} \sum_{\boldsymbol{k}_t} = \frac{2L_z}{V} \int \frac{d\boldsymbol{k_t}}{2\pi} = \frac{1}{\pi L_x L_y} \int_0^\infty \frac{\mathbf{1}}{\boldsymbol{k_t}} d\boldsymbol{k_t} = \int_0^\infty dE_t \rho_r^{1D} \tag{B.11}$$

$$\rho_r^{1D} = \frac{(m_r^*)^{\frac{3}{2}}}{m_e^* L_x L_y} \frac{\mathbf{1}}{\sqrt{(\hbar\omega - E_g)}} \tag{B.12}$$

where $L_z L_x L_y = V$, L_x, L_y, L_z are effective period of the quantum wire along different directions, L_z along the axial of the quantum wire, and V is a volume of a period. The delta function gives the contribution at $E_{\mathrm{hm}}^{\mathrm{en}} + E_t = \hbar\omega$, and the absorption edges occur at $\hbar\omega = E_{\mathrm{hm}}^{\mathrm{en}}$. For an unpumped semiconductor, $f_v^m = 1 \; and \; f_c^n = 0$, we have the absorption spectrum at thermal equilibrium $\alpha_0\left(\hbar\omega\right)$

$$\alpha_0\left(\hbar\omega\right) = C_0 \sum_n \left|I_{\mathrm{en}}\right|^2 \left|\hat{e} \cdot \boldsymbol{p}_{\mathrm{cv}}\right|^2 \rho_r^{1D} H(\hbar\omega - E_{\mathrm{hm}}^{\mathrm{en}}) \tag{B.13}$$

Because the integration of the delta function gives the step function, shown as H or the Heaviside step function, $H\left(x\right) = 1 \; for \; x > 0, \; and \; 0 \; for \; x < 0$. The summation of I_{en}becomes the integral of conduction band electron envelope function, using an infinite wire model, and the absorption spectrum is

$$\alpha_0\left(\hbar\omega\right) = C_0 \sum_n \left|I_{\mathrm{en}}\right|^2 \left|\hat{e}\cdot\boldsymbol{p}_{\mathrm{cv}}\right|^2 \frac{\left(m_r^*\right)^{\frac{3}{2}}}{\pi\hbar m_e{}^* L_x L_y} \frac{\mathbf{1}}{\sqrt{\left(\hbar\omega - E_g\right)}} \tag{B.14}$$

$$C_0 = \frac{\pi e^2}{n_r \varepsilon_0 c m_0^2 \omega} \tag{B.15}$$

We can see that the factors containing A_0^2 are canceled because the linear optical absorption coefficient is independent of the optical intensity.

APPENDIX C

SEMICONDUCTOR LASER MODELING

In this section, we are trying to delve into the mechanics of how an injected current actually results in an optical output in a semiconductor heterojunction laser by providing a systematic derivation of the dc light-current characteristics. First, the rate equation for photon generation and loss in a laser cavity is developed. This shows that only a small portion of the spontaneously generated light contributes to the lasing mode. Most of it comes from the stimulated recombination of carriers. All of the carriers that are stimulated to recombine by light in a certain mode contribute more photons to that same mode. Thus, the stimulated carrier recombination/photon generation process is a gain process. We find the threshold gain for lasing which is the gain necessary to compensate for cavity losses. The threshold current is the current required to reach this gain.

For electrons and holes in the active region of a diode laser, only a fraction, η_i, of injected current will contribute to the generation of carriers. We assumed the active regions that are undoped or lightly doped, so that under high injection levels, charge neutrality applies and the electron density equals the hole density (i.e., $N = P$ in the active region). Thus, we can greatly simplify our analysis by specifically tracking only the electron density, N.

We start with the governing equations of carrier density and photon density in the active region which is governed by a dynamic process.

$$\begin{aligned}\frac{dN}{dt} &= \frac{\eta_i I}{qV} - \frac{N}{\tau} - R_{st}, \\ \frac{dN_p}{dt} &= \Gamma v_g g N_p + \Gamma \beta_{sp} R_{sp} - \frac{N_p}{\tau_p},\end{aligned} \tag{C.1}$$

where β_{sp} is the spontaneous emission factor, defined as the percentage of the total spontaneous emission coupled into the lasing mode. And it is just the reciprocal of the number of available optical modes in the bandwidth of the spontaneous emission for uniform coupling to all modes. The g is the incremental gain per unit length.

The first term of Eq. C.1 is the rate of injected electrons $G_{gen} = \Gamma_i I/qV$, $\Gamma_i I/q$ is the number of electrons per second being injected into the active region, where V is the volume of the active region. The rest terms are the rate of recombining of electrons per unit volume in the active region. There are several mechanisms should be considered, including a spontaneous recombination rate, R_{sp}, a nonradiative recombination rate, R_{nr}, a carrier leakage rate, R_l and a net stimulated recombination, R_{st}, including both stimulated absorption and emission. Which looks like:

$$R_{rec} = R_{sp} + R_{nr} + R_l + R_{st} \tag{C.2}$$

The first three terms on the right refer to the natural or unstimulated carrier decay processes. The fourth one, R_{st}, require the presence of photon.

The natural decay process can be described by a carrier lifetime, τ. In the absence of photon or a generation term, the rate equation for carrier decay is $dN/dt = -N/\tau$, where $N/\tau = R_{sp} + R_{nr} + R_l$.

The natural decay rate can also be expressed in a power series of the carrier density, N. We can also rewrite $R_{rec} = BN^2 + (AN + CN^3) + R_{st}$. Where $R_{sp} \sim BN^2$ and $R_{nr} + R_l \sim (AN + cN^3)$. The coefficient B is the bimolecular recombination coefficient, and it has a magnitude, $B \sim 10^{-10} cm^3/s$ for most AlGaAs and InGaAsP alloys of interest.

When a laser is below threshold, in which the gain is insufficient to compensate for cavity losses, the generated photons do not receive net amplification. The spontaneous photon generation rate per unit volume is exactly equal to the spontaneous electron recombination rate, R_{sp}, because an electron-hole pair will emit a photon when they recombine radiatively. Under steady-state conditions ($dN/dt = 0$), the generation rate equals the recombination rate with $R_{st} = 0$.

$$\frac{\eta_i I}{qV} = R_{sp} + R_{nr} + R_l \tag{C.3}$$

The spontaneously generated optical power, P_{sp}, is obtained by multiplying the number of photons generated per unit time per unit volume, R_{sp}, by the energy per photon, $h\upsilon$, and the volume of the active region, V.

$$P_{sp} = h\upsilon V R_{sp} = \eta_i \eta_r \frac{h\upsilon}{q} I \tag{C.4}$$

The main photon generation term above threshold is R_{st}. Electron-hole pair is stimulated to recombine, another photon is generated. But since the cavity volume occupied by photons, V_p, is usually larger than the active region volume occupied by electrons, V, the photon density generation rate will be $[V/V_p]R_{st}$, not just R_{st}. The electron-photon overlap factor, $[V/V_p]$, is generally referred to as the confinement factor, Γ.

C.1 Threshold or Steady-State Gain in Lasers

The cavity loss can be characterized by a photon decay constant or lifetime, τ_p, and the gain necessary to overcome losses, and thus reach threshold. By assuming steady-state conditions (i.e. $dN_p/dt = 0$), and solving for this steady-state or threshold gain, g_{th}, where the generation term equals the recombination term for photons. We assume only a small fraction of the spontaneous emission is coupled into the mode (i.e. β_{sp} is quite small), then the second term can be neglected, and we have the solution:

$$\Gamma g_{th} = \frac{1}{v_g \tau_p} =< \alpha_i > +\alpha_m \tag{C.5}$$

The product, Γg_{th}, is referred to as the threshold modal gain because it now represents the net gain required for the mode as a whole, and it is the mode as a whole that experiences the cavity loss. $< \alpha_i >$ is the average internal loss, and α_m is the mirror loss if we considered an in-plane wave laser.

The optical energy of a nano-cavity laser propagates in a dielectric waveguide mode, which is confined both transversely and laterally as defined by a normalized transverse electric field profile, $U(x, y)$. In the axial direction this mode propagates as $exp^{(-j\beta z)}$, where β is the complex propagation constant, which includes any loss or gain. Thus, the time- and space-varying electric field can be written as

$$\xi = \hat{e}_y E_0 U(x, y) e^{j(\omega t - \beta z)} \tag{C.6}$$

where $\hat{e}_y$ is the unit vector indicating TE polarization and E_0 is the magnitude of the field. The complex propagation constant, β, includes the incremental transverse modal gain, $< g >_{xy}$ and internal modal loss, $< \alpha_i >_{xy}$. If we consider a Fabry-Perot laser with the propagating mode is reflected by end mirrors, and the reflection coefficients are r_1 and r_2. respectively. In addition, the mean mirror intensity reflection coefficient, $R = r_1 r_2$.

Define the mirror lass as α_m

$$\alpha_m \equiv \frac{1}{L} \ln(\frac{1}{R}) \tag{C.7}$$

The photon decay lifetime is given by,

$$\frac{1}{\tau_p} = \frac{1}{\tau_i} + \frac{1}{\tau_m} = v_g(< \alpha_i > +\alpha_m) \tag{C.8}$$

Thus, we can also write

$$\Gamma g_{th} =< \alpha_i > +\alpha_m = \frac{1}{v_g \tau_p} \tag{C.9}$$

C.2 Threshold Current and Output Power

We construct together a below-threshold and an above-threshold characteristic to illustrate the output power versus input current for a normal diode laser. The first step is to use the below-threshold steady-state carrier rate equation,

$$\frac{\eta_i I_{th}}{qV} = (R_{sp} + R_{nr} + R_l)_{th} = \frac{N_{th}}{\tau} \tag{C.10}$$

Then, recognizing that $(R_{sp} + R_{nr} + R_l) = AN + BN^2 + CN^3$ depends monotonically on N, we observe from $N(I > I_{th}) = N_{th}$ that above threshold $(R_{sp}+R_{nr}+R_l)$ will also clamp at its threshold value, given by Eq. C.10. Thus, we can substitute Eq. C.10 into the carrier rate equation, Eq. C.1 to obtain a new above threshold carrier rate equations,

$$\frac{dN}{dt} = \eta_i \frac{(I - I_{th})}{qV} - v_g g N_p, \quad (I > I_{th}) \tag{C.11}$$

We also calculate a steady-state photon density above threshold where $g = g_{th}$,

$$N_p = \frac{\eta_i (I - I_{th})}{q v_g g th V} \quad (\textit{steady state}) \tag{C.12}$$

To obtain the power out, we first construct the stored optical energy in the cavity, E_{os}, by multiplying the photon density, N_p, by the energy per photon, hv, and the cavity volume, V_p. That is $E_{os} = N_p hv V_p$. Then, we multiply this by the erngy loss rate through the mirrors, $v_g \alpha_m = \frac{1}{\tau_m}$, to get the optical power output from the mirrors,

$$P_0 = v_g \alpha_m N_p hv V_p \tag{C.13}$$

Substituting from , and using $\Gamma = V/V_p$,

$$P_0 = \eta_i (\frac{\alpha_m}{<\alpha_i> + \alpha_m}) \frac{hv}{q} (I - Ith), \quad (I > I_{th}) \tag{C.14}$$

The output power below-threshold ($I < I_{th}$) can be approximated by neglecting the stimulated emission term and solving for N_p under steady-state conditions.

$$N_p = \Gamma \beta_{sp} R_{sp} \tau p \quad (I < I_{th}) \tag{C.15}$$

and

$$P_0 (I < I_{th}) = \eta_r \eta_i \left(\frac{\alpha_m}{<\alpha_i> + \alpha_m} \right) \frac{hv}{q} \beta_{sp} I, \tag{C.16}$$

We can get the threshold carrier density:

$$N_{th} = N_{tr} e^{g_{th}/g_0 N} = N_{tr} e^{(<\alpha_i> + \alpha_m)/\Gamma g_0 N} \tag{C.17}$$

Using the polynomial fit for the recombination rates, and recognizing that for the best laser material the recombination at threshold is dominated by spontaneous recombination, we have, $I_{th} \cong {BN_{th}}^2 qV/\eta_i$, Thus

$$I_{th} \cong \frac{qVB{N_{tr}}^2}{\eta_i} e^{(<\alpha_i> + \alpha_m)/\Gamma g_0 N} \tag{C.18}$$

where for most $III - V$ materials the bimolecular recombination coefficient, $B \sim 10^{-10} cm^3/s$.

For a multiple quantum-well (MQW) lasers, we have to multiply the single-well confinement factor, Γ_1, and volume, V_1, by the number of wells, N_w.

$$I_{thMQW} \cong \frac{q N_w V_1 B {N_{tr}}^2}{\eta_i} e^{2(<\alpha_i> + \alpha_m)/N_w \Gamma_1 g_0 N} \tag{C.19}$$

APPENDIX D

MEEP SIMULATION CODE

D.1 Cylindrical Core-Shell Nanowire

```
; By Zhihuan Wang, 06-27-2013
; Calculating 1D cylindrical GaAs/AlGaAs core-shell nanowire excitation
   mode using cylindrical coordinates.

;%%% length unit %%%
; fundamental length unit in meep is um
;(define nm 0.001)    ; nano-meter unit
;(define um 1)        ; micro-meter unit

;-------------------------Parameter Setup---------------------------------
(define-param nc 3.4) ; index of nanowire core
(define-param ns 3.1349) ; index of nanowire shell
(define-param w 0) ; width of nanowire

(define-param r 1.1) ; radius of core
(define-param rtotal 1.5) ; radius of total (core+shell)

(define-param pad 0.5) ; padding between waveguide and edge of PML
(define-param gap 0.4) ; padding between cylinder and cell edge in XY plane
(define-param dpml 1.5) ; thickness of PML
```

```

;------------------Dimension and size of the computational cell-----------
(define sxy (* 2 (+ rtotal w pad dpml))) ; cell size in XY plane
(set! geometry-lattice (make lattice (size sxy sxy no-size)))

;-----------------------Geometric Setup--------------------------------
(set! geometry (list
               (make cylinder (center 0 0) (height infinity)
               (radius rtotal ) (material (make dielectric (index ns))))

               (make cylinder (center 0 0) (height infinity)
               (radius r) (material (make dielectric (index nc))))))

;-----------------------------PML layers set up--------------------------
(set! pml-layers (list (make pml (thickness dpml))))
(set-param! resolution 20)
;-------------------------------Source set up----------------------------
(define-param fcen 0.15) ; pulse center frequency
(define-param df 0.1)  ; pulse width (in frequency)
;(define-param nfreq 500); number of frequencies at which to compute flux

(set! sources (list
               (make source
                 (src (make gaussian-src (frequency fcen) (fwidth df)))
                 (component Ez) (center (+ rtotal 0.5) 0))))
; note that the r -> -r mirror symmetry is exploited automatically

;---------------------------run meep--------------------------------------
(run-sources+ 300
                (at-beginning output-epsilon)
                (after-sources (harminv Ez (vector3 (+ rtotal 0.5)) fcen df)))
(run-until (/ 1 fcen) (at-every (/ 1 fcen 20) output-efield-z))
```

snippet/sourcecode/CylindCS.ctl

D.2 Hexagonal Core-Shell Nanowire

```
; Calculating GaAs/AlGaAs single Hexagon core-shell nanowire excitation mode
; By Zhihuan Wang 07-01-2013
; Will examine the diameter varing from 20 50 90 130 170 210 250 290 330
; Incident light source wavelength is 532 nm fcen=0.1879
;------------------------Parameter Setup-----------------------------------
(reset-meep)
(define-param n 3.4) ; index of waveguide
(define-param ns 3.3) ; index of waveguide shell

(define-param w 0) ; width of waveguide
(define-param r 1.65) ; outer radius of ring
(define-param l 10)   ; length of the nanowire
(define-param rc (* 0.4 r)) ; inner radius of ring

(define-param pad 0.5) ; padding between waveguide and edge of PML
(define-param dpml 1) ; thickness of PML

;-----------------Dimension and size of the computational cell-------------
(define C->L (compose cartesian->lattice vector3))
(define sxy (* 2 (+ r w pad dpml))) ; cell size y
(define sxz (* 2 (+ l w pad dpml))) ; cell size z

```

```
;-----------------------Geometric Setup-----------------------------------
(set! geometry-lattice (make lattice (size sxy sxy sxz)))
(set! geometry (append
    (list
     (make block (center 0 0) (size (* r (sqrt (/ 4 3))) (* 2 r) l)
     (e1  (C->L 1 0)) (e2  (C->L 0 1))
       (material (make dielectric (index ns))))
     (make block (center 0 0) (size (* r (sqrt (/ 4 3))) (* 2 r) l)
     (e2 ( C->L (/ (sqrt 3) 2) 0.5)) (e1  (C->L -0.5 (/ (sqrt 3) 2) ))
     (material (make dielectric (index ns))))

     (make block (center 0 0) (size (* r (sqrt (/ 4 3))) (* 2 r) l)
       (e2  ( C->L (/ (sqrt 3) 2) -0.5)) (e1  (C->L 0.5 (/ (sqrt 3) 2)) )
     (material (make dielectric (index ns))))
         (make block (center 0 0) (size (* rc (sqrt (/ 4 3))) (* 2 rc) l)
     (e1  (C->L 1 0)) (e2  (C->L 0 1))
     (material (make dielectric (index n))))
     (make block (center 0 0) (size (* rc (sqrt (/ 4 3))) (* 2 rc) l)
     (e2 ( C->L (/ (sqrt 3) 2) 0.5)) (e1  (C->L -0.5 (/ (sqrt 3) 2) ))
     (material (make dielectric (index n))))
     (make block (center 0 0) (size (* rc (sqrt (/ 4 3))) (* 2 rc) l)
     (e2  ( C->L (/ (sqrt 3) 2) -0.5)) (e1  (C->L 0.5 (/ (sqrt 3) 2)) )
     (material (make dielectric (index n)))))))


;----------------------------PML layers set up-----------------------------
(set! pml-layers (list (make pml (thickness dpml))))
(set-param! resolution 10)
;------------------------------Source set up-------------------------------
(define-param fcen 0.1879) ; pulse center frequency
```

```
(define-param df 0.02)  ; pulse width (in frequency)
(set! sources (list
           (make source
             (src (make gaussian-src (frequency fcen) (fwidth df)))
             (component Ez) (center (+ r 0.1) 0))))

;--------------------------run meep---------------------------------------
(run-sources+ 300
              (at-beginning output-epsilon)
              (after-sources (harminv Ez (vector3 (+ r 0.1)) fcen df)))
(run-until (/ 1 fcen) (at-every (/ 1 fcen 20) output-efield-z
    output-tot-pwr))
```

snippet/sourcecode/HexCS3D.ctl

APPENDIX E

GAIN SPECTRUM AND THRESHOLD CALCULATION MATLAB CODE

```
%% gain (Gain Spectral Analysis Method to determin the enhancement factor for reduceced dimensionality
% with Approximations for simple geometry and variables)
% Modified for single band transitions and without scattering broadening effect

% Created on 8/25/2014 By Zhihuan Wang (GaAs/AlGaAs core-shell nanowire)
% Modified by 11/4/2016
clc; close all;

J_eV = 1.60217657e-19; %Joules per eV
eV_J = 6.24150934e18; % eV per Joule

%% Photon energy & system input (variables initiate)
E_ph = 1.2:0.01:2;
n = 6e18:3e18:3e19;
p = 6e18:3e18:3e19;  % Hole carrier concentration, Unit [cm^-3]

k = length(E_ph);
len_n = length(n);
abs_coef3D = size(k);
abs_coef2D = size(k);
abs_coef1D = size(k);
k0_3D = size(k);
gain_3D = size(k, len_n);
```

```
gain_2D = size(k, len_n);
gain_1D = size(k, len_n);
enhance_abs = size(k);
sp_rate3D = size(k);
sp_rate2D = size(k);
sp_rate1D = size(k);
enhance_sp = size(k);
st_rate3D = size(k);
st_rate2D = size(k);
st_rate1D = size(k);
enhance_st = size(k);

f_v = size(k, len_n);
f_c = size(k, len_n);
Fc = size(len_n);
Fv = size(len_n);

maxgain_3D = size(len_n);
maxgain_2D = size(len_n);
maxgain_1D = size(len_n);
%% Refractive index without material dispersion
% Uncommented if need dispersion
n_r = 3.312; % refractive index without material dispersion

%% Parameters in MKS units
H_j = 6.63e-34;%Plancks constant [J.s]
H = 4.14e-15;%Plancks constant [eV.s]
H_rj = 1.05e-34;% Reduced Plancks constant [J.s]
H_r = 6.58e-16;% Reduced Plancks constant [eV.s]
C = 3e10; %speed of light [cm/s]
e = 1.6e-19; %elementary charge [C]
kB = 1.38*10^-23; % Boltzmann's constant [J/K]
T = 300; % room temperature [K]
m0 = 9.11e-31; % Electron rest mass [kg]
```

```
Eg=1.424; %Energy bandgap for GaAs at 300K [eV]
m_e = 0.067*m0; %Electron Effective mass for GaAs[unitless /m0]
m_h = 0.47*m0; %Hole Effective mass for GaAs 3D[unitless /m0]
m_h2D = 0.118*m0; %Hole Effective mass for GaAs 2D[unitless /m0]
m_h1D = 0.027*m0; %Hole Effective mass for GaAs 1D[unitless /m0]
m_hh = 0.50*m0; %heavey hole Effective mass for GaAs[unitless /m0]
m_lh = 0.087*m0; %Light hole Effective mass for GaAs[unitless /m0]
m_r = m_e*m_h/(m_e+m_h); % Reduced effective mass
m_r2D = m_e*m_h/(m_e+m_h2D); % Reduced effective mass 2D
m_r1D = m_e*m_h/(m_e+m_h1D); % Reduced effective mass 1D

m0SI = 5.693e-16; %Electron rest mass [kg]
m_eSI = 0.067*m0SI; %Electron Effective mass for GaAs[unitless /m0]
m_hSI = 0.47*m0SI; %Hole Effective mass for GaAs 3D[unitless /m0]
m_rSI = m_eSI*m_hSI/(m_eSI+m_hSI); % Reduced effective mass

m00 = 9.11*10^-28; %Electron rest mass [kg]
m_ee = 0.067*m00; %Electron Effective mass for GaAs[unitless /m0]
m_hh = 0.47*m00; %Hole Effective mass for GaAs 3D[unitless /m0]
m_rr = m_ee*m_hh/(m_ee+m_hh); % Reduced effective mass
m_rr2D = m_e*m_h/(m_e+m_h2D); % Reduced effective mass 2D
m_rr1D = m_e*m_h/(m_e+m_h1D); % Reduced effective mass 1D

Lx = 50e-8; % 50 A for length [cm]
Ly = 50e-8;
Lz = 50e-8;
Lz3D = 50e-5; % 50000 A for length [cm]
Lz2D = 50e-10; % 5000 A for length [cm]
Lz1D = 50e-6; % 50 A for length [cm]
Lzm = 100e-10;
a = 100e-10; %nanowire crosssection [m]
b = 100e-10;
p_cv = 2.88*10^-18;
f_cv = 23; %oscillator strength 3D [eV]
```

```
f_cv1D = 230; %oscillator strength 1D [eV]
eps_0 = 8.85e-14; % Permittivity of vacuum [F/cm]
Nwr = 1/(Lx*Ly); %nanowire density [cm^-2]
Ep = 25.7; % Energy parameter [eV]
%% quantized energy state for 2D
E_e1 = H_rj^2*pi^2/(2*m_e*Lzm^2)*eV_J;
E_h1 = H_rj^2*pi^2/(2*m_h*Lzm^2)*eV_J;
E_e2 = H_rj^2*pi^2*4/(2*m_e*Lzm^2)*eV_J;
E_h2 = H_rj^2*pi^2*4/(2*m_h*Lzm^2)*eV_J;
E_e3 = H_rj^2*pi^2*9/(2*m_e*Lzm^2)*eV_J;
E_h3 = H_rj^2*pi^2*9/(2*m_h*Lzm^2)*eV_J;

E_e1h1 = Eg+E_e1+E_h1; %E_h should be negative value.
E_e2h2 = Eg+E_e2+E_h2;
E_e3h3 = Eg+E_e3+E_h3;

%% quantized energy state for 1D
E_11 = Eg+H_rj^2/(2*m_r)*((pi/a)^2+(pi/b)^2)*eV_J;
E_12 = Eg+H_rj^2/(2*m_r)*((pi/a)^2+(pi*2/b)^2)*eV_J;
E_22 = Eg+H_rj^2/(2*m_r)*((pi*2/a)^2+(pi*2/b)^2)*eV_J;
E_23 = Eg+H_rj^2/(2*m_r)*((pi*2/a)^2+(pi*3/b)^2)*eV_J;
E_33 = Eg+H_rj^2/(2*m_r)*((pi*3/a)^2+(pi*3/b)^2)*eV_J;

%% Fermi distribution
Na = 1e11;%acceptor doping concentration
Nd = 1e11;%donor doping concentration
Nc = 2*(2*pi*m_e*kB*T/H_j^2)^1.5*10^-6;
Nv = 2*(2*pi*m_h*kB*T/H_j^2)^1.5*10^-6;
for j=1:len_n
Fc(j)= kB*T*(log(n(j)./Nc) + 1/sqrt(8)*(n(j)./Nc))*eV_J;
Fv(j)= kB*T*(log(p(j)./Nv) + 1/sqrt(8)*(p(j)./Nv))*eV_J;
end

% Check Joyce-Dixon approximation applicable range -1<theta<7
```

```
theta = size(len_n);
for j=1:len_n
    theta(j)= log(n(j)/Nc)+2^(-1.5)*(n(j)/Nc);
end

Ec =size(k);
Ev =size(k);
for j=1:len_n
for i=1:k
k0_3D(i) = sqrt(2*m_r*((E_ph(i)-Eg)*J_eV)/H_rj^2);
Ev(i) = -H_rj.^2*k0_3D(i).^2/(2*m_h);
Ec(i) = Eg+H_rj.^2*k0_3D(i).^2/(2*m_e);
f_c(i,j) = (1 + exp((   m_r/m_e*(E_ph(i) - Eg) - Fc(j))/(kB*T*eV_J))).^-1;
f_v(i,j) = (1 + exp(( - m_r/m_h*(Eg - E_ph(i)) + Fv(j))/(kB*T*eV_J))).^-1;
end
end

figure;
plot(E_ph, f_c , E_ph, f_v , E_ph, f_c-f_v);

%% Gain Spectrum: Gain=Absorption Coefficent* fermi distribution (g(hw)=a0(hw)[fv(k0)-fc(k0)])
% Without Linewidth Broadening
fe = size(k,len_n);
for j=1:len_n
for i=1:k
if E_ph(i)< Eg
gain_3D(i,j) = 0;
else
gain_3D(i,j) = (sqrt(2)*m_r^1.5*(e*eV_J)^2*(1.5*m0*Ep*J_eV/6))/(3*pi*n_r*m0*eps_0*C*H_rj^2*E_ph(i))*(E_ph(i)-Eg)^0.5*(f_c(i,j)-f_v(i,j));
end

if E_ph(i)< E_e1h1
```

```
    gain_2D(i,j) = 0;
elseif E_e1h1<= E_ph(i)
    gain_2D(i,j) = (e^2*pi*H_r*(1.5*m0*Ep*J_eV/6)*2)/(3*n_r*eps_0*C*m0^2*E_ph(i))*
        m_r2D/(H_rj^2*pi*Lz)*(f_c(i,j)-f_v(i,j));
end

if E_ph(i)< E_11
   gain_1D(i,j) = 0;
elseif E_11<= E_ph(i)
   gain_1D(i,j) = (e^2*pi*H_r*Nwr)/(3*n_r*eps_0*C*m0^2*E_ph(i))*(m0*Ep*10*J_eV/6)*(
       m_r1D^1.5/(pi*H_rj*m_e*Lx*Ly))*((E_ph(i)-E_11))^-0.5*(f_c(i,j)-f_v(i,j));
end

maxgain_3D(j)= max(gain_3D(:,j));
maxgain_2D(j)= max(gain_2D(:,j));
maxgain_1D(j)= max(gain_1D(:,j));
enhance_abs(i,j) = gain_2D(i,j)/gain_3D(i,j);

end
end

%% Plotting the results
figure;
subplot(2,2,1);
plot (E_ph, gain_3D,'LineWidth',4)
title('Gain coefficient versus photon energy for 3D')
ylabel ('Gain coefficient (/cm)')
xlabel ('photon energy (eV)')
grid on,

subplot(2,2,2);
plot (E_ph, gain_2D,'LineWidth',4)
title('Gain coefficient versus photon energy for 2D')
ylabel ('Gain coefficient (/cm)')
```

```
xlabel ('photon energy (eV)')
grid on,

subplot(2,2,3);
plot (E_ph, gain_1D,'LineWidth',4)
title('Gain coefficient versus photon energy for 1D')
ylabel ('Gain coefficient (/cm)')
xlabel ('photon energy (eV)')
grid on,

subplot(2,2,4);
plot (n, maxgain_2D,'LineWidth',4)
title('Maximum gain versus carrier density')
ylabel ('Gain coefficient (/cm)')
xlabel ('Carrier density (1/cm^2)')
grid on,
%% Curve fitting in order to find the threshold carrier density
% which is nth = 4.533*10^18 (1/cm^3)

nth = 4.533*10^18; % Unit (1/cm^3)
% nth = Ntr*exp(gth/g0)

%% Fermi distribution for threshold carrier density
Fc_th= kB*T*(log(nth/Nc) + 1/sqrt(8)*(nth/Nc))*eV_J;
Fv_th= kB*T*(log(nth/Nv) + 1/sqrt(8)*(nth/Nv))*eV_J;

f_vth = size(k);
f_cth = size(k);
for i=1:k
f_vth(i) = (1 + exp(( - m_r/m_h*(E_ph(i) - Eg) + Fv_th)/(kB*T*eV_J))).^-1;
f_cth(i) = (1 + exp((   m_r/m_e*(E_ph(i) - Eg) - Fc_th)/(kB*T*eV_J))).^-1;
end

%% Calculating rsp and Rsp based on the threshold carrier density
```

```
% Spontaneous Emission Spectrum: sp_rate = Emission Probability * Density of States *
     fermi distribution
% (sp_rate(hw)=Pem*Nj(hw)*[fv(k0)-fc(k0)])

for i=1:k
if E_ph(i)< Eg
sp_rate3D(i) = 0;
else
sp_rate3D(i) = (n_r*e^2*E_ph(i)*Ep*J_eV/6)/(pi*m0^2*eps_0*C^3*H_r^2)*((2*m_r)^1.5)
    /(2*pi^2*H_r^3)*((E_ph(i)-Eg)*J_eV)^0.5*(f_cth(i)*(1-f_vth(i)));
end

if E_ph(i)< E_e1h1
    sp_rate2D(i) = 0;
elseif E_e1h1<= E_ph(i)
sp_rate2D(i) = (n_r*e^2*E_ph(i)*J_eV*Ep*J_eV/6)/(pi*m0^2*eps_0*C^3*H_r^2)*(m_r2D*2)/(
    pi*H_r^2*Lz2D)*(f_cth(i)*(1-f_vth(i)));
end

if E_ph(i)< E_11
   sp_rate1D(i) = 0;
elseif E_11<= E_ph(i)
sp_rate1D(i) = (n_r*e^2*E_ph(i)*J_eV*Ep*J_eV/6)/(pi*m0^2*eps_0*C^3*H_r^2)*(m_r1D
    ^1.5/(pi*H_r*m_e*Lz1D*Lz1D))*(E_ph(i)-E_11)^-0.5*(f_cth(i)*(1-f_vth(i)));
end


end

Rst_3D = trapz(sp_rate3D');
Rst_2D = trapz(sp_rate2D');
Rst_1D = trapz(sp_rate1D');

%% Threshold current calculation
```

```

Jth_3D = e*Lz*Rst_3D;
Jth_2D = e*Lz*Rst_2D;
Jth_1D = e*Lz*Rst_1D;

%% Optical Outpul Power

P_3D = (Eg+0.0257/2)*Lz*Rst_3D;
P_2D = (Eg+0.0257/2)*Lz*Rst_2D;
P_1D = (Eg+0.0257/2)*Lz*Rst_1D;
enhance_2D = P_2D/P_3D
enhance_1D = P_1D/P_3D

%% Plotting the results
figure;
subplot(2,2,1);
plot (E_ph, sp_rate3D)
title('Spontaneous Emission Rate versus photon energy for 3D')
ylabel ('Spontaneous Emission Rate (/cm)')
xlabel ('photon energy (eV)')
grid on,

subplot(2,2,2);
plot (E_ph, sp_rate2D)
title('Spontaneous Emission Rate versus photon energy for 2D')
ylabel ('Spontaneous Emission Rate (/cm)')
xlabel ('photon energy (eV)')
grid on,

subplot(2,2,3);
plot (E_ph, sp_rate1D)
title('Spontaneous Emission Rate versus photon energy for 1D')
ylabel ('Spontaneous Emission Rate (/cm)')
xlabel ('photon energy (eV)')
```

```
grid on,

subplot(2,2,4);
barx = [1 2 3];
bary = [Jth_3D, Jth_2D, Jth_1D];
bar (barx,bary);
set(gca,'YScale','log');
set(gca,'XTickLabel',{'3D', '2D', '1D'});
for i1=1:numel(bary)
    text(barx(i1),bary(i1),num2str(bary(i1),'%2.2E'),...
               'HorizontalAlignment','center',...
               'VerticalAlignment','bottom')
end
title('Threshold Current density for different dimensionality')
ylabel ('Threshold Current Density (A/cm^2)')
xlabel ('Dimensions')
grid on,


%% Additional overlapping Plot
figure;
ax1 = gca;
get(ax1,'Position');
set(ax1,'XColor','k',...
    'YColor','b');
line(E_ph,sp_rate1D, 'Color', 'b', 'LineStyle', '-', 'Marker', '.', 'Parent', ax1, 'DisplayName', '1D','LineWidth',4)
legend show
ax2 = axes('Position',get(ax1,'Position'),...
           'XAxisLocation','bottom',...
           'YAxisLocation','left',...
           'Color','none',...
           'YLim',[0,10*10^4],...
           'YTick',[1*10^4, 3*10^4, 5*10^4, 7*10^4, 9*10^4],...
```

```
            'XColor','k',...
            'YColor','r',...
            'XTick',[],'XTickLabel',[]);
        set(gca, 'YTickLabel', num2str(reshape(get(gca, 'YTick'),[],1),'%.d') );
        ylabel ('Spontaneous Emission Rate (/cm.s)')
line(E_ph,sp_rate2D, 'Color', 'r', 'LineStyle', '-', 'Marker', '.', 'Parent', ax2,'DisplayName', '2D','LineWidth',4)
legend show
ax3 = axes('Position',get(ax1,'Position'),...
            'XAxisLocation','bottom',...
            'YAxisLocation','right',...
            'Color','none',...
            'YLim',[0,10*10^3],...
            'YTick',[1*10^3, 3*10^3, 5*10^3, 7*10^3, 9*10^3],...
            'XColor','k',...
            'YColor','g',...
            'XTick',[],'XTickLabel',[]);
line(E_ph,sp_rate3D, 'Color', 'g', 'LineStyle', '-', 'Marker', '.', 'Parent', ax3,'DisplayName', '3D','LineWidth',4)
legend show
ylabel ('Spontaneous Emission Rate (/cm.s)')
xlabel ('Photon energy (eV)')
xlabh = get(gca,'XLabel');
set(xlabh,'Position',[get(xlabh,'Position') - [0 0.2 0]]);
grid on,
```

snippet/sourcecode/gain1band.m

APPENDIX F

SEMICONDUCTOR NANOWIRE LASER MODELING MATLAB CODE

F.1 FDTD Simulation Results Processing

```
%% Mode_CSNW_FDTD.m A program to solve confinement factor, effective
%% refractive index and mode effective area from the FDTD simulation results
%% Drexel University Zhihuan Wang 08-28-2016

clear;
%% 1. Open refractive index file and get directory
[FileName,PathName] = uigetfile('*.h5','Select the Meep hdf5 structure file',...
'C:\Users\wason\OneDrive\Documents\MATLAB\Laser_threshold');
if isequal(FileName,0)
   disp('User selected Cancel')
else
   f_nr=fullfile(PathName, FileName);
   disp(['User selected ', fullfile(PathName, FileName)])
end
% get info and data for the refractive index hdf5 file
hinfo = hdf5info(f_nr);
dset_nr = hdf5read(hinfo.GroupHierarchy.Datasets(1));
DissStruc=ndims(dset_nr)
SzStruc=size(dset_nr)
struc=squeeze(dset_nr(115,:,:));

%% 2. Open photon wave file and get directory
```

```
[FileName,PathName] = uigetfile('*.h5','Select the Meep hdf5 results file',...
'C:\Users\wason\OneDrive\Documents\MATLAB\Laser_threshold');
if isequal(FileName,0)
    disp('User selected Cancel')
else
    f=fullfile(PathName, FileName);
    disp(['User selected ', fullfile(PathName, FileName)])
end
% get info and data for the photon wave hdf5 file
hinfo = hdf5info(f);
dset = hdf5read(hinfo.GroupHierarchy.Datasets(1));
DissA=ndims(dset)
SzA=size(dset)

%% 3. process the data
xx=squeeze(dset(115,:,:));
yy=squeeze(dset(:,33,:));
zz=squeeze(dset(:,:,33));
% get the corners of the domain in which the data occurs.
min_xx = min(min(xx));
min_yy = min(min(yy));
max_xx = max(max(xx));
max_yy = max(max(yy));
min_zz = min(min(zz));
max_zz = max(max(zz));
% the image data you want to show as a plane.
planeimg = abs(xx);

%% 4. plotting the results
% set hold on so we can show multiple plots / surfs in the figure.
figure;
% surf(yy,zz)
surf(xx);
hold on;
```

```
% desired z possition of the image plane.
imgzposition=-0.25;
surf([0 67],[0 67],repmat(imgzposition, [2 2]),...
    planeimg,'facecolor','texture')
% surf([min_yy max_yy],[min_zz max_zz],repmat(imgzposition, [2 2]),...
%     planeimg,'facecolor','texture')
% set the view angle.
view(45,30);
colormap hsv
colorbar
% set a colormap for the figure.
colormap(jet);
% title
title('Volumetric Mode')
% labels
xlabel('x');
ylabel('y');
zlabel('z');

%% 4. Calculation of effective refractive index and confinement factor
idx = size (67,67);
for i=1:67
    for j=1:67
        if struc(i,j)> 1
        idx (i,j) = 1;
        else
            idx(i,j) = 0;
        end
    prm = logical(idx);
    end
end
wv = 1.55; %wavelength, unit: um
k0 = 2*pi/wv;

```

```
H = sparse(sqrt(struc));
[u, d] = eigs(H,2,'LR');

mode1 = xx; % modal profile of fundamental mode
% mode2 =reshape(u(:,2),Nx,Ny); % modal profile of first order mode
eff_neff1 = sqrt(d(1,1))/k0 % effective index of fundamental mode
% eff_neff2 = sqrt(d(2,2))/k0 % effective index of first order mode

% modal profile of fundamental mode in active area
mode1_active = xx(16:53,16:53);
gamma = norm(mode1_active,2)^2/norm(mode1,2)^2 %confinement factor
```

snippet/sourcecode/Mode_CSNW_FDTD.m

F.2 Steady State Rate Calculation

```
%% CSNW_Laser.m Core-shell nanowire lasing behavior by pumping power
%% By Zhihuan Wang 10-13-2016
%% Source code adapted from McMaster University Hua Wang.

clear
hold off
format long e
% Some variables through all program
global taur taup q d P0 h f sigmagp n0 tfinal bit_seq N

%% 1. Basic constants
cc = 2.99793e8; % Velocity of light in free space, unit: m/s
q=1.60218e-19; % Unit electron charge, unit: C
eV=1.60218e-19; % Unit electron voltage, unit: J
h=6.6256e-34; % Planck's constant, unit: Js
kB = 1.38054e-23; % Boltzmann's constant, unit: J/K or Ws/K

%% 2. CSNW laser Data input
```

```
w = 300.0e-9; % Width of active area, unit:m
d=300.0e-9; % Thickness of active area, unit:m
L=3.0e-6; % Length of active area, unit:m
taur = 1.0e-9; % Time constant or lifetime of carrier(electron and hole),unit:s
tausp = 1.0e-9; % Time constant or lifetime of spontaneous emission, unit: s
sigmag = 3.0e-20; % Gain cross-section coefficient, unit: m^2
nth = 4.5e24; % Threshold carrier density, unit: m^(-3)
alphac = 2000.0; % Cavity loss, unit: m^(-1)
gamma = 0.756; % Confinement factor of laser, unit: none
neff = 2.728; % Effective index, unit: none
ng = 3.5; % Group index, unit: none
p0 = 200.0e-6; % pumping power of laser, unit: W
wv =800e-9; % working wavelength, unit:m

%% 3. Calculation of derived parameters
area_I = w*L; % Area of top section of active area, unit:m^2
area_P = w*d; % Area of cross section of active area, unit:m^2
vg = cc/ng; % Group velocity of light, unit: m/s
taup = 1/(vg*alphac); % Time constant or lifetime of photon, unit: s
sigmagp = sigmag*gamma*vg; % sigmagp = sigmag*gamma*vg
P0 = p0/area_P; % Pumping power density, unit: W/m^2
n0 = nth-1/(sigmagp*taup); % Transparency value of electron density,unit:m^(-3)
f = cc/wv; % The operating frequency, unit: Hz
Pth = h*f*d*nth/taur; % Threshold pumping power density, unit: W/m^2
Power_th = Pth*area_P ; % Threshold pumping power, unit: W
power_analyt = w*h*f*vg*taup*(P0-Pth)/q;% Analytical output power,unit: W

%% 4. Calculation of basic gain coefficient
%4.1 gain with carrier density
nn=0.5e24:0.01e24:10.0e24; gg=sigmag.*(nn-n0);
for i=1:length(nn),if gg(i)<0, gg(i)=0.0; end,end
gg1=sigmag.*sqrt(abs(nn-0.83*n0).^3)*1.0e-12;
for i=1:20,gg1(i)=0.0; end
plot(nn*1.0e-6,gg*1e-2,nn*1.0e-6,gg1*1e-2,'--'); grid;
```

```
xlabel('Carrier density n (1/cm^3)');ylabel('Gain coefficient gm (1/cm)');

%4.2 Output power with input pumping power
pp_temp = taup*vg*h*f/q/L;
ii=1.0e-6:0.1e-7:200.0e-6; pp=pp_temp.*(ii-Power_th);
for i=1:length(ii),if pp(i)<0, pp(i)=0.0; end,end
figure,plot(ii*1.0e6,pp*1.0e3); grid;
xlabel('Pumping Power (uW)');ylabel('Output power (mW)');

%% 5. Output power under steady state
tfinal = 0.5e-9; % Final time, unit: s
options = odeset('RelTol',1e-10,'AbsTol',[1e-10 1e-10 ]);
[T,Y] = ode45('rate_eqn_steady',[0 tfinal], [1e-30 1e-30],options);
power = Y(:,1)*h*f*vg*w*d; % Numerical output power,unit: W
figure; plot(T*1e9,power);grid, % Plot steady state optical power
xlabel('Time(ns)');ylabel('The steady state optical power(W)');
gain = sigmagp*(Y(:,2)-n0); % Numerical output gain
for i=1:length(gain),if gain(i)<0, gain(i)=0.0; end,end
figure; plot(T*1e9,gain);grid, % Plot steady state optical gain
xlabel('Time(ns)');ylabel('The steady state gain Gm');

% function of the steady rate equation
function x = rate_eqn_steady(t,y)
global taur taup q d P0 sigmagp n0 h f
Gm = sigmagp*(y(2)-n0);
yp1 = Gm*y(1)-y(1)/taup;
yp2 = -Gm*y(1)-y(2)/taur + P0/(h*f*d);
x = [yp1 yp2]';
```

snippet/sourcecode/CSNW_Laser.m

VITA

Zhihuan Wang

Place and Date of Birth: Beijing, China — 15 August 1986
Address: 3602 Hamilton St., Apt. 2, Philadelphia, PA, 19104, US
Phone: +1 (215) 2068587
email: zw78@drexel.edu

Work Experience

Present - Jun 2015

Brookhaven National Laboratory, Long Island, NY, US
Visiting Scientist

- Performed SEM/TEM imaging of as-grown and dispersed core-shell nanowires in the clean room of center for fundamental nanomaterials.
- Developed contacts of dispersed single nanowire by FIB, then characterized the device by I-V, C-V measurement and Photoluminescence spectroscopy.

Present - Mar 2012

Drexel University, Philadelphia, PA, US
Graduate Research Fellow

The focus of my research is on characterizing the extremely enhanced optical properties of core-shell nanowires and analyzing the fundamental mechanism of such significant enhancement in light absorption, emission and lasing behavior. Specifically optoelectronic characteristics and light-matter interactions of this novel nano-structure are in my interest. Meanwhile, I also participated in writing proposals for research grants from National Science Foundation, and for access permission to center for fundamental nanomaterials at Brookhaven National Lab.

Present - Mar 2012

Drexel University, Philadelphia, PA, US
Teaching Assistant

Involved dynamically in teaching responsibilities, e.g. running lectures, managing labs and carrying recitations and office hours in various courses including Electronic Devices, Analog Devices, Design for Microcontrollers, Digital Systems, Electrical Engineering Lab, Evaluation and Present Experimental Data, Linear and Dynamic Engineering System, and Statistic Analysis of Engineering System, Introduction to Physics.

Aug 2011 - Feb 2011

IM Flash Singapore LLP., Singapore
(*A Joint-Venture of Intel* and *Micron*)
Process Integration Engineer

- Written analyze report for Special Work Requests and Global Conversion to align new process recipes and tools between Singapore and US.
- Developed, maintained and improved a process module on an advance NAND Flash Memory including design rules for alternative flows.
- Optimized existing process flows and developed creative solutions to meet product requirements.
- Extracted, monitored, analyzed and reacted to inline data, param data and probe data to fix yield issues, add process margin and reduce costs.

Education

Present - Sep 2011	**Drexel University**, Philadelphia, PA, US Doctor of Philosophy in Electrical Engineering Research Field: *Solid State and Photonic Devices* — Advisor: Dr. Bahram Nabet Gpa: 3.93/4
Dec 2010 - Aug 2009	**Nanyang Technological University**, Singapore Master of Science in Electronics Thesis: “Numerical Characterization of Nanowire Transistors and Logic Gates with Parametric Variations” — Advisor: Dr. Xing Zhou Gpa: 4.2/5
Jun 2009 - Sep 2005	**Huazhong University of Science and Technology**, Wuhan, China Bachelor of Engineering in Communication Engineering Thesis in Chinese: “Simulation of Wireless Streaming Media Distribution with Performance Evaluation” — Advisor: Dr. Xu Du Gpa: 82/100

Awards and Certificates

2011-present	Dean’s List for graduate students with an outstanding curriculum, Drexel University
Jan 2016	Allen Rothwarf Endowed Fellowship, Drexel University
Oct 2015	Graduate Student Domestic Travel Grant The Graduate College of Drexel University
Sep 2015	Finalist for Jean Bennett Memorial Student Travel Grant out of 200 applications, The Optical Society (OSA)
Apr 2015	Best Poster Award of Drexel IEEE Graduate Forum’s 7th Annual Research Poster Symposium
Apr 2013	Best Student Poster in Physics, Drexel Research Day
Nov 2010	Best M.S. Dissertation, NTU
Aug 2009	Graduate Fellowship from Minister of Education of Singapore, NTU
May 2009	Best Engineering Undergraduate Thesis, Internet Technology and Engineering Research Center at HUST
Oct 2010	GRE®: 1430 (q:800;v:630) 94th percentile; awa: 3.0/6.0

Publications

1. Z. Wang, B. Nabet,”Nanowire Optoelectronics” *Nanophotonics*, 4.1 (2015): -. Retrieved 17 Mar. 2016, from doi:10.1515/nanoph-2015-0025.
2. Z. Wang, B. Nabet,”Enhancement of Optoelectronic Properties of Nanowires” Submitted to Physical Review Letter, 2017.
3. Z. Wang, P. Dianat, K. Montazeri, B. Taskin, M. Currie, P. Prete, N. Lovergine, B. Nabet,”A Core-Shell Nanowire Platform for Silicon Photonics” in Frontiers in Optics 2017, OSA Technical Digest (online) (Optical Society of America, 2017), paper JW4A.45.
4. K. Montazeri, Z. Wang, B. Nabet,”Confining Low Energy Light with Tapered Conical Plasmonic Nanowires” in Frontiers in Optics 2017, OSA Technical Digest (online) (Optical Society of America, 2017), paper JW3A.97.
5. K. Montazeri, Z. Wang, B. Nabet,”Wave-guiding and Cavity Engineering in Core-Shell Nanowires with Two Dimensional Electron Gas Plasmons” in Frontiers in Optics 2017, OSA Technical Digest (online) (Optical Society of America, 2017), paper FM4A.6.
6. M. Currie, A. Persano, A. Taurino, F. Quaranta, A. Cola, P. Prete, N. Lovergine,P. Dianat, Z. Wang, B. Nabet,”Electro-Optically Sampled Time Response of Core-Shell Nanowires” in

Frontiers in Optics 2017, OSA Technical Digest (online) (Optical Society of America, 2017), paper FTh2D.2.

7. K. Montazeri, Z. Wang, B. Nabet,"Plasmonic Effect of Low-Dimensional Electron Gas in Core-Shell Nanowires" in Frontiers in Optics 2016, OSA Technical Digest (online) (Optical Society of America, 2016), paper JTh2A.6.
8. Z. Wang, B. Nabet,"Light and Rate Management in Nanowires" in Frontiers in Optics 2015, OSA Technical Digest (online) (Optical Society of America, 2015), paper FW5C.6.
9. Z. Wang, M. Currie, P. Prete, N. Lovergine, B. Nabet,"Lasing from As Grown GaAs-AlGaAs Core-Shell Nanowires up to Room Temperature" in Frontiers in Optics 2015, OSA Technical Digest (online) (Optical Society of America, 2015), paper LTh2I.4.
10. Z. Wang, M. Currie, P. Prete, N. Lovergine, B. Nabet,"Room Temperature Lasing of GaAs-AlGaAs Core-Shell Nanowires Grown on Silicon Substrate" Accepted in proceeding of: 2^{nd} EOS Topical Meeting on Optics at the Nanoscale (ONS15), At Capri, Italy. Sep 17-19, 2015.
11. Z. Wang, M. Currie, P. Dianat, G. Konica, P. Prete, N. Lovergine, et al., "On Dimensional Dependence of Interaction of Light and Nano Structures," In proceeding of: Frontiers in Optics, At Orlando, FL. Oct 10-12, 2013.
12. M. Currie, Z. Wang, P. Dianat, P. Prete, I. Miccoli, N. Lovergine, et al., "Large Light Emission Enhancement in GaAs/AlGaAs CoreShell Nanowires," In proceeding of: International Conference on One-Dimensional Nanomaterials, ICON2013, At Annecy, France. Sep, 2013.
13. Zhou, X., Zhu, G. J., Srikanth, M. K., Lin, S. H., Chen, Z. H., Zhang, J. B., ... & Wang, Z. (2010). Xsim: Benchmark Tests for the Unified DG/GAA MOSFET Compact Model. Proc. Nanotech, 2, 785-788.

Poster Presentations & Panels

1. Efficiency and Transition Rate Enhancement of Quantum Well and Core-Shell Nanowire Lasers, Drexel IEEE Graduate Forums 9th Annual Research Poster Symposium, March, 2017.
2. A Novel Alternative Infrastructure for Efficient High Volume Computation, Drexel IEEE Graduate Forums 7th Annual Research Poster Symposium, April, 2015.
3. Volumetric Optical Cavity Modes Allow Room Temperature GaAs/AlGaAs Core-Shell Nanowire Lasing, Drexel Research Day, April, 2014 & Nano for Business, Lehigh University, June, 2014.
4. As-grown GaAs/AlGaAs core-shell nanowire lase at room temperature, Drexel IEEE Forum, March, 2014.
5. Strong Photoluminescence Enhancement of Single GaAs/AlGaAs Core-Shell Nanowire, Drexel Research Day, April, 2013.

Languages

Chinese:	Native Proficiency
English:	Full Professional Proficiency
French:	Basic Knowledge

RESEARCH SKILLS

Semiconductor Fabrication and Characterization:	Photoluminescence\Electroluminescence Spectroscopy, Scanning\Atomic\Tunneling Microscopy, THz Time-Domain Spectroscopy, Electron Beam Induced Current, Low and High-Temperature Electronic Probing and e-beam Lithography
Computer:	Microsoft Excel, Word, PowerPoint, PHP, mySQL, HTML, MATLAB, MEEP, Python, Adobe Photoshop and Illustrator, Sketchup, LINUX, ubuntu, LaTeX

PROFESSIONAL & ACADEMIC MEMBERSHIP

Starting Jun 2015	**OSA, Member**
Starting Jun 2015	**APS, Member**
Starting Aug 2013	**IEEE, Member**

INTERESTS AND ACTIVITIES

Present - AUG 2015

Assistant Operation Officer, Drexel IEEE Graduate (DIG)

- Served the Graduate IEEE community for contacting companies and academic professors for sponsorship and technical talks.
- Organized and served as judge for Drexel IEEE Graduate Forum's 8th Annual Research Poster Symposium

Present - AUG 2015

First Drexel Diversity Council Advisory Board,
Student Center for Inclusion and Culture (SCIC)

- Encouraged open communication and dialogue, collaboration and promotion of inclusive programming on campus.
- Created a space where diverse student leaders collaborate and communicate with each other and the SCIC.

Technology, Open-Source, Programming
Paradoxes in Decision Making, Behavioral Finance, Stock
Basketball, Traveling, Running